Quantitative Techniques in Ichnology and Sedimentology with Examples from the Cretaceous McMurray Formation, NE Alberta, Canada

by

Eric Randall David Timmer

A thesis submitted in partial fulfillment of the requirements for the degree of

Doctor of Philosophy

Department of Earth and Atmospheric Sciences

University of Alberta

Abstract

Process ichnology is a relatively new ichnological tool whereby trace fossils are interpreted as the product of changing infaunal stresses including: salinity fluctuation, reduced oxygenation, high sedimentation rates, reduced nutrient availability, and elevated hydraulic energy. In this paradigm, trace fossils can be used as proxies for paleoenvironmental changes and thus provide excellent support for depositional interpretations. This body of work explores the spatial and temporal relations between the physical/chemical environment and infauna preserved in paleo-estuarine deposits of the Cretaceous McMurray Formation in NE Alberta, Canada using a quantitative process sedimentology and process ichnology approach. The purpose of this work is to develop techniques for promoting the use of the process ichnology framework among ichnologists while coincidentally evaluating tidal depositional interpretations of McMurray Formation inclined heterolithic stratification (IHS).

Visual and quantitative time-series analysis of laminae thickness measurements was performed to evaluate tidal depositional interpretations of IHS. Analyzed laminae provided evidence for tidal modulation during IHS deposition and offered insight on the preservation potential of tidal signatures in moderately bioturbated units.

In order to visualize a process ichnology dataset comprising bioturbation index (a proxy for sedimentation rates and salinity fluctuations) and size-diversity index (a proxy for salinity fluctuation) in 3D, a geomodeling workflow was proposed. This workflow, along with a 3D facies model offered a glimpse

at the spatial and temporal variability of sedimentation rates and salinity affecting communities inhabiting IHS sediment.

A software application, PyCHNO, was designed to optimize the data collection aspects of the process ichnology method. This desktop application allows an ichnologist to collect bioturbation index, size-diversity index and ichnogenera abundances on a bed-by-bed basis from core photographs efficiently and systematically. Collected data can be input into geomodels, visualized as process ichnology logs, or analyzed statistically.

Fluctuations in physical and chemical stresses, proxied using data collected with PyCHNO, temporally and spatially affected McMurray Formation deposition. Spatially, ecological stresses were interpreted to represent small-scale (*i.e.* point-bar scale) ecological variability and estuarine-scale ecological variability. Estuarine-scale, cyclical ecological stress patterns are temporally coincident with El Niño cyclicity and were interpreted to represent responses to changes in precipitation during McMurray Formation deposition.

Point-bar scale ichnological variability was examined using a dataset collected within a seismically-constrained point-bar geobody. From ichnonetwork analysis, bed scale ichnogeneric composition measured throughout the point-bar's growth and evolution remained relatively stable, suggesting relatively stable ecological conditions. Time-series analysis of ichnological data did not yield definitive spatial or temporal signals, which further reinforced interpretations of relatively stable ecological conditions during the point-bar's deposition.

Computer simulations and engineering analogues of helical burrowing behavior, similar to *Gyrolithes*, which is locally preserved in dense, monogeneric assemblages in McMurray Formation IHS were programmed to better understand the ecological advantages of this ethology. Resulting computations suggest that helical burrowing behavior can represent a technique for avoiding

iii

existing burrows and that this behavior performs best in homogeneous food distribution landscapes when compared to other deposit feeding strategies.

Preface

This thesis represents the original work of I, Eric Randall David Timmer.

Chapter 2 of this thesis is published as: Timmer, E.R., Gingras, M.K., Morin, M.L., Ranger, M.J. and Zonneveld, J.P., 2016. Laminae-scale rhythmicity of inclined heterolithic stratification, Lower Cretaceous McMurray Formation, NE Alberta, Canada. Bulletin of Canadian Petroleum Geology, 64(2), pp.199-217. I performed data collection, data analysis and wrote the majority of the text; Morin, M.L. wrote the section on continuous wavelet transforms; Gingras, M.K., Ranger, M.J., and Zonneveld, J.P. provided edits and expert input.

Chapter 3 of this thesis is published as: Timmer, E.R., Botterill, S.E., Gingras, M.K. and Zonneveld, J.P., 2016. Visualizing a process ichnology dataset, Lower Cretaceous McMurray Formation, NE Alberta, Canada. Bulletin of Canadian Petroleum Geology, 64(2), pp.251-265. I performed data collection, data analysis and wrote the majority of the paper; Botterill, S.E. wrote sections of the introduction (process ichnology background section); Gingras, M.K. and Zonneveld, J.P. provided edits and expert input.

Chapter 4 of this thesis is published as: Timmer, E.R., Gingras, M.K. and Zonneveld, J.P., 2016. PYCHNO: a core-image quantitative ichnology logging software. Palaios, 31(11), pp.525-532. I wrote the software and wrote the paper. Gingras, M.K. and Zonneveld, J.P. provided edits and expert input.

Chapter 5 of this thesis is published as: Timmer, E.R., Gingras, M.K. and Zonneveld, J.P., 2016. Spatial and temporal significance of process ichnology data from silty-mudstone beds of inclined heterolithic stratification, Lower Cretaceous McMurray Formation, NE Alberta, Canada. Palaios, 31(11), pp.533-548. I collected data, analyzed the data and wrote the paper. Gingras, M.K. and Zonneveld, J.P. provided edits and expert input.

To Thérèse Gervais (1935-2017)

For your openmindness, love of travel, and lifelong dedication to education.

"We take a handful of sand from the endless landscape of awareness around us and call that handful of sand the world."

— Robert M. Pirsig

Acknowledgements

This thesis would not have been possible without the support of numerous people–it takes a village to raise a thesis. I would like to thank the following people:

Dr. Murray Gingras for discussing life and sports, for supporting independent research avenues, and of course providing endless discussions on anything geological; Dr. John-Paul Zonneveld for encouragement, loyalty and for being incredibly expedient with edits and feedback; Dr. Mike Ranger for providing expert advice during McMurray field trips; members of my candidacy committee, Dr. Octavian Catuneanu, Dr. Jeff Kavanaugh, Dr. David Potter. And, members of my defence committee, Dr. George Pemberton, Dr. Stephen Hubbard, and Dr. Mike Ranger.

Members of the McMurray Consortium: especially, Dr. Shahin Dashtgard, Dr. James MacEachern, Dr. Stephen Hubbard, Dr. Doug Stewart, Matt Caddel, Jonah Resnick, Lucian Rinke-Hardekopf, Chloe Chateaux, Cheryl Hodgson, Derek Hayes, and Qi Chen for McMurray Formation sessions and discussions.

Contents

List of Tables

List of Figures

Chapter 1

Introduction

Cretaceous McMurray Formation strata from the Athabasca region in Alberta, Canada, constitute a world class laboratory for exploring marginal-marine depositional processes from sedimentological and ichnological perspectives. Indeed, there are approximately 25,000 cored wells in this region, many of which are publicly accessible. Intense drilling activity is due to the large economic potential of the region's bitumen hosting Cretaceous strata (152.21 x $10^6 m^3$; Hein *et al.* 2013). Extensive coring programs have been undertaken in order to characterize this resource for development. Considering this substantial geological dataset, a relatively large number of recent studies, characterizing subsurface and outcrop study areas have been published (*e.g.* Crerar and Arnott 2007; Hubbard *et al.* 2011; Labrecque *et al.* 2011b; Labrecque *et al.* 2011a; Musial *et al.* 2012; Nardin *et al.* 2013; Martinius *et al.* 2015; Broughton 2016; Harris *et al.* 2016; Jablonski and Dalrymple 2016; Hayes *et al.* 2017). A recurring theme is the lack of agreement on the relative degree of fluvial (freshwater) versus tidal-estuarine (brackish) influence on McMurray Formation deposition.

The McMurray Formation represents one of the first documented examples of brackish water trace fossil suites in paleoenvironmental studies (Pemberton *et al.* 1982). Since this initial work, numerous studies have supported McMurray Formation depositional interpretations with ichnological data (*e.g.* Ranger and Pemberton 1988; Ranger and Pemberton 1992; Ranger and Pemberton 1997; Lettley *et al.* 2005a; Lettley *et al.* 2005b; Crerar and Arnott 2007; Musial *et al.* 2012; Harris *et al.* 2016; Gingras *et al.* 2016). Recent research has focused

on the process ichnology approach (*e.g.* Shchepetkina *et al.* 2016; Timmer *et al.* 2016c). The fundamental axiom of process ichnology is that variability in hydraulic energy, oxygenation, salinity, sedimentation rates, and substrate cohesion can be collectively proxied in the rock record by trace fossil observations and measurements (*cf.* Gingras *et al.* 2011). This thesis employs a quantitative process ichnology and sedimentology approach in order to evaluate tidal depositional interpretations of the McMurray Formation and to refine our understanding of the spatial and temporal effects of paleoecological stresses on infaunal communities.

Chapter 2 focuses on characterising the periodic nature of interlaminated portions of inclined heterolithic stratification (IHS) from Pierre River Area (Township 97, Ranges 10-11W4) cores. Inclined Heterolithic Stratification, characterized by dipping, interbedded and interlaminated sandstone and mudstone lithosomes comprises a major portion of the Athabasca oil sands. In recent studies, fluvial processes have been interpreted to be the major cause of lithological variations and accompanying cyclicity in IHS. The objectives of this research are applying quantitative and visual frequency analysis techniques to determine and interpret the laminae-scale cyclicity of IHS lithosomes. The IHS in the Pierre River area is subdivided into five lithosomes based on distinct ichnological and sedimentological features. For each lithosome, Continuous Wavelet Transforms, applied to measurements of laminae or bed thicknesses, treated as pseudo time-series, convert these time-series to the frequency domain in order to determine the cyclicity of interlaminated portions of lithosomes. Visual identification of cycle breaks is accomplished by splitting series into cycles following troughs and peaks. The results from the analysis demonstrate that the interlaminated portions of Inclined Heterolithic Stratification in the Pierre River Area preserve cyclic patterns that are consistent with semidiurnal synodic neap-spring tidal periodicity. Even in bioturbated intervals, interlaminated sandstone and mudstone is indicative of tidal cyclicity. The thicker sandstone or mudstone beds disrupting the tidally interlaminated portions of IHS are interpreted to reflect variations in fluvial flux. This study gives a better understanding of the tidal regime during Mc-

Murray Formation deposition, of the processes governing IHS laminae scale lithological variability and of the preservation potential of tidal signatures in moderately burrowed intervals.

In Chapter 3, a geomodeling approach is applied for visualizing a process ichnology dataset from the Pierre River Area (Township 97, Ranges 10-11W4) in 3D. Two process ichnology parameters were collected and visualized for this study: (1) bioturbation index (BI), a measure of the degree of bioturbation of a given interval, which can be used as a proxy for sedimentation rate; and (2) size-diversity index (SDI), the product of the maximum burrow diameter and the number of ichnogenera found within a given interval, which can be used as a proxy for salinity condition variability affecting an infaunal population. These data are modeled using standard geostatistical techniques for visualization of spatial trends. The modeled ichnology data are compared to sedimentary facies in order to interpret the dominant stresses occurring at the time of infaunal colonization. Several interpretations are made from the process ichnology model. The size diversity index and bioturbation index values from inclined heterolithic stratification show strong spatial variability related to variable depositional conditions across and along IHS bar forms. And, facies interpreted to represent tidal flat deposition are distinguishable on the basis of relatively high bioturbation index values coupled with intermediate to low size diversity index values. Overall, we interpret variability in salinity and sedimentation rates to be the dominant infaunal stresses in the studied stratigraphic interval.

Chapter 4 demonstrates PyCHNO, a computer software application, which was developed to optimize the process ichnology data collection workflow and to standardize the presentation of process ichnology data. PyCHNO is a desktop application that allows ichnologists to collect BI, SDI, and ichnogenera abundance from core photographs on a bed-by-bed basis. Collecting such detailed process ichnology data was extremely time-consuming and inaccurate before this software was developed. PyCHNO significantly improves the process ichnology data collection workflow. Data collected with PyCHNO can be exported as spreadsheets or as visual logs. Datasets collected with PyCHNO

comprise a large portion of the data analyzed in Chapter 5 and chapter 6.

Chapter 5 focuses on quantitative ichnological data of silty-mudstone beds from IHS in order to understand the spatial and temporal controls affecting bioturbation in IHS. Data collected for this study include bed-scale averaged bioturbation intensity, size-diversity index, and ichnogenera abundances. These data were used to assign each bed into one of 10 clusters using K-Means clustering. The clusters were ranked according to interpreted intensity of cumulative depositional ecologic stress. Time-series, where each silty-mudstone bed represents a time-step with a corresponding ecologic stress value, were constructed from the interpreted ecologic stress cluster analysis results. To identify and interpret spatial and temporal variation in the ichnological time-series, two time-series analysis methods were employed: Dynamic Time-Warping and Continuous Wavelet Transforms. Dynamic Time-Warping is used as a descriptor of the spatial similarity between ecologic stresses, and continuous wavelet transforms are used to interpret cyclical patterns in the ichnological time-series. Spatially, the variability and cyclicity observed in the ecologic stress time-series can be linked to estuary scale stresses and more localized stresses (*i.e.* bar-form scale depositional stress). This is reflected by the relatively similar periodicities observed in the ecologic stress time-series. Temporally, cyclical ecologic stress patterns occur somewhat predictably in periods of approximately four, or multiples of four, which are consistent with El Niño cyclicity.

The purpose of Chapter 6 is to establish a descriptive, statistical ichnological framework for the variability of preserved ichnological characteristics within a meandering brackish water point-bar. The evolution of a point-bar is characterized by distinct chemical and physical ecological parameters. The spatial distribution of these parameters has not been established within an ichnological framework. A seismically and core delineated point-bar in the McMurray Formation presents an ideally defined geobody for determining the relation between process ichnology and point-bar evolution. In order to establish a preliminary framework relating changes in ichnological parameters with point-bar evolution, ichnological parameters including size-diversity index and

4

bioturbation index are analyzed using ichnonetwork analysis (*sensu* Baucon and Felletti 2013) as well as a time-series analysis approaches. From ichnonetwork analysis, ichnogeneric bed composition measured throughout the point-bar's evolution are relatively stable, suggesting stable salinity and sedimentation rates. A cyclical pattern in changes in physical and chemical parameters was not found from time-series analysis, which also suggests that ecological conditions remained stable spatially and temporally during the point-bar's evolution.

Chapter 7 focuses on computer simulations of helical burrowing behaviors, similar to *Gyrolithes*, a trace fossil commonly found in the McMurray Formation. High density, monogeneric assemblages of elongate helical burrows are commonly observed in estuarine strata of the McMurray Formation. However, the advantage of this specific burrow morphology is not properly understood. These high density assemblages likely represent an optimized ethology for specific ecological conditions. In order to elucidate some of the optimization parameters governing this ethology, computer simulations and engineering analogues are used. Computer simulations include (1) testing if helical burrows can form in response to 3D avoidance of existing burrowed space; and (2) comparing helical burrowing behavior to various randomized and optimized feeding behaviors in different 3D food distribution landscapes (*e.g.* random food distribution versus layered food distribution). From this work, we find that helical burrowing can be a response to phobotaxis (avoidance of existing burrows) and that helical burrowing behavior is optimized for exploiting homogeneous food distribution landscapes that are densely populated with other worms. Engineering analogues determine that helical burrowing is a relatively efficient method for burrow irrigation and anchoring compared to vertical burrows.

This thesis explores the spatial and temporal relations between changing physical and chemical environmental parameters with an emphasis on those affecting infauna, as proxied by process ichnology data. These findings, along with sedimentary laminae analysis, support tidal depositional interpretations for the studied intervals of the McMurray Formation.

Chapter 2

Laminae-Scale Rhythmicity of Inclined Heterolithic Stratification

2.1 Introduction

The Lower Cretaceous McMurray Formation, located in northeastern Alberta, Canada, is the primary host of the Athabasca Oil Sands. The McMurray Formation is generally interpreted to represent fluvial to estuarine deposits of a transgression of the Boreal sea over a karsted Devonian landscape during the Aptian to Albian (*e.g.* Ranger and Pemberton 1997; Broughton 2013). Inclined Heterolithic Stratification (IHS) is common in the McMurray Formation. Mossop (1980) and Mossop and Flach (1983), first characterized the IHS of the McMurray Formation in detail. Pemberton *et al.* (1982) described the ichnology of McMurray IHS deposits, formulating the brackish-water ichnology model primarily from these observations. Smith (1988), reported tidal bundles within some McMurray IHS, which combined with trace-fossil interpretations, clearly demonstrated that tides and the presence of brackish water influenced at least some IHS deposition in the McMurray Formation. Lettley *et al.* (2005b), Lettley *et al.* (2005a) completed the most detailed ichnological and sedimentological evaluation of IHS in the McMurray Formation to date. This work focused on the interpretation of the processes responsible for generating lithological variations in IHS in the framework of a schematic tripartite estuary. More recent work has focused on the mud-sand content trends and geometry

of IHS point or counter point bar deposits (*e.g.* Smith *et al.* 2009; Hubbard *et al.* 2011; Labrecque *et al.* 2011b; Labrecque *et al.* 2011a; Fustic *et al.* 2012; and Nardin *et al.* 2013). These papers concluded that the IHS intervals of the McMurray Formation are dominantly fluvial in nature.

Inclined Heterolithic Stratification (*sensu* Thomas *et al.* 1987) is characterized by dipping beds of regularly interbedded sandstone and mudstone, which in the case of the McMurray Formation, are agreed to form by the lateral accretion of point bars. In tidal-fluvial and estuary settings, the mud-sand distributions of IHS may be a product of variable current energies at different temporal scales and from where sediment is sourced. The most general interpretation of IHS is that mud lithosomes are sourced from the fluvial reaches, that there are seaward-transported fluvial-sand lithosomes, and also present are landward-transported tidal-sand lithosomes (*e.g.* Schoengut 2011). Each lithosome is sedimentologically and palaeontologically distinct. Detailed sedimentological and ichnological observations, as well as an understanding of IHS sand-mud distributions, are thus essential to understand the degree of the fluvial or tidal energy that acted on IHS deposition.

Energy variations ascribed to tides result from lunar rhythms and include diurnal, semidiurnal, weekly, fortnightly, seasonal and annual rhythms, but are dominated by diurnal through to fortnightly cycles. Variability in fluvial flux, on the other hand, reflects seasonal, annual or decadal variations in streamflow. As such, detailed documentation and analyses of IHS rhythmicity can clearly differentiate between tidal and fluvial influences on sedimentation. IHS cyclicity based on ichnological data (*e.g.* Gingras *et al.* 2002; Lettley *et al.* 2005b) and thickness data (*e.g.* Choi *et al.* 2004) has been qualitatively examined. However, the quantitative study of the cyclic nature of the interbedded or interlaminated sandstone and mudstone layers of IHS has undergone relatively little study. Labrecque *et al.* (2011a), quantitatively assessed the cyclicity of IHS using gamma-ray logs, which have decimeter-scale resolution. Hovikoski *et al.* (2008) used outcrop datasets with millimeter-scale resolution to identify tidal cyclicity.

This study focuses on the application of quantitative and visual cyclic-
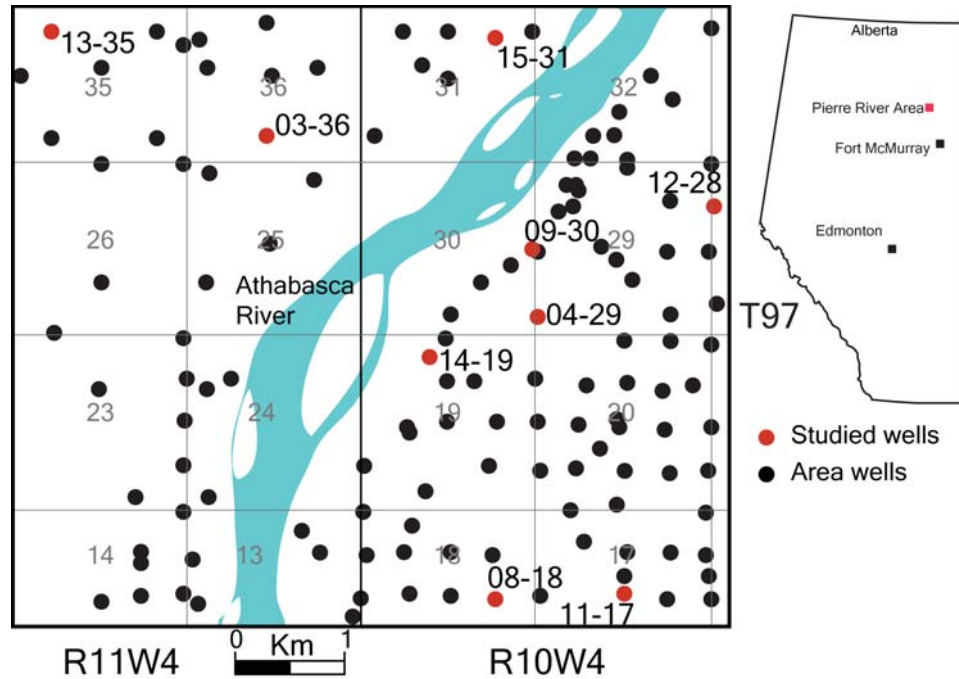
Figure 2.1: Location map of study area showing the distribution of well data used in this study.

ity analysis methods to determine IHS laminae-scale cyclicity. The IHS is split into 5 lithosomes in order to demonstrate rhythmicity in diverse and sporadically distributed IHS lithologies. The purpose is to determine if tidal modulation is preserved in these wavy interlaminated mudstone and sandstone lithologies. And, in doing so, provide crucial evidence of some aspects of the McMurray Formation tidal processes.

2.2   Study Area

The study area is located within Township 97, Ranges 10-11, west of the Fourth Meridian approximately 85 kilometres northwest of Fort McMurray, in northeastern Alberta, Canada (Figure 2.1). The study area contains 148 cored wells, 12 of which are available at the Alberta Energy Regulators Core Research Centre. Of these, 9 wells were selected for this study on the basis of vintage and appreciable IHS preservation.

In the study area, the McMurray Formation overlies the Devonian Beaverhill Lake Group, which consists of calcareous mudstone and brachiopod-floatstone

8

and -rudstone units. The Devonian strata in the study area are part of a regional structural trough, which influenced McMurray Formation deposition (*cf.* Broughton 2013). The Clearwater Formation, which generally overlies the McMurray Formation, has been erosionally removed from the study area with the exception of a small sliver in the southwest region and was consequently not observed in core. Instead, Quaternary sand and gravel deposits overlie the McMurray Formation over most of the study area. Erosional truncation of the McMurray Formation section in the study area makes choosing an appropriate stratigraphic datum difficult within this area. The schematic stratigraphy of the study area is outlined in Figure 2.2. Note that age dating of the formation within the study area has not been conducted.

2.3 Methods

2.3.1 Data Collection

Lithology, contact types and physical and biogenic sedimentary structures were recorded from 9 cored wells. Bioturbation index (BI) was recorded following the Reineck (1967), and Taylor and Goldring (1993) scheme wherein BI 0 represents no bioturbation and BI 6 represents complete bioturbation. Additionally, high-resolution photographs of the core were obtained. These were subsequently lens corrected to remove distortion biases using Adobe Photoshop®. From the core data (*i.e.* lithology, contact types, physical and biogenic sedimentary structures, and BI), IHS intervals were identified, and subdivided into 5 lithosomes.

From each lithosome, intervals with the largest number of interlaminated sandstone and mudstone were selected for cyclicity analysis. In the selected intervals, the thickness of each sandstone and mudstone lamina were measured and tabulated. In order to collect consistent data, the thickness measurements were collected vertically (*i.e.* parallel to the core-sleeves). The data collection and quantitative analysis workflow is summarized in Figure 2.3.
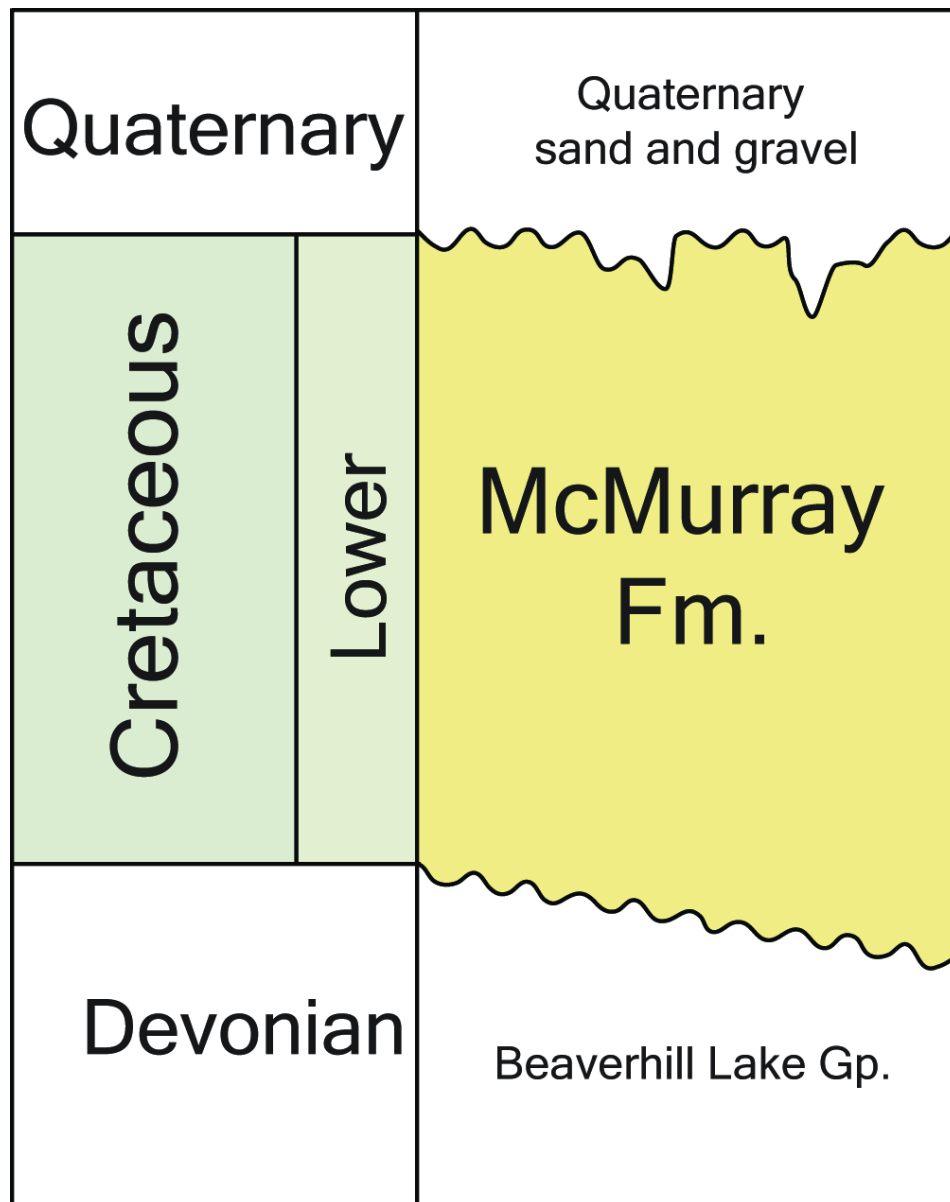
Figure 2.2: Generalized stratigraphic chart of the study area, showing the Cretaceous McMurray Formation unconformably overlying Devonian Carbonates. The McMurray Formation is eroded by Quaternary sediment to variable extent in the study area. The McMurray Formation is generally agreed to be Albian to Aptian in age; however, no age dating has been completed in the study area.
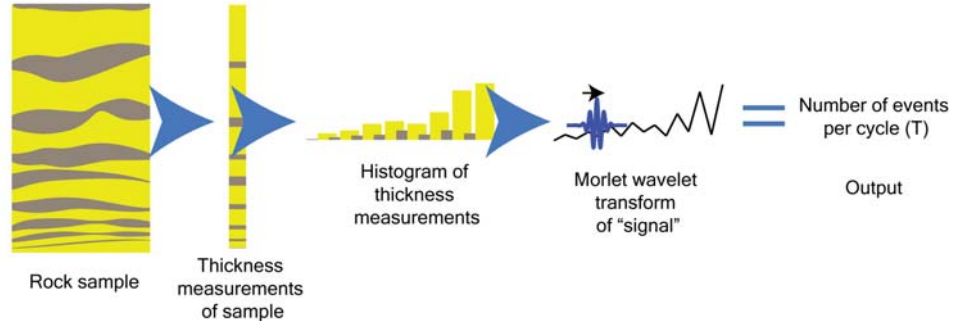
Figure 2.3: Schematic diagram highlighting the quantitative methods used in this study. Core thickness data is collected and converted into a pseudo-time signal, where consecutive laminae measurements represent time-steps, and thickness data represents the signal at each time step. The signal is then analyzed with a Morlet wavelet transform, from which the main periodicities (*i.e.* number of events per cycle) are determined.

2.3.2 Continuous Morlet Wavelet Transform

To determine cyclicity from variations in sediment thicknesses, the thickness variations are considered as a time-series, where each depositional event corresponds to a successive time step. The periodicities of a signal, or the inverse of frequencies, are determined by converting time-series signals from the time domain to the frequency domain. The Fourier Transform, the method most widely used for determining the cyclicity of signals, calculates the strength of each individual frequency that is present in the original time signal; however, it does not retain any of the original signal's temporal (time or space) information. Therefore, if the signal has a strong frequency component localized in a specific temporal region of the data, the Fourier Transform will see this information, but it cannot distinguish where in the signal the frequency component is. In order to locate the changes in frequency power over the signal length, a Wavelet Transform, is applied instead.

A Wavelet Transform (WT) analyzes a time signal, $f(t)$, using a normalized zero mean wavelet that is limited in the time domain, $\psi(t)$ as a base function (Goupillaud *et al.* 1984). The original wavelet (*i.e.* mother wavelet) is dilated and translated into numerous daughter wavelets:

$$\psi_{a,b}(t) = \frac{1}{\sqrt{a}}\psi\left(\frac{t-b}{a}\right) \qquad (2.1)$$

where a is the scale (dilation) of the mother wavelet, b is the position (translation) and $\psi_{a,b}$ is the resulting daughter wavelet. These daughter wavelets are compared to the time signal by a convolution:

$$WT(a,b) = \frac{1}{\sqrt{a}}\int \psi * \left(\frac{t-b}{a}\right)f(t)dt \qquad (2.2)$$

where $\psi*$ is the complex conjugate of the wavelet. The outputs of the WT are wavelet coefficients at varying scales and positions. The WT maps a 1-dimensional time signal into 2-dimensional wavelet coefficients. Increasing (or decreasing) the scale of the wavelet stretches (or narrows) the wavelet, focusing the transform on low (or high) frequencies. Therefore, the scale or dilation of the analyzing daughter wavelet in the WT corresponds to the frequency component of the signal. As the scale of the wavelet is varied at each position in the original time signal, low frequency components are seen at large scale values and high frequency components are seen at small scale values. The WT coefficients show the amplitude of the features versus the scale and how it varies with time. The WT coefficients are then converted to the square signal power and the scale is converted to the signal period.

2.4 Results: IHS Lithosomes

The IHS in the study area has been subdivided into five lithosomes based on the presence or absence of bioturbation, BI, the presence or absence of interlaminated sandstone and mudstone, and the lithology of the sediment separating interlaminated sandstone and mudstone or structureless mudstone packages. The purpose of separating IHS into lithosomes is to relate the cyclicity analysis to the various IHS lithologies observed in the study area. The lithosomes are summarized in Table 2.1 and shown in Figures 2.4A-G, 2.5A-H and 2.6A-D. The schematic representations of the lithosomes are depicted in Figure 2.7A-E. The interpreted spatial distributions of the IHS lithosomes are shown in Figure 2.8. Lithosomes 1 and 2 occur sporadically throughout

12

and lithosomes 3, 4 and 5 are more spatially consistent. It is important to note that without dipmeter or seismic data, the inter-well genetic relations of lithosomes are impossible to resolve.

2.4.1 L1: Interlaminated sandstone and mudstone separated by thick sandstone (Figure 2.4A-C; 2.7A)

Lithosome 1 (L1) consists of very fine- to medium-grained sandstone interlaminated with mudstone, interbedded with dm-thick, generally medium grained-sandstone packages. The interlaminated sandstone and mudstone ranges from flaser to lenticular bedding, but is primarily wavy bedded. Soft-sediment deformation features may be present within the interlaminated units. Locally, the interlaminated unit grades upwards into the decimeter thick sand beds. However, the bases of the dm-scale sandstone packages are typically sharp. The sandstone beds appear to be structureless, but faint current ripples can be observed. Bioturbation is virtually absent, but where present, exhibit low bioturbation intensities, and consists of a monospecific *Planolites* suite. Bioturbation is limited to the interlaminated sandstone and mudstone packages.

Table 2.1: Summary of IHS lithosome characteristics.

IHS Lithosome	Description	Contacts	Package Thicknesses (m)	Grain Size	Sedimentary Structures	Bioturbation
L1	Wavy parallel rhythmically interlaminated sandstone and mudstone separated by thick sandstone packages.	Interlaminated top: sharp; interlaminated base: generally sharp	Lithosome:0.2-1.25; interlaminated: 0.10-0.20, thick:0.10-0.60.	Silt and very fine- to medium- well; sand in interlaminated sandstone and mudstone intervals; medium-grained sand in thick sandstone packages	Wavy parallel, lenticular to flaser as well; sediment deformation features present in interlaminated sandstone and mudstone intervals; generally structureless thick sandstone packages.	Virtually absent; rare *Planolites* in interlaminated sandstone and mudstone packages.
L2	Wavy parallel rhythmically interlaminated sandstone and mudstone separated by thick structureless mudstone packages.	Interlaminated top: generally gradational; interlaminated base: generally gradational	Lithosome:0.25-4.25; interlaminated: 0.05-0.10; thick: 0.05-0.15;	Silt and fine- to medium-grained sand in interlaminated sandstone and mudstone portions.	Wavy parallel laminae and syndepositional faulting in the interlaminated mudstone and sandstone packages; generally structureless thick mud intervals.	Very low bioturbation index; monospecific *Planolites* in both the interlaminated mudstones and sandstones and the structureless mud intervals.
L3	Bioturbated structureless mud packages separated by relatively thick sand intervals.	mudstone top: biogenically pitted, sharp; mudstone base: sharp or gradational	Lithosome: 0.15-11.25; mudstone 0.03-0.20; sandstone 0.10-0.40.	Fine- to medium-grained thick sandstone packages .	Occasional wavy parallel interlaminated otherwise structureless mud intervals, the bioturbated mudstone packages; Overall, both the bioturbated mudstone and the thick sandstones are structureless.	Bioturbation occurs mostly at the top of the otherwise structureless mud intervals. Bioturbation consists of *Arenicolites*, *Skolithos*, *Planolites* and more rarely robust *Gyrolithes*. Bioturbation indexes here range from 1-5. Sandstone intervals are generally devoid of visible traces, but when present, bioturbation consists of *Cylindrichnus*.
L4	Bioturbated wavy parallel interlaminated sandstone and mudstone separated by thick sandstone packages.	Interlaminated top: sharp; interlaminated base: sharp or gradational	Lithosome: 0.5-8.5; interlaminated: 0.1-0.3; thick: 0.05-0.4;	Thick sandstone packages consist of silt and fine- to medium-grained sand; interlaminated sandstone and mudstone; thick sandstone packages consist of silt to medium-grained sand.	Interlaminated sandstone and mudstones range from wavy parallel to lenticular to more rarely flaser bedding; Synaeresis cracks in mudstone component of interlaminated sandstone and mudstone; thick sandstone packages are generally structureless, but may contain climbing ripples, mud clasts and soft sediment deformation features.	*Cylindrichnus, Planolites, Arenicolites* and *Skolithos* dominate interlaminated sandstone and mudstone packages. *Cylindrichnus* extending into the sandstone packages from the interlaminated mudstones and sandstones is observed. Biognic pitting at the top of the interlaminated packages represents the only other example of bioturbation in the thick sandstone packages.
L5	Variably bioturbated interlaminated mudstone and sandstone packages to structureless mudstone packages separated by very thick structureless to cross-bedded sandstone intervals	mudstone top: sharp ; mudstone base: sharp	Lithosome: 0.5-17.35; mudstone: 0.03-0.2; thick: 0.1-3.5;	Medium-grained sand in the thick sandstone packages; thin interlaminated mudstone and sandstone packages generally have fine-grained sand.	Curent ripples, sporadic mud clasts and soft-sediment deformation features in otherwise structureless thick sandstone intervals; wavy bedded interlaminated sandstone and mudstone to structureless mudstone units.	Bioturbation is overall rare to absent. Pitting of mudstone layers represents the most common features. *Cylindrichnus* descending from overlying mud horizons as well as extremely rare *Arenicolites* have been observed as well. Very rare silt-lined occuring within the thick sandstone intervals have observed as well.

14
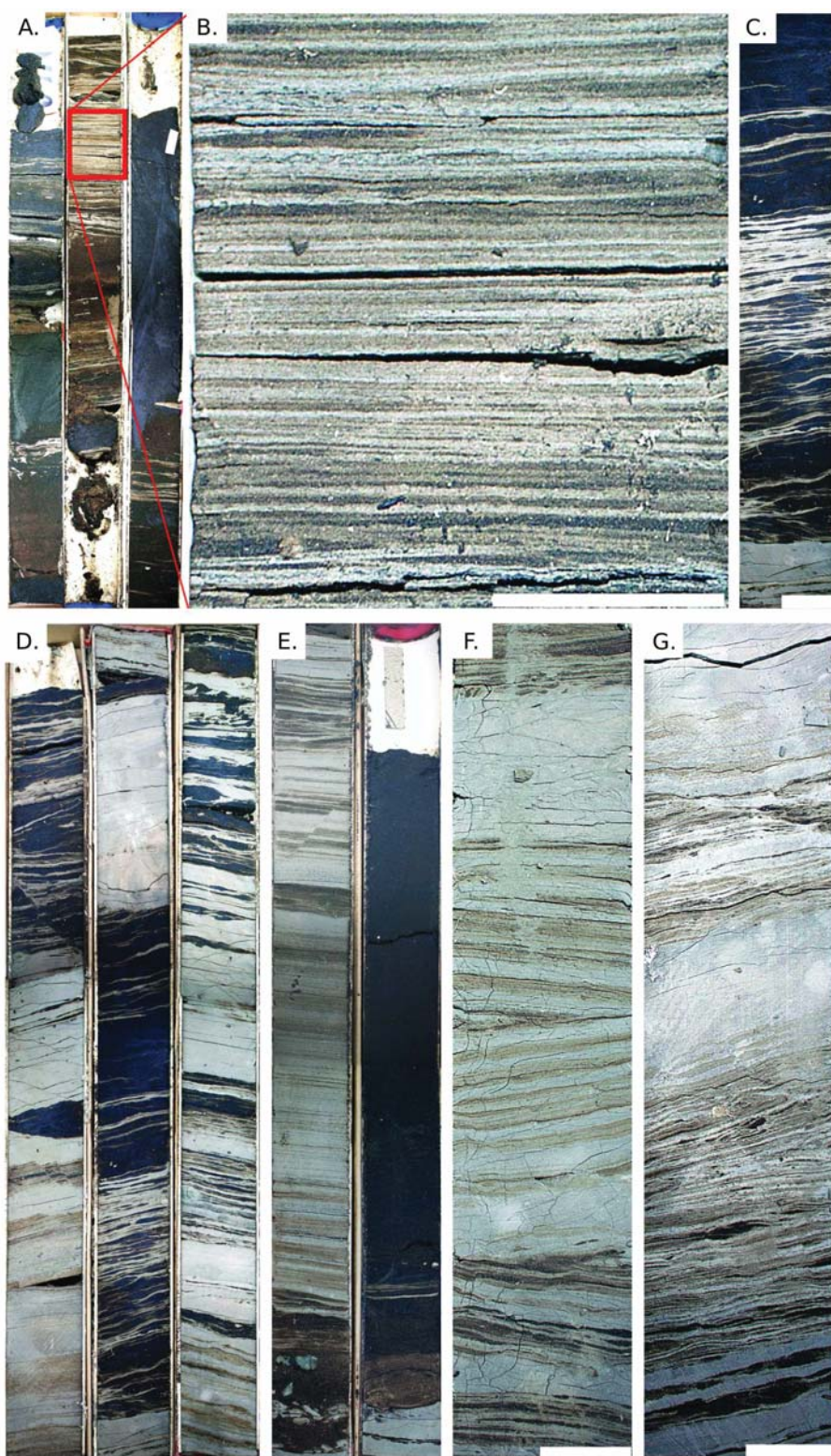
Figure 2.4: (Continued on the following page.)

Figure 2.4: A–G. A. Boxshot of L1 example (sleeves are 75 cm in length) showing inclined and thinly interlaminated sandstone and mudstone punctuated by a thick sandstone interval. The red box denotes the area of Figure 2.4B. Boxes are from 03-36-097-11W4M. B. Close up of Figure 2.4A, showing rhythmically interlaminated sandstone and mudstone. White box is 5 cm in width. C. Close up of L1 example from 14-19-097-10W4M showing an interlaminated sandstone and mudstone interval capped by a thick sand package. The mudstone intervals are overall thicker within this specific example than the example from Figure 2.4A. White box is 5 cm in width. D. Boxshot of L2 example (sleeves are 75 cm in length) showing inclined and interlaminated sandstone and mudstone bound by thick mud packages from 14-19-097-10W4M. E. Boxshot of L2 example (sleeves are 75 cm in length) showing more thinly interlaminated sand and mud separated by thick mud packages from 15-31-097-10W4M. F. Close up of lithosome 2 from 03-36-097-11W4M. White box is 5 cm in width. G. Close up of Lithosome 2 from 14-19-097-10W4M. White box is 5 cm in width.

2.4.2 L2: Interlaminated sandstone and mudstone separated by structureless mudstone (Figure 2.4D-G; 2.7B)

Lithosome 2 (L2) consists of very fine- to fine-grained sandstone interlaminated with mudstone separated by thick (cm to dm) structureless mudstone. The interlaminated sand and mudstone succession is generally wavy parallel bedded. Laminae from these intervals commonly show thickness variations. The mud/sand content of the interlaminated packages is variable. Micro-faulting is common in the interlaminated packages. The mudstone beds that bound the interlaminated beds are generally structureless. The bases of the structureless mudstone packages are typically sharp. Bioturbation is rare. Where present, bioturbation consists of BI 1-2, monospecific *Planolites* assemblage, which can be found in both the interlaminated sandstone and mudstone packages and the structureless mudstone packages.

2.4.3 L3: Bioturbated structureless mudstone separated by thick sandstone (Figure 2.5A-D; 2.7C)

Lithosome 3 (L3) contains mudstone beds that are either sharp based over structureless sandstone, or grade from interlaminated mudstone and sandstone. The sandstone beds are fine- to medium-grained and sharply overlie mudstone beds. Bioturbation within the mudstone is generally concentrated at the top, but in some examples burrows penetrate through the mudstone bed into the underlying sandstone. Bioturbation within the structureless mudstone consists of *Planolites*, *Skolithos*, and *Arenicolites*. In the 15-35 well, the mudstone is bioturbated by a robust *Gyrolithes* assemblage that is not observed in other wells. Bioturbation within the sandstone packages consist of *Cylindrichnus* that extend from overlying mudstone packages. The BI varies from 1 to 5.
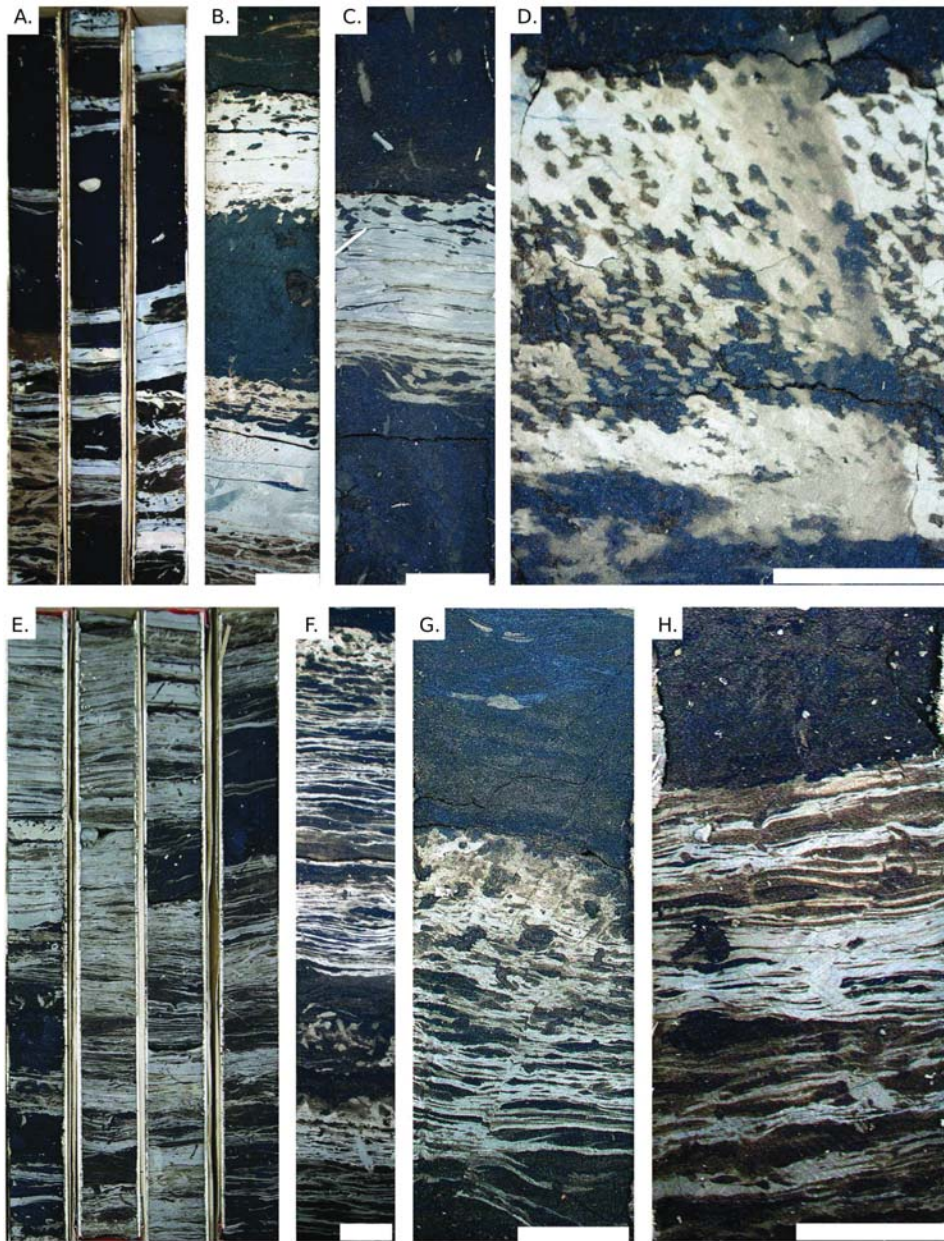
Figure 2.5: (Continued on the following page.)

Figure 2.5: A–H. A. Boxshot of L3 example (sleeves are 75 cm in length) showing structureless mud intervals, with bioturbation at the top of beds separated by thick sand packages. Boxes are from 08-18-097-10W4M. B. Close up of L3 example from 14-19-097-10W4M. Note the interlaminated sandstone and mudstone interval at the base of the lower mudstone package and the Planolites and Arenicolites burrows, which occur mostly at the top of the mudstone beds. The thick sandstone package is unbioturbated. White box is 5 cm in width. C. Close up of L3 example from 03-36-097-10W4M. Note the *Planolites* burrows occurring at the top of the mudstone beds and the paired *Arenicolites* occurring at the base of the mud bed. *Cylindrichnus* is present in the upper thick sand package. White box is 5 cm in width. D. Close up of L3 example from 13-35-097-11W4M. Note the *Gyrolithes* burrows occurring at the top of the mudstone package. White box is 5 cm in width. E. Boxshot of L4 example (sleeves are 75 cm in length) showing bioturbated interlaminated sandstone and mudstone punctuated by relatively thick, structureless sand intervals. Boxes are from 09-30-097-10W4M. F. Close up of L4 example from 04-29-097-10W4M. Note the common *Cylindrichnus*, *Palaeophycus*, and *Planolites* as well as the preserved interlaminated sandstone and mudstone intervals. White box is 5 cm in width. G. Close up of L4 example from 04-29-097-10W4M. Note the relatively churned appearance of the interlaminated sandstone and mudstone as well as a syndepositional micro-fault. *Planolites* and *Arenicolites* are the only distinguishable burrows. White box is 5 cm in width. H. Close up of L4 example from 09-30-097-10W4M. Trace fossils include *Planolites*, *Skolithos*, *Cylindrichnus* and *Arenicolites*. White box is 5 cm in width.

2.4.4 L4: Bioturbated interlaminated sandstone and mudstone separated by thick sandstone (Figure 2.5E-H; 2.7D)

Lithosome 4 (L4) consists of bioturbated interlaminated sandstone and mudstone packages that are separated by relatively thick (dm-scale) sandstone units. The sandstone packages consist of fine- to medium-size grains. Interlaminated sandstone and mudstone units display lenticular to wavy bedding. The sandstone packages are generally structureless but locally include interbeds with climbing ripples. The bases of the sandstone packages are sharp. Bioturbation is dominated by *Cylindrichnus*, *Planolites*, *Skolithos* and *Arenicolites* in the interlaminated sandstone and mudstone packages. At the top of the sandstone packages, *Cylindrichnus* descending from the overlying mudstone succession is commonly observed. Due to the highly bitumen saturated character of the sandstone packages, bioturbation is overall difficult or impossible to discern in these beds unless the burrows are mud-lined or mud-filled.

2.4.5 L5: Variably bioturbated thin mudstone packages separated by thick sandstone packages (Figure 2.6A-D; 2.7E)

Lithosome 5 (L5) consists of thick (typically > 50 cm) sandstone packages separating thin interlaminated sandstone and mudstone beds or structureless mudstone beds. The thick sandstone units are typically medium- to fine-grained whereas the interlaminated sandstone intervals are most often fine-grained. The interlaminated mudstone and sandstone is generally wavy bedded. Current ripples, sporadic mud clasts, and soft-sediment deformation features are occasionally observed in the otherwise structureless thick sandstone packages. Both the thin mudstone and thick sandstone packages are sharp based. Overall, bioturbation is absent to sparse. *Planolites* represent the main traces present in the thin mud-dominated beds. Extremely rare small-diameter *Arenicolites* have also been observed. *Cylindrichnus* were occasionally observed descending from the thin mudstone packages into the thick sandstone packages.
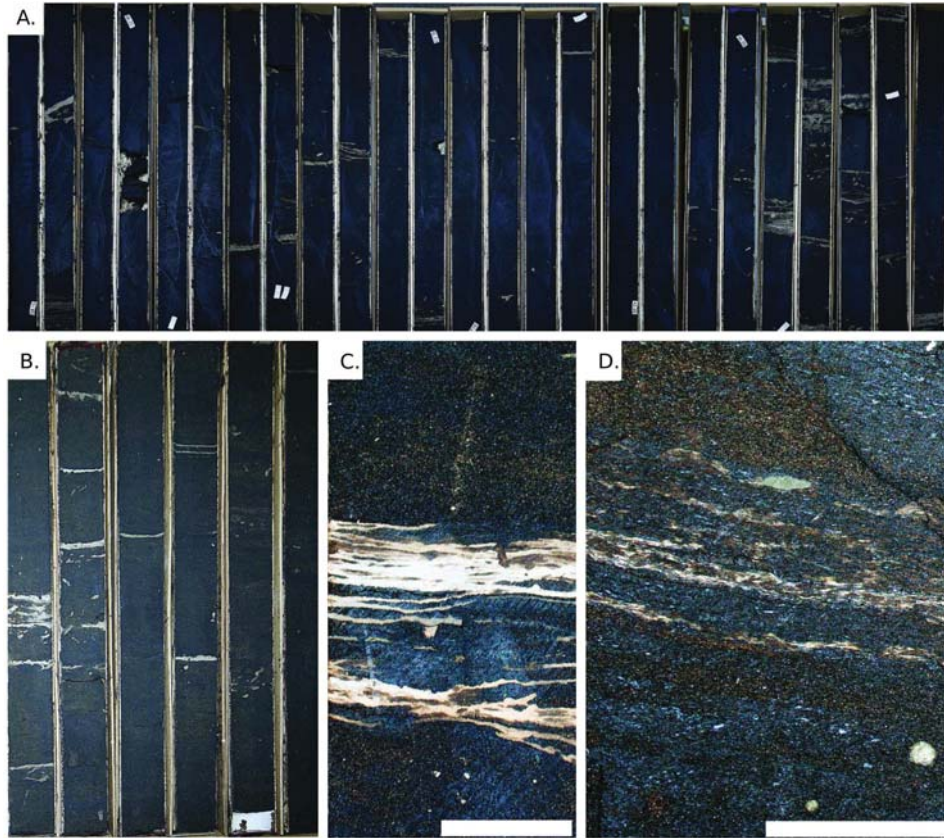
Figure 2.6: A–D. A. Boxshot of L5 example (sleeves are 75 cm in length) showing thick sandstone packages bounded by relatively thin mudstone packages. Note the overall continuity and clean character of the lithosome. Boxes are from 13-35-097-11W4M. B. Boxshot of L5 example (sleeves are 75 cm in length) showing clean sandstone punctuated by thin mudstone packages. Boxes are from 15-31-097-10W4M. C. Close up of L5 example from 14-19-097-10W4M showing a bioturbated interlaminated sandstone and mudstone package. White box is 5 cm in width. D. Close up of L5 from 12-28-097-10W4M showing a faint interlaminated sandstone and mudstone package. White box is 5 cm in width.

Figure 2.7: A–E. A–E. Schematic representations of L1-5 respectively. Sandstone is denoted by shades of yellow and mudstone is denoted by shades of brown.
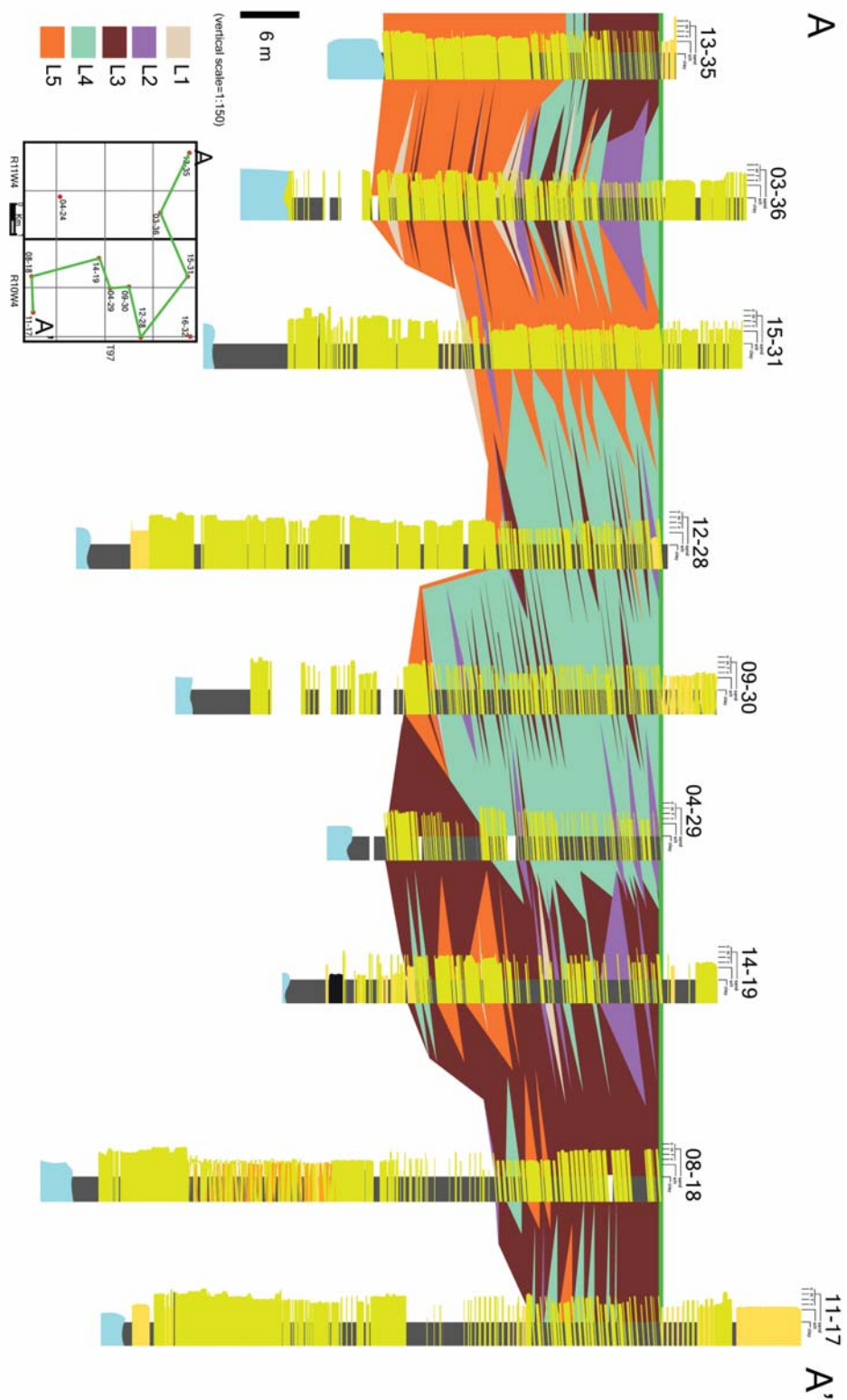
Figure 2.8: Cross-section of IHS lithosomes through wells that have IHS going from Northwest to Southwest portion of the study area. Only the IHS intervals have been correlated as they are the focus of this study. The top of the IHS interval is the datum for the cross-section.

23

Table 2.2: Summary of IHS lithosome cyclicity analysis results.

Lithosome	Sand T	Mud T	Combined T	CWT Sand T	CWT Mud T	CWT Combined T
L1	14	14	15 - 54	52.3	14.6, 39.7	24.9, 59.3
L2	14	14	28 - 61	31.3	24	62
L3	9 - 14	8 - 14	16 - 28	9.4	9.7	14.6, 53.3
L4	14	14 to 30	25 - 66	13.1,	12, 36.4	27.5, 83.3
L5	10 - 14	9 - 11	25-27	19.5	26.4	19.5, 48

2.5 Results: Cyclicity Analysis

The cyclicity analysis results are shown in Figures 2.9- 2.13 and summarized in Table 2. Each figure comprises a photograph, displaying which laminae were used to construct the dataset. Each dataset (mudstone and sandstone combined, sandstone laminae, and mudstone laminae) is plotted as bar graphs, which can be analyzed for cyclicity visually. The CWT scalograms are included in each figure as well.

2.5.1 Visual Cyclicity Analysis

Figures 2.9A- 2.13A show the samples that were measured for the visual cyclicity analysis. Histograms in figures 2.9B- 2.13B show the resulting thickness data for sandstone and mudstone laminae combined, sandstone laminae and mudstone laminae. Arrows are plotted where laminae thicknesses are thinnest (*i.e.* troughs). The number of laminae between each arrow, is noted on these plots. Crossovers, corresponding to the point at which mudstone laminae become thicker than sandstone laminae, or sandstone laminae become thicker than mudstone lamiae are marked with the letter "C".

For L1, combined mudstone and laminae present cycles of 15 to 59 (Figure 2.9B). Crossovers occur near the sequence troughs in many cases, but also appear sporadically throughout. Mudstone and sandstone laminae cycles both comprise approximately 14 laminae on average.

L2 combined mudstone and sandstone laminae measurements range between 28 and 61 laminae per group (Figure 2.10B). Crossovers typically occur near the sequence troughs; however, many random crossovers are also observed. Sandstone laminae and mudstone laminae are arranged in cycles of 14.
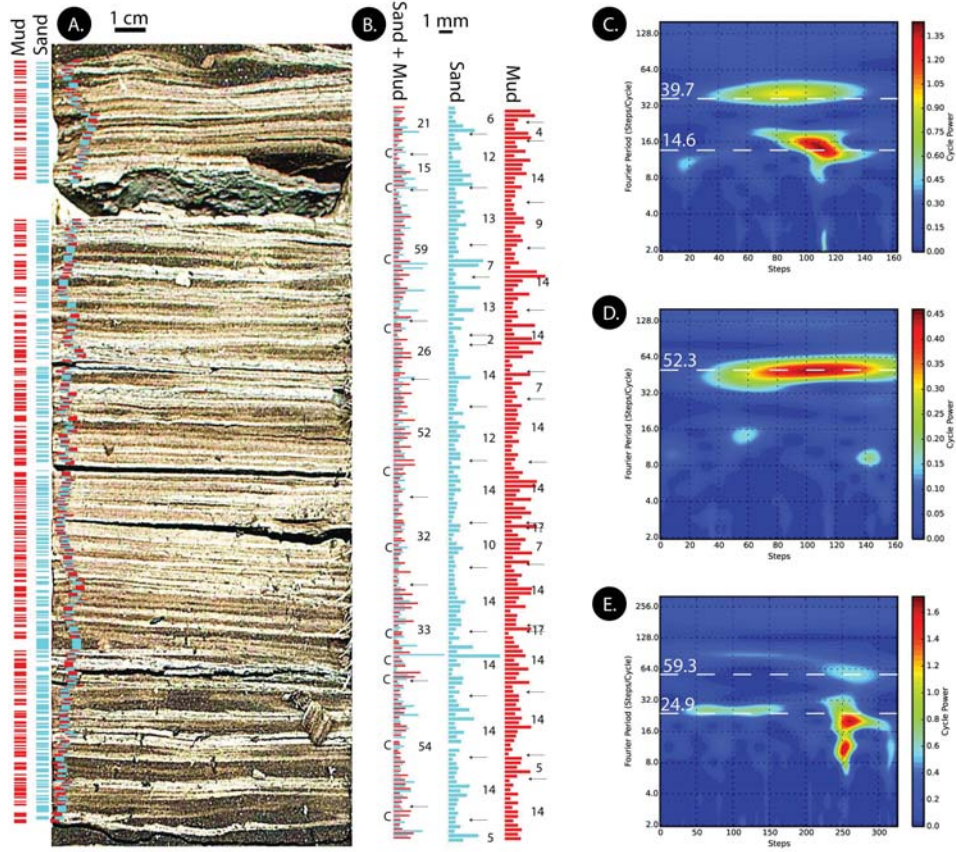
Figure 2.9: A–E. A. Photograph of measured core interval from lithosome 1. The sample is from 03-36-097-11W4M, from box 14.1, the interval is measured from the left box sleeve (47.5–48.25m). Mudstone and sandstone laminae thicknesses are shown on the left of the figure. B. Bar plots of combined mudstone and sandstone measurements, sandstone measurements and mudstone measurements (from left to right). The letter "C" denotes crossovers (when the subordinate and dominated deposition laminae are equal thicknesses). Numbers and arrows on the bar plots indicate the number of laminae between each trough. C. Scalogram of mudstone laminae thickness time-series. The main periodicities are 39.7 and 14.6. D. Scalogram of sandstone laminae time-series. The main periodicity is 52.3. E. Scalogram of combined mudstone and sandstone time-series. The main periodicities are 59.3 and 24.9.

25

Figure 2.10: A–E. A. Photograph of measured core interval from lithosome 2. The sample is from 14-19-097-10W4M, from box 5.1, the interval is measured from the right box sleeve (16.53–17.28 m). Mudstone and sandstone laminae thicknesses are shown on the left of the figure. B. Bar plots of combined mudstone and sandstone measurements, sandstone measurements and mudstone measurements (from left to right). The letter "C" denotes crossovers (when the subordinate and dominated deposition laminae are equal thicknesses). Numbers and arrows on the bar plots indicate the number of laminae between each trough. C. Scalogram of mudstone laminae thickness time-series. The main periodicity is 24. D. Scalogram of sandstone laminae time-series. The main periodicity is 31.3. E. Scalogram of combined mudstone and sandstone time-series. The main periodicity is 62.

26
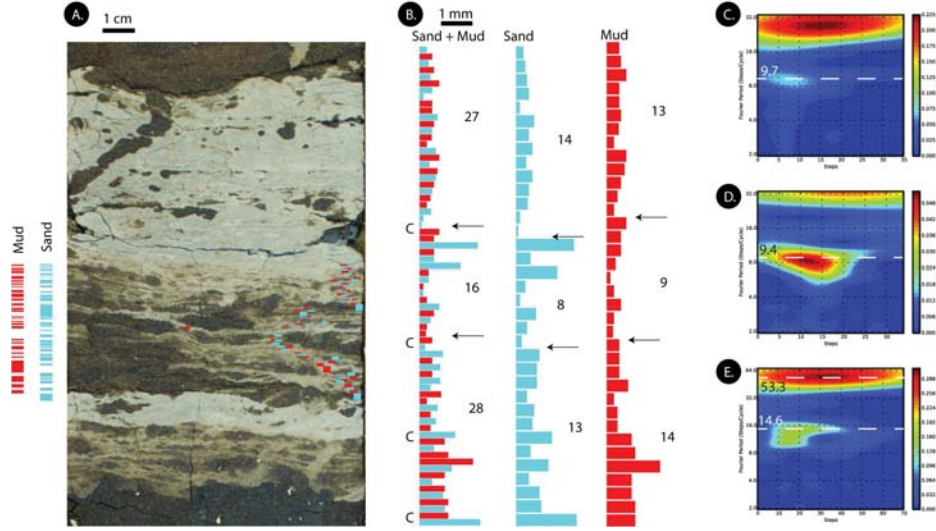
Figure 2.11: A–E. A. Photograph of measured core interval from lithosome 3. The sample is from 14-19-097-10W4M, from box 6.1, the interval is measured from the left box sleeve (18.00–18.75 m). Mudstone and sandstone laminae thicknesses are shown on the left of the figure. B. Bar plots of combined mudstone and sandstone measurements, sandstone measurements and mudstone measurements (from left to right). The letter "C" denotes crossovers (when the subordinate and dominated deposition laminae are equal thicknesses). Numbers and arrows on the bar plots indicate the number of laminae between each trough. C. Scalogram of mudstone laminae thickness time-series. The main periodicity is 9.7. D. Scalogram of sandstone laminae time-series. The main periodicity is 9.4. E. Scalogram of combined mudstone and sandstone time-series. The main periodicities are 53.3 and 14.6.

For L3, combined mudstone and sandstone cycles range from 16 to 28 laminae (Figure 2.11B). Crossovers occur in association with sequence troughs and occur sporadically as well. Mudstone cycles range from 9 to 14 laminae per cycle and sandstone cycles range from 8 to 14 laminae per cycle.

For L4, combined mudstone and sandstone laminae measurements range from 25 to 66 laminae per cycle (Figure 2.12B). Crossovers appear at troughs and half/quarter trough positions in the lower portion of the sequence. Sandstone laminae are thicker than mudstone laminae for the entire upper portion of the sequence. Sandstone laminae cycles average at approximately 14, and mudstone laminae cycles typically contain about 14 laminae, but can range up to 30.

L5 combined mudstone and sandstone laminae are arranged in cycles of 25

Figure 2.12: A–E. A. Photograph of measured core interval from lithosome 4. The sample is from 04-29-097-10W4M, from box 6.1, the interval is measured from the right box sleeve (22.53–23.28 m). Mudstone and sandstone laminae thicknesses are shown on the left of the figure. B. Bar plots of combined mudstone and sandstone measurements, sandstone measurements and mudstone measurements (from left to right). The letter "C" denotes crossovers (when the subordinate and dominated deposition laminae are equal thicknesses). Numbers and arrows on the bar plots indicate the number of laminae between each trough. C. Scalogram of mudstone laminae thickness time-series. The main periodicities are 36.4 and 12. D. Scalogram of sandstone laminae time-series. The main periodicities are 48, 24 and 13.1. E. Scalogram of combined mudstone and sandstone time-series. The main periodicities are 83.3 and 27.5.

Figure 2.13: A–E. A. Photograph of measured core interval from lithosome 5. The sample is from 14-19-097-10W4M, from box 10.1, the interval is measured from the left box sleeve (24.0–24.75). Mudstone and sandstone laminae thicknesses are shown on the left of the figure. B. Bar plots of combined mudstone and sandstone measurements, sandstone measurements and mudstone measurements (from left to right). The letter "C" denotes crossovers (when the subordinate and dominated deposition laminae are equal thicknesses). Numbers and arrows on the bar plots indicate the number of laminae between each trough. C. Scalogram of mudstone laminae thickness time-series. The main periodicities are 39.7 and 14.6. D. Scalogram of sandstone laminae time-series. The main periodicity is 52.3. E. Scalogram of combined mudstone and sandstone time-series. The main periodicities are 59.3 and 24.9.

to 27 laminae per group (Figure 2.13B). Crossovers occur near the sequence troughs. Mudstone cycles range from groups of 9 to 11 laminae and sandstone cycles range from 10 to 14 laminae per cycle.

2.5.2 CWT Cyclicity Analysis

The scalograms from the Morlet Wavelet Transform analysis are provided in Figure 2.9C-E for L1, Figure 2.10C-E for L2, Figure 2.11C-E for L3, Figure 2.12C-E for L4 and Figure 2.13C-E for L5. The x-axis of the scalogram represents the consecutive laminae measured with increasing depth of measurements from left to right. Because the x-axis represents laminae count rather than

depth, the relationship of depth along the x-axis is distorted. The y-axis of the graph shows the cycle periodicities calculated in the analysis. The color spectrum of the scalogram shows the squared cycle power. The warmer colors (*i.e.* red and orange) correspond to larger cycle power, whereas the cooler colors (*i.e.* purple and blue) signify a lower signal power. The most significant periodicities, that is, the periods that are the least likely to be random noise have high frequency power (*i.e.* are red or orange) and are present at a certain period for a considerable number of thickness measurements (*i.e.* are relatively horizontally continuous on the plot). Lines are placed on the scalograms at the periods of the main cycles observed for each sample, with corresponding periods annotated. Note that some periodic signals have wide periodic ranges (*e.g.* Figure 2.10E). The cycle periods determined from the Wavelet Transform analysis are summarized in Table 2.

For L1, the main periodicities correspond to 14.6 and 39.7 for mudstone laminae, 52.3 for sandstone laminae, and 24.9 and 59.3 for successive sandstone and mudstone laminae (Figure 2.9C-E). The periodicities in L2 are 24.0 for mudstone laminae, 31.3 for sandstone laminae, and 62.0 for successive sandstone and mudstone laminae (Figure 2.10C-E). For L3, cycle periods are 9.7 for mudstone laminae, 9.4 for sandstone laminae, and 14.6 and 53.3 for successive sandstone and mudstone laminae (Figure 2.11C-E). The periods obtained from L4 are 12 and 36.4 for mudstone laminae, 13.1, 24.0 and 48.0 for sandstone laminae, and 27.5 and 83.3 for combined sandstone and mudstone laminae (Figure 2.12C-E). For L5, periodicities are 26.4 for mudstone laminae, 19.5 for sandstone laminae, and 19.5 and 48.0 for combined sandstone and mudstone laminae (Figure 2.13C-E).

2.6 Discussion

2.6.1 Interpretation of interlaminated IHS beds Rhythmicity

A synodic month (*i.e.* the time it takes the moon to rotate around the earth) lasts 29.53 days (*cf.* Kvale 2012). There are two neap cycles and two spring

cycles in each synodic month. Each neap or spring cycle lasts approximately 7.4 days (29.53 divided by 4). In a semidiurnal system (*i.e.* two tides per day), a total of 14 subordinate tide laminae and 14 dominant tide laminae are deposited during each neap or spring event ideally. There are 56 laminae deposited per semidiurnal neap-spring cycle, and 112 laminae deposited per semidiurnal synodic month.

Periodicities of 14 are observed in bar plot data for mudstone or sandstone laminae thicknesses. Troughs observed in the bar plots reflect neap tide laminae and peaks represent spring tide laminae. Considering that laminae thicknesses observed in the bar plots are not distributed in pairs of equal thicknesses, a certain degree of semidiurnal inequality exists for both dominant and subordinate current deposition. That is, one flood/ebb event is stronger than the other daily flood/ebb event. Semidiurnal inequality is most obvious in the L2 sandstone bar plot and the L2 mudstone bar plot (Figure 2.10B).

The combined mudstone and sandstone bar plots reflect synodic neap-spring cyclicity as well. Cycle lengths that are under 30, which represent single semidiurnal neap or spring cycles, and cycles of approximately 60, which reflect semidiurnal deposition during half a synodic month, support this. The anomalistic tidal period (related to the elliptic nature of the moon's orbit around the earth), which is 27.55 days (Kvale 2012), seem to have variable preservation depending on the sample studied. Anomalistic periods are recognized by spring-spring and neap-neap inequalities within a synodic cycle. This inequality is especially evident in L5 (Figure 2.13B), but is more difficult to observe in longer sequences (*e.g.* L1 Figure 2.9B).

Crossovers (*i.e.* the point where subordinate and dominant tide laminae are equal thicknesses) variably coincide with neaps. Diurnal inequalities are minimal where crossovers occur. Crossovers are typically attributed to the periodicity of the moon crossing over the equatorial plane, which occurs every twice every 27.32 days (Kvale *et al.* 1999). This period is referred to as the tropical month. Because crossovers do not exclusively coincide with neaps (*i.e.* troughs in the bar plots), the neap-spring cycles observed are likely more in phase with synodic cycles rather than tropical cycles (Kvale 2006). Lunar

31

declination (*i.e.* tropical month) periodicity affects the cyclicity preserved, as reflected by the presence of crossovers; however, synodic driven cyclicity dominates.

For the L1 sample, there are at least three nearly complete synodic neap or spring cycles, which range from 54 to 59 laminae per cycle (Figure 2.9B). The cycles that are greater than 56 are likely artifacts of the noisy dataset. There are many incomplete cycles as well, that may represent amalgamation of thinner laminae, episodes of non-deposition, or erosion. The L2 sample (Figure 2.10B) comprises nearly perfect synodic neap or spring cycles (52-61). As with L1, the cycle made of 61 laminae is likely due to noise. And, incomplete cycles reflect amalgamation, erosion and non-deposition. The L3 sample (Figure 2.11B) does not contain complete spring or neap synodic cycles. Rather, half cycles or truncated cycles are preserved. This suggests that either semidiurnal deposition is not preserved (*i.e.* only a diurnal event is preserved), or only a portion (approximately half) of each neap or spring tidal deposition is preserved. For the L4 sample (Figure 2.12B), cycles tend to be slightly longer or significantly shorter than the ideal neap or spring semidiurnal synodic cycle. The noisy nature of the dataset likely contributes to this effect. As with L3, the L5 sample (Figure 2.12A) does not contain any full synodic neap or spring cycles. The number of laminae per cycle corresponds closer to half neap or spring cycles.

2.6.2 Visually Identified versus Continuous Wavelet Transform Cycles

The scalograms that match the visual cyclicity analysis the closest are L2 (Figure 2.10E) for the combined mudstone and sandstone laminae thickness dataset, L1 (Figure 2.9C) for the mudstone laminae thickness dataset, and L4 (Figure 2.12D) for the sandstone laminae thickness dataset. However, for most of the samples analyzed, there can exist significant differences between the visual interpretation of cyclicity and the CWT analysis.

The wavy nature of the interlaminated sediment creates noisy thickness data. Noise evidently affects the periodicities calculated with the CWTs. Very

large amplitude peaks can obscure low amplitude troughs that separate cycles that are otherwise observable with the naked eye. Considering that synodic fortnightly inequality is generally not pronounced or preserved, multiple cycles, bounded by large amplitude peaks are prone to be lumped together into an artificially long period. Inversely, if a single spring cycle, or a relatively high amplitude (large laminae thicknesses) neap-spring cycle is present in the time-series, this can have the effect of picking up false smaller periodicities. Both of these effects are demonstrated in L4, where manual cycles and CWT cycles differ significantly in the combined mudstone and sandstone series (Figure 2.12E). Lumping of multiple cycles together due to a lack of high amplitude beds separating cycles creates artificially long periodicities in mudstone and sandstone scalograms for most samples studied (*e.g.* Figures 2.9D, 10C-D, 12C).

In shorter time-series, edge effects, which are due to padding finite length series with zeros, can significantly affect calculated periodicities (Torrence and Compo 1998). As the width of the wavelet increases (when finding larger periods), the effects of edge effects are more pronounced. When the length of a time-series is similar to the width of a wavelet corresponding to a periodicity of interest, edge effects are more pronounced. This leads to inaccurate larger periodicities in short time series. Edge effects are most present in L3 (Figure 2.11C-E) and L5 (Figure 2.13C-E) due to the shortness of these series. Considering that we are interested in periodicities of approximately 60 (for semidiurnal deposition during a full synodic neap-spring cycle), time-series containing less than 2 complete cycles (*i.e.* 112 laminae) are likely to yield inexact CWT results. Shorter time-series are also more prone to erroneous cycle lumping or splitting if less than 2 complete cycles are preserved.

2.6.3 Formation of Lithosomes

Following the work of Smith 1988; Hubbard *et al.* 2011; Labrecque *et al.* 2011a; Musial *et al.* 2012; and Nardin *et al.* 2013 for example, the lithosomes in this study represent the product of the interplay of tidal and fluvial processes. The interlaminated portions of each lithosome dominantly reflect tidal modula-

tion. However, it is unlikely that the thicker sandstone and mudstone packages separating tidally modulated interlaminated sandstone and mudstone in IHS are solely the result of tidal forces. Labrecque *et al.* (2011a) demonstrated that the periodicities in thicker IHS packages are consistent with climatic variation periods, which affect streamflow. For example, in the modern Fraser River Delta, the thick sand constituent of IHS is deposited during freshets (Sisulak and Dashtgard 2012; Johnson and Dashtgard 2014). Thick mud deposition, as fluid mud, can also occur during high river flow conditions (*e.g.* Kineke *et al.* 1996). These fluvially dominated episodes overpower tidal sedimentation. Notably, the maximum number of tidal laminae observed in this study (from L1, Figure 2.9A) is 329, which represents approximately 3 full synodic months of semidiurnal deposition.

Ichnology data is sparse in L1, L2, and L5 and therefore presents little evidence for or against brackish water deposition. Reduced or absent bioturbation in the lithosome is likely the consequence high sedimentation rates, but could also be attributed to salinity stress. Tidal forces are sufficient to generate interlaminated intervals; therefore marine-based larval recruitment is not likely to have been a limiting factor. The trace fossils observed within L3 and L4 (*i.e. Arenicolites*, *Cylindrichnus*, *Planolites*, *Skolithos* and *Gyrolithes*) are very strongly linked to brackish water settings (Pemberton *et al.* 1982; Gingras *et al.* 1999; Gingras *et al.* 2011; Gingras *et al.* 2012). These support brackish water, tidally modulated depositional interpretations.

The lithosomes in this study area form one or multiple tidally modulated bar forms that were deposited within tidally modulated (at least seasonally) brackish water zone of a fluvio-tidal continuum. Interpreting the exact number and boundaries of these bar forms in the rock record is not possible without dipmeter (*e.g.* Fustic 2007) or seismic data (*e.g.* Hubbard *et al.* 2011). However, the variability in lithosome distributions vertically and laterally are best ascribed to evolution and position of the bar. The preservation of tidal laminae within a given lithosome is also likely related to bar form and position. For example, Musial *et al.* (2012) have noted that the preservation of tidal features in Gironde estuary point bars is most common in the upper part of

point bars.

2.7   Summary

Research on IHS in the Pierre River area reveals that tidal dominated deposition sporadically dominates portions of diverse lithosomes deposition for periods of up to 3 months. However, most of the preserved tidal cycles typically represent shorter time periods. The depositional position of lithosomes on one or multiple estuarine bar forms likely influences tidal laminae preservation to a certain extent. Each lithosome comprises thicker beds that represent periods of either relatively increased or decreased streamflow, which disrupt rhythmic tidally dominated deposition.

Daily tidal deposition is a key parameter influencing small-scale lithological variation in IHS of the McMurray Formation. The tidal regime interpreted from both manual and CWT derived laminae periodicities is semidiurnal synodic with subordinate tropical and anomalistic tidal influences. Subordinate and dominate tidal current energy crossovers multiple times in each example; however, these changes do not necessarily align with synodic neap cycles. Trace fossils from these lithosomes support (at least seasonal) brackish-water deposition, which further supports tidal interpretations. Even in bioturbated intervals, interlaminated sandstone and mudstone is indicative of tidal cyclicity.

Chapter 3

Visualizing a Process Ichnology Dataset

3.1 Introduction

Process ichnology is a framework that Gingras *et al.* 2011 proposed for the interpretation of trace fossils emphasizing their sometimes-ignored duality as both paleontological vestiges and as biogenic sedimentary structures. Process ichnology is derivative of ichnofabric studies (*e.g.* Taylor *et al.* 2003) and ichnofacies efforts (*e.g.* MacEachern *et al.* 2010), and builds on earlier studies associating bioturbation with sedimentation rate, identifying hidden bed boundaries, and recognizing physico-chemical stresses (*e.g.* Bromley and Ekdale 1984; Bromley 1996; Taylor *et al.* 2003; Martin 2004; MacEachern *et al.* 2007). As such, trace fossils might be used similarly to how sedimentary structures are used to indicate paleocurrent direction(s), sedimentation rates, erosion, hydraulic energy and depositional cyclicity. Trace fossil characteristics that have process-ichnological significance include: 1) trace fossil size; 2) trace fossil distributions; 3) ethological characteristics and diversity; 4) presence or absence of burrow linings; 5) presence or absence of specific ichnogenera, and; 6) degree of deformation of traces. This dataset is further strengthened by bioturbation index and size diversity index measurements. See Gingras *et al.* (2011) for detailed descriptions of each of these measurements.

Process ichnological datasets typically contain semi-quantitative data. Examples of these data include the diversity of ichnogenera, bioturbation index,

and the diameter of trace fossils. These metrics have typically been used to describe oxygen controlled ichnocoenoses (*e.g.* Savrda and Bottjer 1989) but can be applied to characterize other paleoecological stresses. These data can be modeled using well-documented geostatistical workflows to quantify spatial uncertainty (*e.g.* Goovaerts 1997). These techniques provide an understanding of the limitations and spatial relations of geological properties in 3D space. For example, due to the geological complexity of the McMurray Formation, the formation studied in this paper, well-data can be difficult to correlate at distances of as little as a few 100 m (*e.g.* Ranger and Pemberton 1997; Nardin *et al.* 2013). Therefore, stochastic representations of distributions of mappable features, such as process ichnology data, are often more reasonable, and time-effective than manual correlations. This allows the consideration of multiple different-property distribution scenarios for interpretation and visualization purposes. Considering the large quantity of data that can be collected for process ichnology analyses, incorporating process ichnology into 3D geospatial analyses is a necessary next step towards more detailed characterizations of sedimentary environments.

The following study demonstrates the use of geomodeling techniques for the visualization and interpretation of semi-quantitative process ichnology data using a sedimentary core dataset. The dataset is from the Cretaceous Mc-Murray Formation in the Pierre River Area, NE Alberta, Canada. Note that the methods outlined in this study can be applied to any spatially referenced ichnological dataset.

3.2   Basis of Process Ichnology

Process Ichnology is primarily based upon observations of animal response to environmental stresses in modern settings, and interpretations related to ancient datasets (*e.g.* Seilacher 1978; Pemberton *et al.* 1982; Bromley and Ekdale 1984; Savrda and Bottjer 1989; MacEachern and Pemberton 1992; Gingras *et al.* 1999; Martin 2004; MacEachern *et al.* 2005; Hauck *et al.* 2009; Johnson and Dashtgard 2014). Stresses common in fluvial, marginal marine, and marine

environments, may include: heightened turbidity, high current energy, rapid depositional rates, episodic deposition, substrate consistency, and fluctuations in salinity (Hubbard *et al.* 2004). Combining and interpreting process ichnological parameters can elucidate the influence of many of these stresses, some of which (*e.g.* rapid sedimentation and salinity fluctuations) may otherwise leave little, if any sedimentological evidence (MacEachern *et al.* 2010). Consideration of process ichnological characteristics in association with process sedimentology thus provides a framework for high-resolution interpretations of ancient clastic sedimentary environments.

3.3   McMurray Formation Geological Background

The McMurray Formation consists of fluvial, fluvio-estuarine and estuarine-marine packages that were deposited during a regional transgression of the Boreal Sea in western North America during the Aptian to Albian (Ranger and Pemberton 1997). The base of the McMurray Formation overlies Devonian carbonate units. Large scale McMurray drainage systems incised into the Devonian strata. Some Devonian units underwent kartsting during the deposition of lower McMurray Formation sediment (Broughton 2013, Broughton 2014, Broughton 2015). Karstification that occurred prior to McMurray Formation deposition formed large valley systems that are interpreted to have constrained some deposition laterally (Ranger and Pemberton 1992).

The Wabiskaw Member of the Clearwater Formation normally overlies the McMurray Formation. However, in this study area, Quaternary river erosion removed most of the Clearwater Formation and in some places, the upper parts of the McMurray Formation.

3.4   Study Area

The study area is located approximately 80 km northwest of Fort McMurray, Alberta (Figure 3.1A). The schematic stratigraphy of the study area is shown in Figure 3.1B. 10 cored wells are publicly available at the Alberta Energy Regulator's core research centre and form the basis of the ichnological analysis

for this study.

3.5 Methods

3.5.1 Data Collection

Detailed observations of lithology, nature of contacts, physical sedimentary structures, and biogenic sedimentary structures were recorded for each available core. High-resolution photographs were taken to accompany the recorded core data. These photographs were lens-corrected using Adobe Photoshop® in order to remove lens distortion biases.

Three ichnological metrics that could be readily related to sedimentation patterns were compiled and tabulated for modeling purposes. Bioturbation index (BI) was qualitatively determined following the schemes of Reineck (1967) and Taylor and Goldring (1993), where BI = 0 represents un-bioturbated media and BI 6 equals complete homogenization of sediment. The resolution of bioturbation index data is at the bed scale. The maximum burrow diameter was measured at 0.75 m intervals (*i.e.* 1 core-box sleeve length). Burrow diameters were measured using photographs. The diversity of burrow types was determined on a 0.75 m scale. Diversity in this study was taken to be the number of ichnogenera identified in each 0.75 m interval. For example, the presence of *Cylindrichnus*, *Planolites* and *Skolithos* over a 0.75 m interval corresponds to a diversity of 3. Ichnospecies were not considered in our diversity studies. The Size Diversity Index (SDI) *sensu* Hauck *et al.* (2009) was calculated as the product of the ichnodiversity and the maximum mud-lined burrow diameter for each 0.75 m interval. Note that SDI data was collected from the top of the McMurray Formation downwards (*i.e.* the first sample depth coincides exactly with the top of the McMurray Formation).

3.5.2 Geomodeling Workflow

Schlumberger's Petrel E&P® software platform was used for all steps of the geostatistical workflow. The following section goes over the workflow used to model facies, BI and SDI. Facies, BI and SDI collected from the core dataset
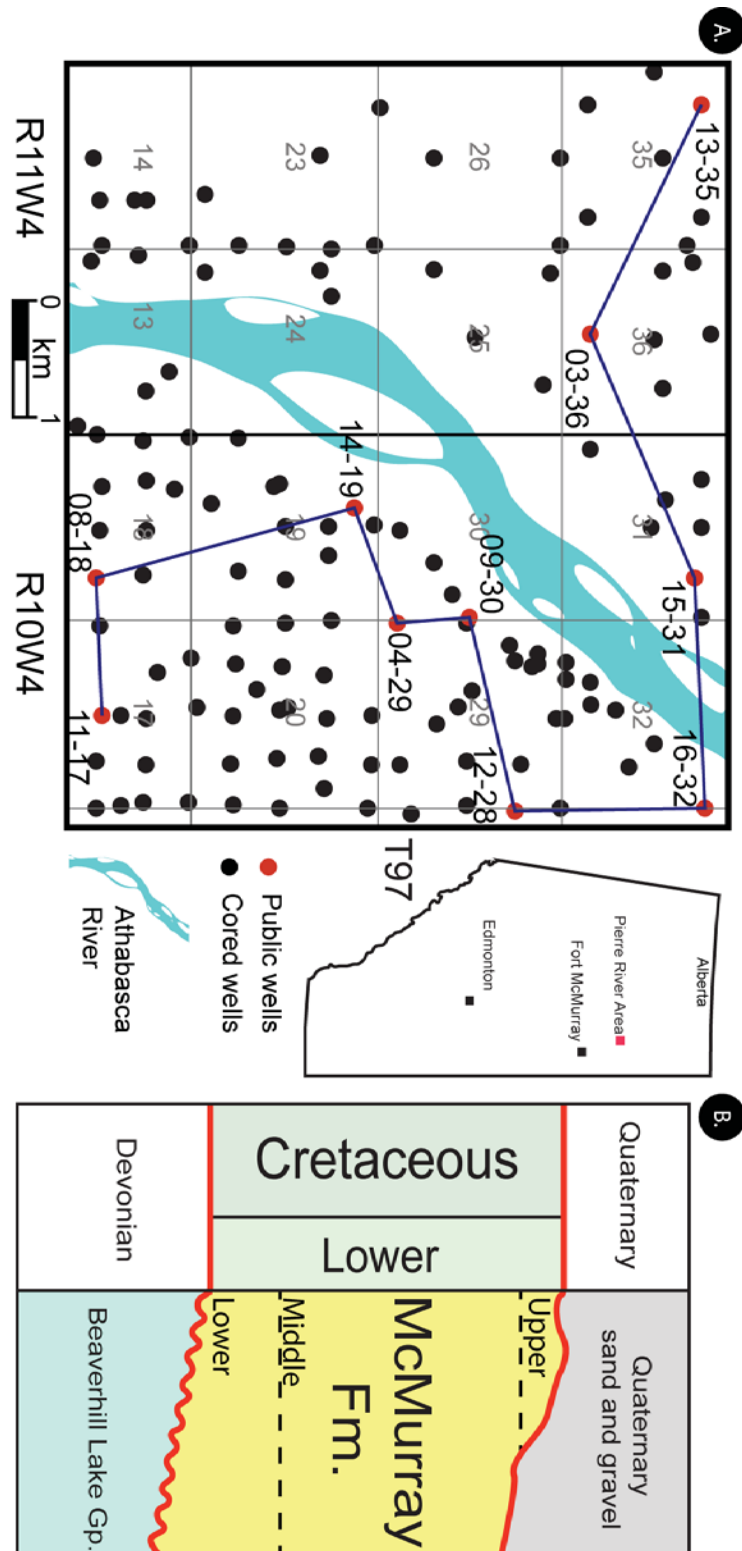
Figure 3.1: A. Study area base map showing dataset and line of section (blue line) for Figures 3.7 to 3.10. B. Schematic stratigraphy of study area.

were imported into Petrel as tab-delimited text files. The workflow is summarized as gridding, upscaling, variogram and simulation steps.

Grids are used to represent geological data using parametric coordinates (Mallet 2002). Surfaces based on geological boundaries are used to constrain the vertical and lateral extents of a grid. The base of the McMurray Formation, base of inclined heterolithic stratification (IHS) interval, top of IHS interval and the top of the McMurray Formation were picked from geophysical logs in order to generate surfaces for constraining a 3D grid (*cf.* Figure 3.2). For more information on IHS see Thomas *et al.* 1987. The grid dimensions used in this study are 6200 m E-W by 5750 m N-S, with 125 x 116 nodes. Z grid sizes (*i.e.* vertical cells) are 0.75 m in height.

Since the vertical grid cell size is not the same as the sampling rate of facies and BI data, this data is required to be "upscaled" in order to populate the grid cells. Upscaling is a method of determining the value that will be used to populate a given cell from well data intersecting that cell. For discrete variables (*i.e.* Facies and BI), the discrete value occupying the largest proportion of each cell was selected (Figure 3.3). This technique is typically referred to as "most of" upscaling. Upscaled data were then compared to well log data in order to quality control the process. Size diversity index data was not upscaled as the sampling interval coincided exactly with the model's cells. For SDI, the collected value for a given 75 cm increment was assigned to the corresponding geomodel cell as the geomodel cells were aligned with the sampled data.

Semivariograms are a key geostatistical parameter used to represent the spatial variability of data (*e.g.* Deutsch and Journel 1998; Deutsch 2002). Semivariograms will be referred to as variograms herein. The empirical variogram is calculated as follows:

$$\gamma(h) = \frac{1}{2N(h)} \sum_{i=1}^{N(h)} (x_i - y_i)^2 \qquad (3.1)$$

where h is the separation distance (*i.e.* lag) between a pair of points, xi and yi are a pair of points, of the same property, that are being compared and N(h) is the number of pairs compared. Variograms were calculated for

41
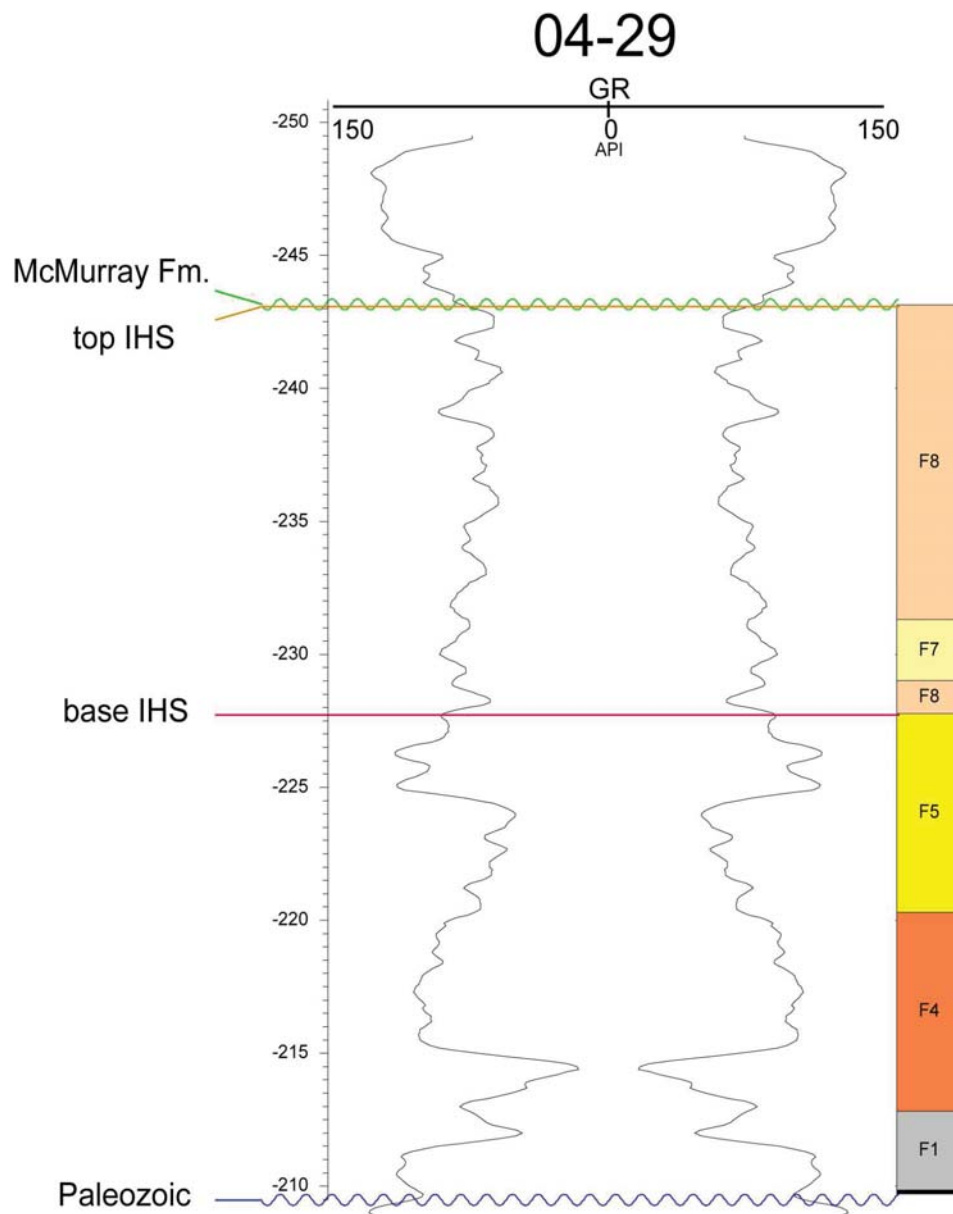
Figure 3.2: Example of stratigraphic horizons picked on a "butterfly" gamma ray log used to create horizons for the geomodeling workflow.
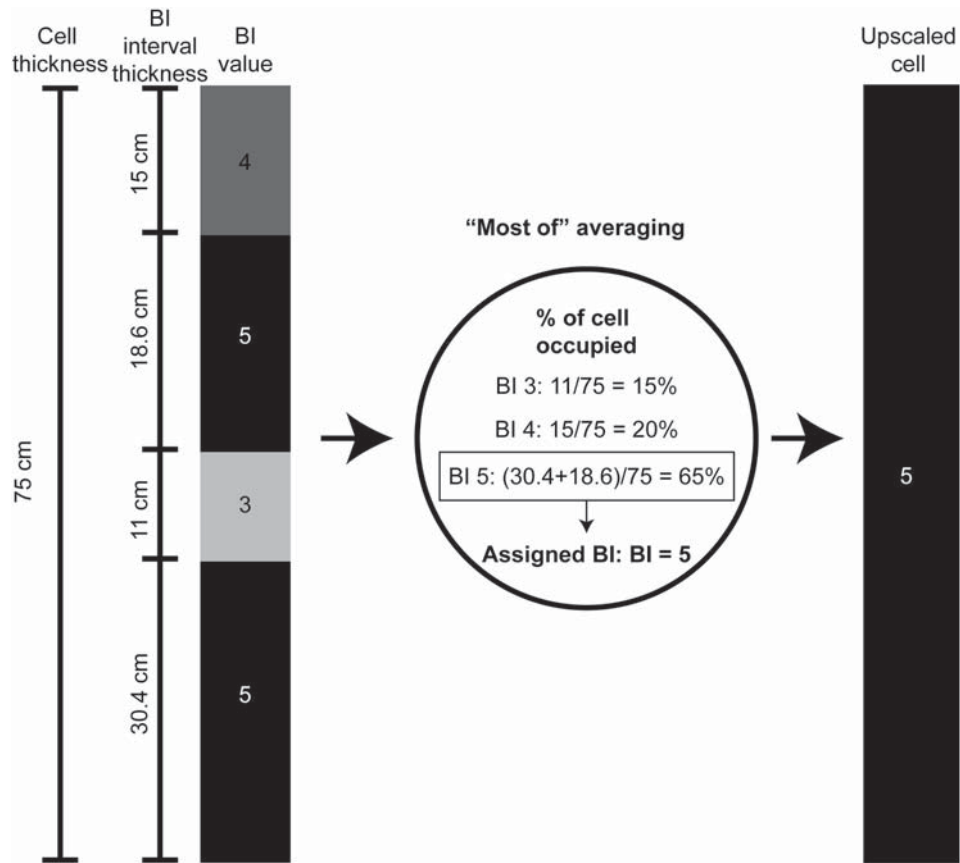
Figure 3.3: Schematic representation of "most of" averaging technique for upscaling data (*i.e.* choosing a representative value) into geomodel cells.

the major direction of anisotropy, minor direction of anisotropy and in the vertical direction. An in-depth review of directional variography is presented in Goovaerts (1997). The major direction of anisotropy corresponds approximately to the dominant paleocurrent direction. This direction was determined to be approximately 340° from north using dipmeter logs and outcrop measurements in the study area from Hein *et al.* (2001). The minor direction of anisotropy is orthogonal to the major direction of anisotropy (*i.e.* 250° from north). To use a variogram to guide interpolation algorithms, a theoretical variogram, based on fitting a spherical function with the empirical variogram was constructed for each modeled property.

For discrete property simulations, a sequential indicator simulation algorithm was used. Continuous property simulations were computed using a sequential Gaussian simulation algorithm. For detailed descriptions on either of these algorithms, see Deutsch and Journel 1998.

3.6   Results

3.6.1   Facies

In order to combine ichnological and sedimentological data, a facies scheme for the study area was constructed. The scheme is based on grain-size, ichnological properties, lithology, sedimentary structures, and facies thickness. Representative examples of each of the facies are shown in Figure 3.4 and detailed elements of these facies are shown in Figure 3.5A-H. The facies scheme and interpretations are summarized in Table 3.1.

3.6.2   Process Ichnology Logs

The depth-matched process ichnology data logs are presented in Figures 3.6 and 3.7. Figure 3.6 shows the 5 southern-most wells, and Figure 3.7 shows the 5 northern-most wells. This data allows for several general observations to be made.
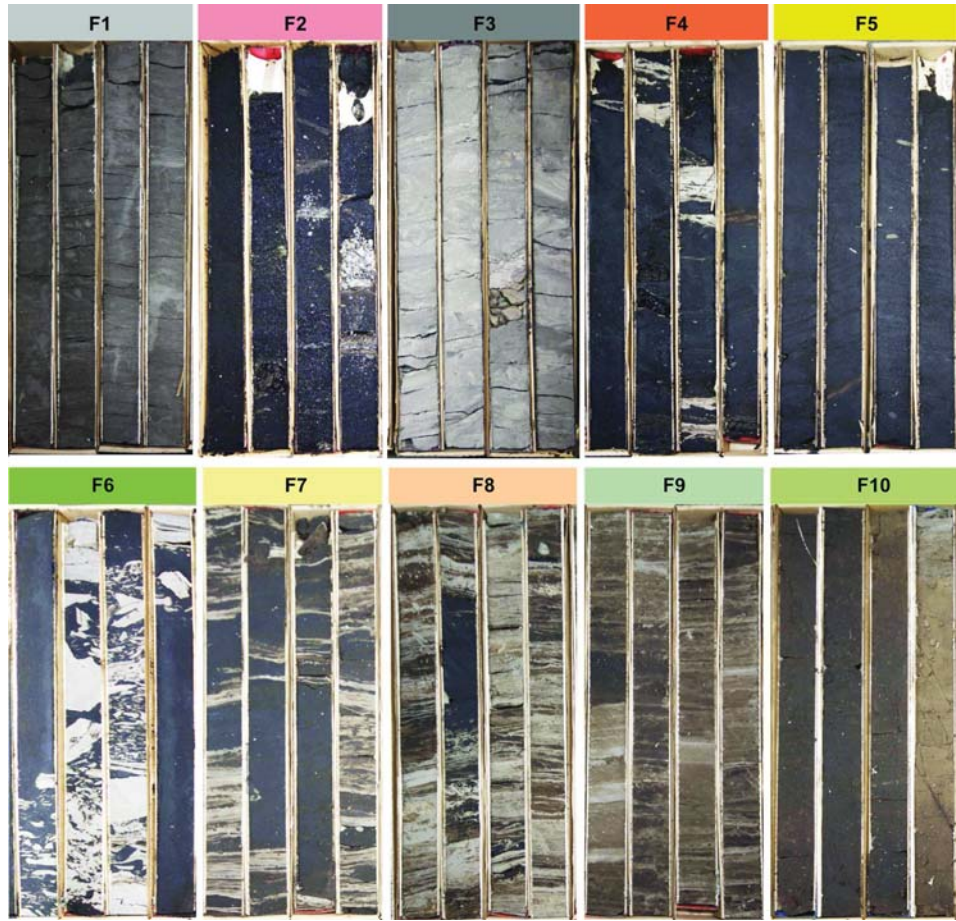
Figure 3.4: Representative photographs of facies 1–10. Core boxes are 75 cm in length. The label colours correspond to the facies geomodel cross-section in Figure 3.8
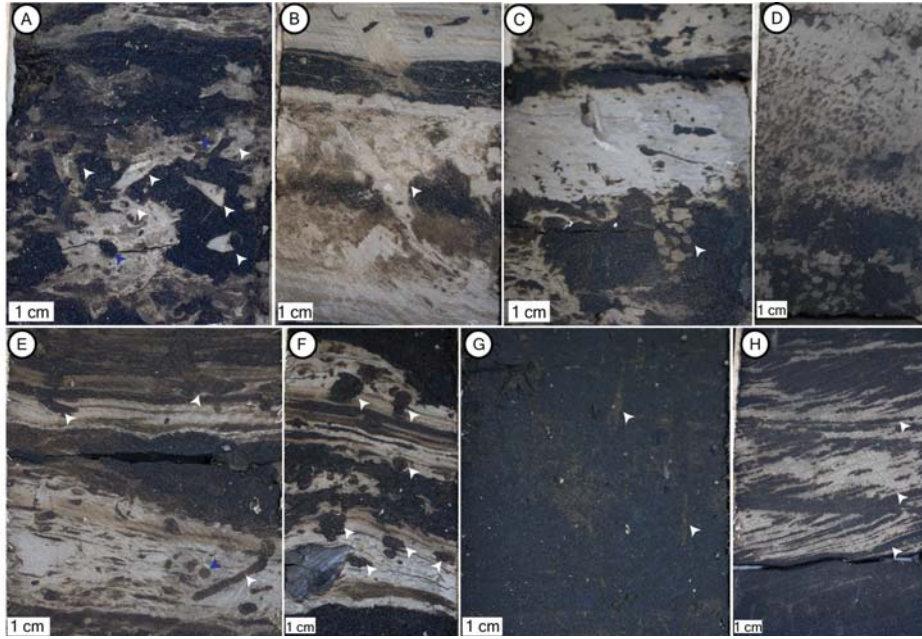
Figure 3.5: A. *Cylindrichnus* (white arrows) and *Planolites* (blue arrows) from 12-28-097-10W4M. B. *Rosselia* (white arrow) from 09-30-097-10W4M. C. *Gyrolithes* (white arrow) from 12-28-097-10W4M. D. Robust *Gyrolithes* assemblage from 13-35-097-11W4M. Note how most the burrows are inclined, which is likely caused by sediment shearing. E. *Arenicolites* (white arrows) and *Planolites* (blue arrow) from 09-30-097-10W4M. F. Compound or composite burrows *sensu* Pickerill (1994) (white arrows) from 11-17-097-10W4M. G. Root traces in F10 from 03-36-097-10W4M. H. Cryptic bioturbation of ripple foresets (white arrows) from 15-31-097-10W4M.

Table 3.1: Summary of study area facies. Grain sizes abbreviations: Lvf = lower very fine, Uvf = upper very fine, Lf = lower fine, Uf = upper fine, Lm = lower medium, Um = upper medium, Lc = lower coarse, Uc = upper coarse. Trace fossil abbreviations: Ar = *Arenicolites*, Cy = *Planolites*, fu = fugichnia, Gy = *Gyrolithes*, Pa = *Palaeophycus*, Pl = *Planolites*, Ro = *Rosselia*, Sk = *Skolithos*, Te = *Teichichnus*.

Facies	Facies Association	Name	Physical Sedimentary Structures	Grain Size	Ichnology Common	Rare	BI	Wells	Interpretation
F1	FA1	Silty, rooted or nodular mud with occasional sand	Nodules, rootlets, soft sediment deformation, rare wavy parallel beds, rare current ripples, coal layers and coal clasts; very organic rich/coal prone in some intervals	mud, silt and occasional Lvf	–	–	0	03-36, 04-24, 04-29, 08-18, 09-30, 11-17, 12-28, 14-19, 15-31, 16-32	Inter-fluvial; floodbasin/swamp; soil
F2	FA1	Coarse-grained structureless sand	pebble horizons, rare trough cross-beds, high angle and graded beds, coal clasts	Uc with pebbles and granules; occasional Um	–	–	0	03-36, 04-24, 08-18, 09-30, 11-17, 15-31	Braided fluvial channel fill
F3	FA1	Wavy to convolute sand, silt and mud	Soft sediment deformation, convolute beds, wavy parallel beds, rare current ripples, coal clasts	Uvf, silt, mud	–	Ar, Cy, Pl	0-1	03-36, 09-30, 14-19, 15-31, 16-32	Fuvial channel margin deposit; channel abandonment; soil
F4	FA2	Trough cross-bedded sand with grain-striping and mud laminae	Trough-cross beds, grain-striping, mud drapes or beds, pebble horizons, rare soft sediment deformation, rare wavy parallel beds, mud clasts, current ripples, coal clasts	Lc-granule, occasionally Lm, mud	Cy, Ar, Pl in mud laminae	Sk	0-3	04-24, 09-30, 12-28, 13-35, 15-31, 16-32	Fluvial to (occasionally) tidally modulated point bar
F5	FA2	Trough cross-bedded sand with grain-striping	Trough-cross beds and grain-striking, current ripples, coal calsts	Lc-granule, occasionally Lm	–	–	0	08-18, 11-17, 12-28, 14-19, 15-31	Fluvial to (occasionally) tidally modulated channel fill (dunes)
F6	FA3	Breccia	Large (2 to > 10 cm) mud clasts in sand matrix	Mud clasts, Lf-Lm matrix	–	–	0	14-19, 15-31, 16-32	Point-bar canibalization; reactivation
F7	FA3	Sandy IHS	Inclined wavy parallel mud and sand interbeds, climbing ripples, current ripples, mud clasts, high angle stratification, low angle stratification, coal clasts, rare synaeresis , cracks, rare lenticular bedding	Lm-Um, mud	Cy, Pl, Ar, Sk in mud laminae	Ro	1-5	03-36, 04-24, 04-29, 08-18, 11-17, 12-28, 14-19, 15-31	Lateral accretion deposits formed by tidal bar migration
F8	FA3	Muddy IHS	Inclined wavy parallel mud and sand interbeds, rare mottled intervals, synaeresis cracks, lenticular beds, load casts, climbing ripples	Lvf-Uvf, silt, mud	Cy, Pl, Ar, Sk	Ro, Gy, fu	2-5	03-36, 04-24, 04-29, 08-18, 09-30, 11-17, 12-28, 13-35, 14-19, 15-31, 16-32	Lateral accretion deposits formed by tidal bar migration
F9	FA3	Wavy low angle mottled mud silt and sand	Wavy parallel beds, lenticular beds, climbing ripples, mottled bioturbation, synaeresis cracks, coal clasts	Lvf	Cy, Pl, Ar, Sk	Gy	3-5	04-24, 08-18, 09-30, 11-17, 15-31, 14-19	Tidal flat
F10	FA3	Structureless to low anglecross-bedded wavy sand	Rare ripples and graded beds, low angle and wavy beds can sometimes be discerned, rare coal clasts, rare massive silt horizons	Silt, Lvf-Uf	–	Pl, Sk	0-4	08-18, 15-31, 16-32	Upper portion of point bars

47
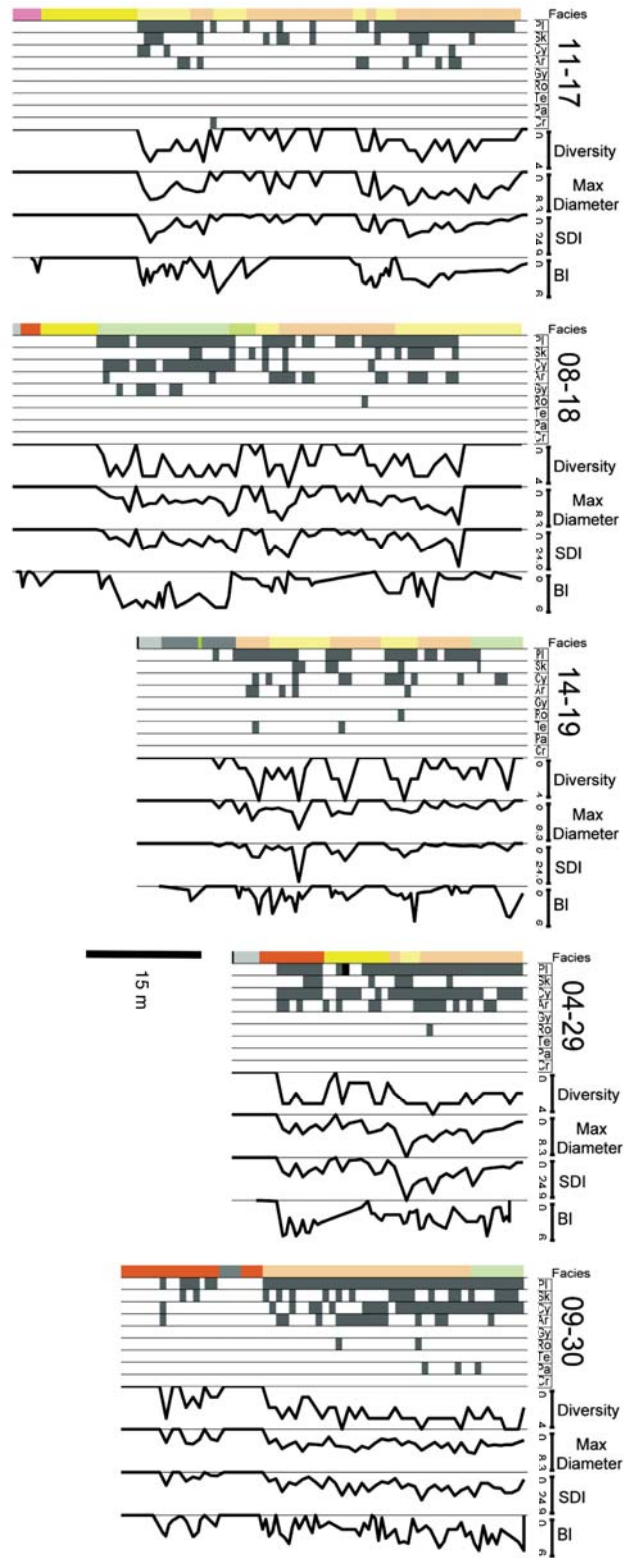
Figure 3.6: (Continued on the following page.)

Figure 3.6: Facies, trace fossils, diversity, maximum burrow diameter and size-diversity index recorded for wells 11-17-097-10W4M, 08-18-097-10W4M, 14-19-097-10W4M, 04-29-097-10W4M, and 09-30-097-10W4M. The presence of a given trace fossil is demonstrated by the greying of the trace fossil column. The vertical scale is 1:500. Trace fossil abbreviations: Ar = *Arenicolites*, Cy = *Cylindrichnus*, fu = fugichnia, Gy = *Gyrolithes*, Pa = *Palaeophycus*, Pl = *Planolites*, Ro = *Rosselia*, Sk = *Skolithos*, Te = *Teichichnus*.
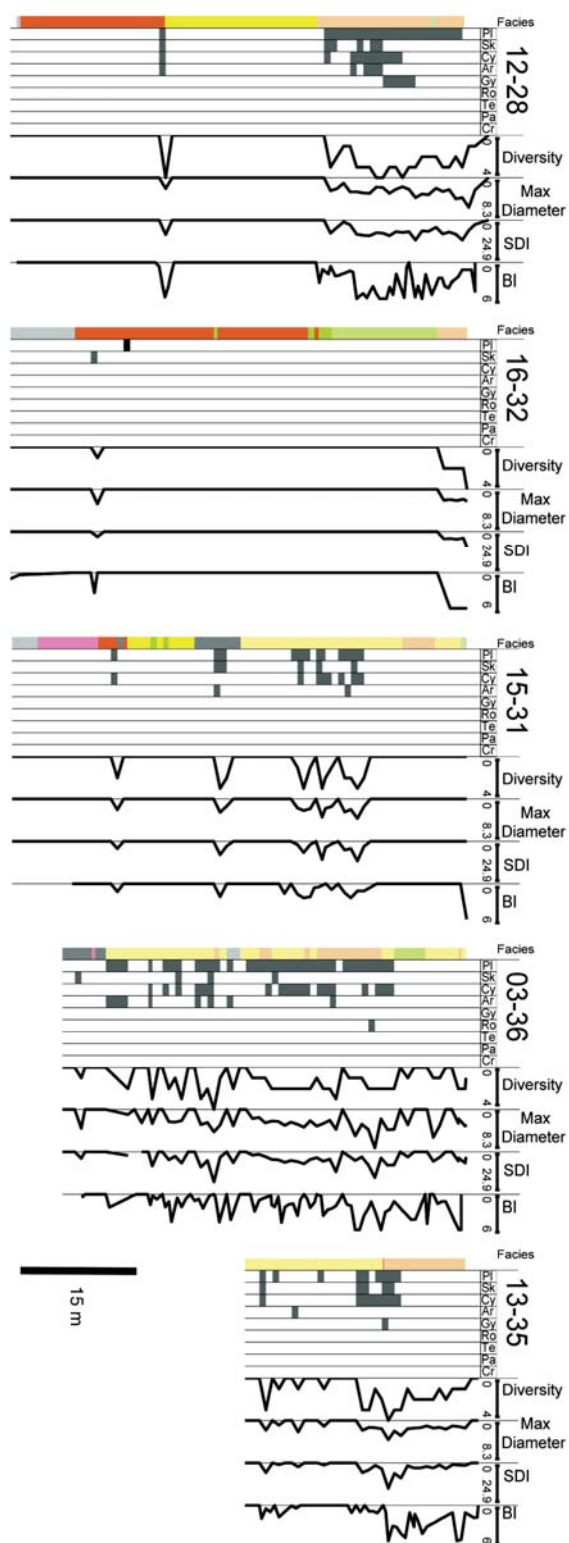
Figure 3.7: (Continued on the following page.)

Figure 3.7: Facies, trace fossils, diversity, maximum burrow diameter and size-diversity index recorded for wells 12-28-097-10W4M, 16-32-097-10W4M, 15-31-097-10W4M, 03-36-097-11W4M, and 13-35-097-11W4M. The presence of a given trace fossil is demonstrated by the greying of the trace fossil column. The vertical scale is 1:500. Trace fossil abbreviations: Ar = *Arenicolites*, Cy = *Cylindrichnus*, fu = fugichnia, Gy = *Gyrolithes*, Pa = *Palaeophycus*, Pl = *Planolites*, Ro = *Rosselia*, Sk = *Skolithos*, Te = *Teichichnus*.

Bioturbation index resolution is at the bed scale, whereas SDI sampling is in 75 cm increments, which explains why there is greater small-scale variability in the BI logs compared to the SDI logs (*e.g.* well 09-30-097-10W4 in Figure 3.6; well 03-36-097-11W4 in Figure 3.7). However, peaks and troughs in SDI and BI otherwise generally coincide. The relative amplitude of BI or SDI peaks and troughs is highly variable.

Bioturbation index and SDI values generally increase upwards stratigraphically. However, this trend is sporadic and irregular. A significant exception to this trend occurs in well 08-18-097-10W4, where peak BI and SDI values occur within F9 near the basal portion of the well (Figure 3.6). The BI and SDI log peaks and troughs generally coincide with facies contacts. Bioturbation index and SDI are highly variable in the IHS facies (*i.e.* F7 and F8). Some IHS intervals contain no bioturbation, whereas others have high SDI and BI values. Overall, IHS facies (F7 and F8), along with F9 are the most bioturbated facies. Overall, wells 12-28-098-10W4, 16-32-097-10W4 and 15-31-097-10W4 are the most sporadically bioturbated. These wells are in the northeastern portion of the study area. Note that these wells also contain the smallest amount of IHS volumetrically.

A large proportion of bioturbated intervals comprises one or two ichnogenera. Wells 04-29-097-10W4 and 09-30-097-10W4 represent the most prominent exceptions to this trend, where *Planolites*, *Skolithos*, *Cylindrichnus* and *Arenicolites* are present together for a significant portion of the cored interval. *Planolites* and *Cylindrichnus*, where present, typically occur over relatively thick depth intervals, whereas other traces are generally distributed over shorter stratigraphic intervals. A notable exception to this distribution occurs in 11-17-097-10W4, where *Cylindrichnus* occurs relatively sporadically over thin intervals. *Rosselia* generally occurs coincidently with peaks in maximum burrow diameter. Note that we measured the burrow diameter interpreted to most accurately represent the burrowing organisms' body size (*i.e.* we measured the mud lined stem and not the inner bulb portion of *Rosselia*).

3.6.3 Geomodel Cross-Sections

The property models resulting from the geostatistical workflow are shown in Figures 3.8- 3.10. Several iterations of each simulation were executed in order to generate and visualize multiple scenarios. However, only a single iteration of each simulation is shown in this paper. Cross-sections through each modeled property along a general southeast-northwest trend are used to demonstrate an iteration of a possible trace-fossil distribution for each property.

The facies geomodel cross-section shown in Figure 3.8 demonstrates that F1 to F5 are exclusive to the lower reaches of the McMurray Formation. Facies 6 is most common beneath the clean gamma ray zones (<65 API). With the exception of well 08-18-097-10W4, F9-10 usually overly F7 or F8. Facies 7 and 8 are typically the most laterally continuous facies.

From Figure 3.9, bioturbation index increases between wells 14-19-097-10W4 to 12-28-097-10W4 (W-E trend) then decreases sharply from wells 16-32-097-10W4 to 15-31-097-10W4 (E-W trend). With the exception of well 08-18-097-10W4, BI values are greatest at the higher stratigraphic reaches. Bioturbation index values observed in the lower reaches of the cross-sections, are non-representative as these largely occur in between well control and are therefore stochastic artifacts. Bioturbation index is typically the highest in F9 and is lowest in F1-5. Bioturbation index is highly variable in F7 and F8 (*i.e.* IHS facies).

The SDI geomodel cross-section shown in Figure 3.10 indicates that SDI decreases from wells 11-17-097-10W4 to 14-19-097-10W4 abruptly (SE-NW trend), peaks at well 04-29-097-10W4 and subsequently decreases between wells 04-29-097-10W4 to 16-32-097-10W4 sharply (SW-NE trend). SDI values are more sporadically distributed between wells 15-31-097-10W4 to 13-35-097-11W4 (E-W trend) than from wells 11-17-097-10W4 to 16-32-097-10W4 (S-N trend). SDI values are generally lowest at both the lowermost and the uppermost reaches of the preserved McMurray Formation.

Null to low BI and SDI values coincide with sandier intervals and F1-F6. SDI values are highest in F7 and F8. SDI is generally slightly higher in F8
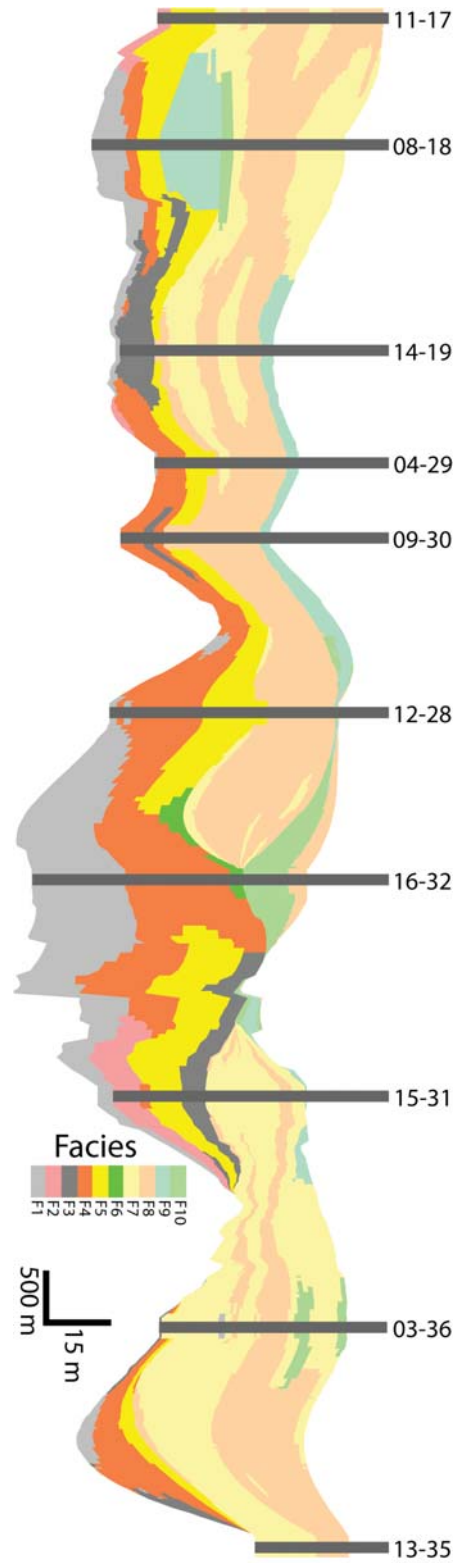
Figure 3.8: Stochastically generated cross-section (line of section shown in Figure 3.1A) of facies. Vertical scale is 1:500.
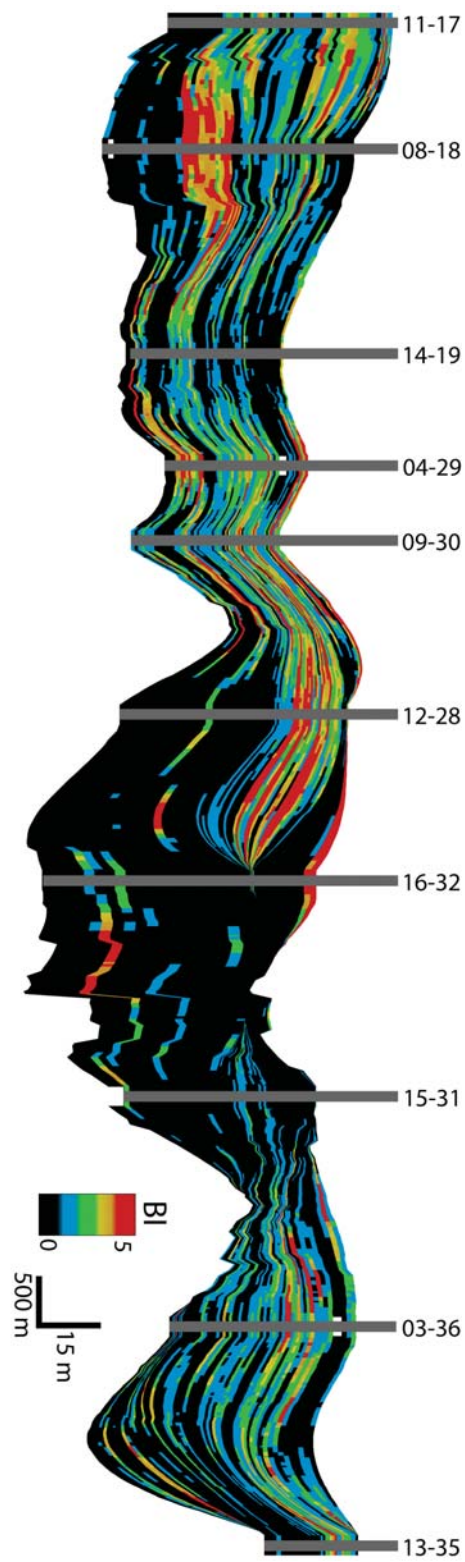
Figure 3.9: Stochastically generated cross-section (line of section shown in Figure 3.1A) of bioturbation index (BI). Vertical scale is 1:500.
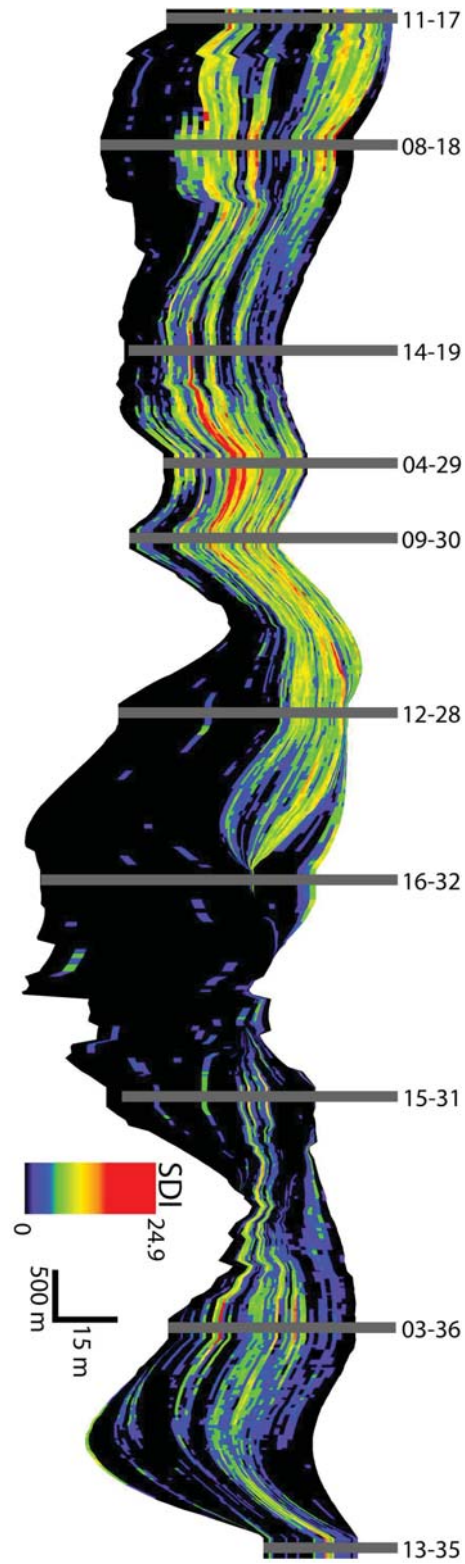
Figure 3.10: Stochastically generated cross-section (line of section shown in Figure 3.1A) of size diversity index (SDI). Vertical scale is 1:500.

than in F7. BI is generally higher in F8 as well. Overall, BI is highest in F9; however, SDI values are usually in the mid-range in F9.

3.7 Discussion and Interpretation

3.7.1 Significance of BI and SDI

Trace fossil assemblages in the Pierre River area reflect burrowing behaviours typical of marine-sourced trophic generalists (*i.e. Cylindrichnus*, *Rosselia*, *Arenicolites*, *Gyrolithes*). Since marine based burrowing organism sizes are directly affected by salinity variability, the maximum burrow diameter within a given interval is a suitable proxy for salinity stress. Further, the diversity of trace fossil assemblages characterized by marine ethologies is directly related to salinity stress (*e.g.* Pemberton *et al.* 1982; MacEachern *et al.* 2007; Jaglarz and Uchman 2010). Multiplying the size and diversity of a given interval therefore provides a metric that amplifies the infaunal population's response signal to salinity stress.

Two types of diminution trends were reported by Gingras *et al.* (2011): "facultative diminution", which is an animal size response to osmotic stress; and more commonly "enforced diminution", wherein salinity stress may lead to shortened life cycles and exclude animals that are poor osmoregulators. Enforced diminution results in larger animal being absent from the burrowing community. SDI includes observations of all trace diameters in an interval, in recognition that facultative diminution cannot be distinguished from enforced diminution in ancient datasets. It could be argued that burrow diameter comparison (and thereby SDI) is only meaningful within a single ichnogenera. However, we support that inter-ichnogenera burrow diameter comparisons are valid for several reasons: 1) single ichnogenera can be made by different types organisms, which may respond to salinity stress differently; 2) single ichnogenera data are typically too sparse to produce a meaningful analytical dataset; and, 3) some organisms show little or no size response to salinity levels (*e.g.* Gingras *et al.* 1999; Gingras *et al.* 2011). Indeed, SDI considers the entire infaunal community's response to salinity fluctuations, rather than the

57

response of individual animals. Documenting an entire community's response to stress fluctuation allows for much more reliable indications of salinity levels and salinity fluctuations, and excellent correspondence between SDI and salinity were demonstrated in modern datasets by Gingras *et al.* (1999) and Hauck *et al.* (2009).

Substrate consistency, sedimentation rates are additional stresses that can affect SDI. However, BI is a metric that is more suitable for tracking variability in sedimentation rates (Gingras *et al.* 1999). Bioturbation index is a function of colonization window length, bioturbation behavior, burrowing organism and population density (Gingras *et al.* 2011). In general, low BI signifies high sedimentation rates and higher BI represent slower sedimentation rates. The variability in BI over a given interval depth interval matches temporal variability in sedimentation rates. This trend is especially evident in the IHS facies (F7-8).

3.7.2 Effects of mud-linings and composite burrows on SDI values

Mud linings can be relatively thick > 1 mm (*i.e.* a minimum of 1/8th of maximum burrow diameter observed). Including mud linings in maximum burrow measurements can therefore significantly skew SDI values. Although the sand-filled inner tube of *Cylindrichnus* is not always visible, care must be taken to avoid incorporating the linings of these traces in the maximum burrow diameter array. The mud linings should be ignored for SDI in any case, as these are not a suitable proxy for the burrowing organisms' size (*cf.* Gingras *et al.* 2011).

Burrows that are formed by either multiple different organisms (*i.e.* composite burrows), or that reflect the complex burrowing history of one organism (*i.e.* compound burrows) are commonly found in the McMurray Formation (*cf.* Figure 3.5F). Pickerill (1994) coined the "compound" and "composite" burrow terms. Care must be taken to distinguish deformed burrows from such burrows when measuring maximum diameter values. Both of these burrow types are not representative of the true size of burrowing organisms.

3.7.3 Main Environmental Stresses

The ichnological character of the dataset, specifically the relatively low but highly variable SDI, and highly variable BI, suggests the presence of significant temporal and spatial infaunal stresses induced by salinity fluctuations and high sedimentation rates during deposition. This is, in part, indicated by the irregular distribution of ichnological data plotted against depth (*cf.* Figures 3.6- 3.7) and the spatial variability observed in the ichnological cross-sections (*cf.* Figures 3.9- 3.10).

Salinity stress is interpreted to be persistent throughout the entire dataset. Evidence for this interpretation comes from the persistently diminutive maximum burrow diameter values (the overall maximum burrow diameter measurement = 8.3 mm), and the preponderance of monospecific to low diversity assemblages. These characteristics are well documented in brackish-water conditions (*e.g.* Pemberton *et al.* 1982; Beynon *et al.* 1988; Pemberton and Wightman 1992; Buatois *et al.* 2005). Although specific ichnogenera are not solely indicative of brackish conditions, the presence of monogeneric assemblages of *Cylindrichnus*, and *Gyrolithes* (both traces are produced by organisms that mature from marine-sourced larvae) are very common elements of high-certainty brackish-water assemblages (*cf.* MacEachern *et al.* 2007).

High sedimentation rates are interpreted to represent another principal infaunal stress. Sedimentation stress, related to seasonal cyclicity in IHS (*cf.* Hovikoski *et al.* 2008) is especially evident in F7 and F8. Sandstone dominated intervals represent periods of rapid deposition, unsuitable for infauna. Climbing ripples observed in sandstone IHS intervals in this study support rapid deposition. Mudstone intervals represent conditions of lower sedimentation rates, suitable for colonization (Gingras *et al.* 2002). The colonization windows are likely annual. *Rosselia* is likely an exception to this process as the presence of local *Rosselia* has been associated with sediments deposited in rapid and periodic deposition (Nara 1997).

The cyclic nature of sedimentation stress is coupled with salinity stress. High sedimentation rates during river flood are associated with lowered salin-

ity. During normal and lower river flood, salinity conditions return those that are conducive to infaunal habitation of the substrate (*e.g.* Sisulak and Dashtgard 2012; Johnson and Dashtgard 2014).

3.7.4 Facies Interpretation

The sporadic lateral distribution of F1-F3 (Figure 3.8), low BI (Figure 3.9), low SDI (Figure 3.10), and features such as root traces in paleosols and coarse-grained trough-cross stratified sandstone (Table 3.1) suggest that these facies comprise a fluvially dominated depositional system. Very rare evidence of marine-based trace fossils (*i.e.* *Arenicolites* and *Cylindrichnus*) suggests limited to non-existent tidal influence. The McMurray Formation is informally subdivided into three units: the lower, middle and upper McMurray (Carrigy 1959). Facies 1-3 are consistent with facies observed in the lower McMurray (*e.g.* Hein *et al.* 2001; Crerar and Arnott 2007) that have been interpreted to represent a regionally fluvial interval.

Facies 4-5 likely represent the channel deposits of a later, separate fluvially dominated system distinct from the system that deposited F2, with slightly more marine influence. This is supported by the stratigraphic position of F4-F5 (usually above F1-F2), and increased evidence of periodic brackish water incursions into the system (*i.e.* presence of *Arenicolites* and *Cylindrichnus*). From Figure 3.9- 3.10, BI and SDI are overall greater than in F1-3 supporting a more brackish system. Overall, F4-F5 are laterally persistent, which suggests that F4-F5 channel fill deposits are part of a meandering system. The intermittent mudstone layers in F4 likely represent seasonal periods of low fluvial flow, where marine based mud and larvae are pushed into the fluvial system. This is supported by the colonization of mudstone intervals by marine-based trace makers (*i.e.* *Arenicolites* and *Cylindrichnus*). However, these incursions were likely short lived, and rare, as very few of the mudstone beds in F4 are bioturbated. Beds that are bioturbated have low BI, and low diversity. There is a distinct separation between F4-5 and F7-8, which marks the boundary between the lower McMurray Formation and the middle McMurray Formation.

Facies 6-10 compose a complex brackish water system including at least

two bar forms (F7-F8), bar cannibalization features (F6), tidal flats (F9) and bar abandonment features (F10). The distinct change in mud:sand content, presence of breccia, BI and SDI at 16-32-097-10W4 and 15-31-097-10W4 likely marks a bar form boundary. The ichnological and sedimentological features observed in the geomodel cross-sections support a genetically related bar complex interpretation. Following this interpretation, F6-10 south of 16-32-097-10W4 represent a single bar form, and associated deposits, while F6-10 north of 16-32-097-10W4 represents another bar form, likely part of the same bar complex. However, without seismic or dipmeter data, it is difficult to ascertain whether or not the bars are genetically related, forming a bar complex, or represent the amalgamation of multiple genetically unrelated depositional episodes.

Lithological variations in IHS character are the results of the interplay of tidal and fluvial forces (*e.g.* Lettley *et al.* 2005a) and downstream variation along bar forms (*e.g.* Labrecque *et al.* 2011b). These lithological variations are associated with environmental stresses such as changes in salinity, changes in hydraulic energy, and turbidity (*e.g.* Ranger and Pemberton 1992). It is expected that these stresses decrease SDI and BI values. Therefore, higher SDI and BI values can be attributed to portions of IHS bars that are relatively sheltered from these stresses. Low BI values can indicate high sedimentation rates (*cf.* Gingras *et al.* 2011), which are also associated with IHS lithological variation. In 04-29-097-10W4, the high SDI values (Figure 3.10) associated with low BI (Figure 3.9) can be attributed to the presence of *Rosselia*, which can exist during higher sedimentation rates (*e.g.* Nara 1997). Nardin *et al.* (2013) provided preliminarily descriptions of bioturbation on a meandering IHS point bar deposit. Their study demonstrated that bioturbation is more prevalent on the downstream section of point bars. The downstream portion of IHS point bars is less affected by seasonal variations in fluvial and tidal energy and concomitant variability in environmental stresses. The strong spatial variability in BI and SDI observed in Figures 3.9- 3.10 is ascribable to along and across bar variations in environmental stresses.

The mottled, bioturbated texture, which characterizes F9 is consistent with

tidal flat deposition (*e.g.* Crerar and Arnott 2007). Facies 9 (F9) generally occurs on the upper portion of IHS deposits (Figure 3.9). This relationship likely represent the encroachment of tidal flats over older IHS bars, following the lateral accretion direction of the IHS point bars. Size diversity index is relatively low in F9 (Figure 3.8 and Figure 3.10); however BI is high (Figure 3.9). This is interpreted to reflect relatively low sedimentation rates and salinity stressed infaunal conditions. Facies 9 (F9) observed in the lower reaches of 08-18-097-10W4 (Figure 3.8) is a stratigraphic outlier, likely from an older, poorly preserved estuarine system. Facies 10 (F10) is interpreted to preserve the intertidal upper portion of IHS point bars, or IHS abandonment (*e.g.* Musial *et al.* 2012). The stressed nature of this facies is shown by simple trace fossils (*Skolithos* and *Planolites*), and relatively low BI, and low SDI.

3.8   Summary

Ichnological geomodeling allows quick spatial visualization of semi-quantitative ichnological parameters. Based on a simulation iteration, multiple visualization scenarios are possible. Employing the geomodeling approach, the following observations were made:

1. Based on the spatial distribution of bioturbation index (BI) and size-diversity index (SDI), significant temporal and spatial variability in ecological stress are interpreted. The main two stresses are salinity and sedimentation rates. Size diversity index tracks changes in salinity, and BI tracks changes in sedimentation rates.

2. Overall, inclined heterolithic stratification (IHS) is characterized by relatively low to moderate BI values associated with intermediate to high SDI values. However, IHS is also characterized by strong vertical and lateral spatial variation in BI and SDI values. This is mirrors infaunal responses to different depositional conditions along and across IHS bar forms.

3. Facies interpreted to represent tidal flat deposition (F9) are characterized by the relatively highest BI values coupled with intermediate to low SDI values. This is an example of how SDI is more attuned to tracking changes in

salinity stress, whereas BI is a better proxy for sedimentation rates. However, for the most part, SDI and BI trends are often coincidental. When SDI and BI trends do not coincide, high SDI and low BI likely indicate high sedimentation rate stresses relative to salinity stress. Inversely, low SDI and high BI imply higher salinity stress relative to sedimentation rate stress.

Further process ichnology research in the McMurray formation should focus on: 1) differentiating process ichnology patterns stemming from genetically related along/across bar variation from un-related variation caused by different depositional episodes; 2) comparison of bed scale SDI curves with depth averaged SDI; 3) incorporating process ichnology in detailed facies modeling workflow for predicting resource distribution; and 4) mapping regional scale changes in SDI to determine regional variability in salinity stress.

Chapter 4

PyCHNO: A Core-Image Quantitative Ichnology Logging Software

4.1   Introduction

Process ichnology is a relatively new trace fossil analysis method that stems from both ichnofabric and ichnofacies analysis. In a process ichnology framework, trace fossils are interpreted via a combination of qualitative and semi-quantitative metrics in order to interpret physico-chemical stresses experienced by infauna (Gingras *et al.* 2011). Two measurements used in process ichnology as proxies for the amount of stress experienced by infauna as reflected by preserved trace fossils are bioturbation index (BI) and size-diversity index (SDI).

To encourage the use of these parameters for process ichnology workflows, a specialized ichnology data collection software package, PyCHNO, has been designed to minimize collection errors and decrease data collection time. The volume and resolution of data that can be collected with this software has hitherto been impossible to collect in a time-efficient manner. A further goal of this software is to standardize the data collection workflow and basic data averaging techniques for ichnological analyses. Therefore, PyCHNO can be used for any ichnological applications that require detailed trace fossil data collection. The name "PyCHNO" is derived from a combination of Python (programming language) and ichnology.

The following work demonstrates how PyCHNO can be used to quickly and effectively gather a large amount of ichnological information from core photographs. The software development, features, and general workflow of PyCHNO are outlined in the following sections. The development sections review the goals of developing quantitative image-based ichnological data collection software. The features section outlines the various data collection/characterization techniques that have been implemented in PyCHNO. A typical data collection workflow is also presented. PyCHNO (along with a demonstration video) is provided and available for free download as Online Supplemental Material. An in-depth demonstration of the application of PyCHNO collected data for interpreting the spatial and temporal variability in paleoenvironmental stresses is presented in Timmer *et al.* (2016c).

4.2   Indices Used in PyCHNO

Bioturbation index (BI) is a qualitative assessment of the proportion of the original sediment that was bioturbated (Reineck 1967; Taylor and Goldring 1993). The most common scheme involves assigning a number between 0 (no bioturbation) and 6 (complete biogenic sediment homogenization) to describe the degree of bioturbation in a given interval (Figure 4.1). A few workers have attempted to measure bioturbation intensity with image analysis workflows (Honeycutt and Plotnick 2008; Dorador *et al.* 2014). The methods in Dorador *et al.* (2014) require commercial software and are inefficient for whole-core descriptions as they are time-consuming. Honeycutt and Plotnick (2008) work, although groundbreaking, is not appropriate for describing the BI of an entire sedimentary core's image. These techniques require significant image processing and user interaction to gather quality data and are thus time-consuming. For this reason, the BI scheme *sensu* Reineck (1967) and Taylor and Goldring (1993) is adopted for the PyCHNO software. Size-diversity index (SDI) is calculated as the product of ichnogenera diversity and maximum causative burrow diameter. The maximum burrow diameter is a proxy for the size of the largest burrowing organism at a given time. The underlying assumption is

that the largest burrow diameter within a given interval is the most indicative of environmental conditions. Size-diversity index can be useful as a proxy for salinity and dissolved oxygen stress (Wignall and Myers 1988; Hauck *et al.* 2009). Because of this, SDI is especially useful for paleoenvironmental interpretations in marginal-marine depositional systems. Users recording SDI data should be aware of the possible pit-falls of measuring burrow diameters from 2D planes, as trace fossils typically occur in 3D (McIlroy 2004).

Using conventional SDI collection workflows, the worker must measure the maximum burrow diameter of most trace fossils within a given depth interval, find the maximum causative burrow diameter from those measurements, identify the ichnogenera present within that interval, and tabulate all of this data manually. Collecting SDI data is time-consuming, which effectively acts as a limiting factor on the adoption of SDI in ichnological analysis.

Depth averaging SDI measurements over a set interval (*e.g.* 75 cm for a core sleeve), also limits the accuracy of SDI. This is especially important if the SDI data are input in a geostatistical grid. In a geostatistical model, the SDI is "upscaled" or averaged into a grid, which may have different vertical cell thicknesses (*e.g.* 1 m) compared to the collected SDI data measurement increment (*e.g.* 75 cm). If the SDI data are already averaged over a specified interval (*e.g.* 75 cm), and then further averaged (*e.g.* 1 m increments) in order to match grid cell sizes, resolution is greatly reduced. For this reason, measurements of SDI over shorter vertical intervals are optimal.

4.3   PyCHNO

4.3.1   Software Development

PyCHNO is written in the Python programming language. Python was chosen as a development language for two reasons: (1) It is free and available on multiple platforms (*i.e.* OS X, Windows, Linux), and (2) It is a simple, easy to use language—a fact that will hopefully encourage further customization and development of the application by other ichnologists and sedimentologists. The major limitation of the Python language is that it is not a compiled language
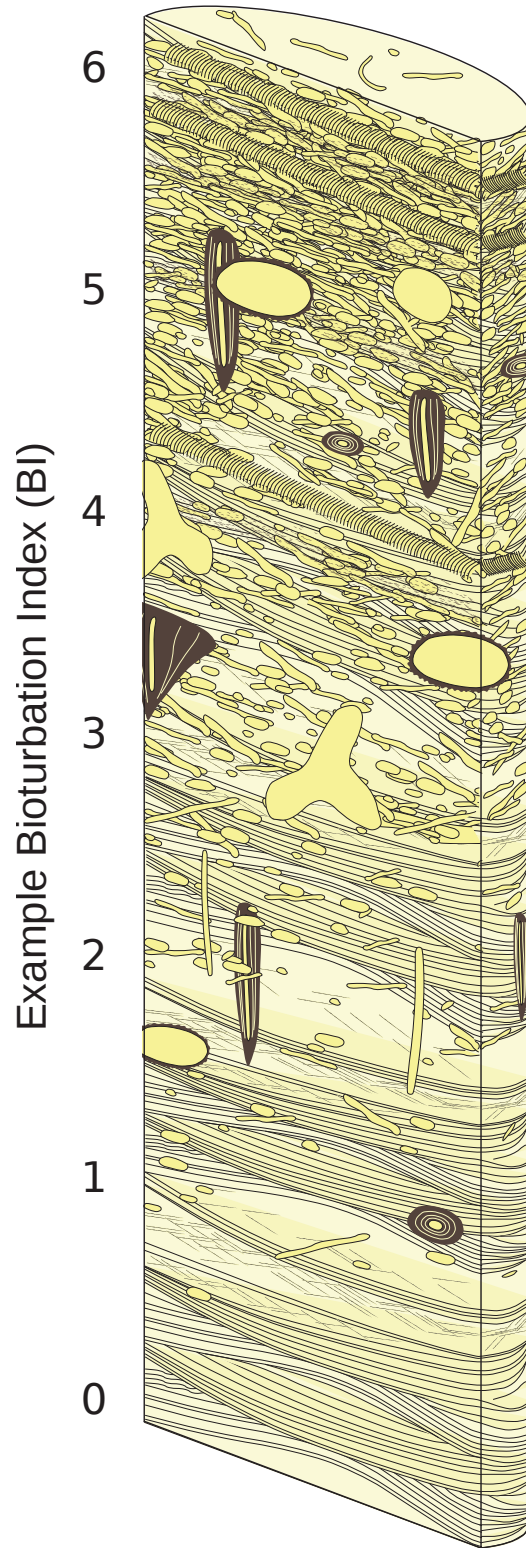
Figure 4.1: Schematic representation of bioturbation index (BI) modified from Gingras *et al.* 2011. BI 0 = 0% bioturbation, BI 1 = 0–1% bioturbation, BI 2 = 1–30% bioturbation, BI 3 = 30–60% bioturbation, BI 4 = 60–90% bioturbation, BI 5 = 90–99% bioturbation, BI 6 = 100%.

and is therefore not typically as fast as other popular languages such as C++ or JAVA.

The guidelines for creating PyCHNO software were as follows: (1) Provide a standardized, graphical user-interface based, data collection module for detailed ichnological work, specifically pertaining to process ichnology data collection; (2) Increase the efficiency of collecting quantitative ichnological data specifically pertaining to decreasing collection time requirements and eliminating data input errors (*i.e.* errors tabulating data); (3) Provide standardized techniques for averaging ichnological data on a user-defined lithology segment basis; (4) Organize quantitative ichnological data into data files that can easily be incorporated into statistical packages such as PAST (Hammer *et al.* 2001) or oil and gas geomodeling software such as Schlumberger's Petrel® for further analysis; (5) Provide a plotting utility for making ichnological logs at various scales; and (6) Provide a freely available, standalone, customizable and extensible tool to the ichnology and sedimentology community.

The features implemented in PyCHNO, and outlined in the next section were designed to follow these guidelines.

4.3.2 Features

The following section describes the features included in PyCHNO. Features are listed in the order that a user typically encounters them.

Lithology Segmentation.—Each cropped image corresponds to a core sleeve (*i.e.* a continuous segment corresponding to half of a core-box, typically 75 cm in length). The user assigns one of two lithologies (*e.g.* sandstone and mudstone or limestone and shale) to each image segment. The bounding box coordinates associated with each image lithology segment is used as the top and bottom coordinates of each segment (Figure 4.2). Lithology segments that are less than 1 cm thick are combined in the data export stage. This feature was implemented in order to merge segments that are continued over the span of more than one core box. Note that this feature can be modified in the source code if a user requires greater data collection resolution. The

software is designed to collect data from horizontal or gently dipping beds. In order to ensure segmentation accuracy, core photos of steeply dipping beds may have to be rotated so that beds are approximately horizontal.

Burrow Measurement and Tagging.—Once an image has been segmented, the user measures the burrow diameter of every burrow within every lithology segment, by clicking and dragging the mouse. Each action generates a line, and a trace fossil tag (*i.e.* a data structure containing the XY coordinates and name of the trace fossil) that documents where a burrow was measured. The user is required to input the trace fossil acronym prior to measuring every burrow, by typing the trace fossil acronym in a box at the bottom of the screen. The user is not required to re-enter the burrow name for each measurement—a feature that is useful when measuring multiple instances of the same ichnogenera in a given picture. The user can label trace fossils without drawing diameter lines by clicking the image where they wish to label a trace fossil. If the user decides to change a burrow measurement or label, right-clicking a burrow diameter line will delete the burrow record. Burrow measurements are saved in a database, therefore, users can reopen PyCHNO projects to verify measurements or change them as needed. This is a useful feature for quality control, and educational purposes. A researcher can verify the ichnological data they collected by reviewing photos they analyzed in PyCHNO. And, ichnological instructors can verify their students' trace fossil identification accuracy with a model answer key.

Bioturbation Index Measurement.—Bioturbation index (BI) is measured by selecting the appropriate index from a drag-down menu. Then, the user clicks, and drags the selected BI over the desired interval. The user can edit BI by clicking and dragging a new BI over a previously measured interval. This generates boxes on the right margin of the core sleeve that have a color fill that corresponds to the selected BI (Figure 4.3). In order to simplify direct comparisons between BI and SDI, BI is upscaled so that there is a unique BI value per measured lithology segment. The currently employed upscaling technique

69

in PyCHNO is a "most-of" calculation. That is, the BI value that occupies the largest proportion of a given lithology segment is taken as the BI of that segment. Intervals that aren't assigned BI values are automatically assigned a BI value of 0.

Data Export.—Once the user has collected data from all their images, in order to export data, the user must first import a file containing the top and base depth of each core sleeve or outcrop section image. The input depths are used to convert the pixel coordinates of each image into meters (for depths) and millimeters (for burrow diameters). Once the depth file is imported, the data can be exported in one of the following ways: (1) raw data (tab-delimited text file), where the output consists of the depth of each trace-fossil occurrence, the trace-fossil name, and the diameter of that trace fossil; (2) lithology segment-averaged data (tab-delimited text file), where the output consists of the maximum burrow diameter, ichnogenus diversity, SDI, abundance of every trace fossil for each lithology segment identified in images; and (3) PDF output (graphs), where the ichnological and lithology segment data are exported as plots at 1:25, 1:50, 1:100, and 1:200 scales.
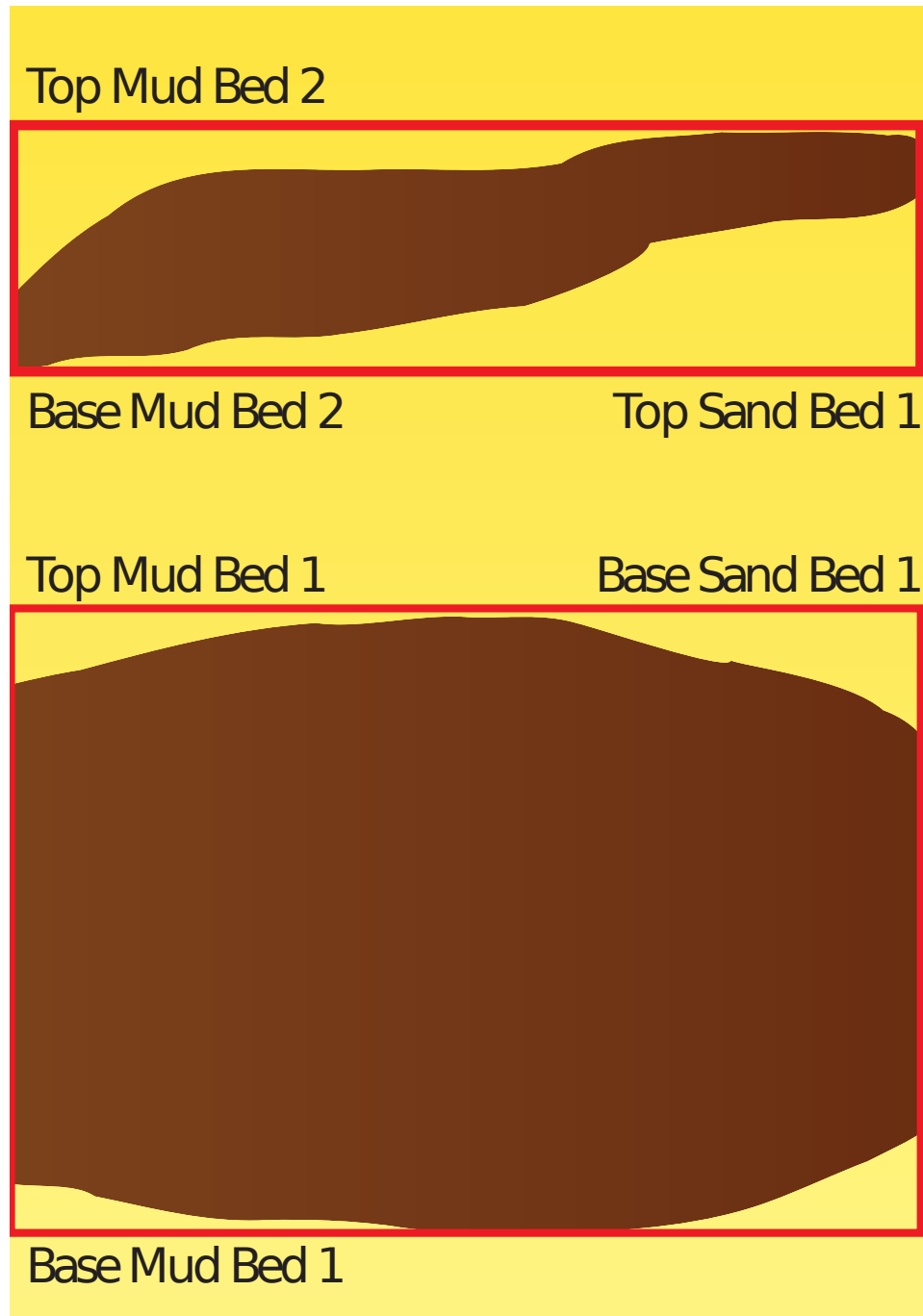
Figure 4.2: Schematic showing bounding boxes (in red) that are used to segment images into different lithology segments. The bounding box coordinates are used as the top and base coordinates of lithology segments.
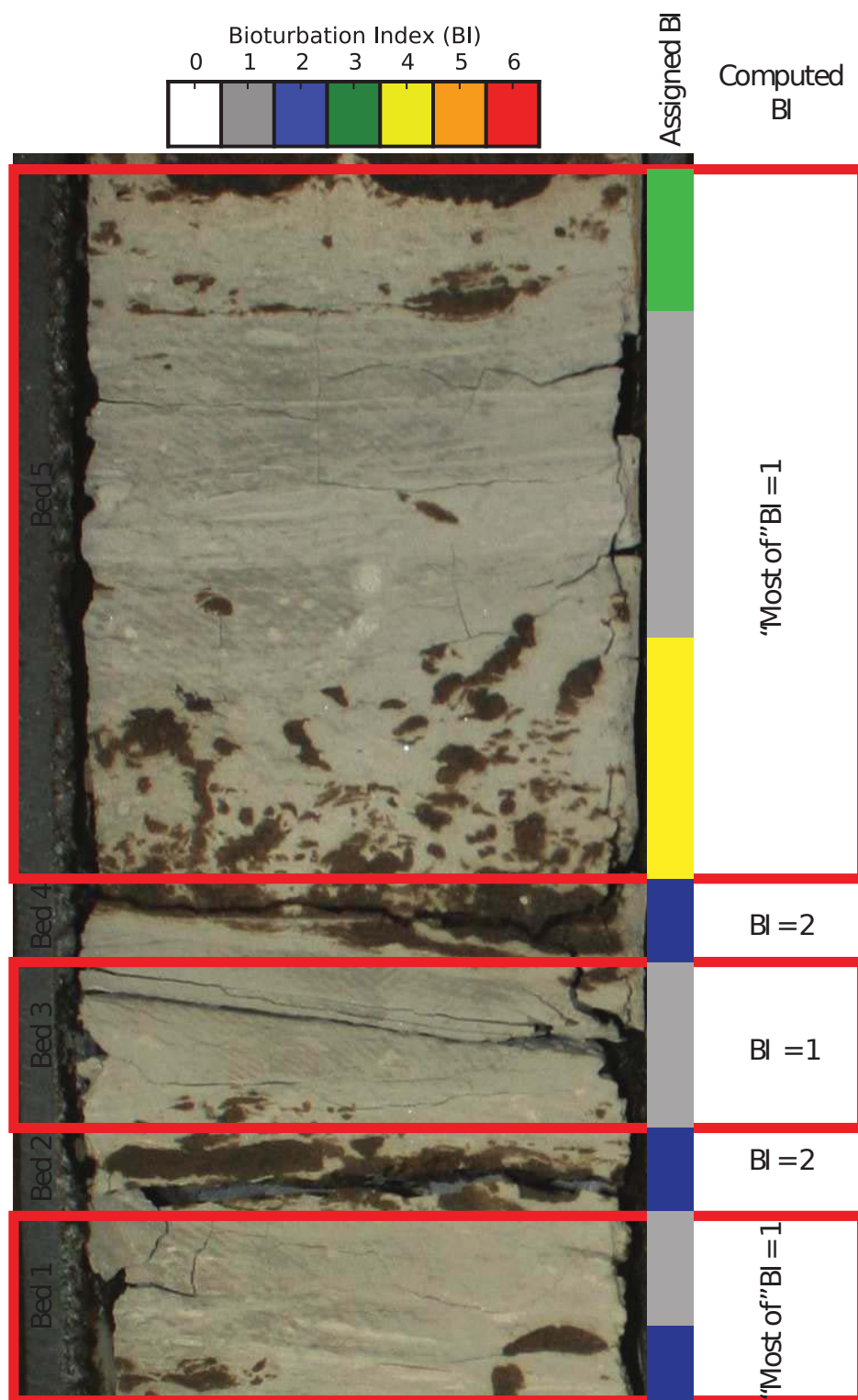
Figure 4.3: (Continued on the following page.)

Figure 4.3: Bioturbation index (BI) plotted next to a core photograph. Bioturbation index is computed using the 'most of' averaging technique, whereby the BI value that occupies the largest proportion of a given lithology segment is assigned as the BI of that lithology segment. In lithology segment 5, BI = 1 occupies the greatest proportion of the lithology segment, therefore the computed BI for lithology segment 5 is BI = 1. Note that the gray lithology corresponds to silty-mudstone, whereas the dark lithology corresponds to bitumen saturated sandstone.

4.4 Demonstration of a Typical Workflow

The typical PyCHNO workflow is summarized in Figure 4.4. Upon running PyCHNO, the user is asked to select a folder containing image files. The user should have a unique folder for every well that will be analyzed. Images should be cropped to a single core sleeve width. Once the user selects the image folder, the first image from that folder is displayed in PyCHNO. The "previous image" or "next image" commands under the "Tools" menu are used to navigate through the pictures. Note that PyCHNO automatically saves all collected data into a file titled: `PyCHNO_data.pkl`. The user will typically segment lithologies, identify trace fossils and assign BI values for a given image before moving on to the next image.

To segment lithologies (*e.g.* demarcate beds), the user draws red boxes by clicking and dragging their left mouse button over a desired interval (Figure 4.5). Boxes are drawn to identify one of two lithologies in a dual lithology system (*i.e.* mudstone beds are marked by boxes and the area between boxes mark sandstone beds). If the user decides to resize a box, he/she can left-click one of the box boundaries, and resize the box accordingly. The user can delete a red box by right clicking on a lithology segment boundary.
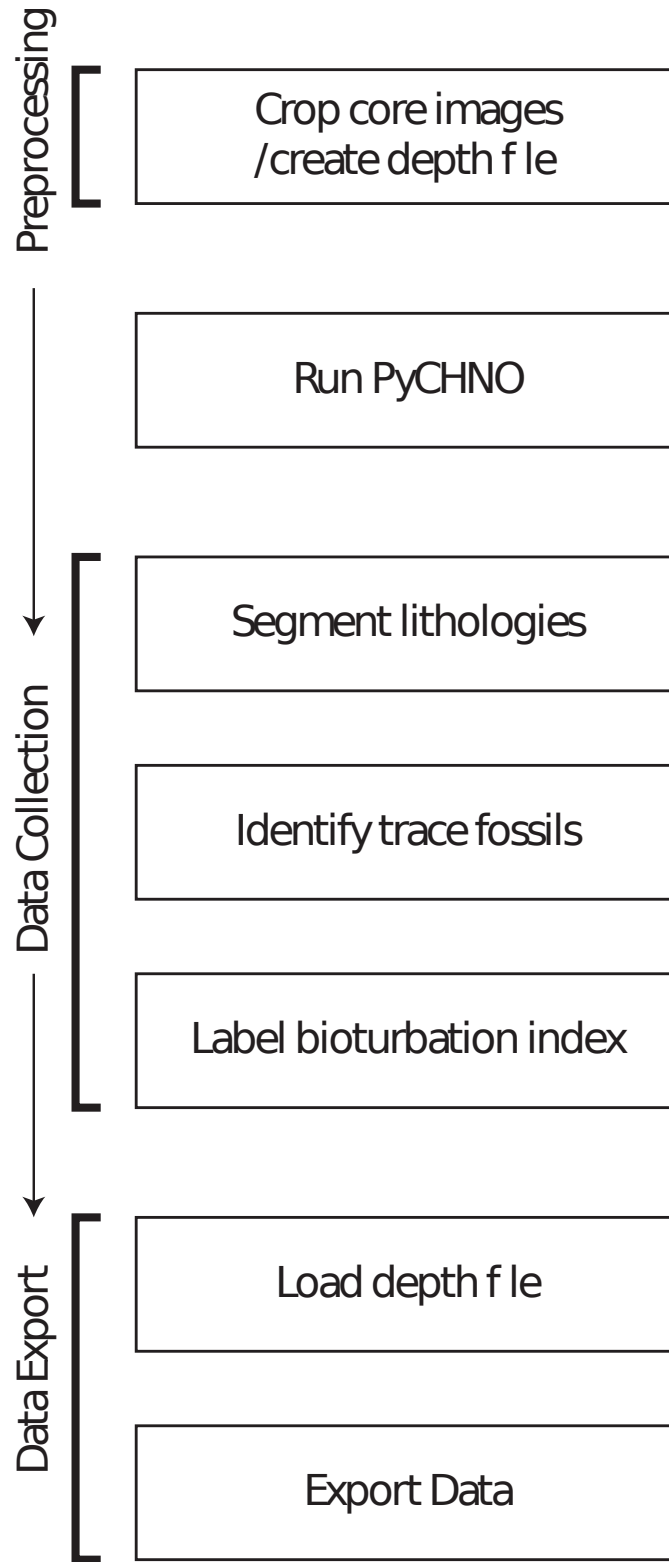
Figure 4.4: PyCHNO workflow diagram showing pre-processing, data collection, and data export steps.
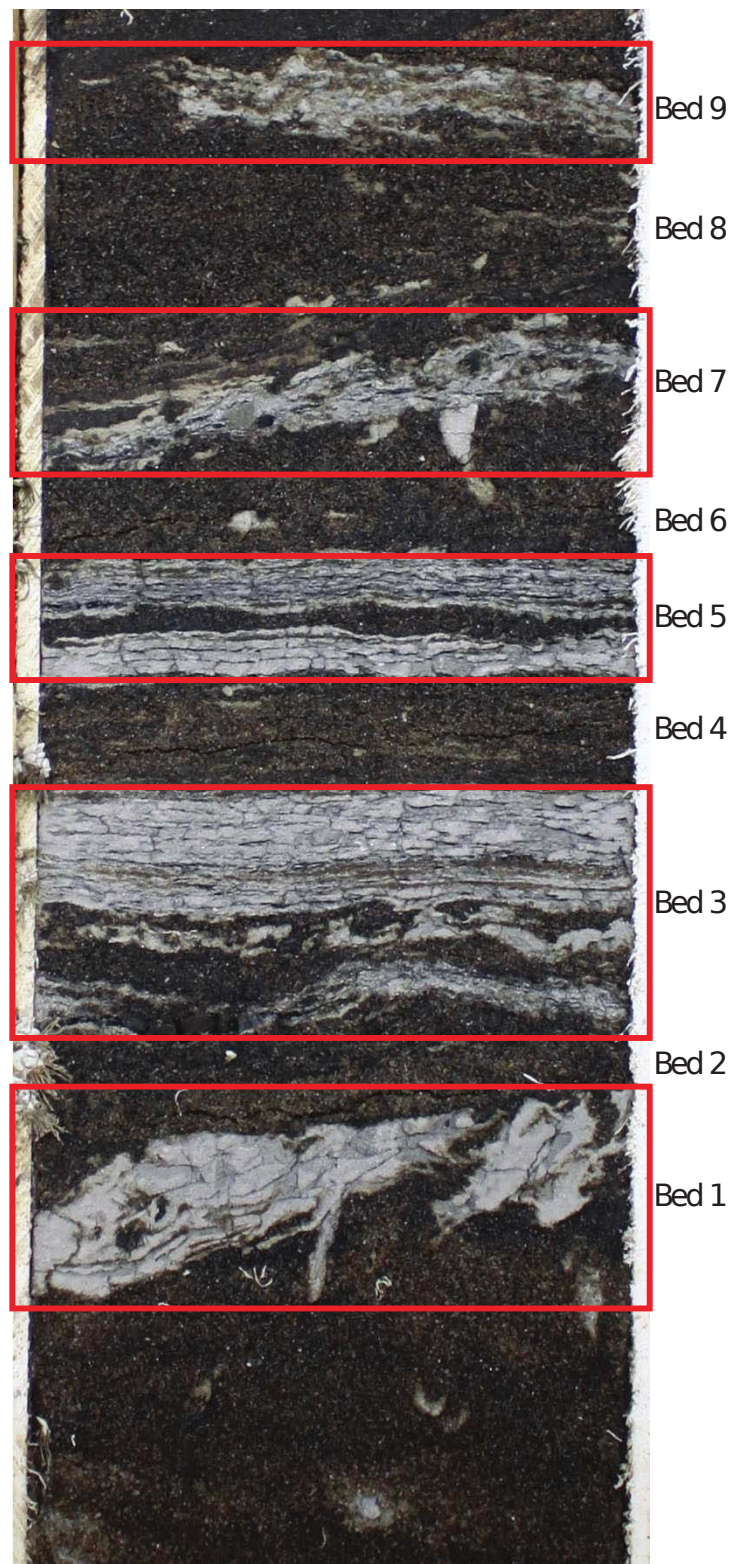
Figure 4.5: (Continued on the following page.)

Figure 4.5: Example of a portion of a single score sleeve photograph that has been segmented into nine lithology segments using PyCHNO. The photograph is from 09-04-098-10W4 (top = 45.37 m, base = 45.60 m). Note that the gray lithology corresponds to silty-mudstone, whereas the dark lithology corresponds to bitumen saturated sandstone.
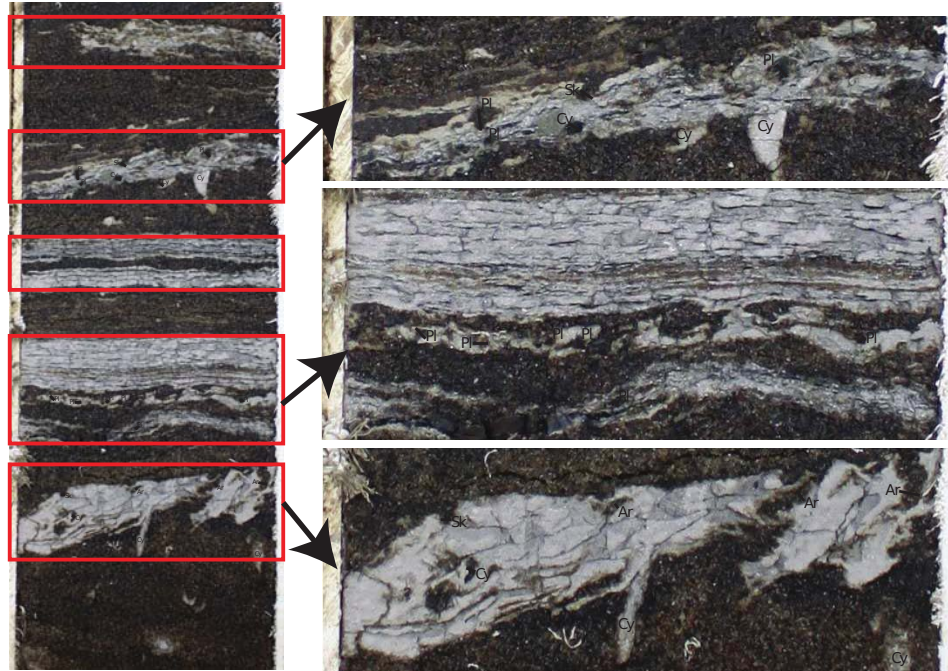
Figure 4.6: Example of a portion of a single core sleeve photograph, where trace fossils have been labeled with PyCHNO. Trace fossil names and diameters are labeled in black. Trace fossils identified include: *Arenicolites* (Ar), *Cylindrichnus* (Cy), *Planolites* (Pl), and *Skolithos* (Sk). The photograph is from 09-04-098-10W4 (top = 45.37 m, base = 45.60 m). Note that the gray lithology corresponds to silty-mudstone, whereas the dark lithology corresponds to bitumen saturated sandstone.

In order to label trace fossils, the user selects the "Measure Trace Fossils" option under the "Tools" menu. When this option is selected, a text input box appears on the bottom left corner of the application. The user types a trace fossil acronym (*e.g.* Gy for *Gyrolithes*) into the text input box. Then, the user can either left click and drag their mouse over the burrow diameter they wish to measure and identify or, he/she can left click and release their mouse to simply label the desired trace fossil without collecting a burrow diameter (*i.e.* a burrow diameter of 0 mm is assigned) (Figure 4.6). When the user is done labeling a certain trace fossil, they can enter a new trace fossil acronym into the text input box. The user can right click on any burrow label to delete a label from record.

To assign bioturbation index (BI) values, the user must select the "Label BI" option under the "Tools" menu. Once this option is selected, a drop

down list containing BI values 0 to 6 appears on the bottom left corner of the application. To assign a given BI value to an interval, the user selects the appropriate BI value from the drop down list, and left clicks and drags the mouse over the desired interval (Table 4.1). The user can resize an assigned BI range by clicking a BI rectangle, and dragging the rectangle to the desired location.

Once the user has finished collecting data, they must load the tab-delimited text file containing photo name, photo top depth, and photo base depth columns. To do so, the user selects "Load Depth Data" under the "File" menu. The user can now export the data. To export the data as a raw text file containing the names of trace fossils and the depth at which they were recorded, the user selects "Export Raw Data (text file)" under the "File" menu. An example of this type of file is shown in Table 4.2. To export the data as a text file containing lithology segment-averaged values, the user selects "Export Bed-Averaged Data (text file) under the "File" menu. Figure 4.7 shows an example of a lithology segment-averaged data text file. These files are easily opened with spreadsheet applications. To visualize the data PDF log, the user selects "Export Data as Graphical PDF Log" under the "File" menu. A window appears prompting the user to select the log's scale, and lithology colors (Figure 4.8). Once the user clicks "Export PDF" PyCHNO begins building the log's PDF. Depending on the quantity of data collected, this operation can take some time. An example of a PDF log is shown in Figure 4.9.

Table 4.1: Example of a PyCHNO raw data export file. The data comprises the depth, name, and burrow diameter of each trace fossil measured. The data are from 09-04-098-10W4 (top = 45.37 m, base = 45.60 m).

Depth of occurrence	Trace	Diameter(mm)
45.42	Pl	1.4
45.43	Sk	2.1
45.43	Pl	2.3
45.43	Cy	1.9
45.43	Cy	0.0
45.43	Pl	0.8
45.51	Pl	1.3
45.51	Pl	0.5
45.51	Pl	0.6
45.51	Pl	1.1
45.51	Pl	1.6
45.51	Pl	1.5
45.53	Ar	1.1
45.54	Ar	1.9
45.54	Ar	1.2
45.54	Sk	1.7
45.55	Cy	0.7
45.56	Cy	0.0

Table 4.2: Example of a PyCHNO bed-averaged data export file. The data comprises depth, lithology (S = sand, M = mud), bioturbation index (BI), maximum burrow diameter, diversity, size-diversity index (SDI), and trace fossil abundance for each measured lithology segment. The data are from 09-04-098-10W4 (top = 45.37 m, base = 45.60 m).

Depth	Lithology	BI	Maximum burrow diameter	Diversity	Size Diversity Index	Ar	Cy	Pl
45.37	S	0	0.0	0	0.0	0	0	0
45.38	M	1	0.0	0	0.0	0	0	0
45.39	S	0	0.0	0	0.0	0	0	0
45.42	M	2	2.3	3	6.8	0	2	3
45.44	S	0	0.0	0	0.0	0	0	0
45.45	M	1	0.0	0	0.0	0	0	0
45.47	S	0	0.0	0	0.0	0	0	0
45.48	M	0	1.6	1	1.6	0	0	6
45.52	S	0	0.0	0	0.0	0	0	0
45.53	M	2	1.9	3	5.6	3	2	0
45.56	S	1	0.0	0	0.0	0	0	0
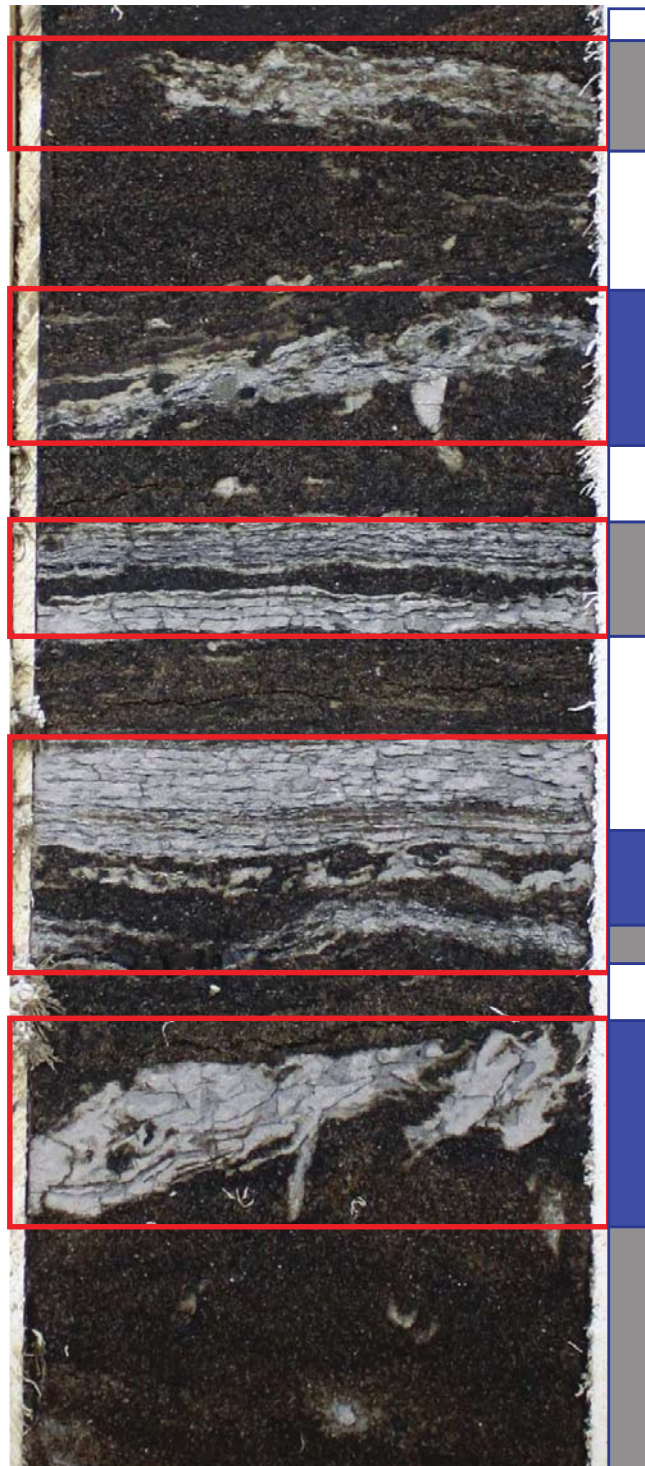
Figure 4.7: (Continued on the following page.)

Figure 4.7: Example of a portion of a single sleeve photograph that has been assigned bioturbation index (BI) values in PyCHNO. The photograph is from 09-04-098-10W4 (top = 45.37 m, base = 45.60 m). Note that the gray lithology corresponds to silty-mudstone, whereas the dark lithology corresponds to bitumen saturated sandstone.

Figure 4.8: Screen capture of PyCHNO PDF export option. The user can export PDF plots at 1:25, 1:50, 1:100, and 1:200 scales. The user can also select the color of measured lithologies.
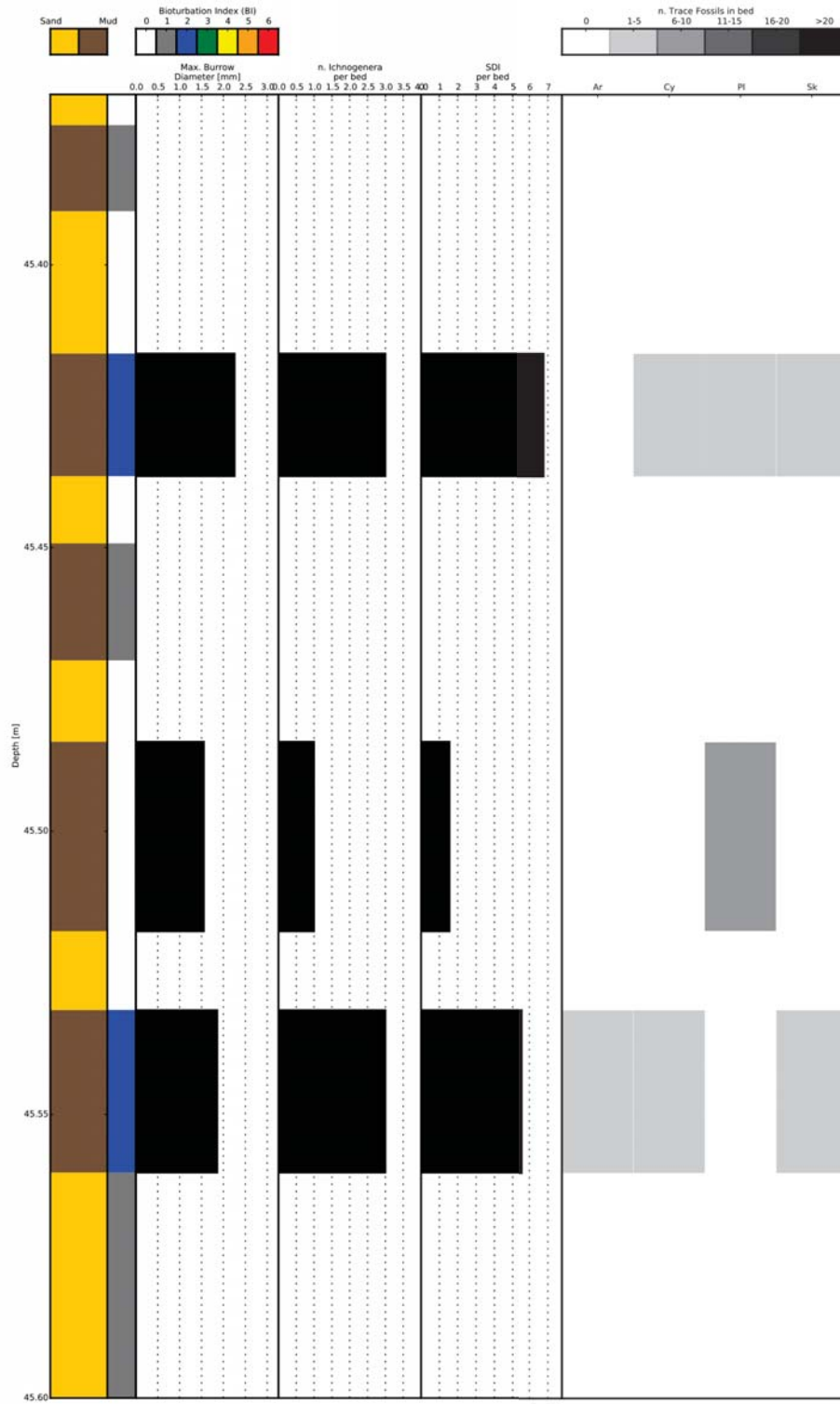
Figure 4.9: (Continued on the following page.)

Figure 4.9: Example of a PyCHNO generated PDF. Plotted data (from left to right) includes lithology, bioturbation index (BI), maximum burrow diameter, diversity, size-diversity index, *Arenicolites* (Ar) abundance, *Cylindrichnus* (Cy) abundance, *Planolites* (Pl) abundance, and *Skolithos* (Sk) abundance for each measured lithology segment. The data are from 09-04-098-10W4 (top = 45.37 m, base = 45.60 m).

4.5 Summary

PyCHNO is a specialized ichnology software designed to optimize and standardize the process ichnology data collection workflow. It presents an improvement upon previous quantitative methods as it allows the user to collect and share standardized data that can be integrated into larger geological datasets. It allows the worker to quickly gather, analyze, interpret and justify ichnological trends. The main features of this application are lithology segmentation and trace fossil data collection. Trace fossil data including SDI and BI, are good proxies for environmental stresses, and are easily gathered with PyCHNO. The ichnological datasets collected with PyCHNO, including lithology segment-scale SDI and BI, are easily exported into text files or PDF logs.

PyCHNO has several limitations that end-users should be considered. First, PyCHNO should be integrated with grain-size profiles, lithofacies schemes or even petrophysical logs in order to form the basis of robust sedimentological interpretations. And, the dual lithology system (*e.g.* mudstone and sandstone) may be oversimplified for some users (especially in carbonates/mixed system). Further software limitations include 1 cm lithology segmentation interval limits and no handling for trace fossil tiering. These users are encouraged to modify the source code to suit their requirements. Next, the user should be aware of the limitations of collecting trace-fossil diameters for calculating SDI from 2D planes. This is especially important if the user is not familiar with the morphology of particular burrows.

Data are available from the PALAIOS Data Archive: `<http://www.sepm.org/pages.aspx?pageid=332>`.

Chapter 5

Spatial and Temporal Significance of Process Ichnology Data From Silty-Mudstone Beds of Inclined Heterolithic Stratification

5.1 Introduction

Variations in physical and chemical ecological stresses greatly impact the behavior of burrowing animals. The characteristics of trace fossils and trace-fossil assemblages are therefore ideal for studying the temporal and spatial variability of paleoecological stresses (*e.g.* Buatois and Mangano 2002; McIlroy 2004; MacEachern *et al.* 2007; Buatois *et al.* 2008; Carmona *et al.* 2009; Phillips *et al.* 2011; Virtasalo *et al.* 2011; Uchman *et al.* 2013; Baucon *et al.* 2014; Hurd *et al.* 2014). In marginal-marine settings, stresses that affect infauna typically include salinity, sedimentation rates, substrate cohesion, oxygenation, and hydraulic energy (*e.g.* Pemberton *et al.* 1982; Goldring 1995; Gingras *et al.* 1999; Taylor *et al.* 2003; Hubbard *et al.* 2004; Buatois *et al.* 2005; Savrda 2007; Gingras and MacEachern 2007; Hauck *et al.* 2009). Bioturbation preserved in the rock record can be used as paleoecological proxies using process ichnology principles.

Process ichnology combines qualitative and quantitative measurements, whereby trace-fossil data are used as proxies for interpreting the chemical

and physical environmental stresses suffered by burrowing organisms (Gingras *et al.* 2011). Some ichnological measurements that reflect paleoenvironmental stresses over a given interval, and that do not require collection from an ichnological specialist, include maximum burrow diameter, the number of ichnogenera present, the degree of bioturbation, and the presence or absence of specific ichnogenera. These measurements can be taken and averaged at a bed scale, or binned into specified depth increments (*e.g.* 10-cm increments).

The degree of bioturbation can be collected using the semiquantitative bioturbation index (BI) (*sensu* Reineck 1967; Taylor and Goldring 1993). Bioturbation index is used as a proxy for determining sedimentation rates, especially if the original biomass can be inferred (Dafoe *et al.* 2008; Gingras *et al.* 2008), and for estimating the periodic nature of fluctuating physico-chemical stress (Pollard *et al.* 1993; Buatois *et al.* 1997; Gingras *et al.* 2002; Hovikoski *et al.* 2008). Maximum burrow diameter and the number of trace-fossil genera present in a given interval are represented by the size-diversity index (SDI) (*sensu* Hauck *et al.* 2009). The size-diversity index reflects physiological stress, such as water salinity variability, which causes organism diminution and diversity reduction (*e.g.* Botterill *et al.* 2015).

This paper focuses on understanding the distribution of the above bioturbation parameters in inclined heterolithic stratification of the McMurray Formation. Inclined heterolithic stratification (IHS) forms by the lateral or vertical accretion of point bars in channelized settings (Thomas *et al.* 1987) and is widely preserved in the McMurray Formation. Inclined heterolithic stratification comprises dipping, alternating beds of silty-mudstone and sandstone. The heterolithic nature of these deposits reflects variations in energy and sediment supply. In estuarine settings, these energy and sediment supply variations are caused by the interplay of seasonal or longer term climatic induced variations in streamflow along with tidal cyclicity (*e.g.* Allen 1991; Dalrymple *et al.* 1992; Hovikoski *et al.* 2008). Variations in streamflow, sediment supply, and fluvial/tidal energy directly control sedimentation rates, salinity, substrate consistency, and hydraulic energy (Gingras *et al.* 1999; Hubbard *et al.* 2004). Therefore changes in these parameters are the main contributors to

the physical and chemical stresses experienced by infauna within channelized portions of estuarine successions.

In this study, we quantitatively explore the spatial and temporal variability of ecologic stress in fine-grained (*i.e.* comprising varying proportions of silt and clay) beds of IHS of the Lower Cretaceous McMurray Formation by measuring key ichnofaunal characteristics such as BI, SDI, and the abundance of ichnogenera. We subsequently assess these data with a quantitative approach. Although qualitative discussions of ichnological periodicity in IHS have been published (*e.g.* Gingras *et al.* 1999; Gingras *et al.* 2002; Hovikoski *et al.* 2008), quantitative assessments of bioturbation periodicity in IHS have not. The primary objective of this study is to determine whether or not trace fossil data have cyclical patterns, to observe if those patterns are similar between wells, and to see if these patterns can be linked to climatic events such as El Niño/Southern Oscillation (ENSO) cycles. The overall goal of these observations is to better understand Cretaceous estuarine dynamics related to trace fossils.

5.2 McMurray Formation Background

The McMurray Formation is interpreted to reflect deposition stemming from the southward transgression of the Boreal Sea over Devonian carbonates during the Lower Cretaceous (Ranger and Pemberton 1997). Significant karstification of the Devonian carbonates occurred prior to McMurray deposition, with dissolution and cavern expansion continuing today (Broughton 2013, Broughton 2014, Broughton 2015). The McMurray Formation is informally divided into three units: the lower, middle and upper McMurray Formation (Carrigy 1959). The lower McMurray Formation is often interpreted to represent dominantly fluvial deposition, with increasing estuarine and marine depositional affinity moving into the middle and upper McMurray Formation (Crerar and Arnott 2007; Musial *et al.* 2012).

Due to the large geographical extent of the McMurray Formation, the above interpretations and subdivisions are not applicable in all areas. Specif-

ically, the tidal/brackish influence on the deposit is widely debated (*e.g.* Crerar and Arnott 2007; Hubbard *et al.* 2011; Labrecque *et al.* 2011b; Fustic *et al.* 2012; Jablonski and Dalrymple 2016; Timmer *et al.* 2016a). Trace-fossil datasets can be used for determining the tidal versus fluvial affinities of many McMurray Formation intervals. For example, one of the first published examples of an ancient brackish-water trace fossil assemblage demonstrates observations from the Lower Cretaceous McMurray Formation (Pemberton *et al.* 1982). Since then, multiple studies have used trace fossils to support brackish water paleoenvironmental interpretations of the McMurray Formation (Ranger and Pemberton 1988; Ranger and Pemberton 1992; Ranger and Pemberton 1997; Wightman and Pemberton 1997; Lettley *et al.* 2005b; Lettley *et al.* 2005a; Crerar and Arnott 2007; Musial *et al.* 2012).

5.3   Study Area and Dataset

The study area is located within a 10 km (north-south) by 20 km (east-west) box centered on 57°31.131'N, 111°37.077'W (Township 98 Ranges 10 and 11 west of the fourth meridian) (Figure 5.1A). This location is approximately 80 kilometers north of the city of Fort McMurray in northeastern Alberta and is located within the surface mineable area of the oil sands. There are 43 wells in this study area. Of these, four wells (11-17-098-10W4, 12-11-098-11W4, 13-02-098-11W4, and 14-13-098-11W4) were selected for detailed description on the basis of vintage (more recently cored wells typically have better core recovery/quality), availability at the Alberta Energy Regulator's core research center, inter-well proximity, greater McMurray Formation thickness and abundance of IHS. High-resolution photographs of the cored section from each well were taken using a Canon D50 camera and saved as JPEG images. The core photographs form the basis of this study.

Argillaceous and brachiopod-rich floatstone and rudstone limestone units of the Devonian Beaverhill Lake Group (Figure 5.1B) lie directly below the McMurray Formation. The top of the McMurray Formation is truncated by a Quaternary sand and gravel unit (Figure 5.1B).
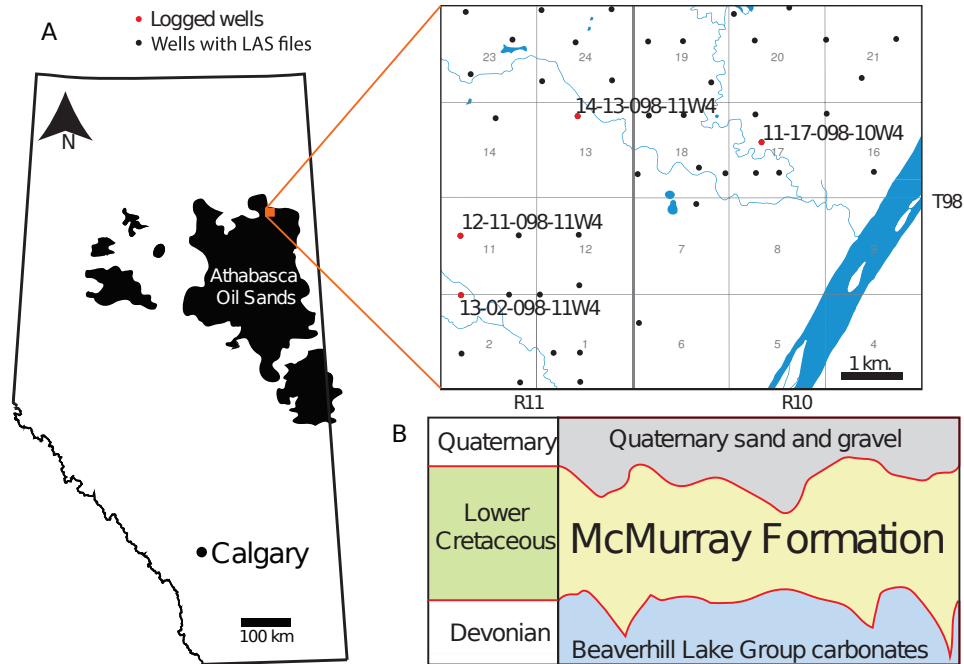
Figure 5.1: Location map and stratigraphic chart. A) Map showing the extent of the oil sands in Alberta and the location of the study area. The study area comprises 43 wells (black dots), four of which were logged for this study (red dots). B) Schematic stratigraphy of the study area.

Inclined heterolithic stratification from the study area (Figure 5.2A– 5.2D) comprises two silty mudstone lithosomes. The first lithosome comprises silty mudstone interlaminated with fine- to medium-grained sand separated by thick, apparently massive sandstone beds (Figure 5.2E), is variably bioturbated. Identified trace fossils include: *Arenicolites* (Figure 5.3A), *Cylindrichnus* (Figure 5.3B), *Gyrolithes* (Figure 5.3C), *Planolites* (Figure 5.3D), *Rosselia* (Figure 5.3F), and *Skolithos* (Figure 5.3F). The second lithosome is a brecciated unit with silty-mudstone clasts forming bedding in a fine- to medium-grained sand matrix (Figure 5.2E).

The IHS interval from each well displays a characteristic decrease in sandstone content upwards. The base of the IHS interval from 11-17-098-10W4 is characterized by brecciated silty-mudstone clasts, overlayed by interlaminated mudstone/silt and sand (Figure 5.2A). The basal portion of the IHS from 11-17-098-10W4 contrasts with the IHS interval of the other wells (Figure 5.2B– 5.2D), which comprises sandstone-dominated bedding separated by
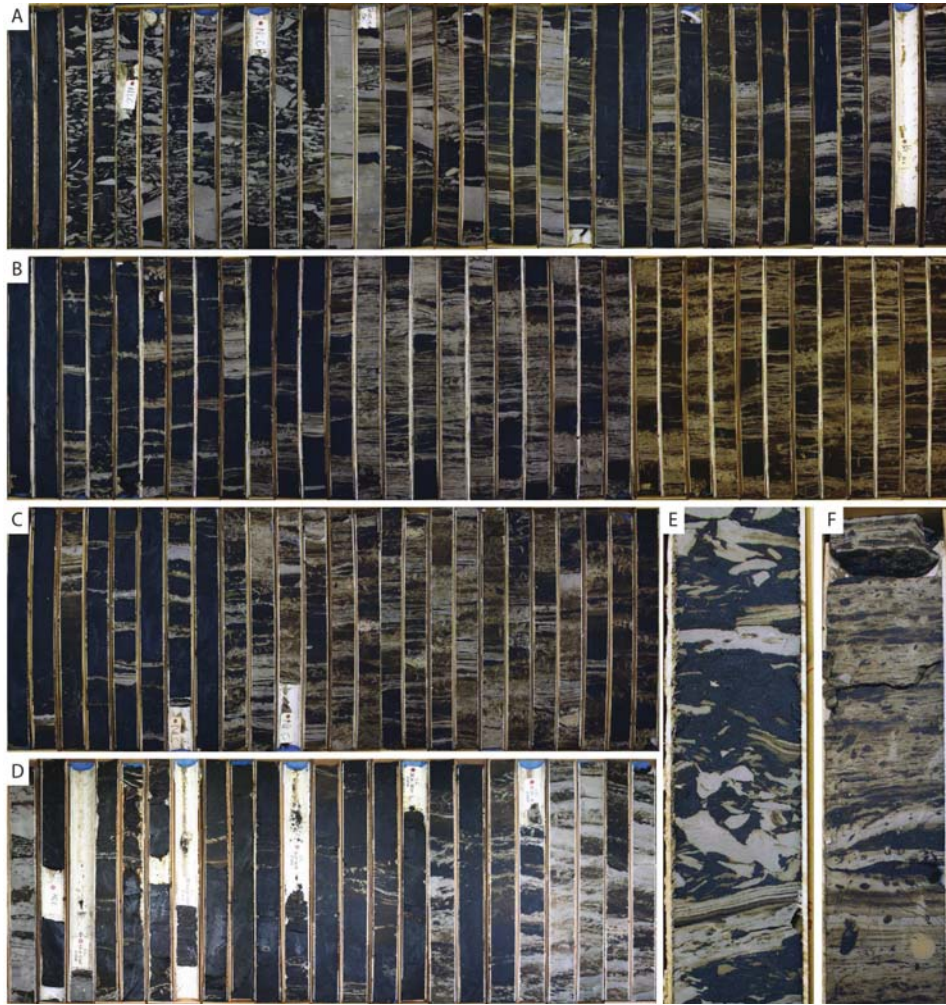
Figure 5.2: Photos showing inclined heterolithic stratification (IHS) measured for this study. Darker intervals comprise bitumen saturated sand, and lighter (gray) intervals correspond to silty-mudstone lithologies. A) Boxshots from 11-17-098-10W4 showing brecciated IHS and bioturbated interlaminated silty-mudstone beds. Depth decreases from left to right. Each core sleeve is 75 cm in length. B) Boxshots from 13-02-098-11W4 showing interlaminated silty-mudstone IHS beds. Depth decreases from left to right. Each core sleeve is 75 cm in length. C) Boxshots from 12-11-098-11W4 showing interlaminated silty-mudstone IHS beds. Depth decreases from left to right. Each core sleeve is 75 cm in length. D) Boxshots from 14-13-098-11W4 showing interlaminated silty-mudstone IHS beds. Depth decreases from left to right. Each core sleeve is 75 in length. Boxshot photos courtesy of Eric Ditzler. E) Close up photo of brecciated IHS lithosome from 11-17-098-10W4. Note that some clasts maintain relatively consistent bedding dips. F) Close up photo of bioturbated interlaminated IHS lithosome from 12-11-098-11W4.
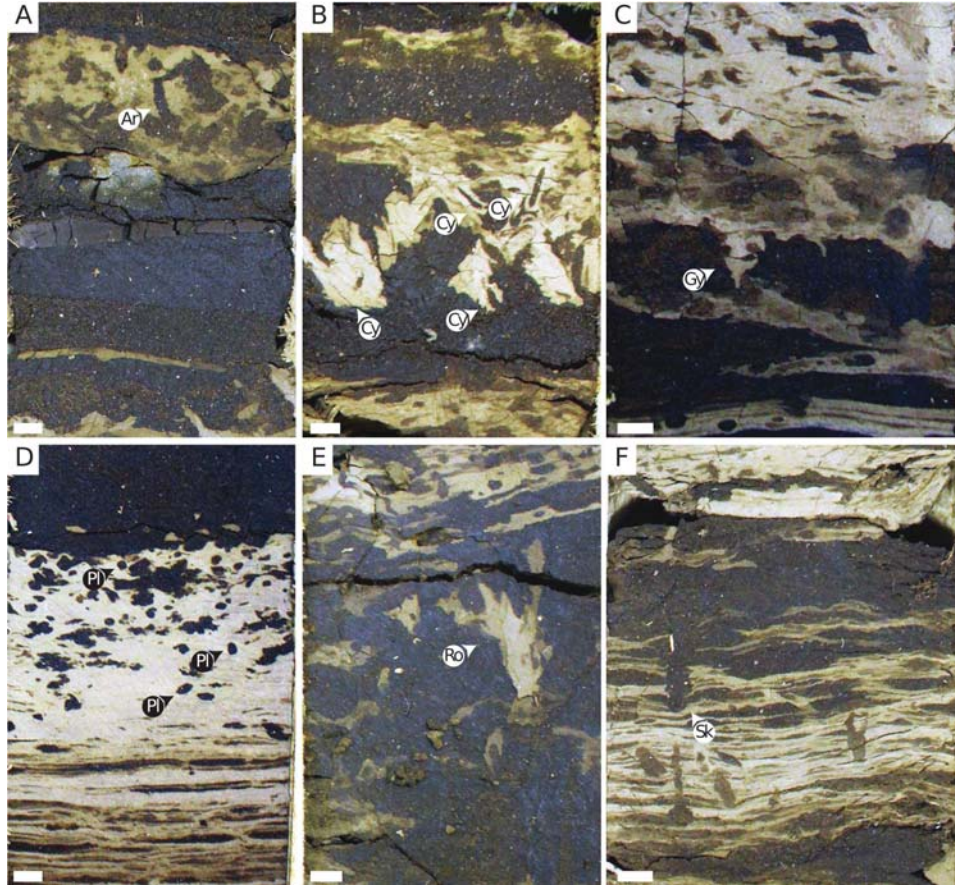
Figure 5.3: Examples of trace fossils preserved in inclined heterolithic stratification (IHS) from study area wells. A) *Arenicolites* (Ar) in bioturbated silty-mudstone IHS bed. Photo from 12-11-098-11W4. B) Multiple *Cylindrichnus* (Cy) crossing interlaminated silty mudstone IHS bed. Photo from 13-02-098-11W4. C) *Gyrolithes* (Gy) at base of interlaminated silty mudstone IHS bed. Photo from 13-02-098-11W4. D) *Planolites* (Pl) from upper portion of silty mudstone IHS bed. Photo from 11-17-098-10W4. E) *Rosselia* (Ro) beneath interlaminated silty mudstone IHS bed. Photo from 12-11-098-11W4. F) *Skolithos* (Sk) crossing interlaminated silty-mudstone IHS bed. Photo from 13-02-098-11W4. All scale bars = 1 cm.

relatively thin silty mudstone beds. Note that the preserved IHS intervals for 11-17-098-10W4 and 13-02-098-11W4 (Figure 5.2A, 5.2B) are thicker (24 m and 25 m respectively) compared to approximately 18 m for 12-11-098-11W4 and 16 m for 14-13-098-11W4 (Figure 5.2C, 5.2D).

5.4 Methods

5.4.1 Data Collection

Each core photograph was cropped so that the top and base of the photograph corresponded exactly to the recorded top and base depth of the core photo. The quantitative ichnological collection software PyCHNO (Timmer *et al.* 2016b) was used to collect process ichnology data from the core photographs. With PyCHNO, fine-grained beds (*i.e.* mudstone or siltstone beds) that were separated by $\geq$ 1 cm and that were $\geq$ 1 cm in thickness were recorded. The BI of each bed was also recorded. Then, the name and inner diameter (*i.e.* the part of the burrow corresponding to the body diameter) of every identifiable burrow was collected. For burrows where the inner diameter was not observable (*e.g. Gyrolithes*), or non-representative of the size of the burrowing organism (*e.g. Rosselia*), a burrow diameter of zero was assigned. The SDI was calculated as the product of the maximum burrow diameter and diversity of each fine-grained bed: see Botterill *et al.* (2015) for an expanded explanation justifying the use of SDI. The BI, SDI, and abundance of each trace fossil genus present in each bed were exported as a tabulated text file for each well. Plotted values of each of these parameters were exported as PDFs.

5.4.2 Data Processing and Clustering

In order to simplify the simultaneous analysis of multiple process ichnology parameters (*i.e.* SDI, BI, and the abundance of ichnogenera per bed), these values were clustered and manually ranked into 10 "cumulative stress groups" using a K-means clustering analysis before performing dynamic time warping (DTW) and continuous wavelet transform (CWT) analyses. These techniques are explained later in the methods section.

95

The ichnological community has commonly employed cluster analysis techniques for identifying the structure of trace fossil assemblages, and splitting trace fossil data into groups (Bjerstedt 1988; Jones and Pemberton 1989; Ranger and Pemberton 1991; Ranger and Pemberton 1997; Draganits *et al.* 2001; Davies *et al.* 2006; Smith *et al.* 2008; Pervesler *et al.* 2011; Baucon and Felletti 2013; Baucon *et al.* 2014; Bell *et al.* 2013; Simo and Tomasovych 2013; El-Sabbagh *et al.* 2015; Hils and Hembree 2015). Note, however, that the above listed studies used the presence or absence of trace fossils rather than a full suite of ichnological parameters in their cluster analyses.
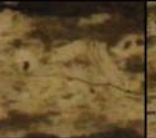
A Python (programming language) script was written to process the data collected in PyCHNO that was exported as text files. This script executes the following operations:
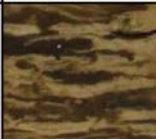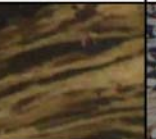
1. Pool data from all wells into a single data structure.

2. Scale each of the data categories (*i.e.* BI, SDI, genus abundance) onto a scale of 0 to 1 so that each category is weighted equally for clustering.

3. Cluster each bed into one of ten different clusters using K-means clustering. The clustering library is from Scikit Learn (Pedregosa *et al.* 2011).

4. Crop a photo of each bed, and place the cropped photo into a folder that corresponds to the bed's assigned cluster.

5. Allow the user to drag images into different folders to change the group assigned to the image's bed, in order to quality control the clustering process.

6. Allow the user to rank the clusters in terms of stress (i.e, cluster in terms of least stressed [cluster 1] to most stressed [cluster 10]).

7. Create and export a log for each well as text files, where the cluster numbers are arranged in stratigraphic order. Create graphical plots of these logs.

The script was run iteratively until the clustering results were judged to be accurate (*i.e.* a small number of images had to be moved into different folders to reform clustering assignments). We ranked the ichnological clusters according to interpreted increasing intensity of cumulative ecologic stress. This was completed on the basis of average cluster SDI, BI and visual examination of images in each cluster (see Table 5.1). After this, the clustered data were

Table 5.1: Summary of number of beds, average bioturbation index (BI), and size diversity index (SDI) of each ichnological clusters. Clusters are arranged on the basis of interpreted overall stress from least stressed (1) to most stressed (10). Core photos are approximately 7 cm in width.

Ichno Cluster	1	2	3	4	5
Photo					
n. beds	51	21	41	105	51
Average BI	3.5	4.4	5.0	4.0	2.0
Average SDI	7.3	3.9	1.9	1.9	4.5

Ichno Cluster	6	7	8	9	10
Photo					
n. beds	58	65	74	117	212
Average BI	3.0	0.7	2.0	1.0	0.0
Average SDI	1.7	3.7	0.8	0.5	0.1

exported for the time-series analysis workflow.

With K-means clustering, the number of clusters, K, is predetermined before the clustering operation begins. A K value of 10 was deemed appropriate for this study for two reasons: (1) Ten clusters effectively divide the process ichnology data into a sufficient number of categories for interpretation without oversimplifying the dataset; and (2) clustering results were manually verified to determine that each cluster contains beds with distinct ichnological characteristics (*i.e.* BI, SDI, genus abundance). Results were manually (*i.e.* visually) verified (step 5 of the clustering workflow) by examination of the cropped image of each bed in a cluster, and by comparing the image to the other images assigned to that cluster.

5.4.3 Dynamic Time Warping

To analyze this quantitative ichnological data, we treat ichnological data as categorical time-series. Time-series are essentially functions describing how a variable (or multiple variables) changes through time (or depth). Dynamic

Time Warping (DTW) was used to compare two ecologic stress cluster series in order to understand the spatial variability of series, and to identify the intervals of both series that are the most similar along depth.

Dynamic time warping is an algorithm for finding the similar portions of two time-series along the length of the time-series that are characterized by events that have different lengths (*i.e.* differential preservation of a given sedimentary package/differential initial accommodation/differential sedimentation rates), different magnitudes, or truncated events (*i.e.* erosion).

The algorithm maps points from the first sequence onto the second sequence, generating a warping function based on the minimized Euclidean distance between each pair of points. To visually compare the time-series, one time-series is placed on the x-axis of a plot, and the other time-series is placed on the y-axis of a plot. The warping function defines a line that starts at the plot's origin moving in the direction of minimal difference between the two time-series. If two identical time-series are input in a DTW algorithm, the warping function is diagonal. The more dissimilar two series are from each other; the more horizontal or vertical the warping function.

We employed the Machine Learning Python (MLPY) (Albanese *et al.* 2012) DTW algorithm based on Keogh and Pazzani (2001). Dynamic time warping has not been used for sedimentological or ichnological applications with the exception of the work by Hladil *et al.* (2010) and Chadimova *et al.* (2015) on the application of DTW for magnetostratigraphy. Further details of the DTW method are available in Hladil *et al.* (2010).

5.4.4 Continuous Wavelet Transform

To quantitatively assess the degree of cyclicity with regard to ecologic stress cluster assignments along depth, each well's succession was considered a time-series, where each bed corresponds to a successive time-series step. To determine the periodicity of a signal, it is useful to convert the time-series into the frequency domain. The continuous wavelet transform (CWT) (Goupillaud *et al.* 1984) converts a series into the frequency domain, while simultaneously preserving the time domain component. This way the cyclical components of

a signal can be situated in the time domain.

Essentially, the wavelet transform performs a convolution of time-series with a wavelet (for this study we used the Morlet wavelet), which is scaled to correspond to different frequencies. This generates a correlation coefficient matrix, where the vertical axis comprises each of the wavelet scales (*i.e.* frequencies), and the horizontal axis consists of the time-series steps. This matrix is contoured, whereby the larger values can be interpreted to represent more cyclical components of the signal and the lower correlation values are the less cyclical signal components. These plots are referred to as scalograms. This allows for observations of where the frequency driving components of a time-series are located in time, what the dominant frequency at any given time step is, and variations in driving frequency over the length of the time-series. Areas where a strong frequency component is not present can be identified with a scalogram. These gaps can indicate noise (*i.e.* high frequency spikes) or breaks in periodicity. Note that gaps in cyclicity do not indicate that the observed periodic component is of lesser statistical value. The edges of time-series are affected by zero padding (*i.e.* adding zeros to the start and the end of the time-series) when converting to the frequency domain. A cone of influence, a shaded area representing values of limited reliability, demarcates this region.

Additional information on the CWT is available in Torrence and Compo (1998). Although CWT analysis has not previously been applied to trace fossil data, note that, Fourier analysis of bioturbation index in laminae has been studied previously (Davies *et al.* 2012).

5.5   Results

5.5.1   Ichnological Logs

The ichnological logs are described from the wells in turn from south to north. The logs reveal the vertical distribution of silty mudstone and sandstone beds, BI, maximum burrow diameter, the number of ichnogenera per bed, SDI, and the presence/abundance of ichnogenera for each bed. The data used to generate these logs is from IHS intervals exclusively.
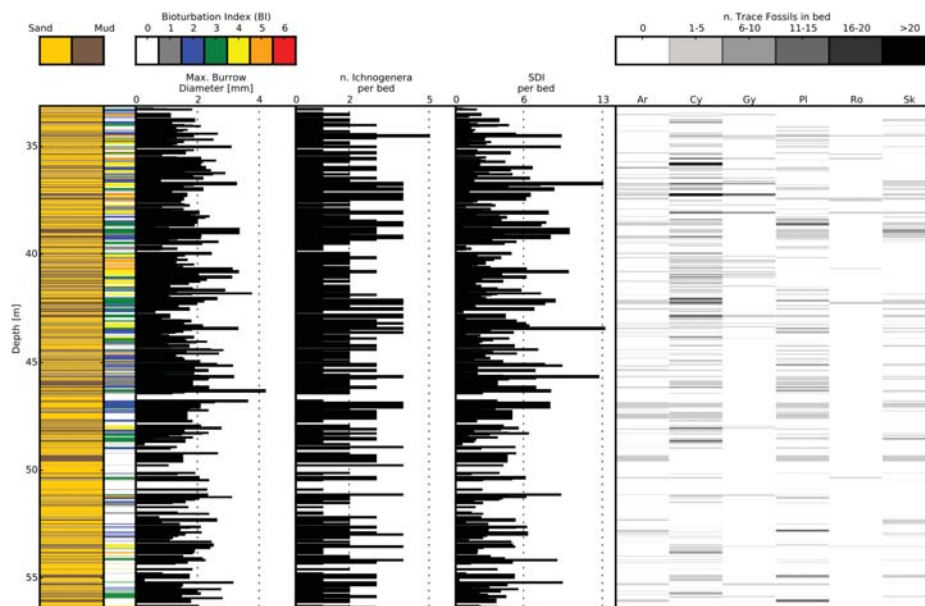
Figure 5.4: PyCHNO generated log of silty-mudstone and sandstone beds from core photographs of 13-02-098-11W4 from inclined heterolithic stratification intervals. Data shown (from left to right): bed thickness/lithology, bioturbation index (BI), maximum burrow diameter, number of ichnogenera per bed, size-diversity index (SDI), and the abundance of each trace fossil genus present in each bed. Abbreviations: Ar = *Arenicolites*; Cy = *Cylindrichnus*; Gy = *Gyrolithes*; Pl = *Planolites*; Ro = *Rosselia*; Sk = *Skolithos*. The log is at a 1:200 scale. Note the sinusoidal trend of bioturbation index, maximum burrow diameter, number of ichnogenera per bed, size diversity index (SDI) logs.

The PyCHNO generated log for 13-02-098-11W4 shows highly variable BI (from BI 0 to BI 5), and SDI (from SDI 0 to SDI 13) as well as multiple alternations of silty mudstone and sandstone beds (Figure 5.4) The SDI curve appears to contain a sinusoidal component. *Arenicolites*, *Cylindrichnus*, *Gyrolithes*, *Planolites*, and *Skolithos* are present, albeit at variable abundances throughout the well. In contrast, *Rosselia* is preserved sporadically throughout the well.

The log for 12-11-098-11W4 also shows highly variable BI (from BI 0 to BI 5) and SDI (from SDI 0 to SDI 19), and a greater abundance of thinly bedded sandstone and silty-mudstone than in the other wells (Figure 5.5). The SDI curve does not appear as sinusoidal as in 13-02-098-11W4 (Figure 5.4). *Cylindrichnus* dominates in terms of abundance of ichnogenera in the

100
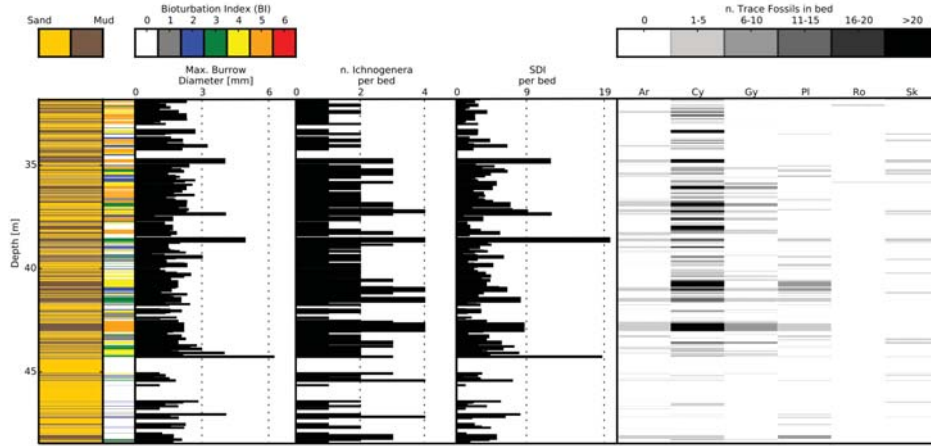
Figure 5.5: PyCHNO generated log of silty-mudstone and sandstone beds from core photographs of 12-11-098-11W4 from inclined heterolithic stratification intervals. Data shown (from left to right): bed thickness/lithology, bioturbation index, maximum burrow diameter, number of ichnogenera per bed, size-diversity index, and the abundance of each trace fossil genus present in each bed. Abbreviations: Ar = *Arenicolites*; Cy = *Cylindrichnus*; Gy = *Gyrolithes*; Pl = *Planolites*; Ro = *Rosselia*; Sk = *Skolithos*. The log is at a 1:200 scale. Note the sinusoidal trend of bioturbation index, maximum burrow diameter, number of ichnogenera per bed, size diversity index (SDI) logs, especially in the upper part of the well.

middle portion of the well. Other ichnogenera are less common. *Rosselia* occurrence is very sporadic.

Bioturbation Index values are relatively sparsely distributed in 11-17-098-10W4 (Figure 5.6) compared to 13-02-098-11W4 and 12-11-098-11W4. Bed thicknesses are more variable in 11-17-098-10W4 compared to the other wells. Bioturbation Index overall increases (from BI 0–1 to BI 2–4) from the base of the well up to approximately 35 m and then decreases again (to BI 0–2). *Planolites* and *Cylindrichnus* are the most dominant ichnogenera in the upper portion of the well but are sparse in the lower portion of the well. *Skolithos* is relatively rare and *Gyrolithes* and *Rosselia* are very rare throughout the well. The basal portion of the well (from the base of the well to 47 m) comprises brecciated IHS beds.

Well 14-13-098-11W4 is characterized by thick sandstone beds separated by thin silty mudstone beds in the lower and middle portions (from approximately
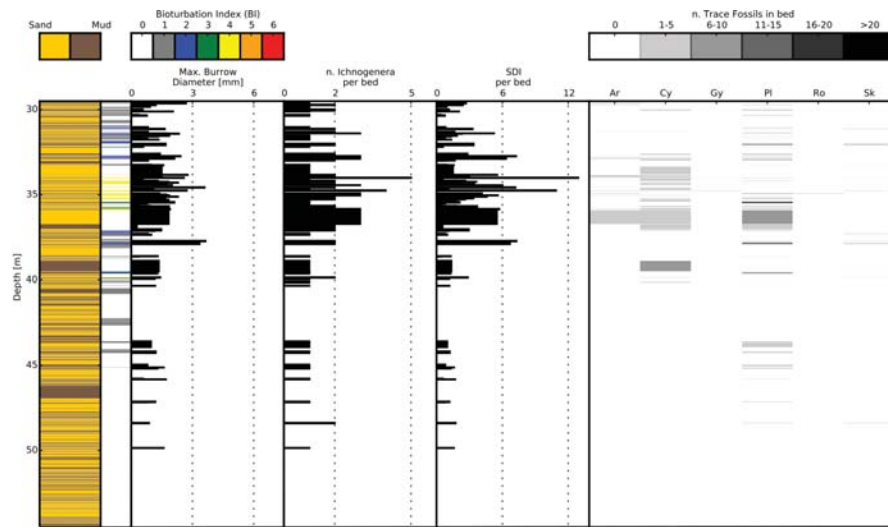
Figure 5.6: PyCHNO generated log of silty-mudstone and sandstone beds from core photographs of 11-17-098-10W4 from inclined heterolithic stratification intervals. Data shown (from left to right): bed thickness/lithology, bioturbation index, maximum burrow diameter, number of ichnogenera per bed, size-diversity index, and the abundance of each trace fossil genus present in each bed. Abbreviations: Ar = *Arenicolites*; Cy = *Cylindrichnus*; Gy = *Gyrolithes*; Pl = *Planolites*; Ro = *Rosselia*; Sk = *Skolithos*. The log is at a 1:200 scale. Note the overall sparser distribution of trace fossils in this well. From a depth of approximately 47 meters downward, the well is dominated by brecciated inclined heterolithic stratification.

38 m to the base) of the well (Figure 5.7). This gives SDI and BI relatively blocky shapes compared to other wells. The upper portion of the well (at depths shallower than 38 m) contains more thinly bedded sandstone and silty-mudstone units. The bioturbation index in this portion is relatively consistent compared to the BI in the thinly interbedded portions of other wells (*e.g.* Figs. 4, 5). *Cylindrichnus* and *Gyrolithes* dominate the upper portion of the well. This well's IHS is much more sandstone dominated than the other wells, which contain greater mudstone/siltstone proportions.

5.5.2 Ichnological Clusters

The average BI, SDI, and description of the ichnological clusters are summarized in Table 5.1. In total 775 mudstone beds were measured. The clusters are ranked from 1 to 10 based on interpreted ecologic stress levels as determined from SDI and BI. Each cluster therefore represents incremental increases in cumulative paleoecological stress. Cluster 1 represents the intervals interpreted to be the least stressed and cluster 10 represents the intervals interpreted to be the most stressed.

The ichnology cluster bar plots display silty mudstone bed numbers (increasing along depth), and the cluster associated with each bed (Figure 5.8A–5.8D). Along the x-axis, cumulative paleoecological stress increases to the right. The log associated with 11-17-098-10W4 (Figure 5.8A) displays consistently high ecologic stress cluster values (*i.e.* 8–9) for a large portion of the well. The 100 uppermost beds display lower ecologic stress cluster values (*i.e.* 0–6). The log generated for 14-13-098-11W4 displays a blocky shape as well, but there is overall more variation in ichnological cluster numbers (Figure 5.8B). Possible sinusoidal variation between lower stresses (*i.e.* stress clusters 2–4) and higher stresses (*i.e.* stress clusters 7–9) in 12-11-098-11W4 (Figure 5.8C), and especially in 13-02-098-11W4 (Figure 5.8D), suggest cyclicity in the depositional system.

Cluster 9 and 10 contain the largest number of beds from the clustering operation. The lithologies within those clusters are also highly variable and include interlaminated, brecciated, and apparently structureless intervals.

103
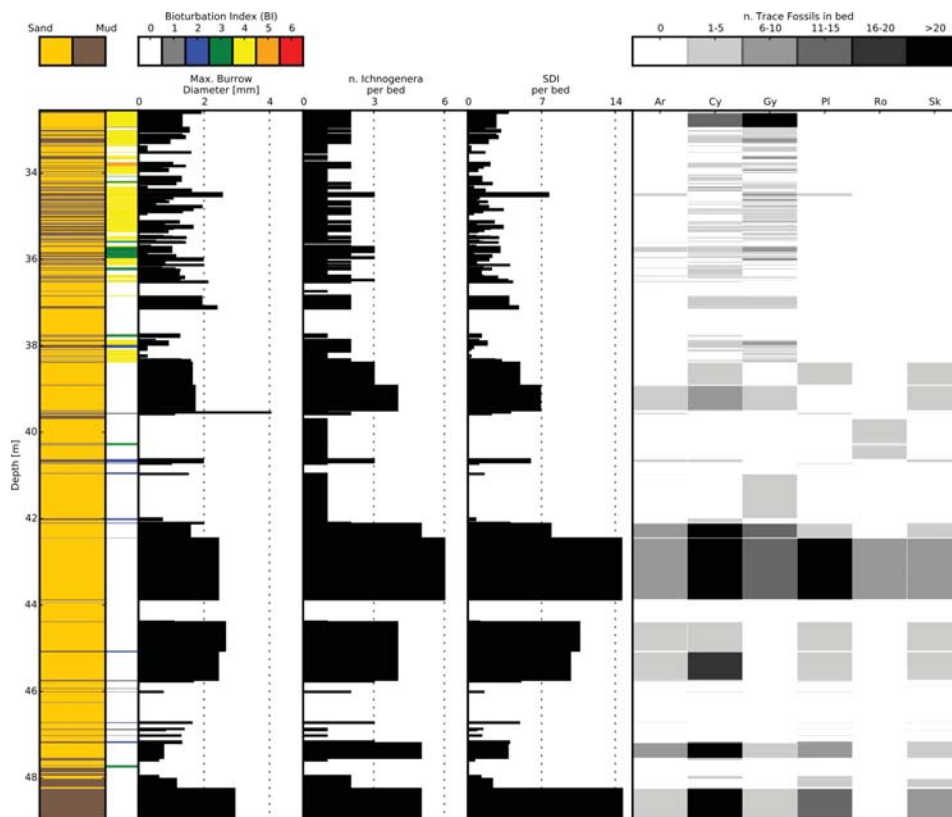
Figure 5.7: PyCHNO generated log of silty-mudstone and sandstone beds from core photographs of 14-13-098-11W4 from inclined heterolithic stratification intervals. Data shown (from left to right): bed thickness/lithology, bioturbation index, maximum burrow diameter, number of ichnogenera per bed, size-diversity index, and the abundance of each trace fossil genus present in each bed. Abbreviations: Ar = *Arenicolites*; Cy = *Cylindrichnus*; Gy = *Gyrolithes*; Pl = *Planolites*; Ro = *Rosselia*; Sk = *Skolithos*. The log is at a 1:200 scale. Note that 14-13-098-11W4 is much more sandstone dominated compared to the other wells, and that bioturbation index is stable at approximately BI = 4 for a large portion of the upper part of the well.
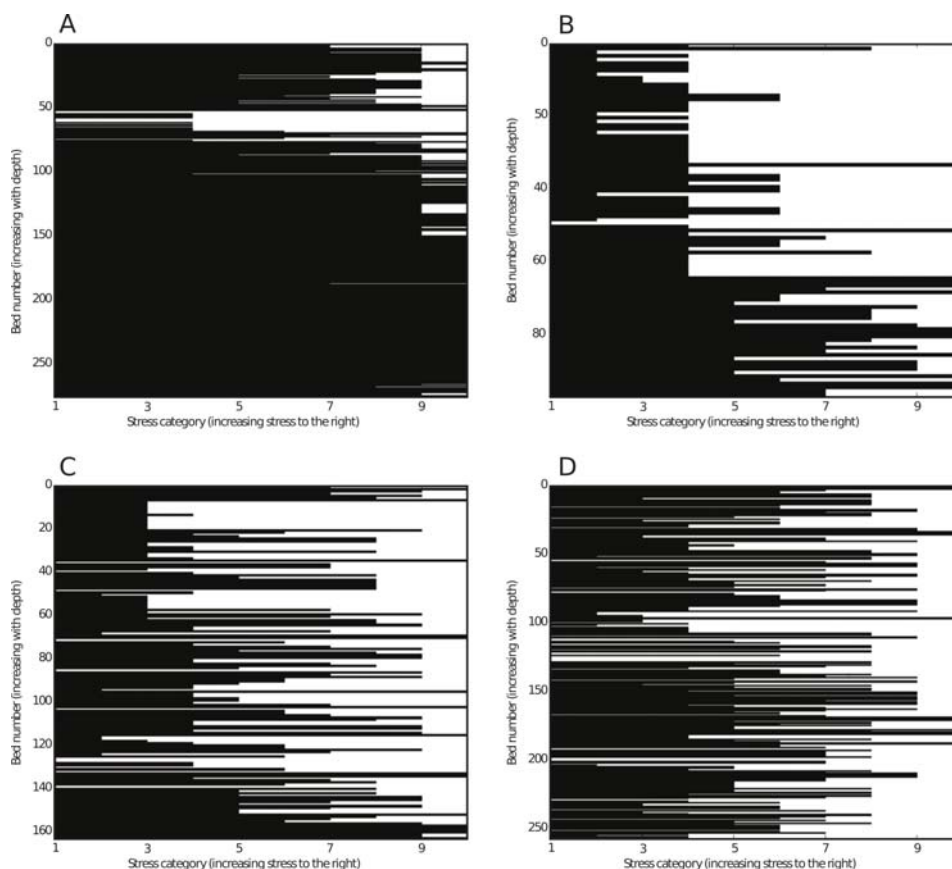
Figure 5.8: Barplots of interpreted intensity of ecologic stresses based on K-means clustering. Intensity of stresses increases to the right (10); the lowest stress intensities are 1. The numbers on the y-axis correspond to the successive number of mud/silt beds that are recorded from the top of the IHS interval to the base of the IHS interval. A) Ecologic stress intensity cluster barplot for 11-17-098-10W4. Note the lack of variability in the deeper beds. Stress intensity in this region is high (9). B) Ecologic stress intensity cluster barplot for 14-13-098-11W4. Note the relatively consistent stress intensity toward the top portion of the plot. Also note the overall decrease in stress intensity moving upwards. C) Ecologic stress intensity cluster barplot for 12-11-098-11W4. Note the sinusoidal nature of the variability in stress intensity. D) Ecologic stress intensity cluster barplot for 13-02-098-11W4. Note the cyclical nature of the variability in stress intensity.

105

This is because the clustering method is unable to differentiate between these lithologies without additional data (*i.e.* facies descriptions).

5.5.3 Dynamic Time Warping and Continuous Wavelet Transforms

Six DTW plots were generated, corresponding to the compared time-series between each of the wells (Figure 5.9A– 5.9F). A diagonal optimal warp path (OWP) (white line) signifies a perfect match between two time-series, whereas horizontal and vertical deviations from the diagonal represent portions where there is no match (or relatively less matching) between two time-series. The background grayscale spectrum correspond to a contoured accumulated cost matrix (*i.e.* minimized Euclidean distance for reaching a time-series point from the origin). Darker grays/black correspond to comparable values at given time-series steps (*i.e.* a smaller Euclidean distance), and the lighter grays/white correspond to more dissimilar values at those steps.

The OWP from the DTW plot comparing 14-13-098-11W4 and 12-11-098-11W4 is relatively diagonal (Figure 5.9A). The series of data from these two wells are therefore relatively similar. There are three short dissimilar vertical or horizontal lines (occurring at approximately 35, 75, and 120 on the 12-11-098-11W4 axis) signifying intervals that are dissimilar or missing. The two time-series have significantly different lengths (*i.e.* due to different numbers of measured silty-mudstone beds), which makes comparison of depositional time-equivalent beds more challenging.

Computing the DWT between 12-11-098-11W4 and 13-02-11W4 also yields a relatively diagonal OWP (Figure 5.9B). The portion of the OWP between 80 and 140 on the 12-11-098-11W4 axis displays a shallower slope; however, considering that the lengths of the two time-series are very different, the two series are broadly similar. Visual examination of the ecologic stress cluster logs (Figure 5.8C, 5.8D) confirms the high level of similarity between the two wells.

The number of beds within the successions in 14-13-098-11W4 and 13-02-098-11W4 are dissimilar. This is reflected in the OWP from their DWT plot

106
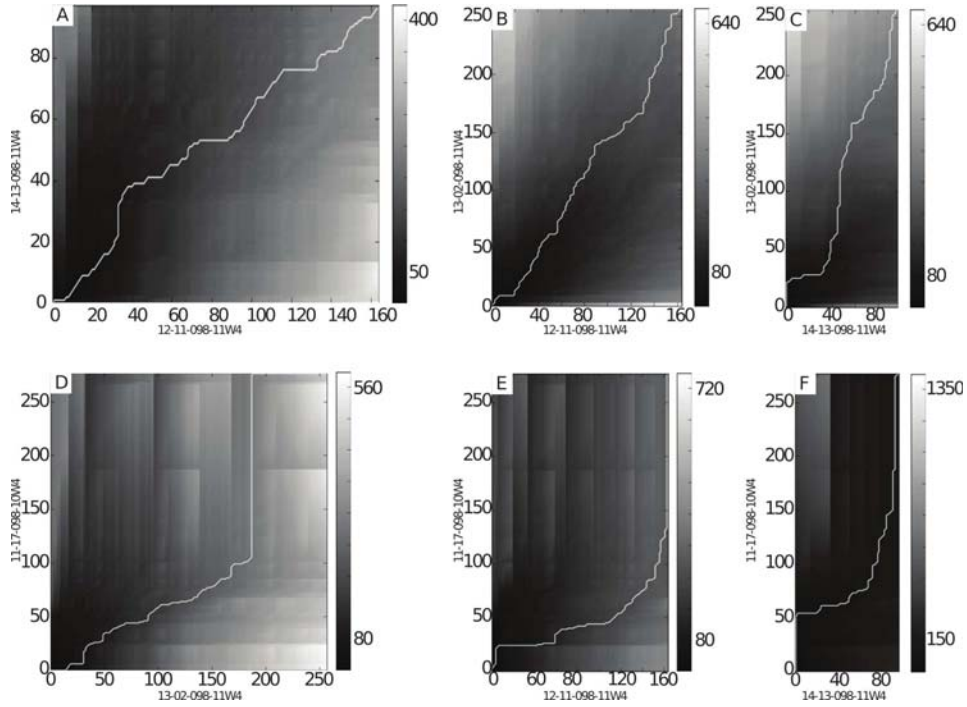
Figure 5.9: Dynamic Time Warping (DTW) plots comparing ecologic stress cluster successions. The x and y axes correspond to measured bed numbers. The white line extending from the bottom left corner to the top right corner is the optimal warp path (OWP). The more diagonal the OWP, the more similar the two successions compared. Horizontal and vertical deviations highlight intervals of no match between successions. The grayscale spectrum corresponds to the contoured accumulated cost matrix. The OWP selects the path with the lowest accumulated cost. A) DTW plot of 12-11-098-11W4 and 14-13-098-11W4. The OWP is relatively diagonal suggesting strong similarity between the two successions. B) DTW plot of 12-11-098-11W4 and 13-02-098-11W4. The OWP is broadly diagonal suggesting strong similarity between the two successions. C) DTW plot of 14-13-098-11W4 and 13-02-098-11W4. The OWP is still relatively diagonal, but much less than 7a, 7b. This suggests some degree of similarity. D) DTW plot of 13-02-098-11W4 and 11-17-098-10W4. The OWP is significantly deviated from the diagonal for a large portion of the plot, suggesting limited similarity. The portion from approximately 25 to 200 on the 13-02-098-11W4 shows some degree of similarity. E) DTW plot of 12-11-098-11W4 and 11-17-098-10W4. Overall, the OWP strays strongly from the diagonal, which suggests relatively little similarity between the two successions. F) DTW plot between 14-13-098-11W4 and 11-17-098-10W4. The OWP strays from the diagonal, which suggests relatively little similarity between the two successions.
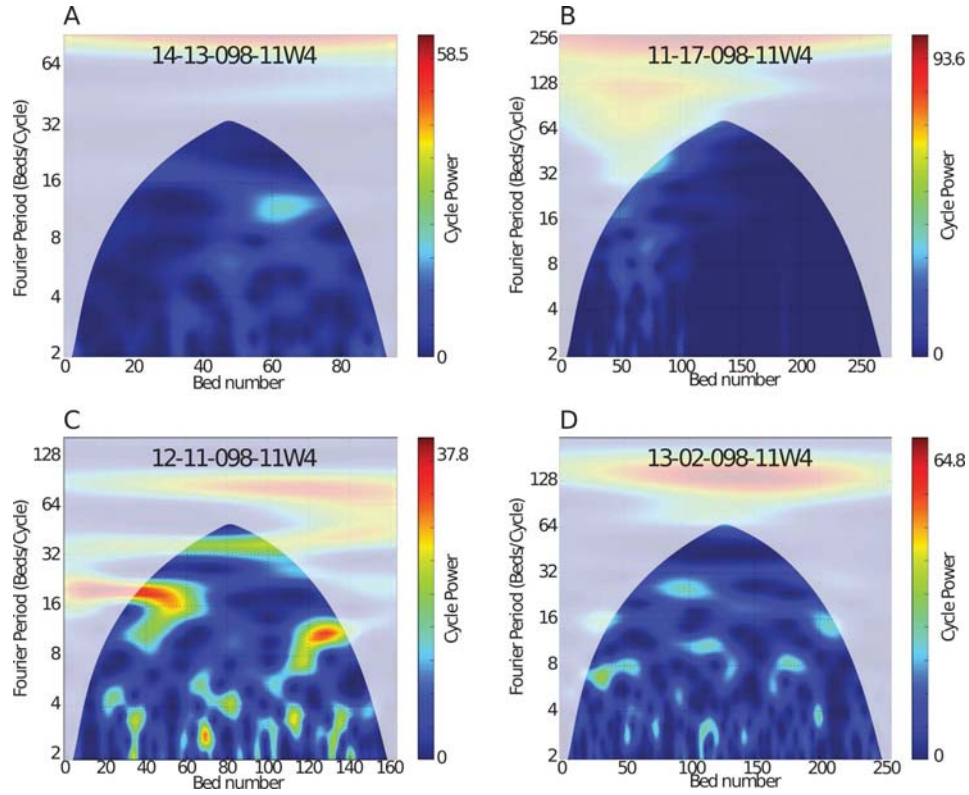
Figure 5.10: Scalograms for Continuous Wavelet Transforms (CWT) applied to ecologic stress cluster successions. The x-axis corresponds to successive steps in each series, and the y-axis correspond to the period (inverse of frequency) of observed cycle power. The color spectrum corresponds to the cycle power. Higher cycle powers correspond to stronger statistical presence of a given periodic component within a signal. The grayed out area corresponds to the cone of influence. Contours within the cone of influence are statistically meaningless. A) Scalogram of 14-13-098-11W4 ecologic stress cluster succession. Note the overall weak periodic signals occurring at periods of approximately 3, 7, and 12 events per cycle (approximately 4, 8, 12; *i.e.* multiples of four). B) Scalogram of 11-17-098-11W4 ecologic stress cluster succession. Note the weak periodic signals occurring at periods of approximately 3, 7, and 12 events per cycle (approximately 4, 8, 12; *i.e.* multiples of four). C) Scalogram of 12-11-098-11W4 ecologic stress cluster succession. Note the strong periodic signals occurring at periods of approximately 3.5, 5, 12 and 20 events per cycle (approximately 4, 12, 20; *i.e.* multiples of four). D) Scalogram of 13-02-098-11W4 ecologic stress cluster succession. Note the strong periodic signals at approximately 3, 8, 16, and 25 (approximately 4, 8, 16, 24; *i.e.* multiples of four) events per cycle.

(Figure 5.9C). Overall, the OWP strays from diagonal; however, the portion following step 60 on the 14-13-098-11W4 axis, is closer to diagonal and suggests relatively strong similarity for that interval.

The OWP for 13-02-098-11W4 and 11-17-098-10W4 strays from diagonal (especially from steps 0 to 60 on the 14-13-098-11W4 axis) (Figure 5.9D). The succession from 60 to 85 (on the 14-13-098-11W4) of the OWP is relatively diagonal. This supports a relatively strong degree of similarity between the two wells for that interval, but otherwise dissimilar intervals for the remainder of the successions.

The DWT plot comparing 12-11-098-11W4 and 11-17-098-10W4 demonstrates that the two successions match poorly (Figure 5.9E). The OWP doesn't approach diagonal, and there are significant horizontal (between steps 20 and 40 on 12-11-098-11W4 axis) and vertical line portions. Similarly, the plot comparing 14-13-098-11W4 and 11-17-098-10W4 (Figure 5.9F) display poor succession matching as well.

The scalograms generated by CWTs applied to the cluster logs (Figure 5.8A– 5.8D) are shown in Figure 5.10 (views A–D). The y-axis of the graphs corresponds to the number of events per cycle (*i.e.* periodicity), and the x-axis corresponds to the time-series steps. The contoured values correspond to the cycle power. Warmer colors (*i.e.* red, orange) present stronger evidence for cyclicity, and cooler colors (*i.e.* blue, green) are areas of weak or non-existent cyclicity. The length of a warmer colored area along the time-series corresponds to the length at which that periodicity is present in the signal. The shaded gray area corresponds to the cone of influence. Values that fall within the cone of influence shaded area hold little statistical value.

There is relatively little evidence for cyclicity in the scalograms for wells 14-13-098-11W4 and 11-17-098-10W4 (Figure 5.10A, 5.1B). These periodicities correspond to the number of beds forming a cycle. However, weak cycles occurring at periods of approximately 8, 12, and 16 are observed in the CWT plots for both wells. The scalograms for 12-11-098-11W4 and 13-02-098-11W4 present compelling evidence for cyclicity. The main periodicities in 12-11-098-11W4 are at approximately 3.5, 5, 12, and 20 events per cycle (Figure 5.10C).

Dominant periodicities in 13-02-098-11W4 are at approximately 3, 8, 16, and 25 events per cycle (Figure 5.10D). Overall periodic signals are relatively weaker in 13-02-098-11W4 than in 12-11-098-11W4. It is important to note that for both of these more cyclical examples, the cyclicities are relatively sporadic. Indeed, none of the stronger periodic signals occur over the entire length of the time-series.

5.6 Discussion

5.6.1 Spatial Significance of Ichnological Data

In fluvio-tidal settings, physical and chemical stresses occur at two main scales (Gingras *et al.* 1999): (1) at a local scale (*e.g.* point bars, bars or dunes); and (2) at the estuary scale. Bioturbation textures preserved in the rock record reflect variations in stresses at both of these scales. It is important to note that the ichnological character of the studied IHS supports brackish water depositional interpretations for the middle McMurray Formation. Variable trace fossil diameters, low trace fossil diversity, and highly variable BI support this interpretation.

At the local scale, the main impacting stresses include hydraulic energy along and across bars (*e.g.* point bars, counter point bars, transverse bars, and dunes) with lithological variations directly related to hydraulic energy distributions and sedimentation rates. Sediment on point bars is typically segregated with the finer-grained portion prevalent on the downstream side, and coarser-grained sediment on the upstream side (Labrecque *et al.* 2011b). However, this trend is not universal, as the reverse trend is documented at Willapa Bay where bioturbation intensity is typically higher on the downstream side of point bars and lower on the upstream side (Gingras *et al.* 1999; Schoengut 2011). This trend can be reversed in the inner estuary. Brecciated intervals are typical in the upstream portion of point bars due to increased erosion and cannibalization related to higher overall hydraulic energies (Nardin *et al.* 2013). These trends have been observed in point bar complexes in the McMurray Formation in both mine pit walls and natural outcrop sections but

are difficult to interpret in datasets composed exclusively of core. With the exception of recent work on counter point bars (Smith *et al.* 2009; Hubbard *et al.* 2011), little has been done on localized sedimentological and ichnological descriptions of other heterolithic bar forms in the McMurray Formation.

At the estuary scale, stress associated with variations in salinity and oxygenation is a dominant control on bioturbation (MacEachern *et al.* 2005). Salinity stress can be directly influenced by climate (Goldring *et al.* 2004), fluvial seasonality and tidal cyclicity (*e.g.* Gingras *et al.* 2002; Johnson and Dashtgard 2014). In terms of intensity of salinity stress, one of the most important parameters is the position within an estuary (*i.e.* inner, middle, outer) that is colonized (Lettley *et al.* 2005b). For example, in the inner estuary, increased streamflow can significantly shift the position of the salt wedge in a basinward direction (Dalrymple *et al.* 2012). This is significant because infaunal organisms living in brackish water conditions are sourced from the marine realm (Gingras *et al.* 2012). On the other hand, if streamflow is sufficiently low, brackish water can penetrate deeper into the estuary, concomitantly allowing marine larvae to colonize otherwise fluvially dominated intervals. Estuary scale variations in stresses, specifically applied to the McMurray Formation, are summarized by Lettley *et al.* (2005b).

Similarity between ichnological time-series, as observed on DTW plots (Figure 5.9A– 5.9E) is interpreted to show the effects of ecologic stresses at both of these spatio-temporal scales. Along a contiguous point bar, closely spaced wells should display relatively diagonal DTW paths, whereas further distanced wells should display more horizontal and vertical DTW path segments. At a larger scale, DTW paths should show some weak similarity regardless of well distance due to estuary scale cyclicity.

The relatively strong level of similarity between the ichnological logs of 12-11-098-11W4 and 13-02-098-11W4 (Figure 5.9B) suggests that these wells penetrate a genetically linked bar. The CWT generated from the ichnological data in these wells show the strongest cyclicity as well, which suggests that localized stresses are similar between the two wells. From the DTW plots, there is some similarity between 14-13-098-11W4 and 12-11-098-11W4 (Figure

5.9A), which could suggest that some of the local stresses affecting 14-13-098-11W4 may be affecting 12-11-098-11W4 as well. However, the greater dissimilitude between further spaced wells (*i.e.* 13-02-11W4 and 14-13-098-11W4; Fig 9C) suggests different localized stresses in the northern well (14-13-098-11W4) compared to the southern well (13-02-098-11W4). It is likely that estuary-scale stresses contribute significantly to the overall similarity between the three wells.

There are two possible interpretations for the mismatch between 11-17-098-10W4 and the three other wells (*i.e.* Figure 5.9D, 5.9E): (1) the deposit preserved in 11-17-098-10W4 is not chronostratigraphically equivalent to those found in the other wells (*i.e.* it is significantly younger or older) and therefore was affected by different magnitudes of estuary scale stresses; or (2) localized stresses were significant enough to override and obscure the estuary-scale stress signature. Considering that a large portion of the 11-17-098-10W4 core is represented by brecciated/reworked IHS beds, higher hydraulic energy at this part of the point bar is very likely to have overprinted the estuary scale stress time-series. Whether or not this well intersects the same bar complex as any of the other study wells is more difficult to assess from the ichnological data due to this overprinting.

5.6.2 Temporal Significance of Ichnological Data

The cyclicity of thickness variations in the interlaminated portions of IHS has been quantitatively linked to tidal periodicities by Hovikoski *et al.* (2008) and Timmer *et al.* (2016a). Labrecque *et al.* (2011a) examined the meter-scale cyclicity of IHS point bars from gamma ray log Fourier transforms periods and matched these to El Niño/Southern Oscillation (ENSO) patterns and to solar cycles (sunspots). However, the cyclicity of ichnological data, specifically related to ecologic stresses, has not been quantitatively assessed previously.

The periodicity of ecologic stress as observed from the scalograms correspond to multiples of approximately four (*i.e.* 4, 8, 12, 16, 20) (Figure 5.10A– 5.10D). These periodicities do not correspond with tidal periodicity (*cf.* Kvale 2012). The interlaminated portions of each bed may reflect tidal

cyclicity to some extent (Timmer *et al.* 2016a). However, the bioturbation within those intervals likely occurred after the entire interlaminated intervals were deposited, as the sedimentation rate during tidal laminae deposition would likely have been too high for infauna to survive. Sedimentation rates are estimated to be within the range of approximately 1–10 mm per day on average based on both lamina thicknesses in interlaminated portions of IHS and the number of laminae in ideal tidal cycles. However, seasonal variation can lead to sedimentation rates outside of this range. Seasonally lower sedimentation rates offer an open infaunal colonization window (*e.g.* Pollard *et al.* 1993). Furthermore, the intensity and diversity of bioturbation in many of the beds suggest that colonization windows would have been sufficiently long (*i.e.* seasonal to annual scale) to allow such a texture to develop (*e.g.* Gingras *et al.* 2002). Colonization windows on daily, twice-daily, fortnightly, or monthly scales, which would be likely controlled by tides, are likely insufficient to generate such textures (*i.e.* bioturbated-interlaminated beds).

El Niño/Southern Oscillation cycles have occurred approximately every 2–8 years during the Holocene (Moy *et al.* 2002) and occur in the present. El Niño events occur during intervals with increased sea surface temperature in the east tropical Pacific Ocean and can last for months to several years (Trenberth 1997). Similar cycles likely occurred during the Cretaceous (Davies *et al.* 2011; Davies *et al.* 2012; Labrecque *et al.* 2011a). The cycles observed in this study that correspond to multiples of four to eight fall within the range of these reported cycles. Following this interpretation, each silty mudstone bed represents annual deposition. Considering that the time-series analyzed were relatively noisy, multiple other causes such as non-deposition, erosion, reworking, and localized stresses could cause these larger cycles to appear in the dataset. It is interesting that silty mudstone bed ecologic stress cycles match relatively closely the periodicities observed in decimeter-scale lithological variations by Labrecque *et al.* (2011a). The relatively lower strength periodicities observed in 11-17-098-10W4 and 14-13-098-11W4 (Figure 5.10A, 5.10B) can be explained by localized stresses (*i.e.* hydraulic energy in 11-17-098-10W4 brecciated zone) and/or localized less stressed intervals (*i.e.* relatively consis-

tent BI and SDI in 14-13-098-11W4).

Davies *et al.* (2011) documented El Niño periodicity in Cretaceous Arctic Ocean sediment. Davies *et al.* (2012) noted similar trends in the Late Cretaceous Marca Shale in California. Both studies support the possible occurrence of El Niño events during the deposition of the McMurray Formation. Labrecque *et al.* (2011a) suggests that El Niño events in the McMurray Formation coincide with warmer temperatures and decreased precipitation, whereas La Niña events correspond to cooler temperatures and increased precipitation. However, the link between El Niño/La Niña events and precipitation in northwestern Canada are poorly understood, especially in the Cretaceous. In the present, El Niño events in the northwest region of North America generally coincide with warmer temperatures, whereas La Niña events typically correspond to lower temperatures (Ropelewski and Halpert 1986). The effects of El Niño on precipitation in this region are less predictable. For example, in the southern portion of the Canadian prairies, El Niño events coincide with decreased precipitation, whereas in the northern portion of the Canadian prairies, these events coincide with moderate increases in precipitation (Byrne and Berg 1998). The effects of El Niño on this region during McMurray Formation deposition, is likely different due to the Boreal Sea encroachment, and warmer Cretaceous temperatures.

Intervals of increased ecologic stress, specifically related to reduced water salinity likely coincided with periods of increased precipitation, which in turn coincided with either El Niño or La Niña events. El Niño episodes have been directly correlated to increased salinity and La Niña events to decreased salinity in Texas estuaries (Tolan 2007). Inversely, El Niño episodes can be associated with increased streamflow (Chiew and McMahon 2002). Addition of fresh water to the estuary during these periods can significantly decrease salinity within the estuary. For example, increased streamflow at Chesapeake Bay has been associated with 27.5 ppm decreases in salinity near the river mouth, and 0.5 ppm decreases in salinity near the outer estuary (Gibson and Najjar 2000). Decreased salinity in estuaries can negatively affect marine-based infauna (Gingras *et al.* 1999). Periods of decreased salinity stress can

coincide with decreased precipitation. Decreased freshwater input into the estuarine system increases salinity, effectively increasing the efficacy of marine based larvae infaunal colonization in the inner estuary.

5.7   Summary

This study has demonstrated that fluctuations in physical and chemical paleoecological stresses as proxied by quantitative trace fossil data are both spatially and temporally significant in the Cretaceous in age McMurray Formation. The quantitative trace fossil data was analyzed as time-series. We used Continuous Wavelet Transforms (CWT) to characterize the frequencies of temporal variability of these ichnological time-series and, Dynamic Time Warping (DTW) to characterize the spatial variability between ichnological time-series collected from different wells. Neither of these techniques has been applied to ichnological datasets previously. In order to simplify the simultaneous analysis of multiple process ichnology parameters (*i.e.* size-diversity index, bioturbation index, and the abundance of ichnogenera per bed), these values were clustered and ranked into 10 "cumulative stress groups" using a K-means clustering analysis before performing DTW and CWT analyses. Clustering, CWT, and DTW applied to ichnological time-series proves to be useful for observing spatial and temporal trends in ichnological cyclicity.

Spatially, the variability and cyclicity of ecologic stresses can be linked to changes in estuary scale stresses and more localized stresses (*i.e.* stresses occurring on a bar-form scale). Evidence for estuary scale stresses are present in the four ichnological time series studied, but are overridden by more local stresses. This has the effect of producing similar ecologic stress periodicities in the ichnological time-series studied. Temporally, the variation in stresses occur relatively predictably in periods of approximately four (or multiples of four) as proxied by the ichnological time-series. We suggest that these cycles can be linked to ENSO cycles, which affect bioturbation cyclicity on an estuary scale.

Chapter 6

Statistical analysis of ichnofossils in a seismically-defined estuarine point-bar deposit

6.1 Introduction

Trace fossil characteristics such as size, diversity, trace-fossil taxon, and degree of bioturbation can be used as proxies for variations in physical and chemical ecological parameters of the depositional environment (Gingras *et al.* 2011). Changes in physical and chemical parameters subject infaunal organisms and populations to stress in predictable ways. For example, the size of trace-making organisms tends to decrease as salinity is lowered from baseline marine conditions (*e.g.* Remane 1934; Howard and Frey 1975; Pemberton *et al.* 1982; Gingras *et al.* 1999; LaCroix *et al.* 2015; Botterill *et al.* 2015). Reasonable behavior-environment interpretations based on modern animal responses to fluctuating salinity, lowered salinity, and lowered oxygen availability are well documented (*e.g.* Rhoads and Morse 1971; Goldring 1995; Gingras *et al.* 1999; Taylor *et al.* 2003; Buatois *et al.* 2005; Savrda 2007).

Pemberton *et al.* 1982 proposed brackish-water depositional conditions in the Cretaceous McMurray Formation in NE Alberta, Canada based on several qualitative ichnological characteristics. These include: (1) low ichnogeneric diversity; (2) a poorly developed marine trace-fossil assemblage; (3) morpholog-

ically simple ichnotaxa; (4) the dominance of ichnofossil assemblages by single ichnotaxa; (5) diminutive ichnotaxa; and (6) locally high-density preservation of some ichnospecies. Several quantitative measurements can support these qualitative observations. Size-diversity index (SDI) represents a quantitative way to represent the impact of salinity stress on infaunal populations (Hauck *et al.* 2009). Bioturbation index (BI) is a semi-quantitative assessment of bioturbation intensity that can be used to support depositional rate interpretations and water chemistry variation (*e.g.* Gingras *et al.* 2008). If systematically observed and recorded, several ichnological parameters are amenable to statistical analysis. These include SDI, BI, ichnotaxon present and their relative abundances. Resulting models should be informative regarding the interpretation of sedimentary conditions and environments.

The objective of this study is to quantitatively describe trace fossils from a geomorphologically well-defined point-bar deposit in order to establish a statistical process ichnological model that can be used to interpret the variability of physical and chemical stresses affecting infauna during the evolution of the point-bar. Data collected from 9 wells using the ichnological data collection software PyCHNO (Timmer *et al.* 2016b) form the dataset used in this study. Primary statistical techniques employed in this study include: (1) ichnonetwork analysis (*cf.* Baucon and Felletti 2013); and (2) continuous wavelet transforms (*cf.* Timmer *et al.* 2016a).

6.2 Study Area and Dataset

The studied point-bar was deposited within the lower Cretaceous McMurray Formation. The McMurray Formation has been interpreted to represent a transition from fluvial dominated deposition to increasingly marine influenced deposition (*e.g.* Ranger and Pemberton 1992; Crerar and Arnott 2007; Musial *et al.* 2012). The ichnology of the McMurray Formation has recently been summarized by Gingras *et al.* 2016. Although ichnological data generally supports brackish-water depositional affinities (Pemberton *et al.* 1982), the relative influence of tidal/brackish water during depositionhas recently been contested

due to geomorphological similarities between 3D seismic datasets and meandering fluvial systems (Hubbard *et al.* 2011). High quality 3D seismic slices offer a unique opportunity to describe and interpret ichnological data from a well-defined and constrained geobody. This removes much uncertainty for relating data from multiple wells in order to model a large, spatial dataset.

The study area is located south of the city of Fort McMurray (Figure 6.1 A). Strata examined for this study belongs to the lower Cretaceous McMurray Formation (Figure 6.1 B). This area was selected because the geology of the area is well constrained with high quality 3D seismic data (Hubbard *et al.* 2011). This seismic data outlines a point-bar (Figure 6.2). The dataset for this study area consists of 9 wells that penetrate the entire point-bar interval. The top of the seismically defined point-bar is used as a datum for interval slices and for cross-sections. The ichnology data collection software, PyCHNO (Timmer *et al.* 2016b) was used to collect ichnological data from high resolution photographs. Data collected with PyCHNO forms the basis of this study.

This area has been studied from a sedimentological perspective (Hubbard *et al.* 2011).

6.3   Methods

Bed thickness, mud/sand lithology, bioturbation index (BI), and the causative burrow diameter of each identifiable trace fossil were collected using the trace fossil data collection software PyCHNO (Timmer *et al.* 2016b) from core-sleeve photographs of 9 wells. These wells were selected on the basis of even spatial distribution within the seismically-defined point bar interval. For this study, we refer to the term "bed" as a relatively continuous vertical lithological unit, therefore, some "beds" can be greater than 50 cm.

Although bioturbation is present in many sand dominated portions of oil sands, especially inclined heterolithic stratification lithosomes, hyperspectral or x-ray techniques are often necessary to describe trace fossils from these intervals since the bitumen often masks sedimentary structures and trace fossils (Speta *et al.* 2016). Considering this, we only use data collected from muddy-
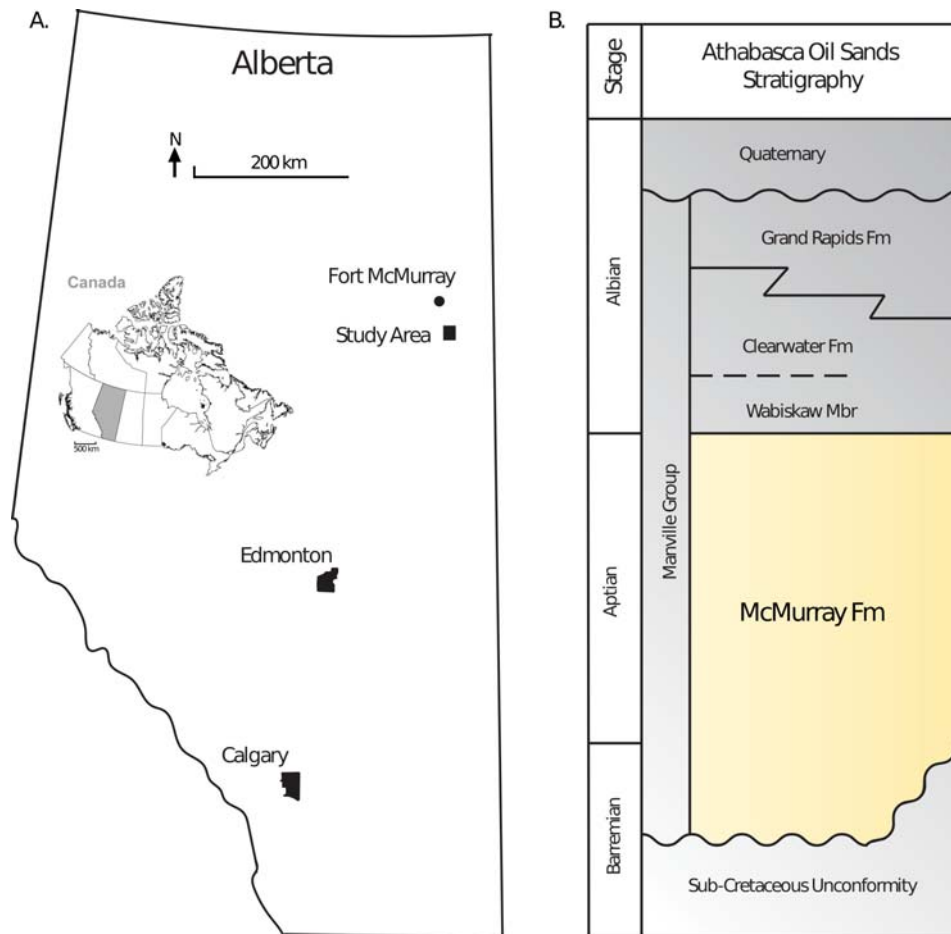
Figure 6.1: (A) Location of the study area in relation to Alberta and Canada, modified from Crerar and Arnott (2007). The study area is located south of the city of Fort McMurray. (B) Simplified schematic stratigraphy of the study area. The studied point-bar was deposited within the lower Cretaceous McMurray Formation. Modified from Crerar and Arnott (2007).
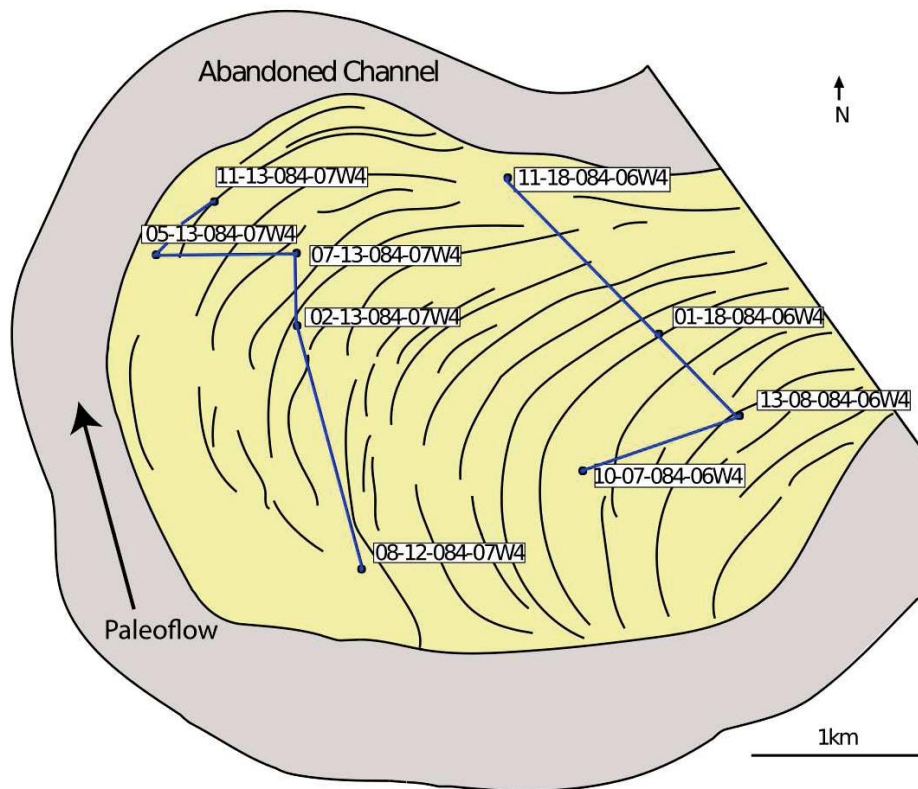
Figure 6.2: Traced outline of a seismic slice showing the top of the point-bar interval. Traced seismic is from Hubbard *et al.* (2011) (Figure 2A). Data from all wells on this diagram were collected using PyCHNO. The lines of section shown are for cross sections presented in Figures 10-11.

siltstone beds for this study, as sandstone ichnological characteristics are not sufficiently clear to yield accurate statistical results.

Data collected with PyCHNO were exported as tab-delimited text files. The Python programming language was used to perform various operations including: (1) calculating and plotting the relationship between observed trace fossils, BI, SDI, bed trace fossil count and bed diversity as histograms; (2) calculating the relative abundance of ichnogenera for 1 m increments, for all wells, descending from the top of the point bar as a stacked bar plot; (3) calculating and plotting the relationship between BI and size, diversity, SDI, total bed trace count, and bed thickness as boxplots containing data contribution density maps; (4) calculating Bray-Curtis similarity indices for ichnonetwork analysis; (5) calculating Bray-Curtis bed composition similarity indices for time-series analysis; and (6) generating depth-converted wavelet transforms of bed composition similarity index time-series.

6.3.1 Ichnonetwork Analysis

First proposed by Bray and Curtis (1957) as a dissimilarity index, when subtracted by one, the Bray-Curtis similarity index is commonly used to compare the composition of ecological sites (*e.g.* Somerfield 2008). The Bray-Curtis index can be used to compare the relative abundance of two ichnogenera for all beds and for all wells from a given interval. These indices are calculated as:

$$s_{jk} = 1 - \frac{\sum\limits_{i=0}^{n} |x_{ij} - x_{ik}|}{\sum\limits_{i=0}^{n} (x_{ij} + x_{ik})} \tag{6.1}$$

Where s_{jk} is the Bray-Curtis similarity index for trace fossils j and k, x_{ij} is the number of trace fossil j in bed i of n beds (pooled from all wells), and x_{ik} is the number of trace fossil k found in bed i. Beds where both x_{ij} and x_{ik} are zero were not included into the similarity index calculations as these would result in zero division errors. A value of 1 was assigned in these cases instead.

In order to determine the variation of trace fossil associations coupled with the evolution of the point bar development, we sliced the dataset into 5 m increments, starting from a top of the bar datum. Bray-Curtis similarity indices were calculated for all traces present within each 5 m interval. These similarity indices serve as edge weights for network graphs. Edge weights were calculated using Python and exported to the open source network drafting software Gephi (`<https://gephi.org/>`). This methodology loosely follows the procedures for generating ichnonetworks proposed by Baucon and Felletti (2013). Our approach uses relative trace abundances for edge weights rather than presence/absence data, calculated with a Jaccard similarity index as proposed by Baucon and Felletti (2013), the pioneers of ichnonetwork analysis.

6.3.2 Time-Series Analysis

In this study, we use a modified Bray-Curtis similarity index to calculate the difference in ichnological composition for successive beds for each well:

$$s_i = 1 - \sum_{j=0}^{m} \frac{\sum_{i=0}^{n-1} \left| x_{ij} - x_{(i+1)j} \right|}{\sum_{i=0}^{n-1} (x_{ij} + x_{(i+1)j})} \tag{6.2}$$

Where s is a vector containing bed similarity values for a given well, s_i is the Bray-Curtis similarity index of bed_i compared to bed_{i+1}, x is an attribute of the array containing BI, SDI, and ichnogenera abundance, where m is the number of columns in x, and n is the number of beds within a given well.

Since data from each measured bed can be considered a time-averaged event, the Bray-Curtis similarity index vector for each well can be analyzed as a time-series. The purpose of time-series analysis is to observe periodic trends in ichnological bed composition values. In order to locate periodic changes and their amplitudes in the time-domain Morlet continuous wavelet transforms were applied to each Bray-Curtis similarity index time-series. An extensive review of the theory and application of Morlet wavelet transforms is presented in Torrence and Compo (1998). Morlet wavelet transforms have been applied to ichnological time-series by Timmer *et al.* (2016c).

For this procedure, a Morlet wavelet (*i.e.* a periodic mathematical function) is scaled (*i.e.* squeezed or compressed) then shifted over a time-series in order to generate a matrix of correlation coefficients between the time-series at any given point and the Morlet wavelet at a specific scale. Each Morlet wavelet scale corresponds approximately to a fourier frequency. In other words, the degree of correlation between the Morlet Wavelet at a given frequency and the time-series at a given location are calculated. Wavelet transform results are typically analyzed via a contoured representation of the correlation coefficient matrix, referred to as a scalogram.

Typically, scalograms represent time and signal frequency correspondence. However, for geological applications, it is often useful to observe signal correspondences in depth. For this reason, we propose a modified scalogram herein whereby we have replaced wavelet matrix indices with depth values after calculating the correlation coefficients for each wavelet scale. The output is a depth-converted scalogram. Depth-converted scalograms can be used in geological cross-sections in order to observed changes in signal frequency spatially.

6.4 Results

Data from 1141 silty-mudstone beds were collected. Of these, 1033 beds displayed identifiable trace fossils. In total, six ichnogenera were observed in the point-bar deposit. In alphabetical order, these include: *Arenicolites*, *Cylindrichnus*, *Gyrolithes*, *Planolites*, *Skolithos*, and *Thalassinoides*. Characteristic manifestations of each of these ichnogenera are shown in Figure 6.3A-G.

6.4.1 Ichnogenera relations with BI, SDI, bed-diversity and bed trace fossil count

The relation between each observed ichnogenus with various ichnological parameters is summarized in figures 6.4 and 6.5. Figure 6.4A-D shows the range of bioturbation indices (BI) associated with each ichnogenus. The range of size-diversity index (SDI) values associated with each ichnogenus is shown in Figure 6.4E-H. The range of bed ichnogeneric-diversity associated with each
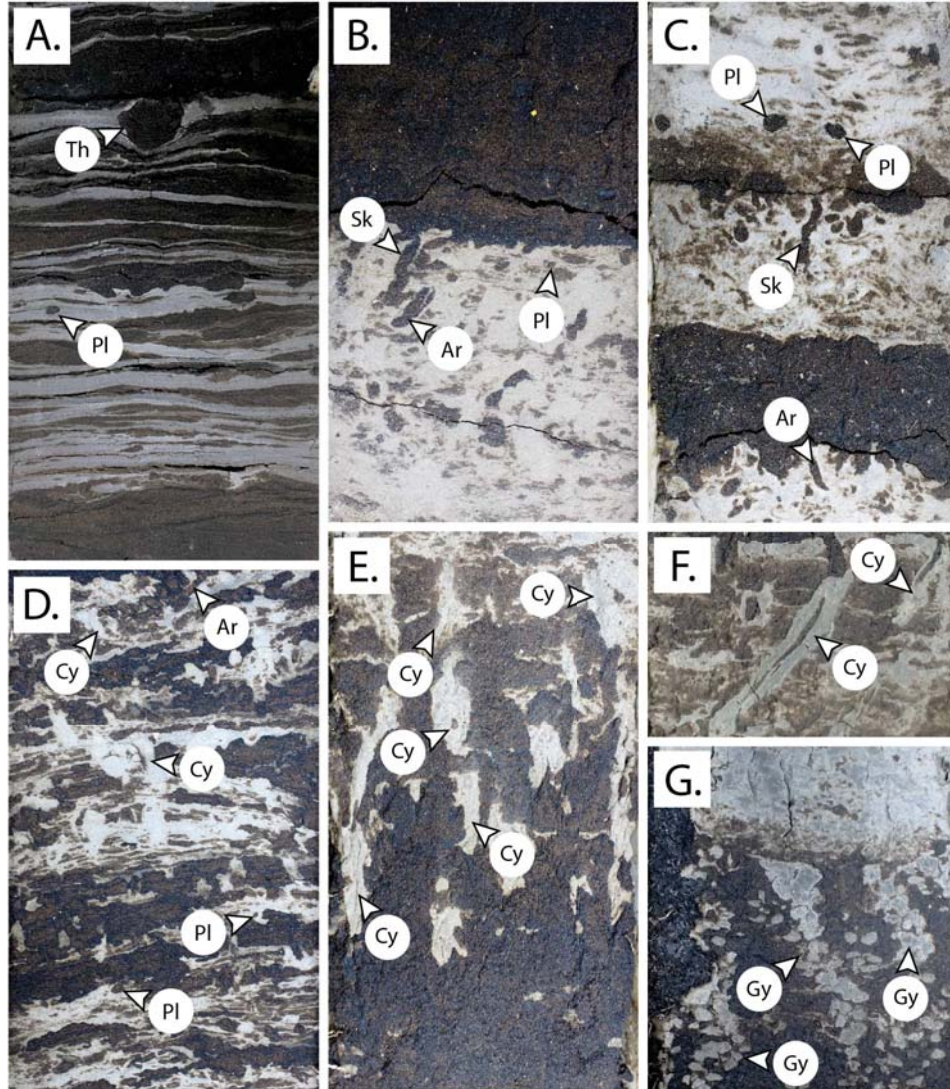
Figure 6.3: Photos of ichnofossils from the seismically-delineated point bar deposit in the Kinosis area that were statistically analyzed in this study. Note that each core photo is 7cm wide. (A) *Thalassinoides* (Th) trace fossil cross-cutting wavy mud beds. The section of core is from 13-08-084-06W4 at 289.35m. (B-C) *Skolithos* (Sk) burrows extending down from the base of sand beds. Sand-filled *Planolites* (Pl) are present within mud beds. Images are from the 15-12-084-07W4 core at 285.8m (B) and 01-21-084-07W4 at 365.3m (C). (D) Examples of *Arenicolites* (Ar), *Cylindrichnus* (Cy), and *Planolites* (Pl) from 15-12-084-07W4 at 288.2m. (E-F) Monospecific assemblages of robust *Cylindrichnus* (Cy) burrows from 05-15-084-07W4 at 313.43m (E) and 11-19-084-06W4 at 258.7m (F). G) A monospecific assemblage of *Gyrolithes* (Gy) in the 11-19-084-06W4 core at a depth of 259.75m.

124
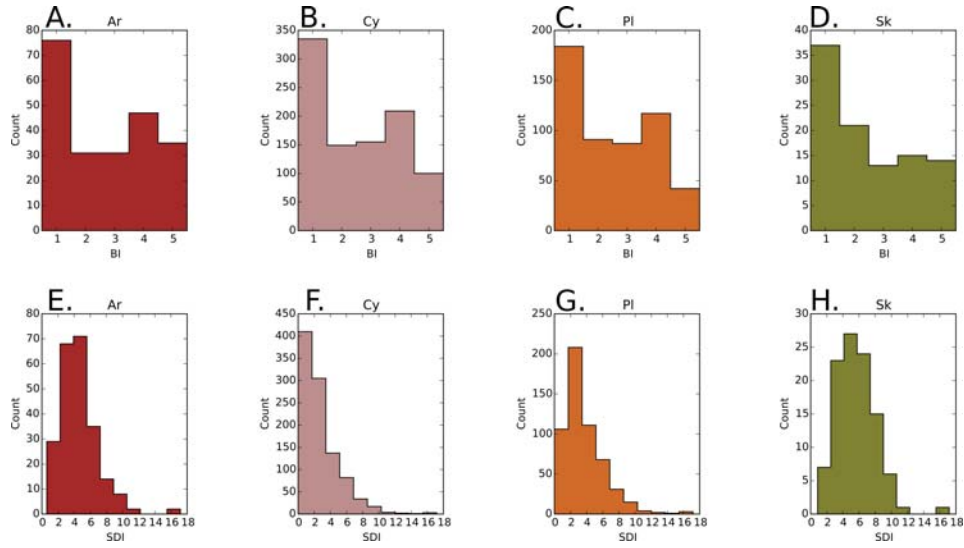
Figure 6.4: (A-D) Histogram of bioturbation index of measured beds containing *Arenicolites* (Ar: 4A), *Cylindrichnus* (Cy: 4B), *Planolites* (Pl: 4C), and *Skolithos* (Sk: 4D). (E-H) Histogram of size-diversity index (SDI) of measured beds containing *Arenicolites* (Ar: 4E), *Cylindrichnus* (Cy: 4F), *Planolites* (Pl: 4G), and *Skolithos* (Sk: 4H).

ichnogenus is shown in Figure 6.5 A-D. Figure 6.5 E-H summarizes the distributions of trace fossils counts from a given ichnogenera present in each bed. Note that trace fossil counts are a proxy for real abundances as counts are collected from 2D interpretations through a small volume (the sedimentary core).

Arenicolites (Figure 6.3C-D) is observed in 229 beds (22% of bioturbated beds). Bioturbation index of beds containing *Arenicolites* is most commonly BI =1; however, *Arenicolites* is also observed in beds with BI = 2 to BI = 5 (Figure 6.4A). Size-diversity index of beds containing *Arenicolites* ranges from SDI = 1 to SDI = 25 (Figure 6.4E). These values are right-skewed, as *Arenicolites* most frequently coincides with SDI values of SDI = 1 to SDI = 10. In a single given bed, 1 to 8 instances of *Arenicolites* are commonly observed; however, up to 12 instances of *Arenicolites* within one bed are recorded (Figure 6.5A). Within a single given bed, *Arenicolites* is most commonly found with two other ichnogenera and is very rarely found by itself (Figure 6.5E).

Cylindrichnus (Figure 6.3D-F) is observed in 995 beds (96% of bioturbated beds). Beds that contain *Cylindrichnus* typically have BI values of BI

125
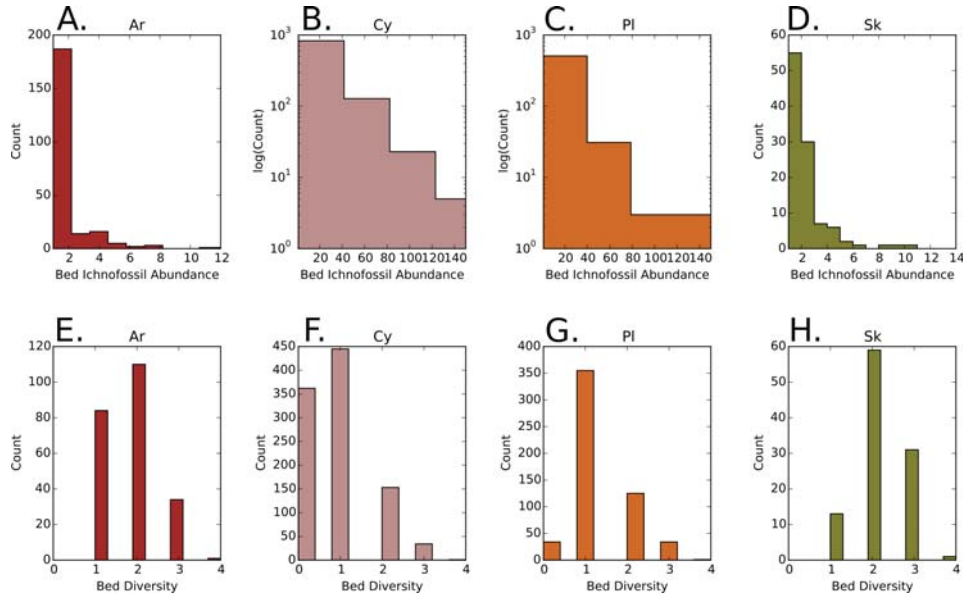
Figure 6.5: (A-D) Histogram of the total number of trace fossils found in association with *Arenicolites* (Ar: 5A), *Cylindrichnus* (Cy: 5B), *Planolites* (Pl: 5C), and *Skolithos* (Sk: 5D). (E-H) Histogram of the number of trace fossils found in addition to *Arenicolites* (Ar: 4E), *Cylindrichnus* (Cy: 4F), *Planolites* (Pl: 4G), and *Skolithos* (Sk: 4H) in beds containing those traces.

$= 1$ (Figure 6.4B). As with *Arenicolites*, there are slightly more beds containing *Cylindrichnus* that have BI $= 4$, compared to BI $= 2$ to BI $= 5$, which are also commonly observed. Beds containing *Cylindrichnus* have SDI values that are generally higher than SDI $= 17.5$; however, *Cylindrichnus* is found in association with SDI values of up to SDI $= 30$ (Figure 6.4F). Up to 150 instances of *Cylindrichnus* have been recorded in a single bed (Figure 6.5B). This large count occurs when a largely continuous mud interval, designated as a bed in PyCHNO, spans multiple decimetres. 1 to 40 *Cylindrichnus* instances per bed is more typical. *Cylindrichnus* is generally found by itself or with one other ichnogenera within a given bed (Figure 6.5F).

Planolites (Figure 6.3A-B) is observed in 549 beds (53% of bioturbated beds). Bioturbation indices of beds containing *Planolites* are relatively evenly distributed between BI $= 1$ and BI $= 4$, with a sharp drop off at BI $= 5$ (Figure 6.4C). Size-diversity index values of beds containing *Planolites* are typically SDI $= 5$ (Figure 6.4G). The right-skewed distribution of SDI values is similar to the *Arenicolites* SDI value distributions. As with *Cylindrichnus*, up to 150

126

instances of *Planolites* have been measured in a single bed multi-dm scale bed; however, 40 or less occurrences of *Planolites* in a given bed is much more common (Figure 6.5C). *Planolites* is often associated with just one other trace, and is associated with two other ichnogenera in a given bed approximately half as frequently as it is with one other trace (Figure 6.5G). This trace fossil is very rarely associated with more than 3 other ichnogenera within a single bed.

Skolithos (Figure 6.3B-C) is observed in 104 beds (10% of bioturbated beds). In beds containing *Skolithos*, BI values of BI = 1 occur twice as frequently as BI = 2 to BI = 5 (Figure 6.4D). *Skolithos* typically coincides with SDI values of SDI = 5 to SDI = 7.5 (Figure 6.4H). As with *Arenicolites*, *Skolithos* is generally observed in groupings of 6 or less expressions per bed (Figure 6.5D). In contrast to other previously listed trace fossils, *Skolithos* is most frequently observed in association with 2 or more other ichnogenera within a given bed (Figure 6.5H).

Gyrolithes (Figure 6.3G) is found in 13 beds and *Thalassinoides* (Figure 6.3A) is found in 2 beds respectively. Therefore the histograms generated for these ichnogenera are not likely to be statistically representative: as such, these ichnogenera are therefore not presented or discussed further.

6.4.2 Relative proportion of ichnogenera per bed with depth from top of point-bar

The relative proportion of *Arenicolites*, *Cylindrichnus*, *Planolites*, and *Skolithos* for beds binned in 1 m intervals from the top of the point-bar is shown in Figure 6.6. Data from all wells were pooled into these 1 m bins.

Cylindrichnus is the most abundantly observed ichnogenus on a bed-by bed basis throughout the entire point-bar deposit (typically > 70% of all traces observed are *Cylindrichnus* (Figure 6.6). *Cylindrichnus* is generally the only ichnogenus present below 26 m from the top of the point-bar. The next most abundant trace is *Planolites*, which typically comprises approximately 25% of relative trace fossil abundance. *Skolithos* and *Arenicolites* relative abundances are the greatest between 21 m to 26 m. In this interval, *Skolithos* and *Arenicolites* counts each make up approximately 5% of all trace fossil counts.

127
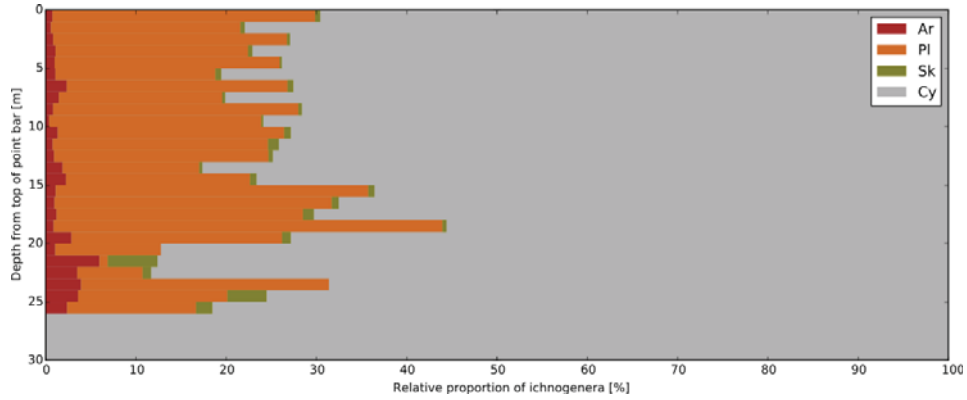
Figure 6.6: Pooled data, showing the relative abundance of ichnogenera on a bed by bed basis in 1 m bins for all wells starting at the top of the point-bar interval (0 m) descending to 30 m.

6.4.3 Relationships between measured ichnological parameters and bioturbation index

The relation between measured bed BI with bed maximum burrow diameter, diversity, trace fossil abundance, SDI, and bed thickness is shown in Figure 6.7A-F. These figures are standard boxplots showing 1st quartile, median, 3rd quartile and outliers. The color gradient for each figure corresponds to the number of samples that fall within each bin.
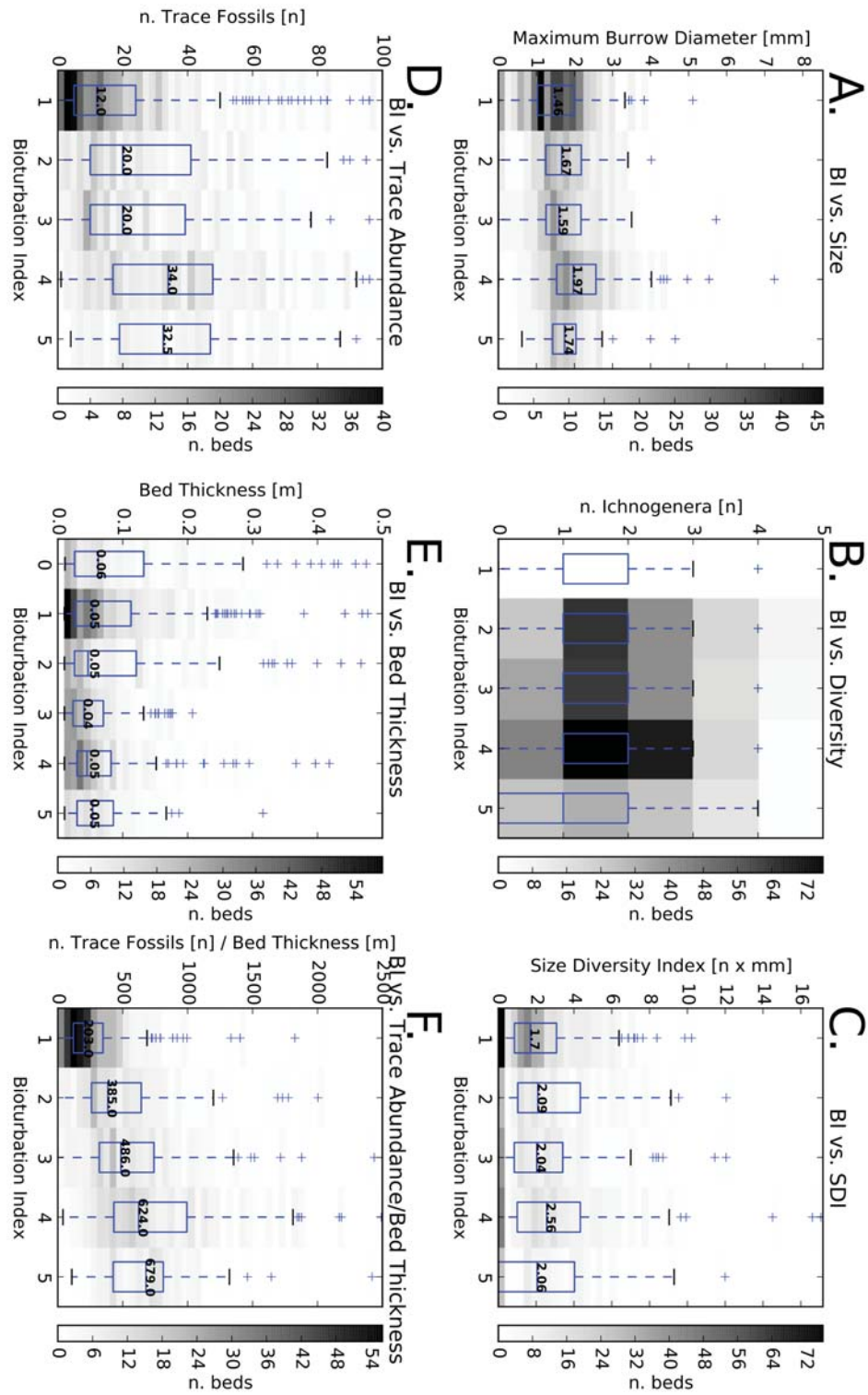
Figure 6.7: (Continued on the following page.)

Figure 6.7: Box plots overlying a 2D histogram color map (in gray scale), showing the number of beds contributing to bins of bioturbation index (BI) plotted against: (A) each bed's maximum burrow diameter; (B) each bed's ichnogenera diversity; (C) each bed's size-diversity index (SDI); (D) the total number of trace fossils observed in each bed; (E) the thickness of each bed; and (F) the total number of trace fossils observed divided by bed thickness for each bed. The small number within the box plots correspond to the median value for each category that is compared to BI.

From Figure 6.7A, maximum burrow diameter per bed compared to BI increases non-monotonically from BI = 1 / burrow diameter median = 1.5 mm until BI = 4 / burrow diameter median = 2.0; however, at BI = 5, the median burrow diameter value decreases to 1.7 mm. Bioturbation index = 5 also contains the fewest number of size-measurements (typically < 20 measurements per bin). Each BI category contains outlier (measurements from < 5 beds) maximum burrow diameters that range from 3.5 mm to 7.2 mm.

The number of ichnogenera per bed (*i.e.* diversity) containing trace fossils ranges from 1 to 6 ichnogenera (Figure 6.7B). The median number of ichnogenera per bed is 2 for all BI categories. Diversity greater than 4 ichnogenera per bed is rare (generally observed in < 20 beds per BI category). Note that low BI beds (BI = 1-2) were observed to contain multiple ichnogenera. Trace fossil diversity > 2 is most commonly observed at BI = 4. BI = 5 contains the smallest number of diversity measurements.

Size-diversity index median values increase irregularly, from BI = 0, where the SDI median value is SDI = 1.7, to BI = 4, where the SDI median value is SDI = 2.56 (Figure 6.7C). Size-diversity index does not generally reach values greater than SDI = 9.5, with the exception of outliers, which reach up to SDI = 17.

Bioturbation index from a given bed increases in correspondence with the total number of trace fossils observed within that bed (Figure 6.7D). BI = 1 corresponds to approximately 2-4 traces per bed in most cases, with a median value of 12 traces per bed. BI = 2 and BI = 3 correspond to a median value of 20 traces per bed. While BI = 4 corresponds to a median value of 34 traces per bed. Considering that a relatively small number of trace fossil measurements were made for BI = 5, the number of trace fossils observed in a bed with BI = 5 is likely larger than the calculated median value of 32 traces per bed.

There does not appear to be a relationship between bed thickness and BI (Figure 6.7E). For all BI values, the median bed thickness is approximately 5 cm. However, BI = 5 almost exclusively coincides with beds that are less than 10 cm, whereas BI = 1 to BI = 4 coincide with a more diverse bed thicknesses

that are generally up to 20 cm.

Median trace abundance divided by thickness versus BI increases monotonically from BI = 1 to BI = 5 (Figure 6.7F). For example, median trace abundance divided by bed thickness increases from 203 at BI = 1 to 385 at BI = 2, and increases from 624 at BI = 4 to 679 at BI = 5. This is the only variable plotted versus BI that displays a continuous and consistent trend.

6.4.4   Ichnonetwork analysis

Figure 6.8A shows the ichnonetwork from the base of the point-bar (> 25 m to 30 m), with successive 5 m increments up the point-bar shown in Figure 6.8B-F. The thickness of the edges (*i.e.* the links) connecting nodes represent Bray-Curtis indices (*i.e.* the similarity of trace fossil abundances for each bed measured). Note that only edge weights greater than 5% are noted on the figures.

The > 25 m to 30 m interval ichnogenera abundance network is shown in Figure 6.8A. *Cylindrichnus* and *Planolites* are 46% similar in terms of bed abundance and *Skolithos* and *Arenicolites* are 15% similar for bed abundance. All other trace fossil abundance relationships are less than 5% similar for any given bed. The > 20 m to 25 m abundance relation network is shown in Figure 6.8B. *Cylindrichnus* and *Planolites* bed relative abundances are 48% similar, while *Arenicolites* and *Skolithos* relative abundance is 32% similar. All other trace fossil abundance relationships are < 5% similar. Figure 6.8C shows the > 15 m to 20 m relative ichnofossil abundance relation network. *Cylindrichnus* and *Planolites* relative abundances are 49% similar for any given bed in this interval. *Arenicolites* and *Skolithos* relative abundance is 26% similar. All other trace fossil relationships are under 5% similar in terms of relative abundance within any given bed for this interval. The > 10 m to 15 m ichnofossil abundance relation network is shown in Figure 6.8D. *Cylindrichnus* and *Planolites* containing beds are 32% similar in terms of relative abundance, whereas *Arenicolites* and *Planolites* abundances are 19% similar. *Arenicolites* and *Planolites* relative trace fossil abundance for any given bed is 7% similar. All other ichnofossil abundance relationships are < 5% similar in abundance.
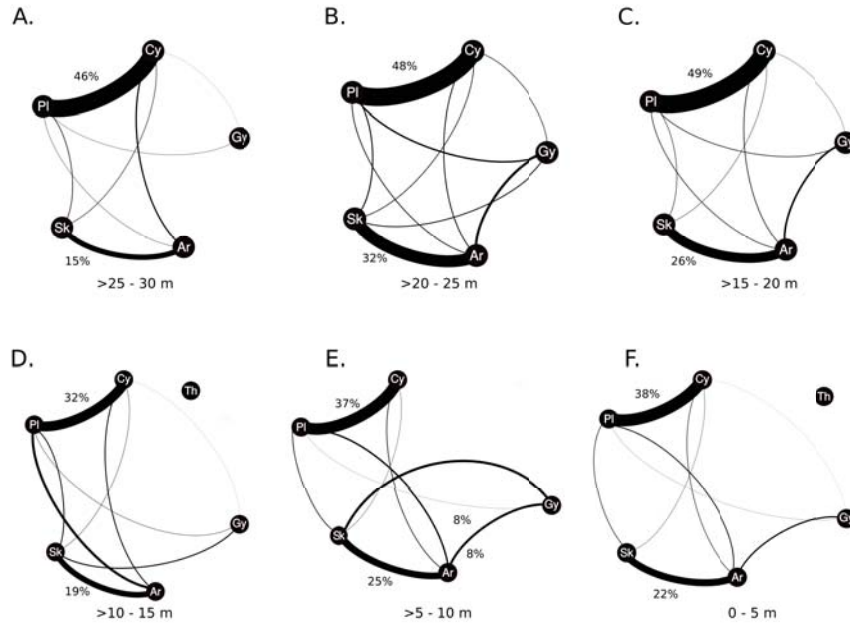
Figure 6.8: Ichnonetworks generated from all measured beds grouped in successive 5 m slices datumed from the top of the point bar. Increments are described from the base to the top to reflect point-bar evolution (A) > 25 - 30 m; (B) > 20 - 25 m; (C) > 15 -20 m; (D) > 10 - 15 m; (E) > 5 - 10 m; (F) 0 - 5 m. Ar = *Arenicolites*, Cy = *Cylindrichnus*, Gy = *Gyrolithes*, Pl = *Planolites*, Sk = *Skolithos*, Th = *Thalassinoides*. The edges weights (or links) correspond to the Bray-Curtis similarity index averaged from all beds and from all wells of any given interval. Edge weights < 5% are not labelled.

Figure 6.8E shows the > 5 m to 10 m slice ichnofossil relations. *Cylindrichnus* and *Planolites* abundances are 37% similar, and *Arenicolites* and *Planolites* abundances are 25% similar. *Gyrolithes* abundance is 8% similar to both *Arenicolites* and *Skolithos* abundances for beds in this interval. All other trace fossil relationships are < 5% similar in abundance. Figure 6.8F shows the 0 m to 5 m ichnofossil relations for all wells. *Cylindrichnus* and *Planolites* abundances in beds for this interval are 38% similar (i.e the trace fossil counts of both ichnogenera is 38% similar on a bed by bed basis) as shown by the boldest edge connecting these two nodes. *Arenicolites* and *Planolites* are 22% similar in abundance within this zone. All other ichnogenera are < 5% similar in abundance on a bed by bed basis.

6.4.5 Time-series analysis

Two depth-converted wavelet transform cross-sections of successive bed composition similarity were generated and are shown in Figures 6.9 and 6.10. The lines of section are shown in Figure 6.2. Both lines of section are oriented obliquely to scroll-bar orientations. Figure 6.9 transects the point-bar closer to the outer edge of the point-bar deposit (*i.e.* relatively younger deposits). Figure 6.10 transects the point bar closer to the core of the point-bar deposit (*i.e.* relatively older deposits).

A high amplitude peak is found in all wells (except 07-13) between 5 and 7.5 m from the top of the point-bar (Figure 6.9). This peak coincides with a low in relative-bed similarity index, which dips below 50% similarity in all wells. The periodicity of these peaks is typically under 4 beds per peak. There is a similar high amplitude peak found in the 02-13, 07-13, and 11-13 wells (at 10-15 m depth), which also coincides with similarity indices below 50%. There is no distinct pattern spatially for the number of beds that are < 50% successively similar, < 75% successively similar and > 75% successively similar (Table 6.1).

For all wells in Figure 6.10, the greatest number of high amplitude peaks is found between 10 and 15 m from the top of the point-bar. As with the section shown in Figure 6.9, the peaks generally coincide with low relative-bed
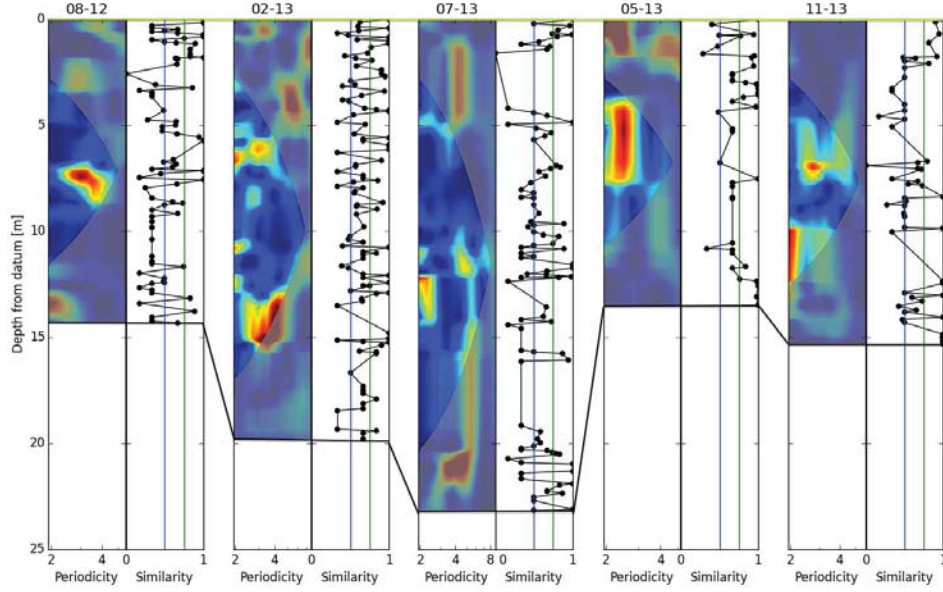
Figure 6.9: Successive Bray-Curtis similarity index (curves) and depth-converted scalograms (contour plots) cross-section showing wells 08-12, 02-13, 07-13, 05-13, and 11-13. The datum corresponds to the top of the point-bar. See Figure 2 for line of section. Periodic signals (warm colors on the scalograms) are observed at approximately 7.5 m from the top of the point-bar and at 15 m from the top of the point-bar.
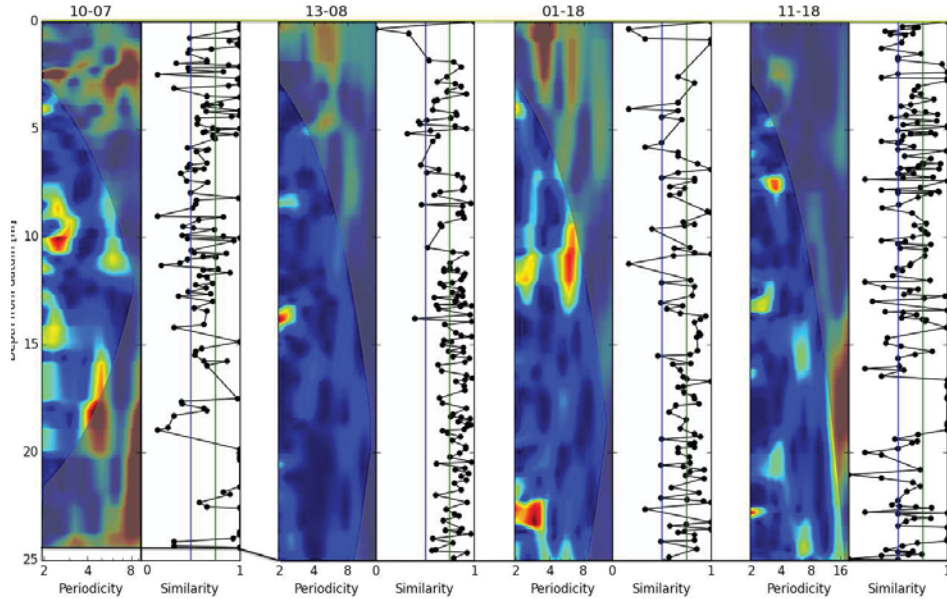
Figure 6.10: Successive Bray-Curtis similarity index (curves) and depth-converted scalograms (contour plots) cross-section showing wells 10-07, 13-08, 01-18, and 11-18. The datum corresponds to the top of the point-bar. See Figure 2 for line of section. A periodic signal (warm colors on the scalogram) is observed between 10-15 m from the top of the point-bar.

135

Table 6.1: Sequential bed similarity (SBS) count calculated with Bray-Curtis indices in < 50 % similarity, 50% < similarity < 75% and > 75% bins for each studied well. Blue, yellow and red colored cells correspond to smallest, median, and largest relative count respectively.

Well	< 50 % SBS	50 < SBS% < 75	> 75 SBS%
10-07	31	52	49
13-08	12	59	125
01-18	32	69	76
11-18	86	102	83
08-12	43	19	16
02-13	23	46	34
07-13	43	25	25
05-13	8	15	21
11-13	27	11	18

similarity indices. However, the periodicity of these peaks is relatively higher with periods of approximately 7 beds per peak. A similar peak is found in the 01-18 and 11-18 wells, at a depth of approximately 22.5 m, with periodicities of approximately 4 beds per peak. In contrast to the wells shown in Figure 6.9, the majority of successive beds are 50% similar in the wells shown in Figure 6.10 (also see Table 6.1).

6.5 Discussion

6.5.1 Statistical characteristics of trace fossils associated with brackish water

Pemberton *et al.* (1982) presented the first examples of an ichnofossil suite associated with a brackish water depositional setting in the McMurray Formation. Trace fossil assemblages associated with brackish water conditions, as synthesized by MacEachern *et al.* (2007); Gingras *et al.* (2011), have the following characteristics: low ichnodiversity (sometimes dominated by a single ichnogenus) assemblage of diminutive, morphologically simple, vertical and horizontal traces that represent an impoverished marine assemblage with some ichnogenera present in high densities. Gingras and MacEachern (2012) note that

trace fossils assemblages typically associated with brackish-water conditions include: *Planolites*, *Thalassinoides*, *Arenicolites*, *Cylindrichnus*, *Skolithos*, and *Gyrolithes*. This assemblage is identical to the suite reported in this study. Additional characteristics such as: the dominance of the studied interval by a single ichnogenus (*Cylindrichnus*) (Figure 6.6), diminutive trace fossil sizes (rarely > 4 mm in internal diameter) (Figure 6.7), and low SDI (rarely > SDI = 10) (Figure 6.7) support the interpretation that the studied point-bar was deposited during dominantly brackish water conditions (*e.g.* Hauck *et al.* 2009; Botterill *et al.* 2015; Timmer *et al.* 2016c) .

As shown in the figure plates of (Pemberton and Wightman 1992 : Fig. 6B-C); (Ranger and Pemberton 1992: Fig 8A); (MacEachern *et al.* 2005: Fig 4A); (Gingras *et al.* 2011: Fig 3C); and (Gingras and MacEachern 2012: Fig. 4.3i) sporadic, monogeneric, and high intensity *Gyrolithes* is an important component of trace fossil assemblages characteristic of brackish water conditions. The network graphs support their assertion as *Gyrolithes* is only weakly linked to *Arenicolites* and *Skolithos* (maximum Bray-Curtis similarity index = 8% at slice > 5 to 10 m; Figure 6.8B) in one interval and otherwise is generally less than 5% similar in terms of abundance with any other trace for any given network graph slice. Globally, *Gyrolithes* is weakly linked to *Arenicolites*, *Cylindrichnus*, *Planolites* and *Skolithos* (Figure 6.9). These weak links may present transitionary phases of ecological conditions whereby the colonizers adjust to new environmental conditions with different behaviors. These behaviors are likely associated with the final stages of the point-bar.

Although Gingras *et al.* (2011) note that *Thalassinoides* is a common element of trace fossil assemblages associated with brackish water conditions, it is only observed in 2 out of 1033 beds assessed for this study. *Thalassinoides* is very weakly associated with the dominant *Cylindrichnus* and *Planolites* (Figure 6.9). This suggests that environmental conditions during the time of point bar deposition were mostly unsuitable for the generation or preservation of *Thalassinoides*. The paucity of *Thalassinoides* occurrences could also represent a larval recruitment problem.

The ichnonetworks constructed for this study show the relative pervasive-

137

ness of specific ichnogenera within a point-bar deposited during brackish water conditions (Figures 8-9). From Figure 6.4, BI and SDI ranges are similar for *Arenicolites*, *Cylindrichnus*, *Planolites* and *Skolithos*. Total bed ichnofossil abundances (the count of all ichnofossils within a bed) bearing *Cylindrichnus* or *Planolites* can be up to 10 times larger than either *Arenicolites* bearing beds or *Skolithos* bearing beds (Figure 6.5A-D). This suggests that organisms responsible for generating *Cylindrichnus* and *Planolites* were likely either present in greater abundances, were more adapted to specific environmental conditions, had a proclivity for generating multiple burrows within one lifespan, or that other environmental parameters beyond salinity influenced burrowing behavior. *Arenicolites* and *Skolithos* are most typically found in beds containing more than one or two other ichnogenera, whereas *Cylindrichnus* is often found in monogeneric beds or with one other trace fossil (typically *Planolites*) (Figure 6.5E-H). This suggests that *Planolites*, followed by *Arenicolites* and *Skolithos* typically compliment the *Cylindrichnus* dominated trace fossil assemblage. This is also demonstrated in Figure 6.6.

Based on ichnonetwork analysis combined with trace fossil parameters several interpretations can be made: (1) *Cylindrichnus* is well suited for ambient point-bar conditions and therefore represents the ambient point-bar environment. It has a lining that resists exhumation and deformation, and it is optimized as a platform to forage organic detritus at the sediment interface, a behaviour that in tidal settings has shown to be important; (2) *Arenicolites* and *Skolithos* in some cases can be difficult to discriminate in 2-D slabbed examples; (3) *Planolites* represents a shift to harvesting food below the sediment-water interface and as such may indicate times of abrupt or rapid sedimentation when organics became stored in the sediment; (4) Where *Skolithos* and/or *Arenicolites* appear, these are likely comparably more opportunistic than *Cylindrichnus*. This might present evidence recruitment levels; and (5) seasonal changes likely influence salinity levels and larval recruitment parameters.

Considering that the characteristics of trace fossils preserved in the studied point-bar are consistent with brackish water depositional conditions, their

statistical analysis can serve as building blocks for establishing mathematical parameters for the recognition of brackish-water depositional conditions in the rock record.

6.5.2 Spatial and temporal fluctuations in ecological conditions

From the relative abundance of trace fossils plotted against depth (Figure 6.6), the main trace fossil components are present at relatively similar proportions during the entire depositional history of the point-bar. This suggests that baseline environmental conditions remained similar during the evolution of the point-bar. However, based on the Morlet wavelet transform of sum successive bed similarity (figures 6.9-6.10), there exists several periods of physical or chemical environmental variability. For example, in Figure 6.9, well 08-12 shows a relatively continuous trend of successive bed similarity < 50%. Intervals like this support that environmental conditions varied significantly, on occasion, from baseline ecological conditions at a bed-deposition temporal scale.

With the exception of a few wavelet transform-determined high amplitude peaks (warm colors in the scalograms), that occurred at similar depths (between 5 and 7.5 m in Figure 6.9; between 10 and 15 m in Figure 6.10) with periodic signals of approximately 4 beds per peak, no consistent periodic bed composition variation signal is observed. The different depths of peaks between cross-sections is the only evidence for spatial differences in bed composition periodicity differences within the point-bar. Timmer *et al.* (2016c) demonstrated the presence of ichnological interpreted stress time-series periodic signals of approximately four (or multiples of four) in the McMurray Formation. However, the periodic signals found in that study were significantly better defined compared to the weak periodic signals found in this present study. The study conducted by Timmer *et al.* (2016c) is located approximately 150 kilometres north. It is perhaps not directly chronostratigraphically linked to the present study, therefore it is likely that this area was subject to different tidal-fluvial and/or climate interplay.

Size-diversity index values are relatively small (most values are between SDI = 1.5 and SDI = 2) throughout the studied interval (Figure 6.7C). Reduced infaunal animal size and diversity is a defining characteristic of brackish water environments (*e.g.* Hauck *et al.* 2009). This suggests that with the exception of a few events, salinity presented a significant and persistent stress on the infaunal population. This is further supported by the wavelet transforms, which did not detect significant periodicity of changes in ichnofossil bed composition characteristics (Figures 6.10). Relatively low salinity was therefore likely a persistent stress during the evolution and deposition of the point-bar.

Bioturbation index can be related to sedimentation rates (Dafoe *et al.* 2008; Gingras *et al.* 2008). Considering that a wide range of BI values were recorded (BI = 0 to BI = 5), but that BI = 1 is the most common bioturbation index (Figure 6.7), variable sedimentation rates also likely affected the preserved trace fossil assemblages during point-bar deposition. Figure 6.7C demonstrates that BI is only weakly related to SDI; this relation is due to slight burrow size increases with increasing bioturbation (Figure 6.7A), but it is not a well defined relation. This suggests that temporal variations in salinity did not necessarily exclusively coincide with temporal variation in sedimentation rates. In estuarine systems, sedimentation rates, especially of mud, can be related to variations in fluvial discharge (*e.g.* Allen *et al.* 1980; Lettley *et al.* 2005b). Since changes in fluvial discharge are also associated with salinity variations, the weak coupling between BI and SDI suggests that other ecological stressors had an independent effect on the infaunal population characteristics.

6.5.3 Trace fossil abundance divided by thickness as a proxy for bioturbation index

Bioturbation index represents an estimation of the quantity of a given portion of originally unbioturbated sediment that has been bioturbated (*sensu* Reineck 1967; Taylor and Goldring 1993). Typically, bioturbation index is assessed on a BI = 0 (0% bioturbation) to BI = 6 categorical scale (100% bioturbation). This is the bioturbation index scale adopted by the ichnology data collection software PyCHNO (Timmer *et al.* 2016b). Considering that visual estimations

of bioturbation index can be difficult, especially for novice ichnologists, multiple workers have attempted to measure bioturbation intensity using image analysis (Honeycutt and Plotnick 2008; Dorador *et al.* 2014). Image analysis methods for determining bioturbation index have, however, not been sufficiently developed for widespread adoption by ichnologists.

Considering that bioturbation index represents the volume of biogenically disturbed media within an otherwise undisturbed volume, it is not unsurprising that there is a strong correlation between collected bioturbation index for a given bed and the total number of traces found in that bed divided by bed thickness (Figure 6.7F). We suggest that total trace fossil count divided by bed thickness is therefore a useful proxy for bioturbation index, within certain conditions. Since this measurement is similar to a population point count within an area, for this proxy to be valid and comparable between wells, core sleeve width or imaged widths must be identical. Total bed trace fossil count divided by bed thickness is also likely only valid for relatively simple trace fossil morphologies that have limited volumetric sediment disturbance potential per trace (*e.g. Arenicolites*, *Cylindrichnus*, *Planolites*, *Skolithos*).

Further work is required in order to refine the numerical cutoffs for this proxy for each BI zone for eventual conversion between BI and total bed trace fossil count divided by bed thickness. However, since total bed trace fossil count divided by bed thickness is acquired during the typical PyCHNO workflow when a bed is delimited and trace fossils are identified within this bed, future studies employing PyCHNO could easily collect this BI proxy and refine the BI zone limits found in this study. This proxy has the potential to remove subjective and ambiguous aspects of BI collection for certain datasets.

6.6   Summary

Data collected with PyCHNO was statistically analyzed to quantify ichnological trends within a well defined point-bar deposit. Several characteristics of the observed trace fossil assemblage support that brackish-water conditions were prevalent during point-bar deposition. These include: trace fossils (*Areni-*

colites, *Cylindrichnus*, *Planolites*, and *Skolithos*) that are typical of brackish water depositional environments; diminutive trace fossil sizes (typically < 4 mm in diameter), low diversity (typically 1 to 3 ichnogenera per bed) and size-diversity index (SDI) typically less than SDI = 10; locally intense bioturbation; and dominance of monogeneric *Cylindrichnus*.

With ichnonetwork analysis using Bray-Curtis indices (comparing the relative abundance of traces) on a bed by bed basis, this study determined that *Cylindrichnus* and *Planolites* 32 to 49% similar abundance and that *Skolithos* and *Arenicolites* typically have approximately 15 to 32% similarity. *Cylindrichnus* and *Planolites* abundances are rarely similar to *Arenicolites* and *Skolithos* abundances (< 5% similarity). The relative importance of links between ichnogenera remained approximately the same throughout the analyzed 5 m slice intervals datumed from the top of the point-bar. This suggests that relatively stable temporal ecological conditions existed during the formation of the point-bar. Rare occurrences of *Thalassinoides* (observed in 2 out of 1033 bioturbated mudstone beds) support rare deviations from lower salinity conditions.

Wavelet transform analysis of modified Bray-Curtis successive bed comparison time-series, did not yield definitive spatial or temporal periodic signals. To visualize wavelet transform scalograms with depth, depth-converted wavelet transforms were generated. Most bed-composition periodic peaks occurred at periodicities of 4 beds per peak; however, rare high amplitude bed composition peaks occurred. This suggests that ecological conditions remained relatively stable temporally and spatially during the evolution of the point-bar.

Finally, our data collection and processing workflow demonstrated that the total number of trace fossils observed in a bed by bed thickness corresponds well with BI. Considering that total trace fossil counts and bed thickness are collected as part of the typical PyCHNO workflow, this proxy is proposed as a suitable alternative to bioturbation index for quantitative ichnological data collection purposes. However, further work is required to test this parameter more rigorously.

Chapter 7

Helical burrows: an optimized deposit feeding strategy?

7.1 Introduction

Elongate helical burrows occurring in high density monogeneric assemblages, form an important constituent of heterolithic stratification in the Cretaceous McMurray Formation in NE Alberta, Canada (Figure 7.1). Micro-helical burrows (Figure 7.1A) are generally assigned to the *Gyrolithes* ichnogenus (*e.g.* Ranger and Pemberton 1988; Bechtel 1996; Harris 2003; Ranger and Gingras 2003; Lettley 2004; Crerar and Arnott 2007; Musial *et al.* 2012), but are in the process of assignment to the new ichnogenus and ichnospecies *Spirascensus conferti*. In this study, for simplicity, we refer to these traces as "helical burrows". Understanding the function of these burrows is an essential step towards more accurately determining paleoecological constraints of intervals dominated by these burrows.

Multiple modern organisms are capable of constructing helical burrows. For example, Dworschak and Rodrigues (1997) ascribe *Gyrolithes*-like burrows to the shrimp *Axianassa australis* from modern deposits of Praia do AraGa, Brazil. Powell (1977) showed examples of *Gyrolithes*-like traces produced by the capetellid worm *Notomastus lobatus* in modern deposits of Banks Channel, North Carolina. These worms were found in proximity to burrowing crustaceans. According to the comprehensive review of *Gyrolithes* by Netto *et al.* (2007), *Gyrolithes* is interpreted to represent an infaunal response for

143

Figure 7.1: Examples of helical burrows from cored intervals of the McMurray Formation. Bioturbation occurs in heterolithic stratification. Lighter colors correspond to mud/silt mixtures and darker colors correspond to bitumen saturated sand. (A) densely packed helical burrows penetrating a heterolithic interval. Photo from 13-35-097-11W4. (B) loosely packed helical burrows or *Gyrolithes* in a sandstone-dominated interval. Photo from 11-22-084-07W4. (C) Loosely packed helical burrows or *Gyrolithes* from a layered heterolithic interval. Photo from 11-22-084-07W4.

buffering salinity fluctuations (*e.g.* Beynon and Pemberton 1992), an anchoring mechanism, a food-rich or dysoxic layer exploitation scheme (*e.g.* Dworschak and Rodrigues 1997), or a response to predation (*e.g.* Felder 2001).

For this study, we use computer simulations to demonstrate that helical burrows can form as a response to phobotaxis (*i.e.* the self-avoidance or the avoidance of other organisms). We also use computer simulations to test the efficacy of helical burrowing strategy for deposit-feeding compared to other simulated behaviors in various 3D food distribution landscapes. This is the first 3D ethology-based ichnological computer model implemented with intra-species food competition. From a mechanistic perspective, we also examine the advantages of helical burrowing for resisting burrow pullout via predation and for burrow irrigation efficiency.

7.2 Ichnological computer simulations background

Detailed reviews of behavioral-based ichnological simulations are found in Hayes (2003) and Plotnick (2003). Bioturbation is also modeled from a mechanistic approach (*e.g.* Choi *et al.* 2002; Trauth 2013). However, physics-based models do not necessarily provide information for *why* certain types of trace fossils or trace fossil morphologies are generated. These simulations focus on the distribution of bioturbation (*e.g.* the rate of reworking of a given media) rather than the morphological end products. We therefore focus on an ethological modeling approach.

Raup and Seilacher (1969) modeled basic 2D foraging behaviors in the first demonstration of computer simulations applied to ichnological data. Modeling was based on foraging behavior principles introduced by Richter (1928) that include: (1) strophotaxis, which makes an animal turn 180 degrees at given intervals; (2) phobotaxis, which makes an animal avoid crossing their own tracks or other organisms' tracks; and (3) thigmotaxis, which makes an animal maintain close contact with former tracks. The simulated animal from Raup and Seilacher (1969) can make four types of movements: (1) continue straight ahead; (2) turn towards a pre-existing track; (3) turn away from a pre-existing track; or (4) make a 180 degree turn. The animal decides which movement to complete based on a search of adjacent x-y cells, which have previously been intersected by the animal. Raup and Seilacher (1969)) were able to successfully recreate the meandering patterns of various trace fossils based on this approach.

Papentin (1973) published one of the first example of evolutionary algorithms applied to feeding patterns of the polychaete *Paronis fulgens*. Based on 6 parameters (derived from strophotaxis, phobotaxis, and thigmotaxis), Papentin (1973) made a population of computer-simulated worms "learn" to produce 2D trackways similar to those produced by *P. fulgens*. Hofmann (1990) produced random feeding paths based on the probability of taking a 'left' or 'right' path deviation of some arbitrary fixed deviation angle along a 2D

plane. These paths were similar to those of *Helminthoidichnites*, and *Torrowangea*, demonstrating that these trace fossils likely originate from random worm decision making. Garlick and Miller (1993) simulated complex *Paleodictyon*-like traces based on behavioral parameters and precise 60 degree turns. This simulation suggests that *Paleodictyon* is generated by an organism more complex than a worm, as the trace-maker is required to accurately measure angles and distances. Hammer (1998) employed artificial neural networks combined with evolutionary algorithms to simulate optimized feeding patterns for pseudo-random food clusters in a 2D matrix. These computer simulated worms learned to move in linear paths outside of food clusters, and to meander within food patches. However, these simulations did not create patterns that can be readily associated with known trace fossil morphologies.

The first 3D simulations of trace fossil behavior were programmed by Plotnick (2003), Plotnick and Koy (2005), Koy and Plotnick (2007), and Plotnick (2007). In these models, a single worm moved within a heterogeneous food distribution matrix and selected a path based on sensing (with simulated chemoreceptors) food values of adjacent cells. These models are the first attempt to incorporate simulated organisms able to sense food in a heterogeneous environment. The Koy and Plotnick (2007) model employed simulated organisms capable of evaluating and selectively consuming food in order to minimize energy expenditures incurred during locomotion to food patches. This experiment demonstrated that strophotaxis, phobotaxis, and thigmotaxis is ingrained in foraging behavior without having to be hardwired genetically. Plotnick (2003) also demonstrated that *Palaeodictyon*-like and *Chondrites*-like morphologies can be formed in 3D by employing a L-systems algorithm, which is typically used to model branching systems like those of plants.

In contrast with the above listed chemoreceptor work done by Plotnick and his colleagues, Sims *et al.* (2014) contend that 2D Lévy random walks, an optimized foraging behavior in resource-sparse substrates, may have originated from strophotaxis. In their study, step-length measurements supported that *Scolicia* displayed Lévy random walk foraging behavior. However, Sims *et al.* (2014) do not take into account the fact that many infaunal organisms are

capable of sensing food with chemoreceptors.

7.3   Computer Simulations

To demonstrate that helical burrows can form as a response to phobotaxis, a simulation based on Raup and Seilacher (1969) was constructed. In this simple simulation, 4 worms, starting from equally spaced origins in a $x_{max} = 11$ by $y_{max} = 11$ by $z = 5$ cell volume take a step $(x+1, x-1, y+1$ or $y-1)$ one after the other and turn right when they encounter another worm (demonstrating a proclivity for coiling in a given direction). The 4 worms have constant penetration rates (p) of $1/(x_{max} + y_{max} - z/2)$ per step. Cells within the volume visited by a worm are saved in a visited coordinates data structure that is referenced by each worm when making a decision on where to take the next step. The depth values z (a real number) are rounded to integers before they are saved in the visited coordinates data structure. In order to generate helical burrow shapes, an origin parameter was created that made worms turn right once they had reached their x and y origin.

To test the efficacy of helical burrows as a deposit feeding trace compared to other deposit feeding trace behaviors, we constructed a 3D model where n worms simultaneously battle for food resources in various food distribution landscapes using one of five deposit feeding strategies. The food distribution volume has wrapped spatial coordinates (*e.g.* $x > x_{max}$ is converted to 0, $x < 0$ is converted to x_{max}) to eliminate boundary effects. For this model, we arbitrarily set the volume to 100 by 100 by 30. Regardless of deposit feeding strategy, all worms start at equally spaced coordinates. Each time a worm visits a cell within the food volume, the cell is assigned a value of zero. The "ingested food" value is added to the cumulative food count of each individual worm. In order to compare the amount of "food" ingested between trace types, each simulated worm has the same length (*i.e.* each worm visits the same number of cells). This is because, given a random food distribution, the worm that visits the most cells will typically obtain the most food.

The food foraging strategies employed are: (1) w1: a cylindrical helical

burrower with a constant penetration rate; (2) w2: a "smart" burrower that adapts its burrow path based on contact chemoreceptors. This worm enters the substrate at the same penetration rate (p = n cells on given z plane that are visited before descending to the next z plane) as the cylindrical helical burrow; (3) w3: a "smart" burrower that adapts its burrow path based on contact chemoreceptors. This worm can move up and down and is not constrained by a constant penetration rate; (4) w4: a worm that randomly transits throughout the volume; and (5) w5: a worm that randomly transits throughout the volume. This worm (w5) is constrained to enter the substrate at the same penetration rate as the cylindrical helical burrower.

The cylindrical helical burrow path (x, y, z coordinates) is given by:

$$x(t) = cos(t), \; y(t) = sin(t), \; z(t) = \frac{1}{2\pi}t \tag{7.1}$$

Where t are radians between 0 and t_{max}. To determine t_{max}, the length of each helical segment is calculated based on the radius of each segment. The cylindrical helical burrow (w1) takes a helical path where the radius (r) of each helical segment is:

$$r = \frac{\frac{1}{2}(x_{max} + y_{max})}{2\sqrt{N}} - b \tag{7.2}$$

Where x_{max} is the model x cell width in the model, y_{max} is the model y cell width, N is the number of worms in the model, and b is a buffer value between worms typically set at 0.75 (each worm burrow is separated by 1.5 cell width at all times). The length (l) of each of each helical segment is calculated as:

$$l = \sqrt{h^2 + (2\pi r)^2} \tag{7.3}$$

Where h is the vertical separation between each helical segment (typically set to 1). Finally, t_{max} is calculated as:

$$t_{max} = 2\pi \frac{L}{l} \tag{7.4}$$

148

Where L is the total worm length. Each $x(t)$, $y(t)$, $z(t)$ ($0 \leq$ t $\leq t_{max}$) is rounded to the nearest integer so that these coordinates can reference a food value from the food volume. For w1, a data structure keeps track of each x, y, z integer so that each x, y, z combination references a food value only once. The number of cells that are intersected is stored so that w2-w5 also intersect the same number of cells.

The adaptive worm (w2) enters the substrate at a constant penetration rate (p) determined as the number of cells intersected by w1 divided by z_{max}. At each step, w2 picks the maximum food value for the 8 adjacent cells at the same z unless the step is a multiple of p. When the step is a multiple of p, w2 picks the maximum food value for the 9 adjacent cells at $z = z + 1$ (Figure 7.2).
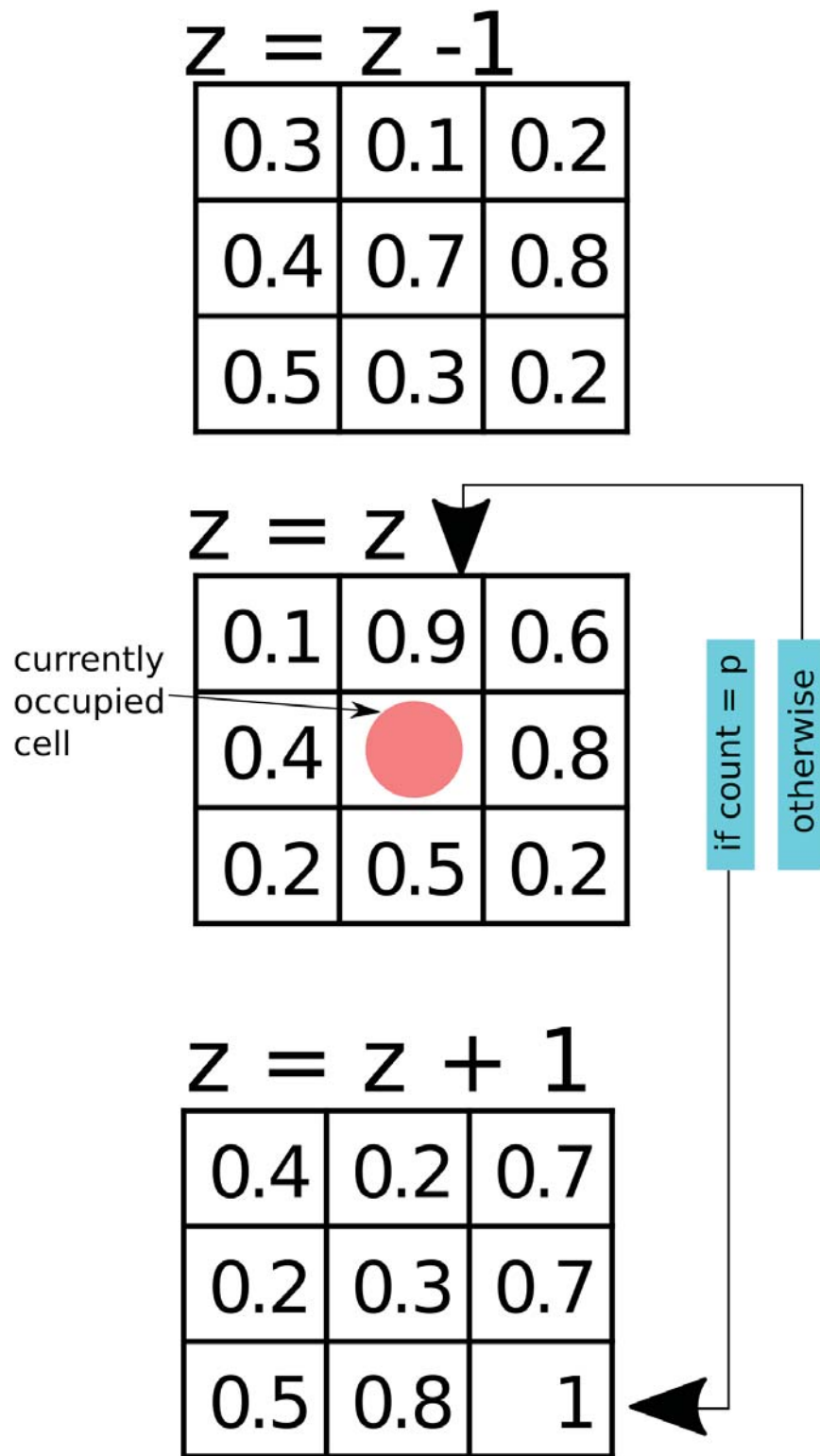
Figure 7.2: (Continued on the following page.)

Figure 7.2: Schematic representation of the decision process made by simulated worms that choose pathways based on maximizing the value of each successive occupied cell. The values in each of the cells correspond to a "food" value between 0 and 1. The pink circle represents the cell that is currently occupied by a simulated worm. The blue boxes highlight the decision process of the worm (w2) restricted to a constant penetration rate (p). Penetration rate refers to the number of cells that are visited (count) per z plane. The simulated worm that is not restricted by penetration rate (w3) can evaluate food values from z -1, z and z + 1 and chooses the maximum food value from any of these planes.

The adaptive worm (w3) is free to move in any z direction within the model. For each step, the worm picks the maximum food value from the 26 adjacent cells (8 horizontally adjacent cells, 9 adjacent cells below and 9 adjacent cells above) (Figure 7.2).

The random worm (w4) randomly picks one of the 26 adjacent cells for each step. The random worm (w5) randomly picks one of 9 adjacent cells for each step if the step number is not a multiple of p. If the step number is a multiple of p, the worm randomly picks one of 10 cells from the adjacent cells at $z = z + 1$.

7.4 Simulation results

Figure 7.3 shows the results of a simple simulation where approximately helical burrows are generated by simulated worms that enter the substrate at the same penetration rate. These simulated worms are programmed to coil to the right. The simulation demonstrates that approximately helical shapes can be generated with a simple set of rules (*i.e.* phobotaxis and taking right turns).

Several simulations were run with 100 worms competing for food distributed in a 100x100x30 unit volume. Figure 7.4 shows a 3D representation of helical burrows (w1) (Figure 7.4A), "smart" burrows (w2) that are constrained to move downwards at the same penetration rate as the helical burrows (Figure 7.4B), "smart" burrows (w3) that can move in any direction within the matrix (Figure 7.4C), random burrows (w4) that can move in any direction within the matrix (Figure 7.4D), and random burrows (w5), that are constrained to move downwards at the same rate as the helical burrows (Figure 7.4E).
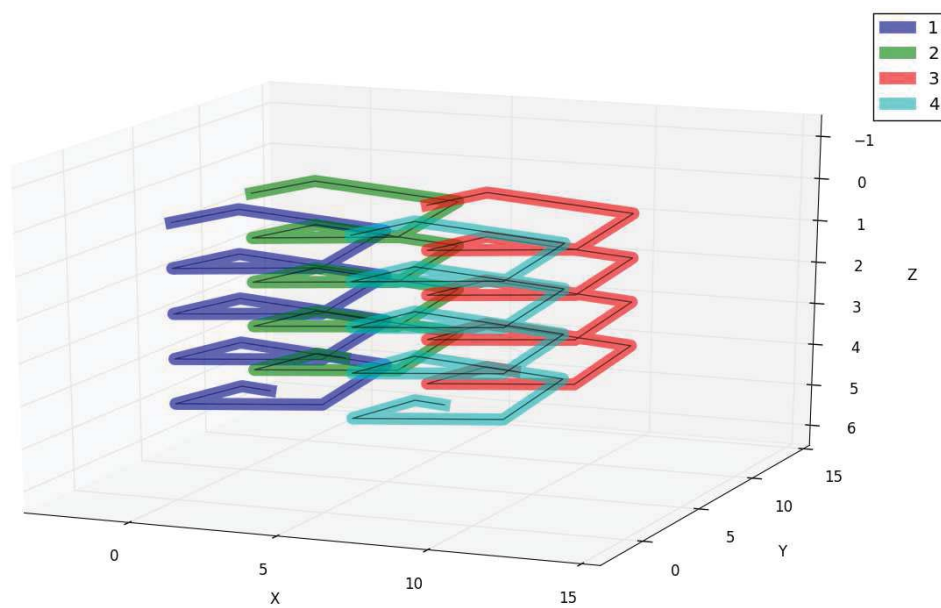
Figure 7.3: 3D representation of geometric shapes generated by simulated worms that adhere to phobotaxis (*i.e.* avoiding the trackways of oneself and others). The simulated worms turned right every time they encountered another worm.

A.

w1

B.

w2

C.

w3

D.

w4

E.

w5
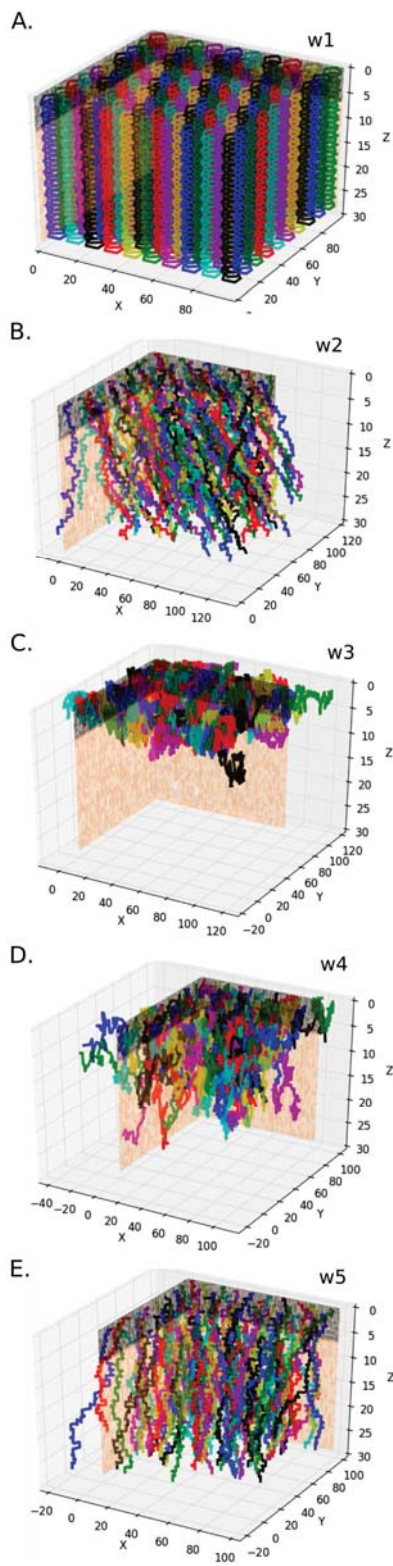
Figure 7.4: (Continued on the following page.)

154

Figure 7.4: 3D representation of simulated burrowing behaviors in a layered volume, where the top (thinner) layer is food rich (values between 0.8 and 1.0) and the bottom (thicker) layer is populated by food values between 0.0 and 0.2. The volume size is 100x100x30. There are 100 simulated worms in each volume. (A) plot of helical burrowers (w1). (B) plot of selective burrowers (w2) that are restricted to move downwards at the same rate as the helical burrowers. (C) plot of selective burrowers (w3) that are free to move up and down in search of food. (D) plot of random burrowers that select paths that can go in any direction (w4) (E) plot of random burrowers (w5) that adhere to the same penetration rate as the helical burrowers.

Figure 7.5A shows the amount of food ingested by each simulated behavioral worm type in a food volume comprising unit food values (*i.e.* all volume cells have food values of 1). The helical burrows (w1) perform slightly better than w2 and w3. Organized strategies outperform random strategies for this food distribution scenario. Figures 7.5B-F show the distribution of visited volume cells (outlined in white) along a slice of the volume (y = 25). The helical burrow distribution (Figure 7.5B) resembles McMurray Formation helical burrow expressions from core. Figure 7.5C demonstrates that w2 employed a shingling technique in order to maximize ingested food, whereas Figure 7.5D shows that w3 did not attempt to penetrate very deeply within the volume and chose to compete for food resources near the top of the model. figures 7.5E-7.5F show random worm paths (there does not appear to be a significant difference between the distribution of w4 and w5 from this cross-section). Figure 7.5G shows the quantity of food consumed by each simulated worm behavior within a food volume populated by random values from a Gaussian distribution with a mean value of 0.5. The adaptive burrowing strategies (w2 and w3) perform best. The helical burrows (w1) perform slightly better than the random burrows (w4 and w5). Figure 7.5H-L shows a cross-section along slice y = 9. Figure 7.5I contrasts with Figure 7.5C, whereby w2 optimizes resource consumption by moving arbitrarily within the food matrix. Similarly, Figure 7.5J contrasts with Figure 7.5D since w3 penetrates deeper within the Gaussian-distributed food model compared to the unit food distribution model.

Figure 7.6A-F shows results from a simulation where food values are distributed along a gradient of increasing values. Figure 7.6A shows the amount of food ingested by each simulated behavioral worm type. The helical burrows (w1) perform slightly better than w2. These two strategies outperform the other three strategies. The random burrow that has a constant penetration rate (w5) performs slightly better than w3 and w4. Figures 7.6B-F show cross-sections of volume slice y = 9. Figure 7.6C and 7.6D show that the adaptive burrows (w3) and the random burrow (w4) do not penetrate the volume deeply to take advantage of the downward increasing food value gradient. The

Figure 7.5: Cumulative food resources acquired versus worm count for the helical burrowers (w1) (red line), selective burrowers with constant penetration rate (w2) (green line–hidden by red line in this plot), selective burrowers with no spatial restriction (w3) (blue line), random burrowers with no spatial restriction (w4) and random burrowers with constant penetration rate (w5) in: (A) a unit-populated food volume; (G) a random gaussian (0.5 mean) populated food volume. (B-F) show volume slices along y = 25. White boxes correspond to cells that were visited by (B) w1; (C) w2; (D) w3; (E) w4; (F) w5. (H-L) show volume slices along y = 9. White boxes correspond to cells that were visited by (H) w1; (I) w2; (J) w3; (K) w4; (L) w5.

helical burrows (w1) (Figure 7.6B), w2 (Figure 7.6C), and w5 (Figure 7.6F) subtend deeper into the model, which explains why cumulative food values are relatively high. Figures 7.6G-L show simulation results where food values are distributed along a decreasing food value gradient. From Figure 7.6G, w3 significantly outperforms all other behaviors. This is because w3 stays nears the top of the model where food values are highest. In contrast, random burrowing (w4) performs better than w1, w2, and w5 as these burrows are forced to descend along the decreasing food value gradient (figures 7.6H-I, 7.6L) while w4 remains in the optimal food zone for the most part (Figure 7.6K).

Figure 7.7A-L shows simulation results for a periodically layered food value model. Food rich layers are assigned random values between 0.8 and 1.0, whereas food poor layers are assigned random values between 0.0 and 0.2. The layers in figures 7.7A-F are 3 z units thick, whereas layers in figures 7.7G-L are 5 z units thick. The thickness of layers significantly affects the smart burrower (w3), whereas the helical burrows are relatively unaffected. This is because the thicker poor resource layer distracted approximately 50% of w3 worms from penetrating to richer layers.

Simulation results for a two layer system, where the top, relatively thinner, layer is food rich and the bottom layer is food poor are shown in figures 7.8A-F. In this simulation, the helical burrows perform worse than the random burrow (w4) and performs similarly to the random burrow with constant penetration (w5). The smart burrower (w3) that is not restricted to move downwards performs much better compared to all other strategies. Simulation results for a two layer system where the thinner top layer is relatively food poor and the bottom layer is relatively food rich are shown in figures 7.8G-L. The smart burrower (w3) is confused by the top layer and rarely penetrates into the deeper food rich layer. This is the same phenomenon shown in Figure 7.7A.

Figure 7.9A-F shows simulation results for food clusters (n clusters = 10, cluster size = 12x12x12, cluster food values = 1) randomly placed within a 0.5 mean Gaussian randomly distributed food volume with values 0 to 1. Simulation results are similar to the Gaussian randomly distributed food volume simulation results (Figure 7.5G-L); however, there are significant consumed
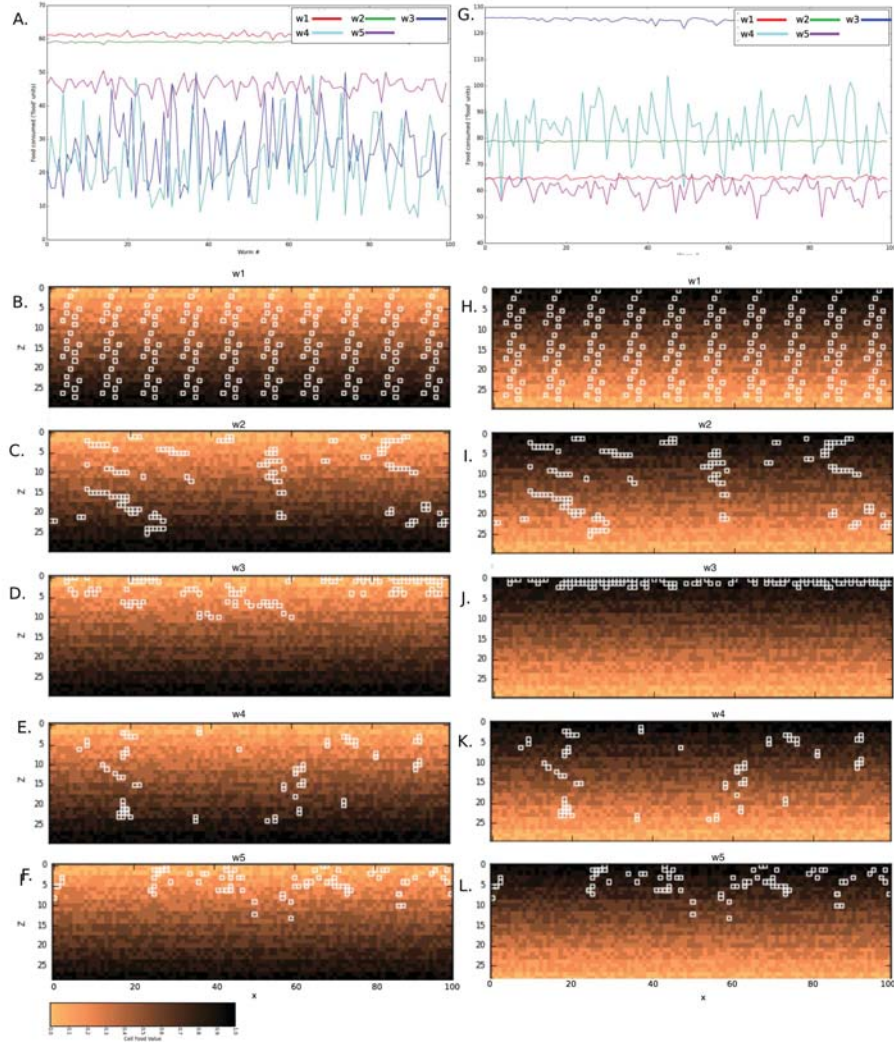
Figure 7.6: Cumulative food resources acquired versus worm count for the helical burrowers (w1) (red line), selective burrowers with constant penetration rate (w2) (green line–hidden by red line in this plot), selective burrowers with no spatial restriction (w3) (blue line), random burrowers with no spatial restriction (w4) and random burrowers with constant penetration rate (w5) in: (A) a unit-populated food volume; (G) a random gaussian (0.5 mean) populated food volume. (B-F) show volume slices along y = 25. White boxes correspond to cells that were visited by (B) w1; (C) w2; (D) w3; (E) w4; (F) w5. (H-L) show volume slices along y = 9. White boxes correspond to cells that were visited by (H) w1; (I) w2; (J) w3; (K) w4; (L) w5.

Figure 7.7: Cumulative food resources acquired versus worm count for the helical burrowers (w1) (red line), selective burrowers with constant penetration rate (w2) (green line–hidden by red line in this plot), selective burrowers with no spatial restriction (w3) (blue line), random burrowers with no spatial restriction (w4) and random burrowers with constant penetration rate (w5) in: (A) a volume distributed with food following an increasing downwards gradient; (G) a volume distributed with food following a decreasing downwards gradient (0.5 mean) populated food volume. (B-F) show volume slices along $y = 9$. White boxes correspond to cells that were visited by (B) w1; (C) w2; (D) w3; (E) w4; (F) w5. (H-L) show volume slices along $y = 9$. White boxes correspond to cells that were visited by (H) w1; (I) w2; (J) w3; (K) w4; (L) w5.
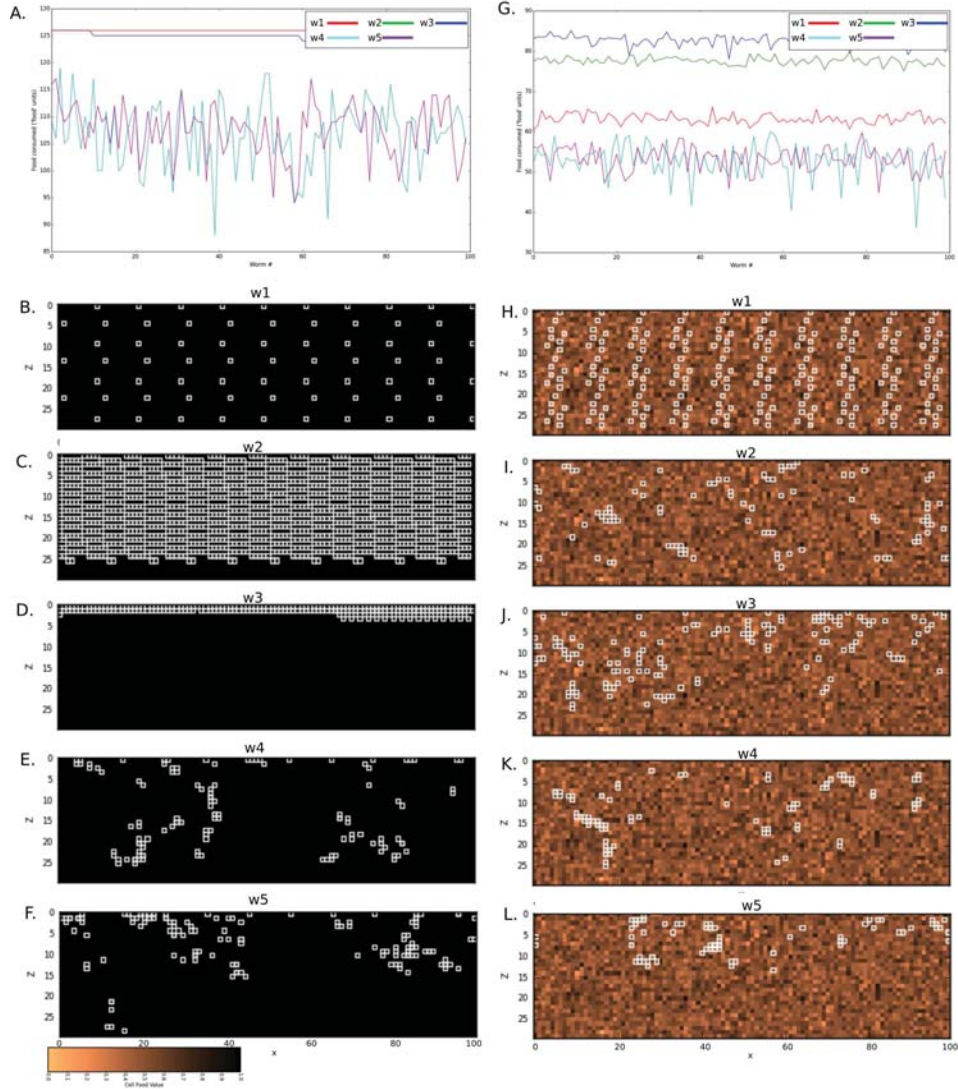
160
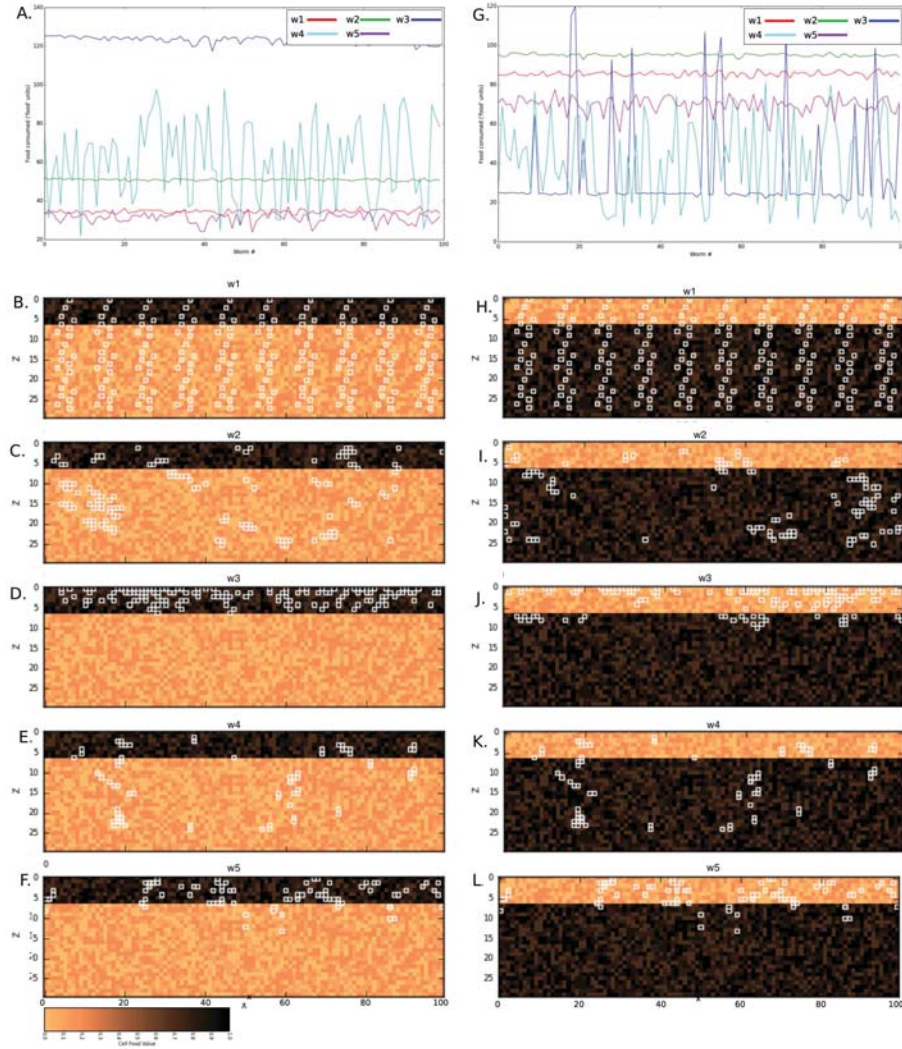
Figure 7.8: Cumulative food resources acquired versus worm count for the helical burrowers (w1) (red line), selective burrowers with constant penetration rate (w2) (green line–hidden by red line in this plot), selective burrowers with no spatial restriction (w3) (blue line), random burrowers with no spatial restriction (w4) and random burrowers with constant penetration rate (w5) in: (A) a 2 layer volume comprising a thinner rich food layer at the top (values between 0.8 and 1.0) and a thicker poor food layer at the base (values between 0 and 0.2); (G) a 2 layer volume comprising a thinner poor food layer at the top (values between 0 and 0.2) and a thicker rich food layer at the base (values between 0.8 and 1.0). (B-F) show volume slices along y = 9. White boxes correspond to cells that were visited by (B) w1; (C) w2; (D) w3; (E) w4; (F) w5. (H-L) show volume slices along y = 9. White boxes correspond to cells that were visited by (H) w1; (I) w2; (J) w3; (K) w4; (L) w5.

161

food peaks, especially for smart worms (w2 and w3) that occurred whenever these worms intersected a rich food interval. These worms did not consume food from entire discovered clusters (Figure 7.9C-D). This is likely because the worms have no "memory" of where the clusters are, and could move out of the cluster following randomly distributed food values of 1, without knowing how to return to the food clusters.
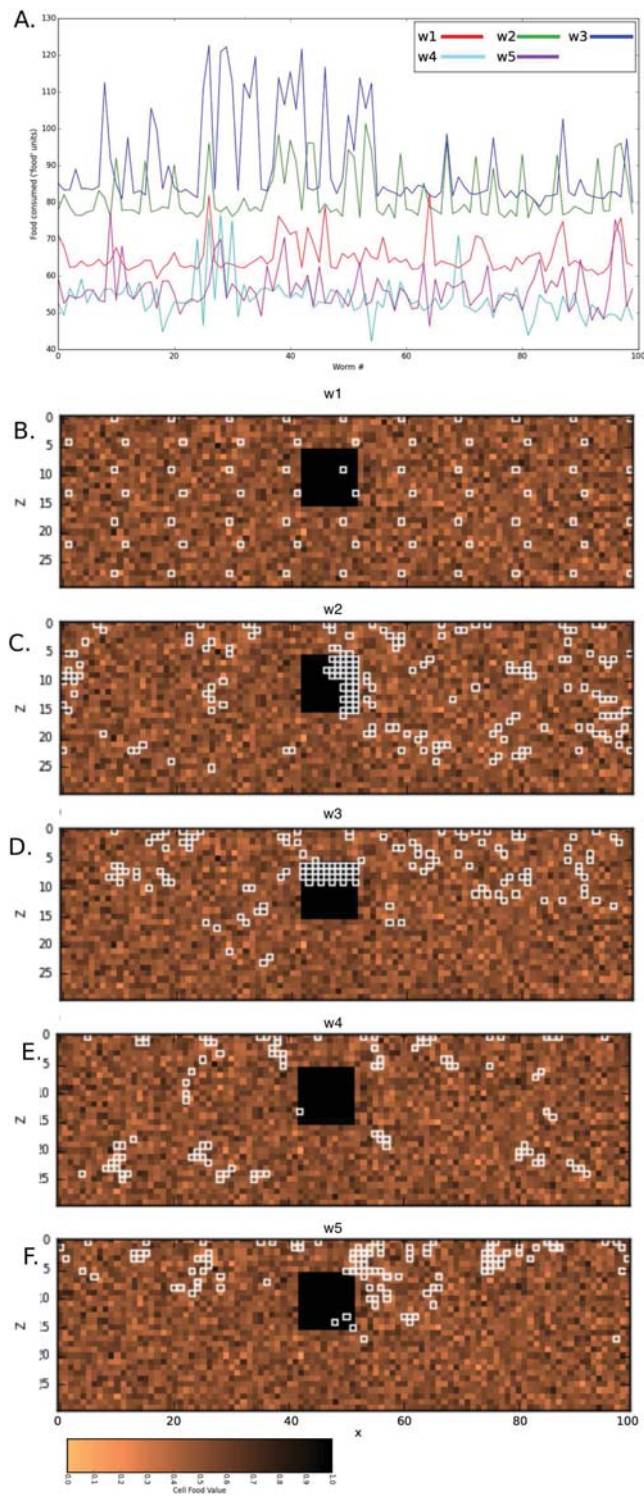
Figure 7.9: (Continued on the following page.)

Figure 7.9: Cumulative food resources acquired versus worm count for the helical burrowers (w1) (red line), selective burrowers with constant penetration rate (w2) (green line–hidden by red line in this plot), selective burrowers with no spatial restriction (w3) (blue line), random burrowers with no spatial restriction (w4) and random burrowers with constant penetration rate (w5) in: (A) a gaussian (mean=0.5) randomly distributed food volume containing 10 randomly placed 12x12x12 clusters of food value 1. (B-F) show volume slices along y = 15. White boxes correspond to cells that were visited by (B) w1; (C) w2; (D) w3; (E) w4; (F) w5.

7.5 Discussion

7.5.1 Significance of simulations

Hammer (1998) stated that he was extremely cautious about interpreting results from ichnological simulations, especially if the goal of the simulation was to create morphologies similar to existing trace fossils based on a set of rules. Therefore, our simulation results should be viewed as a proof that relatively complex 3D trace morphologies can be generated by simple rules (expanding on Raup and Seilacher 1969) rather than an assertion that helical burrows are generated by organisms adhering to phobotaxis rules solely. For example, many *Gyrolithes* burrows are generated by crustaceans (Dwo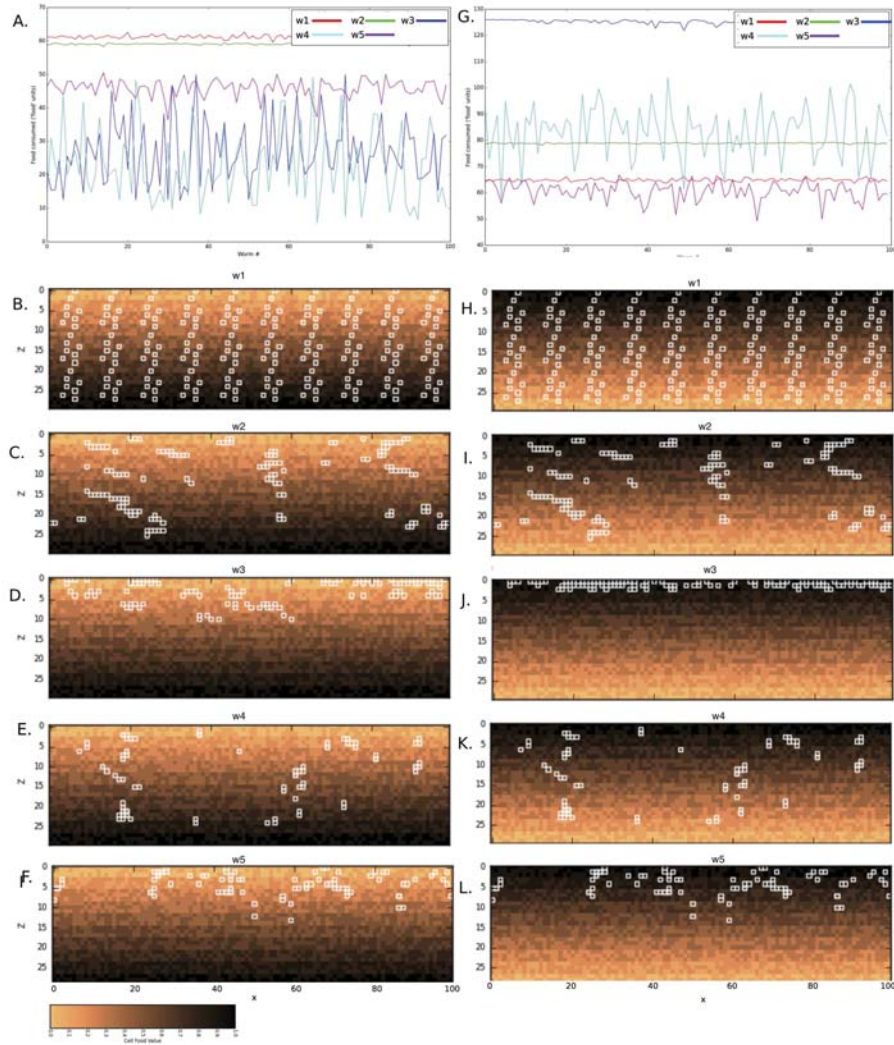rschak and Rodrigues 1997) in environments that do not show evidence for space competition as intense as that demonstrated by McMurray Formation helical burrows (Figure 7.1A). However, in environments where population pressure is significant, phobotaxis may explain why worms generate micro-helical coils. This is supported by our phobotaxis simulation (Figure 7.2).

The helical burrowing strategy performed with varying success depending on the food distribution landscape. For example, in the unit food volume, helical burrowing performed on par with the selective worm that abides to a constant penetration rate (Figure 7.5A). The helical burrowing technique outperformed other burrowing techniques in the increasing downward food-value volume (Figure 7.6A). For all other simulation iterations, food-detection techniques outperformed the helical burrowing strategy. In the reverse gradient scenario, where food values increase upwards, the helical burrowing strategy performed significantly worse compared to the food-detection strategy (Figure 7.6G).

These simulations support several conclusions: (1) micro-helical burrowing strategy is an effective deposit-feeding behavior in densely populated, relatively homogeneous food distribution landscapes; (2) micro-helical burrowing strategies are effective in substrates where organized self-avoidance, or avoidance of other burrowers presents a greater reward than optimized food location and consumption, which is ineffective in homogeneous food volumes; (3)

micro-helical burrowing strategy performs poorly as a deposit feeding strategy in densely populated intervals where food is distributed in clusters, thin layers, or heterogeneously; (4) strategies implemented with a constant downward penetration rate generally perform similarly or better than strategies where depth steps are unregulated.

7.5.2   Limitations of simulations

The simulations of 3D volume intra-species food competition (figures 7.6-7.9) have several limitations. For example, we did not implement a rule so that worms could not occupy the same physical space within the volume. This is not an issue for cylindrical burrows as burrow trajectories are calculated explicitly so that a buffer of 1.5 cells or more is present between any cylindrical burrow. This is a relatively limited issue for the smart worms. Considering that once a cell is occupied it is assigned a value of 0, following the approach proposed by Plotnick and Koy (2005), implying that that cell is unlikely to be visited again since the smart worms chooses paths based on selecting maximum food value cells. Random burrowing behaviors are potentially affected by simulated worms occupying the same space within the volume. There is no control restricting a worm from revisiting a previously visited cell. We did not emplace a control for this as we did not want to restrict the randomness of those behaviors. Indeed, such a control is essentially a phobotaxis rule. The purpose of the random burrowing simulations is to demonstrate that organized burrowing behaviors, are generally superior compared to random burrowing behaviors for deposit feeding purposes. Our simulation results demonstrate this.

Another limitation of this simulation is that all simulated worms begin burrowing from equally spaced coordinates. This simplification is necessary in order to directly compare helical burrowing efficacy to other burrowing behaviors. Helical burrows have to originate approximately equidistantly from each other in dense population to represent an efficient burrowing technique.

Helical worms were modelled after helical curves rather than explicitly programmed decision processes. This simplification assumes that the worms

166

generating these burrows have an innate instinct to form coils of a given diameter and descend at a specific rate based on how much room is available for burrowing. However, it is not likely that worms possess such mathematical ability. High population density helical burrow formation is likely a response to phobotaxis and genetic proclivity for coiling as shown in our first simulation (Figure 7.3).

Simulated food detecting worms were easily confused in layered or gradient-type food distribution scenarios. These worms can only sense food values of cells that share vertices with the cell they occupy for any given simulation step. This type of food detection is referred to as contact chemoreception (*e.g.* Koy and Plotnick 2007). However, worms can likely sense food by distance chemoreception, whereby food is sensed without direct contact (*e.g.* Plotnick and Koy 2005). Distance chemoreception can be modelled via a number of distance-weighted functions (*e.g.* inverse distance squared). Depending on the modelled capacity of distance chemoreception the simulated smart worms in our model could potentially avoid confusion in some of the scenarios.

7.5.3 Other functional hypotheses: anchoring mechanism

Helical piles are often used by engineers in the design of stable structures anchored in soil (*e.g.* Byrne and Houlsby 2015). The number of plates, the diameter of helical plates, and the vertical separation between plates dictate the uplift resistance of a helical pile (Merifield 2010). Ghaly *et al.* (1991) empirically demonstrated that the there is a direct correlation between the depth of the uppermost helical plate and the pull out force required to remove the helical pile. The number of plates in a helical pile is analogous to the number of coils in a helical burrow (*i.e.* the greater number of coils in a helical burrow, the greater uplift resistance capacity). In sandy substrates, assuming constant substrate physical parameters, pullout is positively related to coil diameter (D), coil spacing (S) and the number of coils (n). Based on this relation, it is advantageous for helical burrowers to generate larger coil diameters, larger coil spacings, or a larger number of coils in order to increase pullout

resistance. From (Lettley 2004, Figure 3.7D) a typical McMurray Formation helical burrow diameter (D) is 3 mm with coil spacing (S) is 2 mm and (n) is > 20.

Helical piles have greater lateral stability than tubular/vertical piles (*i.e.* they have a greater resistance to shear), and they are more difficult to uplift or "pullout" from various substrates (*e.g.* Ghaly *et al.* 1991; Prasad and Rao, 1994). Tubular piles are analogous to Skolithos burrows for example. Prasad and Rao (1996) found that helical piles have 1.2 to 1.5 times the pullout resistance of tubular piles. Helical burrows therefore likely present an advantage compared to vertical burrows for resisting predation-related pullout.

7.5.4 Other functional hypotheses: pumping mechanism

Although the flushing action in helical burrows is not yet documented; it is likely an important life process. Darker regions around burrows, which represent biogeochemically altered sediment caused by flushed water, comprise evidence for burrow irrigation in helical burrows. Since no bio-irrigation measurements exist for helical burrows, we use the fluid mechanic characteristics of helical glass pipes to infer the flow characteristics of these burrows.

Characterizing flow in glass tubes is simpler than in burrows since substrate and lining permeability, burrow-wall roughness, and changes in burrow diameter are not taken into account in analytical or numerical solutions. For example, Kristensen (1983) demonstrated that nereid polychaetes can pump water significantly more effectively in glass tubes compared to their natural burrows. And, the pumping action of the worm (see Vogel 2007 for a comprehensive review of biological pumping mechanisms) is likely more sporadic and variable than the steady laminar flow which glass tube experiments often employ. Lastly, empirical measurements of flow in helical tubes versus straight pipes use pipes that have separate outlets and inlets, whereas burrows employ a single outlet/inlet, which further complicates glass pipe analogues compared to burrow fluid flow.

The pressure (P) required to move a fluid against gravity at a head difference Δh of is P = $\rho g \Delta h$, where ρ (fluid density) g (gravitational constant)

are constant. For vertical burrows, Δh is equal to the burrow length (L). For helical burrows Δh is equal to C x L, where C is a constant (C < 1) related to coiling diameter, coiling pitch, and coil tightness. Considering that Δh is therefore always less for helical burrows of length equal to vertical burrow length, less energy is expended by helical burrowing organisms compared to vertical burrowing organisms for burrow irrigation.

However, particular advantages related to helical burrows can be considered what Gould and Lewontin (1979) referred to as "spandrels": byproducts of evolution that are not necessarily the product of adaptive selection. Considering that helical burrows found in the McMurray Formation are likely a high density population response for maximizing deposit feeding efficacy in largely homogeneous food landscapes, increased pullout resistance or increased pumping efficacy are likely byproducts of evolution rather than a response to evolutionary behavioral pressures.

7.6   Summary

Helical burrows found in the McMurray Formation can form as a response to phobotaxis (the avoidance of self/others) by worms that have a preference for coiling. Computer simulations support that helical burrowing is an effective deposit feeding behavior in relatively homogeneous food distribution landscapes that are densely populated. Helical burrows are an effective deposit feeding strategy if adhering to phobotaxis presents a greater reward than optimized food location and consumption. Optimized food location and consumption is not effective in homogeneous food distribution landscapes. The helical burrowing strategy is ineffective for deposit feeding if food is distributed in clusters, thin layers, or heterogeneously. And, overall, trace making strategies that implement a constant penetration rate performed similarly or better than strategies where penetration rates are unregulated.

Using engineered piles as an analogue, helical burrows perform better than vertical burrows for anchoring purposes (1.2 to 1.5 times increased pullout resistance). Helical burrowing therefore likely presents an advantage for resisting

predation-related burrow pullout. Overall, helical burrows are relatively easier to irrigate than vertical burrows of equal burrow length. However, these advantages are likely evolutionary spandrels and are therefore the byproducts of a population of worms' response to high population density or other ecological parameters.

Chapter 8

Conclusion

Process ichnology is an emerging tool for supporting depositional interpretations from the rock record. Process ichnology is a paradigm whereby trace fossils are interpreted as proxies for physical and chemical changes in paleo-depositional systems. One of the advantages of this method is that several process ichnology proxies, such as bioturbation index and size-diversity index, are semi-quantitative variables that can be analyzed statistically. The larger portion of the work contained in this volume applied process ichnology-based interpretations to the McMurray Formation and developed techniques that make the process ichnology methodology easier to apply.

Chapter 2 examined tidally modulated laminae from 5 inclined heterolithic stratification (IHS) lithosomes using a process sedimentology approach. This study revealed that tidal dominated deposition controlled portions of each of the studied lithosomes for periods of up to 3 continuous months. Thus, solid evidence for tidal influence on inclined heterolithic stratification in the McMurray Formation was gathered. This data is supported by the presence of a trace fossil assemblage typical of brackish water deposition. Interestingly, bioturbated intervals that were measured for periodic laminae thickness signals still contained tidal signatures. This study therefore generated a research avenue for completely combining process ichnology and process sedimentology by examining the effects of bioturbation on tidal rhythmites.

As multiple studies have shown (*e.g.* Ranger and Pemberton 1988; Crerar and Arnott 2007; Musial *et al.* 2012), ichnological data are an excellent tool

for supporting paleoenvironmental interpretations. Considering this, modeling ichnological datasets temporally and spatially can provide supporting insight into the frequency and magnitude of the variability of physical and chemical conditions in a depositional environment. Chapter 3 employed basic geostatistics to generate a 3D model of bioturbation index and size-diversity index, process ichnology proxies for infaunal stress. Coupled with a 3D facies model, these process ichnology geomodels showed the spatial and temporal variability of sedimentation rate and salinity affecting infaunal communities during deposition. The applications of the process ichnology geomodeling technique, specific to the McMurray Formation, are: (1) distinguishing genetically related point-bars, which are expected to preserve predictable process ichnology trends, using core datasets; and (2) mapping process ichnology parameters regionally for understanding regional paleo-salinity distributions and variability for more accurate stratigraphic and paleoenvironmental reconstructions.

PyCHNO, a specialized ichnology data collection and visualization software application, outlined in Chapter 4, was developed as a response to the difficulties of collecting data for Chapter 3. This software optimizes and standardizes process ichnology data collection. PyCHNO streamlines user collected bioturbation index, size-diversity index, trace fossil abundance from core photographs on a defined bed-by-bed basis. These data can be subsequently output as "process ichnology logs" or as spreadsheets for input into statistical processing software or geomodeling software. Datasets collected with PyCHNO formed the basis of Chapters 5-6.

Chapter 5 demonstrated that fluctuations in physical and chemical paleoecological infaunal stresses, as proxied by a process ichnology dataset, are both spatially and temporally significant in a McMurray Formation study area. Time-series techniques that had not previously been applied to ichnological datasets, including Continuous Wavelet Transforms (used for determining temporal process ichnology trends) and Dynamic Time Warping (used for determining spatial process ichnology trends) were applied on a K-means clustered dataset. The K-means clusters corresponded to ranked, interpreted, relative infaunal stress values. This analysis proved to be useful for observ-

ing spatial and temporal trends in ichnological cyclicity. Spatially, observed ichnological variability and cyclicity were linked to both estuary-scale and more local (bar-form scale) infaunal stress. Estuary-scale stress was preserved and demonstrated by cyclical patterns, interpreted to be linked to ENSO cycles. Localized, bar-form, scale stresses were interpreted to interfere with estuary-scale infaunal stress signals. However, the precise delineation of localized stresses was not possible without seismic data.

To observe point-bar scale spatial and temporal ichnological variability, Chapter 6 analyzed a process ichnology datasets within a seismically-defined geobody. Ichnonetwork analysis, using Bray-Curtis indices as link weights determined that *Cylindrichnus* and *Planolites* are typically 32 to 49% similar in abundance on a bed-by-bed basis and that *Arenicolites* and *Skolithos* typically have 15 to 32% similar abundance on a bed-by-bed scale. The weight of ichnogenera links remained similar throughout analyzed 5 m slice intervals through the point-bar, which suggests that relatively stable temporal ecological conditions existed during the formation of the point-bar. Time-series analysis of the process ichnology dataset, using depth-converted Continuous Wavelet Transforms did not yield definitive spatial or temporal periodic signals, which further suggests that relatively stable temporal and spatial ecological conditions existed during the deposition of the studied point-bar. A look at other seismically constrained point-bars will offer further insight on localized, genetically related spatial and temporal ichnological variability.

One of the limitations of the process ichnology approach is that the specific physical and chemical stresses impacting infaunal communities are generally difficult to interpret and support. Chapter 7 used a process ichnological approach in order to examine why helical burrows are locally found in dense, monogeneric assemblages in the McMurray Formation. To examine this problem within a framework of infaunal population stress, several computer simulations were generated. Simulations demonstrated that helical burrowing is an effective deposit feeding strategy for infaunal organisms adhering to phobotaxis (the avoidance of self/others) in 3D. The helical burrowing strategy is ineffective for deposit feeding if food is distributed in clusters, thin layers, or

heterogeneously compared to feeding strategies where organisms detect, and move to optimal food locations within a 3D volume. Also, helical burrowing performs better than vertical burrowing for anchoring purposes (1.2 to 1.5 times increased pullout resistance). As well, helical burrows are relatively easier to irrigate than vertical burrows or equivalent length. This research opens the door for future research on simulating other trace making behaviors as responses to infaunal stresses. This research will serve as supporting evidence for interpreting infaunal stresses with a process ichnology approach.

The above listed work provides thorough support for brackish water paleoenvironmental conditions coincident with McMurray Formation IHS deposition. This is based on the analysis of marine-based trace making behaviors preserved in IHS and on evidence for tidally modulated deposition. Although tides are not in of themselves evidence for brackish-water deposition, tidal currents are requisite for marine-based larval recruitment. Upon maturing, these organisms are responsible for generating most of the trace fossils observed in McMurray Formation IHS. The statistical methods employed in this thesis were used to quantify the change in trace fossils characteristics (proxies for environmental change) temporally and spatially within the McMurray Formation IHS depositional systems. These analyses suggest that although trace fossil characteristics can be highly variable from bed to bed, background infaunal stress (related to brackish water conditions) persists. It is interesting to note that similar trace fossils are found in IHS from areas separated by approximately 200 km along the interpreted paleo-estuarine axis of the McMurray Formation. This suggests that brackish-water penetrated deeply within the confines of the McMurray Formation estuary depositional system and influenced IHS deposition.

This thesis proposes and implements many novel techniques for ichnological analysis. However, all of the case studies employing these techniques for this work are based on datasets comprising limited aerial and stratigraphic extent, relatively restricted depositional environment variability, and sparse data. Further research is required to test these techniques on larger and more diverse datasets. For example, a regional study of process ichnological param-

174

eters of the McMurray Formation may yield significant clues on the variability of paleoecological conditions during deposition, which may be vital for understanding the regional stratigraphy of the McMurray Formation. Big data has influenced many scientific disciplines. Perhaps ichnologists and sedimentologists will embrace large, quantitative trace fossil datasets in the near future.

References

Albanese, D., R. Visintainer, S. Merler, S. Riccadonna, G. Jurman, and C. Furlanello (2012). "mlpy: Machine learning Python:" preprint (cit. on p. 98).

Allen, G. P., J. C. Salomon, P. Bassoullet, Y. Du Penhoat, and C. De Grandpre (1980). "Effects of tides on mixing and suspended sediment transport in macrotidal estuaries." In: *Sedimentary Geology* 26, pp. 69–90 (cit. on p. 140).

Allen, G. P. (1991). "Sedimentary processes and facies in the Gironde estuary: a Recent model of macrotidal estuarine systems." In: *Clastic Tidal Sedimentology*. Ed. by D. Smith, G. E. Reinson, B. A. Zaitlin, and R. A. Rahmani. Canadian Society of Petroleum Geologists Memoir, v. 16, pp. 29–40 (cit. on p. 89).

Baucon, A. and F. Felletti (2013). "The IchnoGIS method: network science and geostatistics in ichnology, theory and application (Grado lagoon, Italy)." In: *Palaeogeography, Palaeoclimatology, Palaeoecology* 375, pp. 83–111 (cit. on pp. 5, 96, 117, 122).

Baucon, A., A. Ronchi, F. Felletti, and C. N. De Carvalho (2014). "Evolution of crustaceans at the edge of the end-Permian crisis: ichnonetwork analysis of the fluvial succession of Nurra (Permian–Triassic, Sardinia, Italy)." In: *Palaeogeography, Palaeoclimatology, Palaeoecology* 410, pp. 74–103 (cit. on pp. 88, 96).

Bechtel, D. J. (1996). "The stratigraphic succession and paleoenvironmental interpretation of the McMurray Formation, OSLO area, northeastern Alberta." 153 pp. MA thesis. University of Alberta (cit. on p. 143).

Bell, J. B., D. O. Jones, and C. H. Alt (2013). "Lebensspuren of the Bathyal Mid-Atlantic Ridge." In: *Deep Sea Research Part II: Topical Studies in Oceanography* 98, pp. 341–351 (cit. on p. 96).

Beynon, B. M. and S. G. Pemberton (1992). "Ichnological signature of a brackish water deposit: an example from the Lower Cretaceous Grand Rapids Formation, Cold Lake Oil Sands area, Alberta." In: *Applications of Ichnology to petroleum exploration*. Ed. by S. G. Pemberton. Society of Sedimentary Geologists, pp. 199–221 (cit. on p. 144).

Beynon, B.M., S.G. Pemberton, D.A. Bell, and C.A. Logan (1988). "Environmental implications of ichnofossils from the Lower Cretaceous Grand Rapids Formation, Cold Lake Oil Sands Deposit." In: *Sequences, Stratigraphy, Sedimentology: Surface and Subsurface*. Ed. by James. D.P. and

D.A. Leckie. Canadian Society of Petroleum Geologists, Memoir, pp. 275–290 (cit. on p. 59).

Bjerstedt, T. W. (1988). "Trace fossils from the Early Mississippian Price delta, southeast West Virginia." In: *Journal of Paleontology* 62, pp. 506–519 (cit. on p. 96).

Botterill, S. E., S. G. Campbell, S. G. Pemberton, M. K. Gingras, and S. Hubbard (2015). "Process ichnological analysis of the Lower Cretaceous Bluesky Formation, Alberta." In: *Bulletin of Canadian Petroleum Geology* 63, pp. 123–142 (cit. on pp. 89, 95, 116, 137).

Bray, J. R. and J. T. Curtis (1957). "An ordination of the upland forest communities of southern Wisconsin." In: *Ecological monographs* 27, pp. 325–349 (cit. on p. 121).

Bromley, R. G. and A. A. Ekdale (1984). "Chondrites: a trace fossil indicator of anoxia in sediments." In: *Science* 224, pp. 872–874 (cit. on pp. 36–37).

Bromley, R. G. (1996). *Trace Fossils: Biology, Taphonomy and Applications.* second edition. 361 p. London, Chapman and Hall (cit. on p. 36).

Broughton, P. L. (2013). "Devonian salt dissolution-collapse breccias flooring the Cretaceous Athabasca oil sands deposit and development of lower McMurray Formation sinkholes, northern Alberta Basin, Western Canada." In: *Sedimentary Geology* 283, pp. 57–82 (cit. on pp. 6, 9, 38, 90).

— (2014). "Syndepositional architecture of the northern Athabasca oil sands deposit, northeastern Alberta." In: *Canadian Journal of Earth Sciences* 52, pp. 21–50 (cit. on pp. 38, 90).

— (2015). "Collapse-induced fluidization structures in the lower Cretaceous Athabasca oil sands deposit, Western Canada." In: *Basin Research.* DOI: `10.1111/bre.12120` (cit. on pp. 38, 90).

— (2016). "Alignment of fluvio-tidal point bars in the middle McMurray Formation: implications for structural architecture of the Lower Cretaceous Athabasca Oil Sands Deposit, northern Alberta." In: *Canadian Journal of Earth Sciences* 53.9, pp. 896–930 (cit. on p. 1).

Buatois, L. A., M. G. Mangano, C. G. Maples, and Lanier W.P. (1997). "The paradox of nonmarine ichnofaunas in tidal rhythmites: integrating sedimentologic and ichnologic data from the Late Carboniferous of eastern Kansas, USA." In: *Palaios* 12, p. 467. DOI: `10.2307/3515384` (cit. on p. 89).

Buatois, L. A. and M. Mangano (2002). "Trace fossils from Carboniferous floodplain deposits in western Argentina: implications for ichnofacies models of continental environments." In: *Palaeogeography, Palaeoclimatology, Palaeoecology* 183, pp. 71–86. DOI: `10.1016/s0031-0182(01)00459-x` (cit. on p. 88).

Buatois, L. A., M. Gingras, J. A. MacEachern, M. G. Mangano, J. P. Zonneveld, S. G. Pemberton, R. G. Netto, and A. Martin (2005). "Colonization of brackish-water systems through time: evidence from the trace-fossil record." In: *Palaios* 20, pp. 321–347 (cit. on pp. 59, 88, 116).

Buatois, L. A., Santiago N., K. Parra, and R. Steel (2008). "Animal-substrate interactions in an early Miocene wave-dominated tropical delta: delineating

environmental stresses and depositional dynamics (Tacata Field, Eastern Venezuela)." In: *Journal of Sedimentary Research* 78, pp. 458–479. DOI: `10.2110/jsr.2008.053` (cit. on p. 88).

Byrne, B. W. and G. T. Houlsby (2015). "Helical piles: an innovative foundation design option for offshore wind turbines." In: *Philosophical transactions. Series A, Mathematical, physical, and engineering sciences* 373.2035 (cit. on p. 167).

Byrne, J. M. and A. A. Berg (1998). "Spatial analysis of temperature and precipitation anomalies on the Canadian prairies during two strong El Niño events." In: *Canadian Water Resources Journal* 23, pp. 231–243 (cit. on p. 114).

Carmona, N. B., L. A. Buatois, J. J. Ponce, and M. G. Mangano (2009). "Ichnology and sedimentology of a tide-influenced delta. lower Miocene Chenque Formation, Patagonia, Argentina: trace-fossil distribution and response to environmental stresses." In: *Palaeogeography, Palaeoclimatology, Palaeoecology* 273, pp. 75–86 (cit. on p. 88).

Carrigy, M. A. (1959). "Geology of the McMurray Formation part III, general geology of the McMurray area." In: *Alberta Research Council, Memoir* 1, p. 130 (cit. on pp. 60, 90).

Chadimova, L., F. Vacek, K. Sobien, L. Slavik, and J. Hladil (2015). "Petrophysical record of the late Silurian shallow-water carbonate facies across the Lau Event (Prague Synform Czech Republic) and dynamic time warping alignment of the magnetic susceptibility logs." In: *Geological Society, London, Special Publications* 414, pp. 133–155 (cit. on p. 98).

Chiew, F. H. and T. A. McMahon (2002). "Global ENSO-streamflow teleconnection streamflow forecasting and interannual variability." In: *Hydrological Sciences Journal* 47, pp. 505–522 (cit. on p. 114).

Choi, J., F. Francois-Carcaillet, and B. P. Boudreau (2002). "Lattice-automaton bioturbation simulator (LABS): implementation for small deposit feeders." In: *Computers and Geosciences* 28.2, pp. 213–222 (cit. on p. 145).

Choi, K. S., R. W. Dalrymple, S. S. Chun, and S. P. Kim (2004). "Sedimentology of modern, inclined heterolithic stratification (IHS) in the macrotidal Han River delta, Korea." In: *Journal of Sedimentary Research* 74.5, pp. 677–689 (cit. on p. 7).

Crerar, E. and R. W. C. Arnott (2007). "Facies distribution and stratigraphic architecture of the lower Cretaceous McMurray Formation, Lewis property, northeastern Alberta." In: *Bulletin of Canadian Petroleum Geology* 55, pp. 99–124 (cit. on pp. 1, 60, 62, 90–91, 117, 119, 143, 171).

Dafoe, L. T., M. K. Gingras, and S. G. Pemberton (2008). "Determining Euzonus mucronata burrowing rates with application to ancient Macaronichnus segregatis trace-makers." In: *Ichnos* 15, pp. 78–90 (cit. on pp. 89, 140).

Dalrymple, R. W., Zaitlin B. A., and R. Boyd (1992). "Estuarine facies models; conceptual basis and stratigraphic implications." In: *Journal of Sedimentary Research* 62, pp. 1130–1146. DOI: `10.1306/d4267a69-2b26-11d7-8648000102c1865d` (cit. on p. 89).

Dalrymple, R. W., D. A. Mackay, A. A. Ichaso, and K. S. Choi (2012). "Processes, morphodynamics, and facies of tide-dominated estuaries." In: *Principles of Tidal Sedimentology.* Ed. by R. A. Davis and R. W Dalrymple. Netherlands, Dordrecht: Springer, pp. 79–107 (cit. on p. 111).

Davies, A., A. E. Kemp, and H. Pälike (2011). "Tropical ocean-atmosphere controls on inter-annual climate variability in the Cretaceous Arctic." In: *Geophysical Research Letters* 38. DOI: 10.1029/2010GL046151 (cit. on pp. 113–114).

Davies, A., A. E. Kemp, G. P. Weedon, and J. A. Barron (2012). "El Nino–southern oscillation variability from the late Cretaceous Marca shale of California." In: *Geology* 40, pp. 15–18 (cit. on pp. 99, 113–114).

Davies, N. S., I. J. Sansom, and P. Turner (2006). "Trace fossils and paleoenvironments of a late Silurian marginal-marine/alluvial system: the Ringerike Group (lower Old Red Sandstone), Oslo region, Norway." In: *Palaios* 21, pp. 46–62 (cit. on p. 96).

Deutsch, C. V. and A. G. Journel (1998). *GSLIB: Geostatistical Software Library and User's Guide.* 2nd ed. New York: Oxford University Press (cit. on pp. 41, 44).

Deutsch, C. V. (2002). *Geostatistical Reservoir Modeling.* Applied Geostatistics Series. New York: Oxford University Press (cit. on p. 41).

Dorador, J., F. J. Rodríguez-Tovar, and I.O.D.P. expedition (2014). "Quantitative estimation of bioturbation based on digital image analysis." In: *Marine Geology* 349, pp. 55–60 (cit. on pp. 65, 141).

Draganits, E., S. J. Braddy, and D. E. Briggs (2001). "A Gondwanan coastal arthropod ichnofauna from the Muth Formation (Lower Devonian Northern India): paleoenvironment and tracemaker behavior." In: *Palaios* 16, pp. 126–147 (cit. on p. 96).

Dworschak, P. C. and S. D. A. Rodrigues (1997). "A modern analogue for the trace fossil Gyrolithes: burrows of the thalassinidean shrimp Axianassa australis." In: *Lethaia* 30.1, pp. 41–52 (cit. on pp. 143–144, 165).

Felder, D. L. (2001). "Diversity and ecological significance of deep- burrowing macrocrustaceans in coastal tropical waters of the Americas (Decapoda: Thalassinidea)." In: *Interciencia* 26.10, pp. 440–449 (cit. on p. 144).

Fustic, M. (2007). "Stratigraphic dip analysis–A novel application for detailed geological modeling of point bars, and predicting bitumen grade, McMurray Formation, Muskeg River Mine, northeast Alberta." In: *Natural Resources Research* 16.1, pp. 31–43 (cit. on p. 34).

Fustic, M., S. M. Hubbard, R. Spencer, D. G. Smith, D. A. Leckie, B. Bennett, and S. Larter (2012). "Recognition of down-valley translation in tidally influenced meandering fluvial deposits, Athabasca Oil Sands (Cretaceous), Alberta, Canada." In: *Marine and Petroleum Geology* 29, pp. 219–232 (cit. on pp. 7, 91).

Garlick, G. C. and W. C. III Miller (1993). "Simulations of burrowing strategies and the construction of Paleodictyon." In: *Journal of Geological Education* 41, pp. 159–163 (cit. on p. 146).

Ghaly, A., A. Hanna, and M. Hanna (1991). "Uplift behavior of screw anchors in sand I: Dry sand." In: *Journal of Geotechnical Engineering* 117.5, pp. 773–793 (cit. on pp. 167–168).

Gibson, J. R. and R. G. Najjar (2000). "The response of Chesapeake Bay salinity to climate-induced changes in streamflow." In: *Limnology and Oceanography* 45, pp. 1764–1772 (cit. on p. 114).

Gingras, M. K., S. G. Pemberton, T. Saunders, and H. E. Clifton (1999). "The ichnology of modern and Pleistocene brackish-water deposits at Willapa Bay, Washington; variability in estuarine settings." In: *Palaios* 14.4, pp. 352–374 (cit. on pp. 34, 37, 57–58, 88–90, 110, 114, 116).

Gingras, M. K., M. Rasanon, and A. Ranzi (2002). "The significance of bioturbated inclined heterolithic stratification in the southern part of the Miocene Solimoes Formation, Rio Acre, Amazonia Brazil." In: *Palaios* 17.6, pp. 591–601 (cit. on pp. 7, 59, 89–90, 111, 113).

Gingras, M. K. and J. A. MacEachern (2007). "Recognition of brackish-water trace fossil suites in the Cretaceous Western Interior Seaway of Alberta, Canada." In: *Sediment-Organisms Interactions: A Multifaceted Ichnology.* Ed. by R. G. Bromley, L. A. Buatois, G. Mangano, J. F. Genise, and R. N. Melchor. SEPM Special Publication, pp. 50–59 (cit. on p. 88).

Gingras, M. K., S. G. Pemberton, S. Dashtgard, and L. Dafoe (2008). "How fast do marine invertebrates burrow?" In: *Palaeogeography, Palaeoclimatology, Palaeoecology* 270, pp. 280–286 (cit. on pp. 89, 117, 140).

Gingras, M. K., J. A. MacEachern, and S. E. Dashtgard (2011). "Process ichnology and the elucidation of physico-chemical stress." In: *Sedimentary Geology* 237, pp. 115–134 (cit. on pp. 2, 34, 36, 57–58, 61, 64, 67, 89, 116, 136–137).

— (2012). "The potential of trace fossils as tidal indicators in bays and estuaries." In: *Sedimentary Geology* 279, pp. 97–106 (cit. on pp. 34, 111).

Gingras, M. K. and J. A. MacEachern (2012). "Tidal ichnology of shallow-water clastic settings." In: *Principles of Tidal Sedimentology.* Ed. by R. W. Dalrymple and R.A.J. Davis. New York: Springer, pp. 57–77 (cit. on pp. 136–137).

Gingras, M. K., J. A. MacEachern, S. E. Dashtgard, M. J. Ranger, and S. G. Pemberton (2016). "The significance of trace fossils in the McMurray Formation, Alberta, Canada." In: *Bulletin of Canadian Petroleum Geology* 64, pp. 233–250 (cit. on pp. 1, 117).

Goldring, R. (1995). "Organisms and the substrate: response and effect." In: *Marine Palaeoenvironmental Analysis from Fossils.* Ed. by D. W. J. Bosence and A. Allison. Geological Society Special Publication, pp. 151–180 (cit. on pp. 88, 116).

Goldring, R., G. C. Cadee, D'Alessandro A., J. M. D. Gibert, Jenkins. R., and J. E. Pollard (2004). "Climatic control of trace fossil distribution in the marine realm:" in: *Geological Society London, Special Publications* 228, pp. 77–92. DOI: 10.1144/gsl.sp.2004.228.01.05 (cit. on p. 111).

Goovaerts, P. (1997). *Geostatistics for natural resources evaluation.* Oxford university press (cit. on pp. 37, 44).

Gould, S. J. and R. C. Lewontin (1979). "The spandrels of San Marco and the Panglossian paradigm: a critique of the adaptationist programme." In: *Proceedings of the Royal Society of London B: Biological Sciences* 205.1161, pp. 581–598 (cit. on p. 169).

Goupillaud, P., A. Grossmann, and J. Morlet (1984). "Cycle-octave and related transforms in seismic signal analysis." In: *Geoexploration* 23, pp. 85–102 (cit. on pp. 11, 98).

Hammer, O. (1998). "Computer simulation of the evolution of foraging strategies: application to the ichnological record." In: *Paleontological Electronica*, pp. 1–21 (cit. on pp. 146, 165).

Hammer, O, D.A.T. Harper, and P.D Ryan (2001). "PAST: Paleontological statistics software package for education and data analysis." In: *Palaeontologica Electronica* 4. URL: `http://palaeo-electronica.org/2001_1/past/issue1_01.htm` (cit. on p. 68).

Harris, B. S., E. R. Timmer, M. J. Ranger, and M. K. Gingras (2016). "Continental ichnology of the Lower McMurray Formation inclined heterolithic strata at Daphne Island, Athabasca River, north-eastern Alberta, Canada." In: *Bulletin of Canadian Petroleum Geology* 64.2, pp. 218–232 (cit. on p. 1).

Harris, C. R. E. (2003). "Aspects of the sedimentology, ichnology, stratigraphy, and reservoir character of the McMurray Formation, North-East Alberta." MA thesis. University of Alberta (cit. on p. 143).

Hauck, T. E., S. E. Dashtgard, S.G. Pemberton, and M. K. Gingras (2009). "Brackish-water ichnological trends in a microtidal barrier island/embayment system, Kouchibouguac National Park, New Brunswick, Canada." In: *Palaios* 24, pp. 478–496 (cit. on pp. 37, 39, 58, 66, 88–89, 117, 137, 140).

Hayes, B. (2003). "In search of the optimal scumsucking bottomfeeder." In: *American Scientist* 91.5, pp. 392–397 (cit. on p. 145).

Hayes, D. A., E. R. Timmer, J. L. Deutsch, M. J. Ranger, and M. K. Gingras (2017). "Analyzing Dune Foreset Cyclicity In Outcrop With Photogrammetry." In: *Journal of Sedimentary Research* 87.1, pp. 66–74 (cit. on p. 1).

Hein, F. J., C. W. Langenberg, C. Kidston, H. Berhane, T. Berezniuk, and D. K. Cotterill (2001). *A Comprehensive Field Guide for Facies Characterization of the Athabasca Oil Sands, Northeast Alberta (with maps, Air Photos, and Detailed Descriptions of Seventy-eight Outcrop Sections).* Tech. rep. 13. 335 p. Alberta Energy and Utilities Board/Alberta Geological Survey Special Report (cit. on pp. 44, 60).

Hein, Frances J., Graham Dolby, and Brent Fairgrieve (2013). "A regional geologic framework for the Athabasca oil sands, northeastern Alberta, Canada." In: *Heavy-oil and oil-sand petroleum systems in Alberta and beyond:* ed. by F. J. Hein, D. Leckie, S. Larter, and J. R. Suter. AAPG Studies in Geology, pp. 207–250 (cit. on p. 1).

Hils, J. M. and D. I. Hembree (2015). "Neoichnology of the burrowing spiders Gorgyrella inermis (Mygalomorphae: Idiopidae) and Hogna lenta (Araneo-

morphae: Lycosidae)." In: *Palaeontologia Electronica* 18, pp. 1–62 (cit. on p. 96).

Hladil, J., M. Vondra, P. Cejchan, R. Vich, L. Koptikova, and L. Slavik (2010). "The dynamic time-warping approach to comparison of magnetic-susceptibility logs and application to Lower Devonian calciturbidites (Prague Synform Bohemian Massif)." In: *Geologica Belgica* 13, pp. 385–406 (cit. on p. 98).

Hofmann, H. J. (1990). "Computer simulation of trace fossils with random patterns, and the use of goniograms." In: *Ichnos* 1, pp. 15–22 (cit. on p. 145).

Honeycutt, C. E. and R. Plotnick (2008). "Image analysis techniques and gray-level co-occurrence matrices (GLCM) for calculating bioturbation indices and characterizing biogenic sedimentary structures." In: *Computers and Geosciences* 34, pp. 1461–1472 (cit. on pp. 65, 141).

Hovikoski, J., M. Räsänen, M. Gingras, A. Ranzi, and J. Melo (2008). "Tidal and seasonal controls in the formation of Late Miocene inclined heterolithic stratification deposits, western Amazonian foreland basin." In: *Sedimentology* 55.3, pp. 499–530 (cit. on pp. 7, 59, 89–90, 112).

Howard, J. D. and R. W. Frey (1975). "Regional animal-sediment characteristics of Georgia estuaries." In: *Senckenbergiana Maritima* 7, pp. 33–103 (cit. on p. 116).

Hubbard, S. M., M. K. Gingras, and S. G. Pemberton (2004). "Palaeoenvironmental implications of trace fossils in estuarine deposits of the Cretaceous Bluesky Formation, Cadotte region, Alberta, Canada." In: *Fossils and Strata* 51, pp. 68–87 (cit. on pp. 38, 88–89).

Hubbard, S. M., D. G. Smith, H. Nielsen, D. A. Leckie, M. Fustic, R. J. Spencer, and L. Bloom (2011). "Seismic geomorphology and sedimentology of a tidally influenced river deposit, Lower Cretaceous Athabasca oil sands, Alberta, Canada." In: *AAPG Bulletin* 95.7, pp. 1123–1145 (cit. on pp. 1, 7, 33–34, 91, 111, 118, 120).

Hurd, T. J., C. R. Fielding, and A. J. Hutsky (2014). "Variability in sedimentological and ichnological signatures across a river-dominated delta deposit: Peay Sandstone Member (Cenomanian) of the northern Bighorn Basin Wyoming, USA." In: *Journal of Sedimentary Research* 84, pp. 1–18 (cit. on p. 88).

Jablonski, B. V. J. and R. W. Dalrymple (2016). "Recognition of strong seasonality and climatic cyclicity in an ancient fluvially dominated, tidally influenced point bar: Middle McMurray Formation, Lower Steepbank River, north-eastern Alberta, Canada." In: *Sedimentology* 63, pp. 552–585. DOI: `10.1111/sed.12228` (cit. on pp. 1, 91).

Jaglarz, P. and A. Uchman (2010). "A hypersaline ichnoassemblage from the Middle Triassic carbonate ramp of the Tatricum domain in the Tatra Mountains, Southern Poland." In: *Palaeogeography, Palaeoclimatology, Palaeoecology* 292, pp. 71–81 (cit. on p. 57).

Johnson, S. M. and S. E. Dashtgard (2014). "Inclined heterolithic stratification in a mixed tidal–fluvial channel: Differentiating tidal versus fluvial controls on sedimentation." In: *Sedimentary Geology* 301, pp. 41–53 (cit. on pp. 34, 37, 60, 111).

Jones, B. and S. G. Pemberton (1989). "Sedimentology and ichnology of a Pleistocene unconformity–bounded shallowing-upward carbonate sequence: the Ironstone Formation, Salt Creek, Grand Cayman." In: *Palaios* 4, pp. 343–355 (cit. on p. 96).

Keogh, E. J. and M. J. Pazzani (2001). "Derivative dynamic time warping." In: *Proceedings of the SIAM International Conference on Data Mining*. Society for Industrial and Applied Mathematics, pp. 1–11 (cit. on p. 98).

Kineke, G. C., R. W. Sternberg, J. H. Trowbridge, and W. R. Geyer (1996). "Fluid-mud processes on the Amazon continental shelf." In: *Continental Shelf Research* 16.5, pp. 667–696 (cit. on p. 34).

Koy, K. and R. E. Plotnick (2007). "Theoretical and experimental ichnology of mobile foraging." In: *Trace Fossils Concepts, Problems, Prospects*. Ed. by Miller III. Amsterdam: Elsevier, pp. 428–441 (cit. on pp. 146, 167).

Kristensen, E. (1983). "Comparison of polychaete(Nereis spp.) ventilation in plastic tubes and natural sediment." In: *Marine ecology progress series. Oldendorf.* 12.3, pp. 307–309 (cit. on p. 168).

Kvale, E. P., H. W. Johnson, C. P. Sonett, A. W. Archer, and A. Zawistoski (1999). "Calculating lunar retreat rates using tidal rhythmites." In: *Journal of Sedimentary Research* 69, p. 6 (cit. on p. 31).

Kvale, E. P. (2006). "The origin of neap–spring tidal cycles." In: *Marine Geology* 235.1, pp. 5–18 (cit. on p. 31).

— (2012). "Tidal constituents of modern and ancient tidal rhythmites: criteria for recognition and analyses." In: *Principles of Tidal Sedimentology*. Ed. by R. A. Davis, Davis Jr, R. A., and R. W Dalrymple. Netherlands: Springer, pp. 1–17 (cit. on pp. 30–31, 112).

Labrecque, P. A., J. L. Jensen, and S. M. Hubbard (2011a). "Cyclicity in Lower Cretaceous point bar deposits with implications for reservoir characterization, Athabasca Oil Sands, Alberta, Canada." In: *Sedimentary Geology* 242.1, pp. 18–33 (cit. on pp. 1, 7, 33–34, 112–114).

Labrecque, P. A., S. M. Hubbard, J. L. Jensen, and H. Nielsen (2011b). "Sedimentology and stratigraphic architecture of a point bar deposit, Lower Cretaceous McMurray Formation, Alberta, Canada." In: *Bulletin of Canadian Petroleum Geology* 59.2, pp. 147–171 (cit. on pp. 1, 7, 61, 91, 110).

LaCroix, A. D., S. E. Dashtgard, M. K. Gingras, T. E. Hauck, and J.A. MacEachern (2015). "Bioturbation trends across the freshwater to brackish-water transition: refinement of the brackish-water ichnological model." In: *Palaeogeography Palaeoclimatology Palaeoecolology* 440, pp. 66–77 (cit. on p. 116).

Lettley, C. D. (2004). "Elements of a genetic framework for inclined heterolithic strata of the McMurray Formation." 150 pp. MA thesis. University of Alberta (cit. on pp. 143, 168).

Lettley, C. D., M. K. Gingras, N. J. Pearson, and S. G. Pemberton (2005a). "Burrowed stiffgrounds on estuarine point bars: modern and ancient examples, and criteria for their discrimination from firmgrounds developed along omission surfaces." In: *Applied Ichnology.* Ed. by K. Bann J.A. MacEachern, M. K. Gingras, and S. G. Pemberton. SEPM Short Course Notes: 52, pp. 325–333 (cit. on pp. 1, 6, 61, 91).

Lettley, C.D., S.G. Pemberton, M.K. Gingras, M.J. Ranger, and B.J. Blakney (2005b). "Integrating sedimentology and ichnology to shed light on the system dynamics and paleogeography of an ancient riverine estuary." In: *Applied Ichnology.* Ed. by M. K. Gingras J. A. MacEachern K. Bann and S. G. Pemberton. SEPM Short Course Notes, pp. 144–162 (cit. on pp. 1, 6–7, 91, 111, 140).

MacEachern, J. A. and S. G. Pemberton (1992). "Ichnological aspects of Cretaceous shoreface successions and shoreface variability in the Western Interior Seaway of North America." In: *Applications of Ichnology to Petroleum Exploration, a core workshop.* Ed. by S.G. Pemberton. Society of Economic Paleontologists and Mineralogists: core workshop, pp. 57–84 (cit. on p. 37).

MacEachern, J. A., K. L. Bann, J. P. Bhattacharya, and C. D. Howell (2005). "Ichnology of deltas: organism responses to the dynamic interplay of rivers, waves, storms and tides." In: *River Deltas: Concepts, Models and Examples.* Ed. by J. P. Bhattacharya and L. Giosan. SEPM Special Publication, pp. 49–85 (cit. on pp. 37, 111, 137).

MacEachern, J. A., S. G. Pemberton, K. L. Bann, and M. K. Gingras (2007). "Departures from the archetypal ichnofacies: effective recognition of physico-chemical stresses in the rock record." In: *Applied Ichnology.* Ed. by M. K. Gingras J.A. MacEachern K. L. Bann and S. G. Pemberton. SEPM Short Course Notes, pp. 65–93 (cit. on pp. 36, 57, 59, 88, 136).

MacEachern, J. A., S. G. Pemberton, M. K. Gingras, and K. L. Bann (2010). "Ichnology and facies models." In: *Facies Models, edition 4.* Ed. by James, N. P., and R. W Dalrymple. St. Johns, Newfoundland: Geological Association of Canada, pp. 19–58 (cit. on pp. 36, 38).

Mallet, J. L. (2002). *Geomodeling.* Applied Geostatistics Series. New York: Oxford University Press (cit. on p. 41).

Martin, K. D. (2004). "A re-evaluation of the relationship between trace fossils and dysoxia." In: *The Application of Ichnology to Palaeoenvironmental and Stratigraphic Analysis.* Ed. by D. McIlroy. Geological Society, London, Special Publication, pp. 141–156 (cit. on pp. 36–37).

Martinius, A. W., B. V. Jablonski, M. Fustic, R. Strobl, and J.H Van den Berg (2015). "Fluvial to tidal transition zone facies in the McMurray Formation (Christina River, Alberta, Canada), with emphasis on the reflection of flow intensity in bottomset architecture." In: *Fluvial-Tidal Sedimentology* 68 (cit. on p. 1).

McIlroy, D. (2004). "Some ichnological concepts methodologies, applications and frontiers." In: ed. by D. McIlroy. Geological Society, London, Special

Publication, pp. 3–27. DOI: 10.1144/gsl.sp.2004.228.01.02 (cit. on pp. 66, 88).

Merifield, R. S. (2010). "Ultimate uplift capacity of multiplate helical type anchors in clay." In: *Journal of Geotechnical and Geoenvironmental Engineering* 137.7, pp. 704–716 (cit. on p. 167).

Mossop, G. D. (1980). "Facies control on bitumen saturation in the Athabasca Oil Sands." In: *Facts and Principles of World Petroleum Occurrence.* Ed. by A.D. Miall. Canadian Society of Petroleum Geologists Memoir, pp. 609–632 (cit. on p. 6).

Mossop, G. D. and P. D. Flach (1983). "Deep channel sedimentation in the Lower Cretaceous McMurray Formation, Athabasca Oil Sands, Alberta." In: *Sedimentology* 30.4, pp. 493–509 (cit. on p. 6).

Moy, C. M., G. O. Seltzer, D. T. Rodbell, and D. M. Anderson (2002). "Variability of El Nino/southern oscillation activity at millennial timescales during the Holocene epoch:" in: *Nature* 420, pp. 162–165 (cit. on p. 113).

Musial, G., J. Y. Reynaud, M. K. Gingras, H. Fenies, R. Labourdette, and O. Parize (2012). "Subsurface and outcrop characterization of large tidally influenced point bars of the Cretaceous McMurray Formation (Alberta, Canada)." In: *Sedimentary Geology* 279, pp. 156–172 (cit. on pp. 1, 33–34, 62, 90–91, 117, 143, 171).

Nara, M. (1997). "High-resolution analytical method for event sedimentation using Rosselia socialis." In: *Palaios* 12, pp. 489–494 (cit. on pp. 59, 61).

Nardin, T., H. R. Feldman, and B. J. Carter (2013). "Stratigraphic architecture of a large-scale point-bar complex in the McMurray Formation: Syncrude's Mildred Lake mine, Alberta, Canada," in: *Heavy-oil and oil-sand petroleum systems in Alberta and beyond:* ed. by F.J.Hein, D. Leckie, S. Larter, and J. R. Suter. AAPG Studies in Geology, pp. 273–311 (cit. on pp. 1, 7, 33, 37, 61, 110).

Netto, R.G., L.A. Buatois, M.G. Mangano, and P.R.M.N. Balistieri (2007). "Gyrolithes as a multipurpose burrow: An ethologic approach." In: *Revista brasileira de paleontologia* 10.3, pp. 157–168 (cit. on p. 143).

Papentin, F. (1973). "A Darwinian evolutionary system III: experiments on the evolution of feeding patterns." In: *Journal of Theoretical Biology* 39, pp. 431–445 (cit. on p. 145).

Pedregosa, F., G. Varoquaux, A. Gramfort, V. Michel, B. Thirion, O. Grisel, P. Blondel M. Prettenhofer, R. Weiss, V. Dubourg, J. Vanderplas, A. Passos, D. Cournapeau, M. Brucher, M. Perrot, and E. Duchesnay (2011). "Scikit-learn: machine learning in Python." In: *The Journal of Machine Learning Research* 12, pp. 2825–2830 (cit. on p. 96).

Pemberton, S. G., P. D. Flach, and G. D. Mossop (1982). "Trace fossils from the Athabasca oil sands, Alberta, Canada." In: *Science* 217.4562, pp. 825–827 (cit. on pp. 1, 6, 34, 37, 57, 59, 88, 91, 116–117, 136).

Pemberton, S. G. and D. M. Wightman (1992). "Ichnological characteristics of brackish water deposits." In: *Applications of Ichnology to Petroleum*

Exploration. Ed. by S.G. Pemberton. SEPM Core Workshop, pp. 141–167 (cit. on pp. 59, 137).

Pervesler, P., A. Uchman, J. Hohenegger, and S. Dominici (2011). "Ichnological record of environmental changes in early Quaternary (Gelasian–Calabrian) marine deposits of the Stirone Section, northern Italy." In: *Palaios* 26, pp. 578–593 (cit. on p. 96).

Phillips, C., D. McIlroy, and T. Elliott (2011). "Ichnological characterization of Eocene/Oligocene turbidites from the Grès d'Annot Basin, French Alps, SE France." In: *Palaeogeography, Palaeoclimatology, Palaeoecology* 300, pp. 67–83 (cit. on p. 88).

Pickerill, R. K. (1994). "Nomenclature and taxonomy of invertebrate trace fossils." In: *The palaeobiology of trace fossils*. Ed. by S. K Donovan. Chichester: John Wiley and Sons, pp. 3–42 (cit. on p. 58).

Plotnick, R. E. (2003). "Ecological and L-system based simulations of trace fossils." In: *Palaeogeography, Palaeoclimatology, Palaeoecology* 192.1, pp. 45–58 (cit. on pp. 145–146).

Plotnick, R. E. and K. Koy (2005). "Let us prey: Simulations of grazing traces in the fossil record." In: *Proceedings GeoComputation 2005: 8th International Conference on GeoComputation, Ann Arbor, Michigan*, pp. 1–13 (cit. on pp. 146, 166–167).

Plotnick, R. E. (2007). "Chemoreception, odor landscapes, and foraging in ancient marine landscapes." In: *Palaeontologia Electronica* 10 (cit. on p. 146).

Pollard, J. E., R. Goldring, and Andbuck S.G. (1993). "Ichnofabrics containing Ophiomorpha: significance in shallow-water facies interpretation." In: *Journal of the Geological Society* 150, pp. 149–164. DOI: `10.1144/gsjgs.150.1.0149` (cit. on pp. 89, 113).

Powell, E. N. (1977). "The relationship of the trace fossil Gyrolithes (=Xenohelix) to the family Capitellidae (Polychaeta)." In: *Journal of Paleontology* 51, pp. 552–556 (cit. on p. 143).

Prasad, Y.V. and S.N. Rao (1996). "Lateral capacity of helical piles in clays." In: *Journal of geotechnical engineering* 122.11, pp. 938–941 (cit. on p. 168).

Ranger, M. J. and S. G. Pemberton (1988). "Marine influence on the McMurray Formation in the Primrose area, Alberta." In: *Sequences, Stratigraphy, Sedimentology: Surface and Subsurface*. Ed. by D.P. James and D. A. Leckie. Canadian Society of Petroleum Geologists Memoir, pp. 439–450 (cit. on pp. 1, 91, 143, 171).

— (1991). "Multivariate analysis of ichnofossil associations in the subsurface Bluesky Formation (Albian, Alberta, Canada)." In: *Palaeogeography, Palaeoclimatology, Palaeoecology* 85, pp. 169–187 (cit. on p. 96).

— (1992). "The sedimentology and ichnology of estuarine point bars in the McMurray Formation of the Athabasca Oil Sands deposit, northeastern Alberta, Canada." In: *Applications of Ichnology to Petroleum Exploration*. Ed. by S. G. Pemberton. Society of Economic Paleontologists and Mineralogists, Core Workshop, pp. 401–421 (cit. on pp. 1, 38, 61, 91, 117, 137).

Ranger, M.J. and S. G. Pemberton (1997). "Elements of a stratigraphic framework for the McMurray Formation in south Athabasca area, Alberta." In: *Petroleum Geology of the Cretaceous Lower Manville Group: Western Canada.* Ed. by S.G. Pemberton and D.P. James. Canadian Society of Petroleum Geologists Memoir, pp. 263–291 (cit. on pp. 1, 6, 37–38, 90–91, 96).

Ranger, M.J. and M.K. Gingras (2003). "Discussion of Langenberg, C.W. Hein, F.J. Lawton, D. Cunningham, J.: Seismic modeling of fluvial-estuarine deposits in the Athabasca oil sands using ray-tracing techniques, Steepbank River area, northeastern Alberta." In: *Bulletin of Canadian Petroleum Geology* 51, pp. 347–353 (cit. on p. 143).

Raup, D. M. and A. Seilacher (1969). "Fossil foraging behavior: computer simulation." In: *Science* 166, pp. 994–995 (cit. on pp. 145, 147, 165).

Reineck, H. E. (1967). "Parameter von Schichtung und bioturbation." In: *Geologische Rundschau* 56, pp. 420–438 (cit. on pp. 9, 39, 65, 89, 140).

Remane, A. (1934). "Die Brackwasserfauna." In: *Verhandlungen der Deutschen Zoologischen Gesellschaft* 36, pp. 34–74 (cit. on p. 116).

Rhoads, D. C. and J. W. Morse (1971). "Evolutionary and ecologic significance of oxygen- deficient marine basins." In: *Lethaia* 4, pp. 413–428 (cit. on p. 116).

Richter, R. (1928). "Psychische Reaktionen fossiler Tiere, Helminthoiden und Nereiten als Fragen der Fahrtenkunde an die Tierpsychologie." In: *Palaeobiologica* 1, pp. 225–244 (cit. on p. 145).

Ropelewski, C. F. and M. S. Halpert (1986). "North American precipitation and temperature patterns associated with the El Niño/southern oscillation (ENSO)." In: *Monthly Weather Review* 114, pp. 2352–2362 (cit. on p. 114).

El-Sabbagh, A., H. Mansour, and M. El-Hedeny (2015). "Taphonomy and paleoecology of Cenomanian oysters from the Musabaa Salama area, southwestern Sinai, Egypt." In: *Geosciences Journal* 19, pp. 655–679. DOI: `10.1007/s12303-015-0014-5` (cit. on p. 96).

Savrda, C. E. and D. J. Bottjer (1989). "Trace-fossil model for reconstructing oxygenation histories of ancient marine bottom waters: application to Upper Cretaceous Niobrara Formation, Colorado." In: *Palaeogeography, Palaeoclimatology, Palaeoecology* 74, pp. 49–74 (cit. on p. 37).

Savrda, C. E. (2007). "Trace fossils and benthic oxygenation." In: *Trace Fossils: Concepts, Problems, Prospects: Elsevier, New York, p.* Ed. by W. Miller Iii. 149–158 (cit. on pp. 88, 116).

Schoengut, J. A. (2011). "Sedimentological and ichnological characteristics of modern and ancient channel-fills, Willapa Bay, Washington." 216 pp. MA thesis. University of Alberta (cit. on pp. 7, 110).

Seilacher, A. (1978). "Use of trace fossil assemblages for recognizing depositional environments." In: *Trace Fossil Concepts.* Ed. by B. Basan. Society of Economic Paleontologists and Mineralogists: Short Course, pp. 167–181 (cit. on p. 37).

Shchepetkina, A., M. K. Gingras, S. G. Pemberton, and J. A. MacEachern (2016). "What does the ichnological content of the Middle McMurray Formation tell us?" In: *Bulletin of Canadian Petroleum Geology* 64.1, pp. 24–46 (cit. on p. 2).

Simo, V. and A. Tomasovych (2013). "Trace-fossil assemblages with a new ichnogenus in "spotted" (Fleckenmergel–Fleckenkalk) deposits: a signature of oxygen-limited benthic communities." In: *Geologica Carpathica* 64, pp. 355–374 (cit. on p. 96).

Sims, D. W., A. M. Reynolds, N. E. Humphries, E. J. Southall, V. J. Wearmouth, B. Metcalfe, and R. J. Twitchett (2014). "Hierarchical random walks in trace fossils and the origin of optimal search behavior." In: *Proceedings of the National Academy of Sciences* 111.30, pp. 11073–11078 (cit. on p. 146).

Sisulak, C. F. and S. E. Dashtgard (2012). "Seasonal controls on the development and character of inclined heterolithic stratification in a tide-influenced, fluvially dominated channel: Fraser River, Canada." In: *Journal of Sedimentary Research* 82.4, pp. 244–257 (cit. on pp. 34, 60).

Smith, D. G. (1988). "Tidal Bundles and Mud Couplets in the McMurray Formation, Northeastern Alberta, Canada." In: *Geological Notes: Bulletin of Canadian Petroleum Geology* 36.2, pp. 216–219 (cit. on pp. 6, 33).

Smith, D. G., S. M. Hubbard, D. A. Leckie, and M. Fustic (2009). "Counter point bar deposits: lithofacies and reservoir significance in the meandering modern Peace River and ancient McMurray Formation, Alberta, Canada." In: *Sedimentology* 56.6, pp. 1655–1669 (cit. on pp. 7, 111).

Smith, J. J., S. T. Hasiotis, M. J. Kraus, and D. T. Woody (2008). "Relationship of floodplain ichnocoenoses to paleopedology paleohydrology, and paleoclimate in the Willwood Formation, Wyoming, during the Paleocene–Eocene Thermal Maximum." In: *Palaios* 23, pp. 683–699 (cit. on p. 96).

Somerfield, P. J. (2008). "Identification of the Bray-Curtis similarity index: Comment on Yoshioka." In: *Marine Ecology Progress Series* 372, pp. 303–306 (cit. on p. 121).

Speta, M., M. K. Gingras, and B. Rivard (2016). "Shortwave Infrared Hyperspectral Imaging: A novel method for enhancing the visibility of sedimentary and biogenic features in oil-saturated core." In: *Journal of Sedimentary Research* 86, pp. 830–842 (cit. on p. 118).

Taylor, A. M. and R. Goldring (1993). "Description and analysis of bioturbation and ichnofabric; Organisms and sediments; relationships and applications." In: *Journal of the Geological Society of London* 150, pp. 141–148 (cit. on pp. 9, 39, 65, 89, 140).

Taylor, A. M., R. Goldring, and S. Gowland (2003). "Analysis and application of ichnofabrics." In: *Earth Science Reviews* 60, pp. 227–259 (cit. on pp. 36, 88, 116).

Thomas, R. G., D. G. Smith, J. M. Wood, J. Visser, E. A. Calverley-Range, and E. H. Koster (1987). "Inclined heterolithic stratification—terminology,

description, interpretation and significance." In: *Sedimentary Geology* 53.1, pp. 123–179 (cit. on pp. 7, 41, 89).

Timmer, E. R., M. K. Gingras, M. L. Morin, M. J. Ranger, and J. P. Zonneveld (2016a). "Laminae-scale rhythmicity of inclined heterolithic stratification, lower Cretaceous McMurray Formation, NE Alberta, Canada." In: *Bulletin of Canadian Petroleum Geology* 64, pp. 199–217 (cit. on pp. 91, 112–113, 117).

Timmer, E. R., M. K. Gingras, and J. P. Zonneveld (2016b). "PYCHNO: A core-image quantitative ichnology logging software." In: *Palaios* 31, pp. 525–532. DOI: doi.org/10.2110/palo.2015.088 (cit. on pp. 95, 117–118, 140).

— (2016c). "Spatial and temporal significance of process ichnology data from silty-mudstone beds of inclined heterolithic stratification, Lower Cretaceous McMurray Formation, NE Alberta, Canada." In: *Palaios* 31, pp. 533–548. DOI: doi.org/10.2110/palo.2015.089 (cit. on pp. 2, 65, 122, 137, 139).

Tolan, J. M. (2007). "El Nino-Southern Oscillation impacts translated to the watershed scale: Estuarine salinity patterns along the Texas Gulf Coast, 1982 to 2004." In: *Estuarine, Coastal and Shelf Science* 72, pp. 247–260 (cit. on p. 114).

Torrence, C. and G. P. Compo (1998). "A practical guide to wavelet analysis." In: *Bulletin of the American Meteorological society* 79.1, pp. 61–78 (cit. on pp. 33, 99, 122).

Trauth, M.H. (2013). "TURBO2: A MATLAB simulation to study the effects of bioturbation on paleoceanographic time series." In: *Computers and Geosciences* 61, pp. 1–10 (cit. on p. 145).

Trenberth, K. E. (1997). "The definition of El Nino." In: *Bulletin of the American Meteorological Society* 78, pp. 2771–2777 (cit. on p. 113).

Uchman, A., F. J. Rodriguez-Tovar, E. Machaniec, and M. Kedzierski (2013). "Ichnological characteristics of Late Cretaceous hemipelagic and pelagic sediments in a submarine high around the OAE-2 event: a case from the Rybie section, Polish Carpathians." In: *Palaeogeography, Palaeoclimatology, Palaeoecology* 370, pp. 222–231 (cit. on p. 88).

Virtasalo, J. J., E. Bonsdorff, M. Moros, K. Kabel, A. T. Kotilainen, D. Ryabchuk, A. Kallonen, and K. Hämäläinen (2011). "Ichnological trends along an open-water transect across a large marginal-marine epicontinental basin, the modern Baltic Sea." In: *Sedimentary Geology* 241, pp. 40–51 (cit. on p. 88).

Vogel, S. (2007). "Living in a physical world X. Pumping fluids through conduits." In: *Journal of biosciences* 32.2, pp. 207–222 (cit. on p. 168).

Wightman, D. M. and S. G. Pemberton (1997). "The Lower Cretaceous (Aptian) McMurray Formation: an overview of the Fort McMurray area, northeastern Alberta." In: *Petroleum Geology of the Cretaceous Mannville Group, Western Canada*. Ed. by S. G. Pemberton and D. P. James. Canadian Society of Petroleum Geologists, Memoir, pp. 312–344 (cit. on p. 91).

Wignall, P. B. and K. J. Myers (1988). "Interpreting benthic oxygen levels in mudrocks: a new approach." In: *Geology* 16, pp. 452–455 (cit. on p. 66).